IECO

Volume 9 No 2 Year 2026

- Volume 9
- No 2
- Year 2026

International Journal Of
Industrial Electronics Control and Optimization

IECO

University of
Sistan and Baluchestan

Iranian Association of
Electrical and Electronics Engineers

International Journal Of

Industrial Electronics Control and Optimization

In This Issue:

Research Articles:

- Photovoltaic Fault Diagnosis with CNN-ResNet and Adaptive Learning Rate Scheduling
  Sepehr Shakibi; Amir Mohammad Farahani; Mohsen Hamzeh........119-129
- Improved Method for Capacitor Voltage Balancing Control and Capacitance Monitoring in Modular Multilevel Converter
  Mohsen Rahmani Haredasht; S. Masoud Barakati; Mohammad Bagheri Hashkavayi........131-144
- Multi-Class Short-Term Voltage Stability Assessment Considering the Missing Data
  AmirHossein Babaali; Mohammad Taghi Ameli........145-155
- An Adaptive Robust Square Root Unscented Kalman Filter for State of Charge Estimation for Lithium-ion Batteries
  Ramezan Havangi; Fatemeh Karimi........157-171
- RSS Localization in the Presence of Byzantine Attacks Using MAP Estimation
  Mahdieh Mohammadi; Hadi Zayyani; Mehdi Bekrani........173-181
- A Novel Cascade Control Strategy for Robust Fuel Cell Systems Using Variable Gain Sliding Technique
  Violet Farhad; Seyed Mehdi Mirhosseini-Alizamini........183-198
- Numerical Assessment of Optimal Control Problems with Variable-Order Fractional Integro-Differential Equation Based on Laguerre Wavelets Functions
  Maryam Alipour; Samaneh Soradi zeid........199-209
- State-of-Charge Fusion Estimation of Lithium-Ion Batteries based on the Mathematical Models of the Open Circuit Voltage Curve
  Mohammad Moodi; Mohammad Reza Ramezani-al........211-221
- A Semi-Quadratic Buck-Boost Converter with Two Operating Modes and a Sustained Input-Output Current for PV Applications
  Mustafa Okati; Mohammad Osmani-Bojd........223-238
- A Mathematical Framework for Designing Precise RBW Filters Using Standard Implementation Techniques in EMI Applications
  Seyed Fariborz Zarei; Saeed Hasanzadeh........239-246

Editor-in-Chief's Message

International Journal of Industrial Electronics, Control and Optimization (IECO)Volume 9, No. 2, 2026

It is my pleasure to present Volume 9, Issue 2 (2026) of the International Journal of Industrial Electronics, Control and Optimization (IECO).

This issue highlights the dynamic progress in industrial electronics, advanced control strategies, and optimization methodologies. The published articles cover a wide spectrum of topics, including capacitor voltage balancing in modular multilevel converters, photovoltaic fault diagnosis using deep learning, short-term voltage stability assessment under missing data, and advanced estimation techniques for lithium-ion batteries.

Several contributions focus on robust control and optimization frameworks, such as MAP-based localization under Byzantine attacks, cascade control strategies for fuel cell systems, and fractional integro-differential approaches for optimal control problems. In addition, innovative designs in power electronics are presented, including semi-quadratic buck-boost converters for PV applications and precise RBW filter design for EMI applications.

A recurring theme across these works is the integration of computational intelligence and mathematical modeling into classical engineering challenges. These approaches are reshaping how industrial systems are monitored, optimized, and controlled—enhancing both reliability and efficiency.

IECO remains committed to fostering international collaboration and maintaining rigorous scholarly standards through a transparent peer-review process. We extend our sincere gratitude to our authors, reviewers, and editorial board members for their invaluable contributions.

We look forward to continued advancements that bridge theoretical insight with practical innovation in industrial electronics, control, and optimization.

Prof. S. Masoud Barakati
Editor-in-Chief
International Journal of Industrial Electronics, Control and Optimization

About Journal

The University of Sistan and Baluchestan entered into strategic partnership with Iranian Association of Electrical and Electronic Engineers (IAEEE) to publish the **International Journal of Industrial Electronics Control and Optimization (IECO)**. The IECO is a refereed international journal which presents to the international scientific community important results of work in these fields, whether in the form of modeling simulation, analysis, fundamental research, development, application, design or real-time implementation. The scope of IECO is broad, encompassing all aspects of Industrial Electronics, Control and Optimization.

Note: International Journal of Industrial Electronics, Control and Optimization (IECO) has qualified to **ACADEMIC RESEARCH JOURNAL (ELMI-PAJOHESHI)** status certified by the ministry of Science, Research and Technology of Iran (No. 231566/3/18 dated 1396/10/09), and is published by the University of Sistan and Baluchestan through a formal partnership (No. 952/2/1500 dated 1395/11/04) with Iranian Association of Electrical and electronic Engineers (IAEEE) in order to develop scientific and research cooperation.

Aims and Scope

International Journal of Industrial Electronics, Control and Optimization (IECO) is a Peer reviewed journal of advanced and state-of-the-art in the science and engineering of Industrial Electronics, Control and Optimization. Its Scope encompasses the applications of Industrial Electronics, power systems, control, optimization and computational intelligence for the enhancement of industrial and manufacturing system and processes. The scope of the journal include the following:

I. Industrial Electronics

- Low and high-power converters
- Renewable energy
- Drive control techniques
- Techniques for advanced power semiconductor devices
- Power quality and utility applications
- Communications
- Flexible AC Transmission Systems (FACTS)
- Control in power electronics

- Electromagnetic and thermal performance of electronic power converters
- Motion control, robotics, sensors and actuators
- Fault detection and diagnosis
- Power systems
- Factory automation, communication, and computer networks

II. Control

- Adaptive control
- Control of process systems
- Control theory
- Data processing
- Design of control systems
- Hybrid systems
- Identification and observation
- Intelligent systems
- Model-predictive control
- Optimal control
- Robust control
- Fractional order systems

III. Optimization

- Ant Colony
- Chaos Theory
- Evolutionary Computing
- Fuzzy Computing
- Hybrid Methods
- Immunological Computing
- Neuro Computing
- Particle Swarm
- Probabilistic Computing
- Rough Sets
- Wavelet

Dr. Mehrdad Kazerani-Ryerson University
Dr. Hasan Monsef-University of Tehran
Dr. Massoud Rashidi Nejad-University of Shahid Bahonar Kerman
Dr. Hossein Askarian-Abyaneh-Amirkabir University of Technology (Tehran Polytechnic)
Dr. Mohammad Monfared- Ferdowsi University of Mashhad
Dr. Saeed Tavakoli-University of Sistan and Baluchestan
Dr. Mahmood Joorabian-Shahid Chamran University of Ahvaz
Dr. Reza Ghazi-Ferdowsi University of Mashhad
Dr. Mehri Mehrjoo-University of Sistan and Baluchestan
Dr. Mohammad Reza Aghaebrahimi- University of Birjand
Dr. Bin Wu- Toronto Metropolitan University
Dr. Mahmoud Okati Sadegh-University of Sistan and Baluchestan
Dr. Tahere Fanaei Sheikhosleslami-University of Sistan and Baluchestan

Assistant Editors

Dr. Sobhan Dorahaki- Qatar University
Dr. Abbas-Ali Zamani-Technical and vocational University
Dr. Mojgan MollahassaniPour-University of Sistan and Baluchestan
Dr. Samaned Soradi-zeid-Industry and Mining (Khash)
Dr. Majid Ghadrdan- University of Sistan and Baluchestan
Dr. Alireza HosseinPur-University of Zabol
Dr. Ahmad khajeh-University of Sistan and Baluchestan
Dr. Hamde Torabi-University of Sistan and Baluchestan
Dr. Mahdi Kazeminia- Velayat University
Dr. Masoumeh Rezaei- University of Sistan and Baluchestan
Dr. Poria Jafari-University of Sistan and Baluchestan
Dr. Amin Zarei -University of Sistan and Baluchistan
Dr. Saeed Yousefi-Darmian-University of Sistan and Baluchestan
Dr. Maryam Khamar- University of Isfahan
Dr. Mohammad Ali Azghandi-University of Sistan and Baluchistan
Dr. Ali Hassannia -University of Sistan and Baluchistan
Dr. Ehsan Adibnia- University of Sistan and Baluchestan

Executive Manager

Kazem Piran

International Journal Of
Industrial Electronics Control and Optimization
IECO
Print ISSN: 3517-2645
Online ISSN: 3568-2645
Homepage: https://ieco.usb.ac.ir/

Photovoltaic Fault Diagnosis with CNN-ResNet and Adaptive Learning Rate Scheduling

Sepehr Shakibi | Amir Mohammad Farahani | Mohsen Hamzeh

School of Electrical and Computer Engineering, University of Tehran, Tehran, Iran.
Corresponding author's email: mohsenhamzeh@ut.ac.ir

Article Info

Article type:
Research Article

Article history:
Received: 04-April-2025
Received in revised form:
17-June-2025
Accepted: 30-June-2025
Published online: 22-June-2026

Keywords:
Deep learning,
Fault detection,
Learning rate schedule,
Photovoltaic systems,
Renewable energy reliability.

ABSTRACT

Photovoltaic (PV) systems are a backbone of the infrastructure of renewable energy, with their usage growing significantly. Early fault detection of these systems is essential to enhance their reliability and efficiency. Despite the development of fault diagnosis methods of PV system promoted by machine learning models such as ensemble learning, support vector machine and neural networks, challenges in achieving high accuracy and generalization persist. In this paper, propose a deep learning method based on a ResNet architecture for reliable and efficient fault detection, including the following categories: Normal Operation, Short-Circuit, Degradation, Open Circuit, and Shadowing. Also devise a new learning rate schedule(LRS), which considerably improves the training dynamics and enables a 63% improvement in model performance. The suggested method achieves excellent performance, reaching 99.8% accuracy throughout the training, validation and testing phases. The results obtained showcase the potential of ResNet-based architectures, in addition to prowess in adaptive learning rate strategies, at enhancing the reliability of photovoltaic systems through scalable and precise fault diagnosis.

I. Introduction

Photovoltaic (PV) systems are utilized in various applications, and analyzing fault occurrences can significantly enhance their efficiency and operation. Faults in photovoltaic systems can be caused by reduced output power and damage to healthy modules[1]. Therefore, the automatic monitoring of faults in installed PV arrays is essential. Increasing user awareness about faults and their effects is critical, as this awareness can reduce photovoltaic system losses by up to 15%[2]. Consequently, detecting faults using rapid and accurate approaches is of great importance.

Numerous fault detection and diagnosis (FDD) methods have been proposed, which can be classified into two main categories: visual and thermal methods, and electrical methods. Electrical methods can be further divided into five subcategories, one of which includes artificial intelligence techniques [3]. Due to the characteristics of deep learning (DL) methods, intelligent FDD has become more automated and effective in the context of big data [4].

In the literature, various deep DL methods have explored customized architectures rooted in artificial neural networks, such as multi-layer perceptrons (MLP), convolutional neural networks (CNN), and long short-term memory (LSTM) networks, which are widely employed for fault diagnosis in photovoltaic systems. For instance, [5], introduces an artificial neural network (ANN) that processes three inputs through a single hidden layer of nine neurons, yielding six outputs: normal operation, one, two, or three open diodes, and one or two short-circuited diodes. Another proposed architecture is a dual-stream neural network for diagnosing five fault conditions and normal operation. This architecture incorporates LSTM and 2D-CNN with an attention mechanism. It combines multimodal data, including the I-V curves of PV strings and transformed 2D images, to deeply extract features under various PV shading conditions, ensuring accurate fault diagnosis [6]. In [7], a customized autoencoder-based semi-supervised deep learning method is followed by a hybrid SVM-LR model to classify four types of faults. In [8], a method for fault detection in PV systems using Siamese networks based on MobileNet (SiamMN) and

Publisher: University of Sistan and Baluchestan

panoramic I-V features (PIVF) is presented. SiamMN consists of two parameter-sharing MobileNetv3 subnetworks that compute the similarity between two input PIVF features. These PIVFs are extracted from corrected and normalized I-V curves, and random pairing is employed to enhance the model's generalization capability. In [9], the Compact Convolutional Transformer (CCT) is used. This architecture combines CNNs with transformer mechanisms, allowing for efficient processing of image data while preserving spatial information. The proposed hybrid deep learning model for fault detection and classification in grid-connected PV systems integrates Wavelet Packet Transform (WPT) for preprocessing PV voltage signals, Stacked Autoencoders (SAE) for automatic feature extraction, the Equilibrium Optimizer Algorithm (EOA) for optimal feature selection, and LSTM for classification. This architecture enables the model to effectively detect and classify various faults, achieving an impressive accuracy of 99.93% in noiseless conditions while maintaining robustness against noise. The outputs include precise fault classifications and enhanced operational reliability, significantly improving maintenance scheduling and safety in PV systems [10]. Additionally, [11] introduce a hierarchical classification (HC) approach combined with machine learning techniques to detect and classify Line-Line (LL) and Line-Ground (LG) faults under challenging conditions like high impedance and low mismatch levels, achieving experimental accuracies of 96.66% and 91.66% for LL and LG faults, respectively, with reduced dataset requirements. In [12], PV-YOLO—a lightweight YOLO-based model enhanced with a transformer-based PVTv2 backbone and CBAM attention mechanism—targets fault detection in drone-captured infrared images, reaching a mean Average Precision (mAP) of 92.56% and excelling at identifying small occlusions. Furthermore, [13] transforms I-V and P-V curves into graphical features using the Gramian Angular Difference Field (GADF), employing a CNN with CBAM modules to diagnose faults in dust-affected conditions, attaining accuracies up to 99.17% even with noisy data and proving robust across varied PV configurations. Additionally, [14] propose a Stacked Autoencoder (SAE)-based approach to detect degradation in series resistance (Rs) in PV systems, utilizing Mean Squared Error (MSE) to quantify reconstruction errors, achieving robust fault detection under varying radiation and temperature conditions, with MSE analysis revealing high sensitivity to fault-induced changes. [15] introduce a deep learning framework for crack segmentation in PV cells using ensemble learning with U-Net, LinkNet, FPN, and Attention U-Net models, achieving a mean Intersection-over-Union (mIOU) of 54.19% and linking crack orientation and size to power efficiency losses, offering a comprehensive approach to both detection and impact assessment. [16] present a lightweight CNN optimized by the Energy Valley Optimizer (EVO) with Continuous Wavelet Transform (CWT)-generated scalograms as input, achieving test accuracies of 100%, 99.86%, and 93.75% across balanced, unbalanced, and noisy datasets, respectively, demonstrating superior performance and efficiency for deployment on low-cost edge devices. Additionally, [17] proposes a hybrid DL approach blending CNN with Bidirectional Gated Recurrent Unit (Bi-GRU) to detect and classify faults like open circuits, short circuits, and partial shading in PV systems, harnessing dynamic maximum power point outputs to deliver near-perfect accuracies validated with real-world data. [18] introduces a DL method utilizing an Autoencoder neural network for feature extraction, paired with an ANN for classifying short-circuit faults in a 9.54 kW PV system in Algeria, achieving flawless accuracy in noiseless settings and robust performance with noisy data. In addition to deep learning-based methods, other model-based and sensor-reduction techniques have shown promise. For example, an explicit piecewise quadratic model has been introduced for accurate I-V curve modeling in PV systems, offering linearity in parameters and low computational cost while maintaining high precision [19]. Moreover, innovative group-based monitoring techniques have been applied for open-circuit fault detection in converter systems, enabling fast diagnosis with a reduced number of sensors and minimal computational overhead [20]. These approaches reflect the broader trend toward efficient and accurate fault detection across various PV-related applications. Additionally, in [21] to combine various base classifiers using irradiance, temperature, current, and power as inputs. Its advantage lies in improved accuracy (94.25%) over individual classifiers. However, its limitation is high computational complexity due to ensemble learning. In [22], a hybrid classification system using chaotic-enhanced butterfly optimization and MLP was applied to electroluminescence (EL) images. It achieved 98.2% accuracy and robustness across evaluation metrics. Its strength is strong image-based detection using swarm intelligence, but the system depends on high-quality EL imaging, which can be costly and impractical for real-time industrial use. Another study [23] deployed AI-assisted monitoring across 150 PV stations in Taiwan. It used short-term power prediction combined with fault diagnosis and inverter efficiency tracking. Its advantage is real-world deployment with over 4,700 inverters and scalable architecture. However, its integration requires access to frequent irradiance simulation and high infrastructure setup. A focused method in [24] proposed ANN-based fault detection for standalone PV systems using power loss parameters, achieving 95% accuracy. The advantage is simple, interpretable input and suitability for real-time environments. Yet, it depends on simulation-derived fault data, which may limit generalization.

These diverse methodologies underscore the increasing sophistication of DL techniques in tackling the complex challenges of PV fault diagnosis, adeptly addressing intricate fault patterns and adapting to real-world environmental variations, thus laying a solid groundwork for future advancements in this field.

In this paper, we propose a customized CNN-ResNet architecture that utilizes a learning rate scheduler (LRS). This architecture combines the strengths of CNN and ResNet. CNN architectures, along with some other models, face the vanishing gradient problem as the number of layers increases. As mentioned in [25], ResNet improves this challenge with shortcut connections. These connections in proposed architecture add the output of previous convolutional layers to the input, allowing the model to learn both previous and current features. The proposed model effectively classifies the considered faults, and when combined with a LRS, it results in reduced loss. Besides the model's power, it also provides a lightweight solution that can be used in real-time industrial environments. Moreover, it is important to note that the high accuracy achieved by the proposed method is not easily replicable using conventional classification techniques. As highlighted in [26] and [27], the dataset involves both simulated and real-world PV fault scenarios with overlapping patterns and varying environmental conditions. Classical machine learning methods such as k-NN, SVM, or shallow neural networks struggle with distinguishing between subtle fault types like degradation and shadowing under irradiance and temperature fluctuations. In contrast, our customized CNN-ResNet architecture, together with its adaptive learning strategy, addresses these challenges and provides a more robust and scalable solution.

This study is the first to couple a 1-D CNN–ResNet backbone with a two-phase adaptive learning-rate scheduler (linear warm-up + exponential decay) for photovoltaic fault diagnosis. The scheme achieves 99.8 % accuracy on a hybrid real/simulated dataset that includes five fault categories and severe class imbalance, and lowers validation loss by 63 % relative to the same network trained with a fixed LR. Thanks to lightweight 1-D convolutions and three residual blocks, the final model is suitable for real-time deployment on low-cost edge devices, outperforming MLP-, SVM- and vanilla CNN-based baselines reported in [26] (95.3 %) and [27] (97.4 %).

II. Methodology

A. Dataset and Faults

In this paper, the dataset from [26] was utilized, which was generated using a hybrid approach that combines real data from a PV plant with simulated data. It contains 16 days of data from a grid-tied photovoltaic plant, with two strings, each consisting of 8 PV modules, connected to a 5 kW grid-tied power inverter. Faults were introduced under controlled field conditions using hardware modifications. Short-circuit faults were created by connecting adjacent module terminals using sockets. Degradation was simulated by inserting resistors between modules, representing gradual performance decline. Open-circuit faults were introduced by disconnecting one string entirely from the inverter using circuit breakers. Shadowing was caused by physically blocking sunlight with opaque materials on selected modules. These fault types were also reproduced in simulation using a PSIM/Simulink model calibrated to the real system, enabling broader environmental coverage for training purposes. The details of the faults and their corresponding labels are summarized in Table I. Additionally, the dataset includes six features, with measurements for the voltage and current of each string, as well as irradiance and temperature. The temperature and irradiance ranges for the dataset were fixed, which could impact the model's ability to generalize to environmental conditions outside these predefined limits, potentially affecting its performance under more extreme or varying temperature and irradiance conditions.

TABLE I Fault categories and labels

Label	Fault	Description
0	Normal Operation	No faults
1	Short-Circuit	Short Circuit between 2 modules of a String
2	Degradation	There is a resistance between 2 modules of a String
3	Open Circuit	One String disconnected from the power inverter
4	Shadowing	Shadow in one or more modules

The parameters selected for analysis and used as inputs to the model are: irradiance, module temperature, string 1 voltage, string 1 current, string 2 voltage, and string 2 current. These parameters were chosen based on their strong influence on the power output of the system and their relevance in detecting fault conditions. The final input feature set consists of these six variables, which are available both in real measurements and in the simulated data. This ensures consistency and comparability across the full dataset.

B. Preprocessing

Data preprocessing is a crucial step in deep learning to enhance model performance. It involves cleaning the data by addressing noise, missing values, and irrelevant features. The data is then normalized and scaled to ensure all features are within a similar range, which helps the model learn more effectively. This preprocessing ensures consistency across training, validation, and testing datasets, leading to improved accuracy and faster model training.

To provide a clearer understanding of the dataset preprocessing, the dataset was analyzed and confirmed to not contain any missing values. Additionally, the number of samples for each class, as shown in Table II, is imbalanced, with the majority of the samples belonging to the normal operation class. Nevertheless, the proposed

TABLE II Sample count for each class in the dataset

Class	Count
Normal Operation	1162931
Short-Circuit	5999
Degradation	10371
Open Circuit	6024
Shadowing	188473

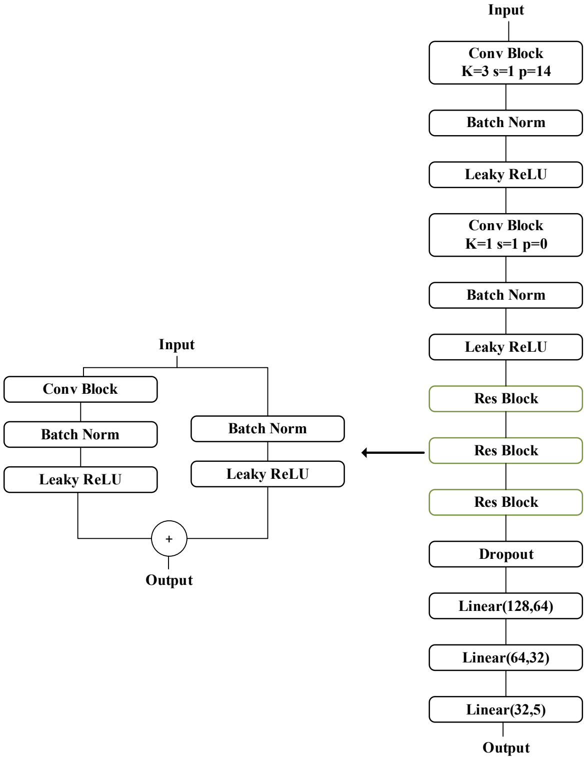

Fig. 1. Proposed model architecture that includes convolutional layers, ResNet blocks, and classifier layers, with the ResNet block providing downsampling and a skip connection.

model is capable of effectively classifying between the different classes. To further improve the model's performance, the dataset was standardized after splitting it into training, validation, and test sets. Specifically, each feature in the dataset was scaled by subtracting the mean of the training data and dividing by the standard deviation of the training data. The values shown in Table II represent the number of 1-second labeled samples recorded at a fixed sampling rate of 1 Hz. These counts do not indicate the number of physical fault-switching events, but rather the total number of seconds during which the system operated under each condition. The data were collected during 16 full days of system operation under natural environmental conditions and controlled fault scenarios. Partial shading occurred naturally at the test site during the early morning and late afternoon hours due to surrounding structures.

C. Model Architecture

To address the multi-class classification problem of photovoltaic (PV) system faults, which are often characterized by complex and subtle variations in time-series data (voltage, current, irradiance, and temperature), a CNN-based architecture is proposed that incorporates key principles from Computer Vision models. Specifically, the concept of Residual Blocks, inspired by the ResNet model [25], is leveraged to effectively capture intricate dependencies within the time-series data while maintaining computational efficiency.

The proposed model, depicted in Fig. 1, consists of a 1D Convolutional Neural Network (CNN) with a series of convolutional layers, followed by custom residual blocks and fully connected layers for classification. As shown in Fig. 1, the input time-series data is first processed by two consecutive convolutional layers. Each convolutional layer is followed by batch normalization and a ReLU activation function. These layers extract low-level features from the time-series data. For photovoltaic fault detection, a CNN-based architecture is chosen to capture both temporal dependencies and local features. Faults, such as short circuits, often occur within a very short time frame, and CNNs are well-suited for identifying these rapid changes in the data. While models like RNNs or LSTMs are effective at capturing long-term dependencies in sequential data, CNNs offer advantages for this specific task due to their ability to efficiently extract local features from time-series data. Additionally, CNNs are expected to achieve higher accuracy than simpler architectures, as they are better suited to handle the complex patterns associated with photovoltaic system faults.

Following the convolutional layers, a sequence of three custom residual blocks is employed. As illustrated in Fig. 1, each residual block consists of two convolutional layers with a kernel size of 9 and a stride of 2. These layers extract higher-level features. Batch normalization and Leaky ReLU activation are applied after each convolutional operation. A downsampling path is incorporated within each block: the original input to the block is downsampled via average pooling, ensuring that the dimensions align for the residual connection. This allows the model to learn deeper representations and capture more complex relationships within the time-series data.

The output from the final residual block is flattened into a 1D vector. Subsequently, three fully connected layers are employed. These layers gradually reduce the dimensionality of the feature representation and ultimately produce the final

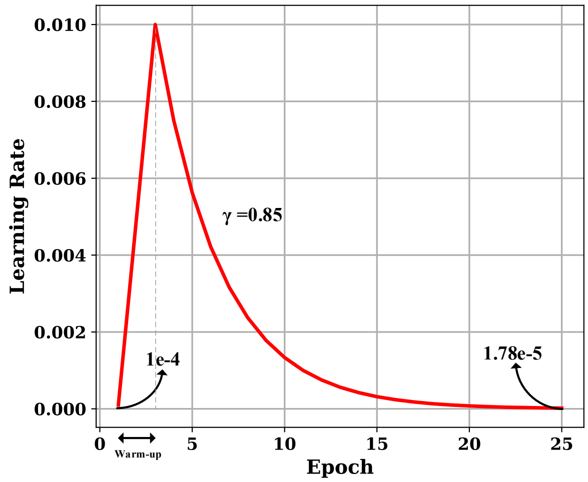

Fig. 2. Custom learning rate Scheduler: The learning rate begins at 0.0001 and increases linearly to 0.01 by the 3rd epoch. Following this, an exponential decay scheduler is applied.

output, consisting of five neurons corresponding to the five distinct PV fault classes.

Furthermore, to mitigate the risk of overfitting and improve generalization, dropout layers are incorporated after each fully connected layer. A dropout mechanism is selected to randomly deactivate neurons during training, ensuring that the model does not rely too heavily on specific features. Additionally, L2 regularization is applied to all convolutional and fully connected layers to penalize excessively large weight values, further promoting a more robust and generalizable model.

This architecture effectively combines the feature extraction capabilities of convolutional layers with the improved information flow and gradient propagation facilitated by residual connections. The downsampling within the residual blocks allows the model to capture both local and global temporal dependencies within the time-series data, while the expanded feature space enables the model to learn more complex and discriminative representations.

D. Model Training

During training, the Custom ResNet adapts its weights and biases with the objective of minimizing the error between the predicted fault labels and their ground-truth counterparts. The model was trained for 25 epochs, starting with an initial learning rate of 0.0001, which was incremented to 0.01 during the warm-up phase. The Adam optimizer was selected due to its known efficiency in updating weights and its adaptive learning rate properties. Adam combines the advantages of AdaGrad and RMSProp, performing particularly well on sparse gradients and non-stationary objectives. The optimizer function is defined as follows:

$$Adam(\theta) = \theta - \alpha \frac{\widehat{m}}{\sqrt{\widehat{v}} + \epsilon} \qquad (1)$$

TABLE III Hyperparameter

Hyperparameter	Value	Role / Description	Selection Method
Initial LR (η_0)	1e-4	Starting learning rate for warm-up phase	Grid search (1e-5 to 1e-3) to prevent early instability
Max LR (η_{max})	0.01	Peak LR after warm-up; starting point for decay	Optimized via LR range test (loss decrease vs. stability tradeoff)
Warm-up Epochs	3	Linear increase of LR to η_{max}	Empirical: Minimum epochs to stabilize gradients (tested 1-5 epochs)
Decay Factor (γ)	0.85	Multiplier in exponential LR decay	Calculated to reach 1.78e-5 at epoch 25
Final LR	1.78e-5	Target learning rate at final epoch	Derived from γ decay
Batch Size	256	Number of samples per iteration	Max stable size for GPU memory
Epochs	25	Total training cycles	With early stopping (no improvement after 5 epochs)
Weight Decay	1e-6	L2 regularization strength	Grid search (1e-8 to 1e-4)

where α is the learning rate, $\widehat{m}$ and $\widehat{v}$ estimates of the first and second moments of the gradients , respectively, and ϵ is a small constant to prevent division by zero.

Cross-Entropy Loss, shown in equation (2), was used as the loss function. It computes the divergence between the predicted probability distribution and the ground-truth distribution, making it a critical metric for optimizing performance in multi-class classification tasks:

$$Cross\ Entropy\ Loss(y, \hat{y}) = -\sum_{i=1}^{c} y_i \log \hat{y}_i \qquad (2)$$

where y is the true label, $\hat{y}$ is the predicted probability distribution and c is the number of classes.

To optimize hyperparameters efficiently, Small Grid Search was used to fine-tune the learning rate and weight decay, ensuring effective hyperparameter selection. This

approach improves model generalization, training stability, and convergence speed while maintaining computational efficiency. Fine-tuning these parameters plays a crucial role in preventing overfitting and achieving better overall performance.

Furthermore, Gradient Clipping was applied during training to prevent gradient explosion, a phenomenon where excessively large gradients cause unstable updates and hinder model convergence. A maximum gradient norm of 5 was used, ensuring that the gradients remain within a controlled range, leading to stable training dynamics.

Additionally, other hyperparameters such as batch size and the number of epochs were determined through empirical analysis, considering their impact on model effectiveness. The final values for all selected hyperparameters are summarized in Table III, reflecting the balance between performance and efficiency achieved during optimization.

The implementation of the proposed deep learning model was carried out using the Python programming language and the PyTorch deep learning framework. PyTorch was selected due to its dynamic computation graph support, flexibility, and ease of integration with GPU-based acceleration. This environment facilitated the efficient implementation of the CNN-ResNet architecture, adaptive learning rate scheduling, and all training, validation, and evaluation procedures.

E. Learning Rate Scheduler

A custom LRS, combining linear warm-up and exponential decay, was employed to optimize training. The warm-up phase begins with a minimum learning rate and linearly increases it to the maximum value over a specified number of warm-up epochs. After the warm-up period, the learning rate exponentially decays at each epoch. This approach allows the model to explore regions of interest during the early stages, where stabilization is crucial, and in the later stages, the model can begin adjusting the weights more effectively.

During the warm-up phase, the learning rate increases from a minimal initial value to a predefined maximum. This guarantees the stability of the training process, ensuring that the model's parameters are not subject to large updates that could destabilize learning. At this stage, the learning rate at the t-th epoch is defined as:

$$LR_{warmup}(t) = initial_{lr} + (max_{lr} - initial_{lr}) \times \left(\frac{t}{warmup_{epochs}}\right) \tag{3}$$

where $initial_{lr}$ is the initial learning rate, max_{lr} is the maximum learning rate and $warmup_{epochs}$ is the number of epochs over which the learning rate is linearly increased.

The learning rate after the warm-up phase follows an exponential decay function, which facilitates model convergence. This decay acts as a regularization mechanism, ensuring that larger updates occur in the beginning, while smaller updates happen as training progresses, thus preventing overshooting of the optimal solution. The learning rate at the t-th epoch during this phase is derived as:

$$LR_{decay}(t) = max_{lr} \times \gamma^{t - warmup_{epochs}} \tag{4}$$

where γ (gamma) is the decay factor and t is the current epoch.

The scheduler promotes stable early training by mitigating disruptive parameter updates, enabling controlled fine-tuning, and offering flexibility through adjustable parameters ($initial_{lr}$, max_{lr}, $initial_{lr}$, γ). These tunable hyperparameters allow adaptation to different datasets and models. This approach helps achieve better performance during training by leveraging the benefits of a high initial learning rate (post-warm-up), followed by exponential decay.

The key hyperparameters used in the learning rate scheduler and training configuration are summarized in Table III. The initial learning rate (η_0 = 1e-4) was selected via grid search to ensure stable gradient updates during the early training steps. The maximum learning rate (η_{max} = 0.01) was determined based on an LR range test, balancing the rate of loss decrease with model stability. The warm-up phase was set to 3 epochs, which was found to be sufficient for smoothing the transition into full training based on empirical analysis across a range of 1 to 5 epochs. After this phase, an exponential decay was applied with a decay factor γ = 0.85, chosen to gradually reduce the learning rate to a final value of approximately 1.78e-5 by epoch 25. This learning rate strategy enables the model to benefit from both rapid early learning and fine-tuned convergence in later stages. Other hyperparameters such as batch size (256), total epochs (25), and weight decay (1e-6) were also tuned via grid search and empirical constraints such as GPU memory limitations. Early stopping was used to prevent overfitting if validation loss failed to improve over five consecutive epochs.

In Fig. 2, the changes in the learning rate during the training epochs are plotted. The plot shows linear growth during the warm-up phase, followed by exponential decay.

III. Simulation Results

This section evaluates the proposed CNN-ResNet architecture and highlights the positive impact of learning rate scheduling. The validation strategy involves evaluating the model on the validation dataset after each epoch and calculating metrics such as loss, accuracy, precision, recall, and F1 score. The validation dataset is considered unseen data, as it is separate from the training process. Additionally, to ensure the model generalizes well to unseen data, performance on the test dataset, which was not part of the training process, is also assessed using the same metrics. Table IV compares the model's accuracy and loss in two scenarios: with and without learning rate scheduling. The results show that the model achieves lower loss for the training, validation, and testing datasets when learning rate scheduling is used. Specifically, the loss decreases by approximately 69.51% for training data, 63.88% for validation data, and 64.86% for test data, compared to the scenario where learning rate scheduling is not used. Moreover, the model attains high accuracy—exceeding 99.8%—across all datasets, with learning rate scheduling contributing to accuracy increases of about 020% for the training dataset, 0.18% for the validation dataset, and 0.18% for the test dataset. Additionally, with learning rate scheduling, the Matthews Correlation Coefficient (MCC) reaches values of 0.9777 for training, 0.9731 for validation, and 0.9960 for testing, reflecting the model's improved ability to classify faults accurately and consistently across different datasets. As shown in Fig. 2, the learning rate starts at 1e-4, increases to 0.01 in the third epoch, and then decreases to approximately 1.78e-5.

This adjustment leads to greater fluctuations in the learning curve shown in Fig. 3 compared to Fig. 4, indicating that learning rate scheduling facilitates faster convergence during the increasing learning rate phase. Additionally, the learning curve becomes smoother after the learning rate decreases, showing reduced fluctuations compared to the scenario without scheduling.

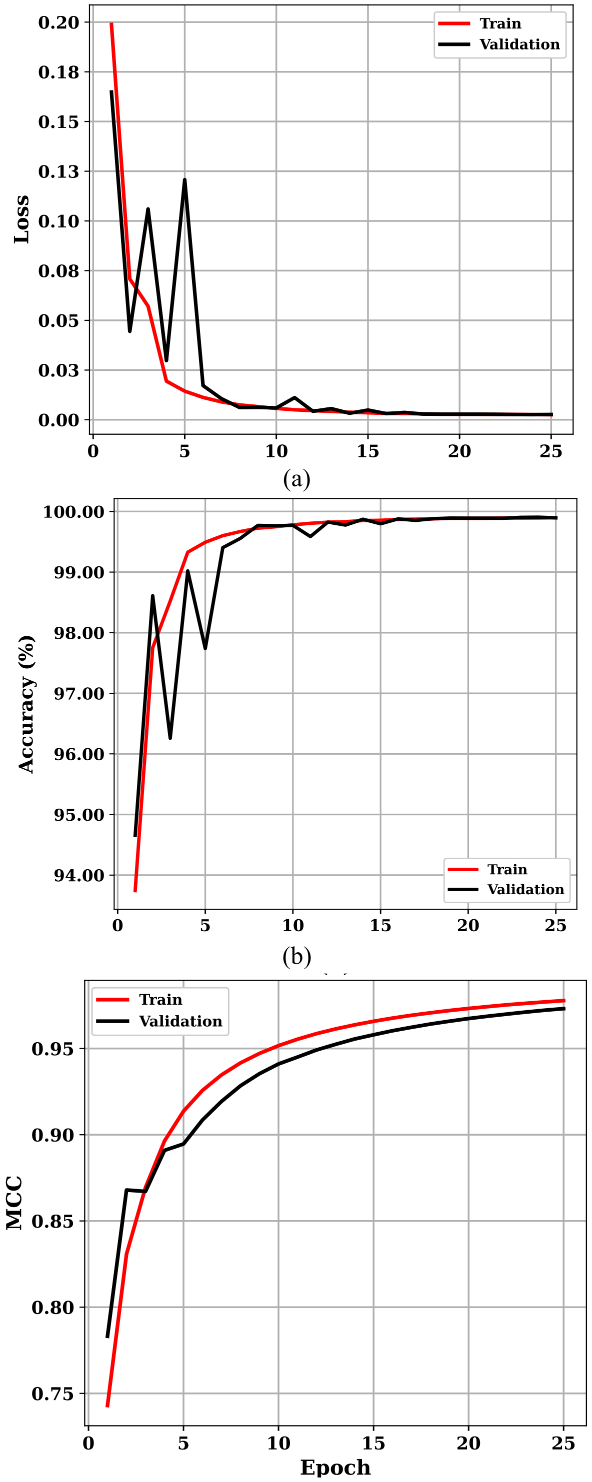

(a)

(b)

(c)

Fig. 3. Learning curve: (a) Loss per epoch, (b) Accuracy per epoch, (c)MCC per epoch with LRS.

Beyond the impact of learning rate scheduling, the proposed CNN-ResNet architecture demonstrates strong precision in

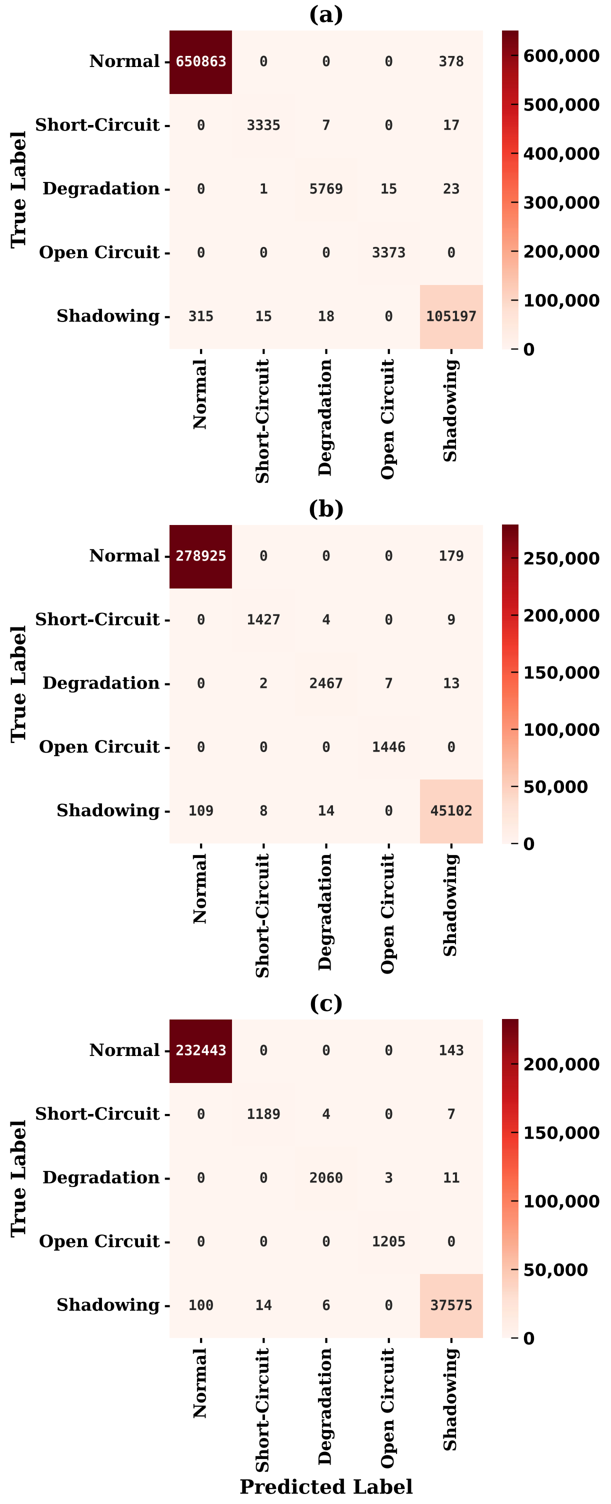

(a)

	Normal	Short-Circuit	Degradation	Open Circuit	Shadowing
Normal	650863	0	0	0	378
Short-Circuit	0	3335	7	0	17
Degradation	0	1	5769	15	23
Open Circuit	0	0	0	3373	0
Shadowing	315	15	18	0	105197

(b)

	Normal	Short-Circuit	Degradation	Open Circuit	Shadowing
Normal	278925	0	0	0	179
Short-Circuit	0	1427	4	0	9
Degradation	0	2	2467	7	13
Open Circuit	0	0	0	1446	0
Shadowing	109	8	14	0	45102

(c)

	Normal	Short-Circuit	Degradation	Open Circuit	Shadowing
Normal	232443	0	0	0	143
Short-Circuit	0	1189	4	0	7
Degradation	0	0	2060	3	11
Open Circuit	0	0	0	1205	0
Shadowing	100	14	6	0	37575

Fig. 4. Classification confusion matrix: (a) Training, (b) Validation, (c) Test.

predicting the target classes. Four key metrics—precision, ecall, F1 score, and AUROC—were used to evaluate model performance. Precision, which measures the proportion of true positive predictions among all positive predictions, and recall, which measures the proportion of true positives among all actual positive instances, both show impressive results. According to Tables V, VI, and VII, recall exceeds 0.99 for all classes across the training, validation, and test datasets, indicating that most actual positive instances are correctly identified, minimizing false negatives.

Furthermore, precision is greater than 0.98 for most classes in all datasets, suggesting that most positive predictions are true positives, thus minimizing false positives. The F1 score exceeds 0.95 for most classes, demonstrating a good balance between precision and recall. The AUROC value of approximately 0.99 for each class indicates excellent class discrimination, with the model effectively distinguishing between true positive instances and other classes (false positives). The confusion matrices in Fig. 4 illustrate the model's classification performance across training, validation, and testing phases. During training, the model effectively classifies a large number of instances across all fault categories. In the validation phase, the classification remains highly accurate, maintaining strong detection across different fault types. The testing phase further confirms the model’s reliability in identifying photovoltaic system faults, demonstrating consistent and precise classification across all conditions. These results highlight the model's effectiveness in accurately detecting and distinguishing various operating states.

TABLE IV Accuracy and loss with/without LRS for training, validation and test data

Metric	LRS	Train	Validation	Test
Accuracy (%)	with	99.89	99.89	99.89
	without	99.69	99.71	99.71
Loss	with	0.0025	0.0026	0.0026
	without	0.0082	0.0072	0.0074
MCC	with	0.9777	0.9731	0.9960
	without	0.9768	0.9792	0.9891

TABLE V Metrics results for training datasets

Metric	LRS	Class0	Class 1	Class 2	Class 3	Class 4
F1Score	with	0.9967	0.9528	0.9552	0.9930	0.9815
	without	0.9965	0.9790	0.9779	0.9941	0.9785
Recall	with	0.9994	0.9928	0.9932	1.	0.9967
	without	0.9984	0.9913	0.9907	1.	0.9881
Precision	with	0.9995	0.9952	0.9956	0.9955	0.9960
	without	0.9981	0.9884	0.9905	0.9955	0.9900
AUROC	with	0.9999	0.9999	0.9999	0.9999	0.9999
	without	0.9999	0.9999	0.9999	0.9999	0.9999

TABLE VI Metrics results for validation datasets

Metric	LRS	Class0	Class 1	Class 2	Class 3	Class 4
F1Score	with	0.9959	0.9683	0.9533	0.9914	0.9768
	without	0.9969	0.9910	0.9844	0.9972	0.9802
Recall	with	0.9993	0.9909	0.9911	1.	0.9971
	without	0.9990	0.9902	0.9931	1.	0.9858
Precision	with	0.9996	0.9930	0.9927	0.9951	0.9955
	without	0.9978	0.9951	0.9860	0.9958	0.9938
AUROC	with	0.9999	0.9999	0.9999	0.9999	0.9999
	without	0.9999	0.9999	0.9999	0.9999	0.9999

TABLE VII Metrics results for test datasets

Metric	LRS	Class0	Class 1	Class 2	Class 3	Class 4
F1Score	with	0.9994	0.9895	0.9942	0.9987	0.9962
	without	0.9984	0.9863	0.9913	0.9983	0.9895
Recall	with	0.9993	0.9908	0.9932	1.	0.9968
	without	0.9989	0.9908	0.9942	0.9991	0.9859
Precision	with	0.9995	0.9883	0.9951	0.9975	0.9957
	without	0.9978	0.9818	0.9884	0.9975	0.9932
AUROC	with	0.9999	0.9999	0.9999	0.9999	0.9999
	without	0.9999	0.9999	0.9999	0.9999	0.9999

To further validate the proposed CNN-ResNet architecture and the contribution of the learning rate scheduler (LRS), a series of model comparisons and ablation studies were conducted. Table VIII summarizes the results of five model variants evaluated on the test dataset: the proposed CNN-ResNet with and without LRS, the same model without residual blocks, a standard CNN architecture, and a standard ResNet without scheduler. As shown, the full CNN-ResNet model with LRS achieves the highest test accuracy (99.89%) and lowest loss (0.0026), confirming the effectiveness of combining residual learning with an adaptive learning rate schedule. Removing the scheduler slightly decreases performance (99.71%, 0.0074), while removing residual blocks causes a significant drop in accuracy (92.44%) and a large increase in loss. The standard CNN and ResNet models also performed well (99.77% and 99.79%, respectively), but did not outperform the proposed approach. These results highlight the synergistic effect of residual connections and learning rate scheduling in improving both accuracy and convergence.

This result is particularly meaningful given the complexity of the dataset and the subtle nature of some fault classes. The dataset includes both real and simulated samples under a variety of realistic environmental conditions, such as irradiance and temperature variations, making accurate classification more challenging. Previous studies on this dataset report lower performance using other architectures: in [26], a Multi-Layer Perceptron (MLP)-based classifier achieved a test accuracy of 95.3%, and in [27], a 1D CNN architecture reached 97.4%. These comparative results highlight that the high performance of the proposed model is not trivially obtainable using standard classification techniques, and instead, results from the tailored integration of residual learning and dynamic learning rate scheduling.

In summary, the results highlight the effectiveness of the proposed CNN-ResNet architecture combined with learning rate scheduling. The model consistently delivers high accuracy, low loss, and robust classification metrics across the training, validation, and test datasets. Learning rate scheduling plays a crucial role in reducing loss by over 74% and slightly increasing accuracy, underlining its importance

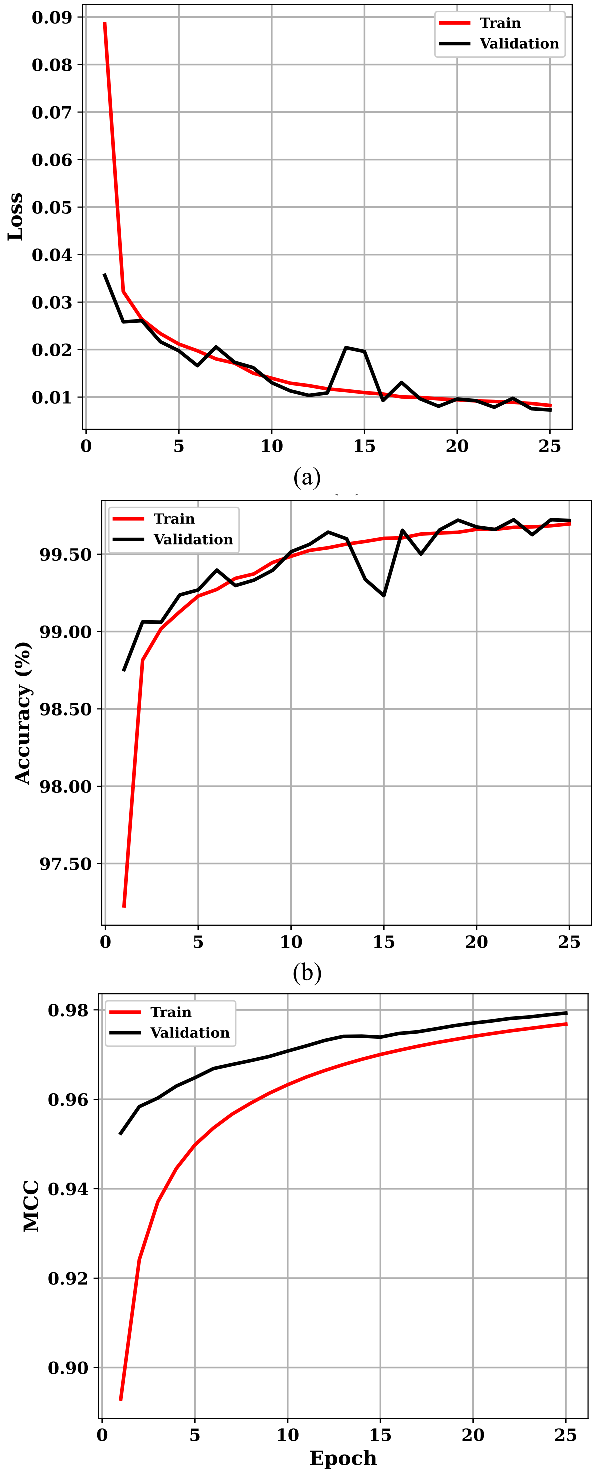

(a)

(b)

(c)

Fig. 5. Learning curve: (a) Loss per epoch, (b) Accuracy per epoch without LRS.further confirm that the model is well-trained and performs accurate predictions.

in improving model performance. Additionally, the model demonstrates excellent precision, recall, F1 score, and AUROC values, confirming its strong ability to distinguish between classes and make accurate predictions. To further validate the design choices, several model variants were implemented and evaluated on the test dataset, including a standard CNN, a standard ResNet, and ablated versions of the proposed architecture without residual connections or without learning rate scheduling. As summarized in Table VIII, the full CNN-ResNet with LRS achieved the best performance, while removing residual blocks or the scheduler led to significant drops in accuracy and increases in loss. These results emphasize the individual and combined impact of residual learning and adaptive scheduling on model generalization and convergence, further supporting the robustness of the proposed approach.

TABLE VIII Baseline comparisons and ablation studies on the test dataset, demonstrating the impact of residual connections and learning rate scheduling on the performance of different model variants.

Model	Accuracy (%)	Loss
CNN-ResNet + LRS	99.89	0.0026
CNN-ResNet (no LRS)	99.71	0.0074
CNN-ResNet (no residual)	92.44	0.1906
CNN	99.77	0.0057
ResNet	99.79	0.0048

IV. Conclusions

To address the challenges of fault detection in photovoltaic (PV) systems, this study aimed to develop a robust ResNet-based deep learning framework. The model was trained using the cross-entropy loss function and the Adam optimizer on a preprocessed and normalized version of the dataset to ensure input data consistency. Key improvements to the learning strategy included learning rate scheduling, with a strong emphasis on early warm-up iterations to prevent fast convergence, followed by fine-tuning of weight updates using an exponential decay function in the later training phases. This approach led to a significant improvement in model generalization, reducing the validation error by 63% compared to baseline training methods.

Our proposed model achieved an impressive accuracy of 99.8% across the training, validation, and test datasets, demonstrating both strong performance and significant generalization, with no overfitting. It also proved to be robust, with class-specific F1-scores of 98.95%, 95.28%, 95.52%, 99.30%, and 98.15% on the test dataset, showing its ability to discriminate between multiple fault types in diverse scenarios.

The results confirm the efficacy of the ResNet-based technique for PV fault detection and suggest its potential for adaptation to complex, real-world scenarios. Future work could integrate visual data (e.g., electroluminescence or thermal images of solar panels), where ResNet's prowess in image recognition could be leveraged. This would enable simultaneous analysis of electrical and physical defects, marking a major improvement for diagnostics.

REFERENCES

[1] S. S. Sakthivel, V. Arunachalam, and K. Jagatheesan, "Detection, classification, and location of open-circuit and short-circuit faults in solar photovoltaic array: an approach using single sensor," *IEEE Journal of Photovoltaics,* 2023, doi: 10.1109/JPHOTOV.2023.3304113.

[2] N.-C. Yang and M. Faizan, "Long Short-term Memory-based Feedforward Neural Network Algorithm for Photovoltaic Fault Detection under Irradiance Conditions," IEEE Transactions on Instrumentation and Measurement, 2024, doi: 10.1109/TIM.2024.3413159.

[3] A. Mellit, G. M. Tina, and S. A. Kalogirou, "Fault detection and diagnosis methods for photovoltaic systems: A review," Renewable and Sustainable Energy Reviews, vol. 91, pp. 1-17, 2018, doi: 10.1016/j.rser.2018.03.062.

[4] M. Mansouri, M. Trabelsi, H. Nounou, and M. Nounou, "Deep learning-based fault diagnosis of photovoltaic systems: A comprehensive review and enhancement prospects," IEEE Access, vol. 9, pp. 126286-126306, 2021, doi: 10.1109/ACCESS.2021.3110947.

[5] M. Dhimish and A. M. Tyrrell, "Photovoltaic bypass diode fault detection using artificial neural networks," IEEE Transactions on Instrumentation and Measurement, vol. 72, pp. 1-10, 2023, doi: 10.1109/TIM.2023.3244230.

[6] Z. He, H. C. Chen, S. Shan, Y. Hu, K. Zhang, and H. Wei, "Shading type and severity diagnosis in photovoltaic systems via IV curve imaging and two-stream deep neural network," Energy Conversion and Management, vol. 324, p. 119311, 2025, doi: 10.1016/j.enconman.2024.119311.

[7] U. Kumar, S. Mishra, and K. Dash, "An IoT and semi-supervised learning-based sensorless technique for panel level solar photovoltaic array fault diagnosis," IEEE Transactions on Instrumentation and Measurement, vol. 72, pp. 1-12, 2023, doi: 10.1109/TIM.2023.3287247.

[8] B. Ren, Q. Wang, N. Zhou, and Y. Chi, "Fault Diagnosis of Photovoltaic Strings Based on SiamMN Networks and Panoramic IV Features," IEEE Transactions on Industrial Electronics, 2024, doi: 10.1109/TIE.2024.3443964.

[9] Y.-Y. Hong, L.-F. Chen, and W. Zhang, "Classification of Photovoltaic Faults Using PSO-Optimized Compact Convolutional Transformer," IEEE Access, 2023, doi: 10.1109/ACCESS.2023.3341889.

[10] M. Alrifaey et al., "Hybrid deep learning model for fault detection and classification of grid-connected photovoltaic system," IEEE Access, vol. 10, pp. 13852-13869, 2022, doi: 10.1109/ACCESS.2022.3140287.

[11] A. Eskandari, J. Milimonfared, and M. Aghaei, "Fault detection and classification for photovoltaic systems based on hierarchical classification and machine learning technique," IEEE Transactions on Industrial Electronics, vol. 68, no. 12, pp. 12750-12759, 2020.

[12] W. Yin, S. Lingxin, L. Maohuan, S. Qianlai, and L. Xiaosong, "PV-YOLO: lightweight YOLO for photovoltaic panel fault detection," IEEE Access, vol. 11, pp. 10966-10976, 2023, doi: 10.1109/ACCESS.2023.3240894.

[13] J. Qu, Q. Sun, Z. Qian, L. Wei, and H. Zareipour, "Fault diagnosis for PV arrays considering dust impact based on transformed graphical features of characteristic curves and convolutional neural network with CBAM modules," Applied Energy, vol. 355, p. 122252, 2024, doi: 10.1016/j.apenergy.2023.122252.

[14] M. Bougoffa, S. Benmoussa, M. Djeziri, and T. Contaret, "Stacked AutoEncoder based diagnosis applied on a Solar Photovoltaic System," IFAC-PapersOnLine, vol. 58, no. 4, pp. 384-389, 2024, doi: 10.1016/j.ifacol.2024.07.248.

[15] A. Sohail, N. U. Islam, A. U. Haq, S. U. Islam, I. Shafi, and J. Park, "Fault detection and computation of power in PV cells under faulty conditions using deep-learning," Energy Reports, vol. 9, pp. 4325-4336, 2023, doi: 10.1016/j.egyr.2023.03.094.

[16] A. Teta et al., "Fault detection and diagnosis of grid-connected photovoltaic systems using energy valley optimizer based lightweight CNN and wavelet transform," Scientific Reports, vol. 14, no. 1, p. 18907, 2024, doi: 10.1038/s41598-024-69890-7.

[17] A. F. Amiri, S. Kichou, H. Oudira, A. Chouder, and S. Silvestre, "Fault detection and diagnosis of a photovoltaic system based on deep learning using the combination of a convolutional neural network (cnn) and bidirectional gated recurrent unit (Bi-GRU)," Sustainability, vol. 16, no. 3, p. 1012, 2024, doi: 10.3390/su16031012.

[18] A. Seghiour, H. A. Abbas, A. Chouder, and A. Rabhi, "Deep learning method based on autoencoder neural network applied to faults detection and diagnosis of photovoltaic system," Simulation Modelling Practice and Theory, vol. 123, p. 102704, 2023, doi: 10.1016/j.simpat.2022.102704.

[19] E. Moshksar, "An Explicit and Accurate I-V Characteristic for Photovoltaic Modules Based on Piecewise Quadratic Function," International Journal of Industrial Electronics Control and Optimization, vol. 7, no. 4, pp. 291-299, 2024, doi: 10.22111/ieco.2024.48517.1554.

[20] M. Rahmani, S. M. Barakati, S. Yousofi Darmian, V. Barahouei, and M. Bagheri Hashkavayi, "Optimized Algorithm for Open-Circuit Fault Detection in Switches and Capacitor Voltage Balancing Control in Modular Multilevel Converters," International Journal of Industrial Electronics Control and Optimization, vol. 7, no. 1, pp. 15-27, 2024, doi: 10.22111/ieco.2024.47310.1509.

[21] B. Liu, K. Sun, X. Wang, J. Zhao, and X. Hou, "Fault diagnosis of photovoltaic strings by using machine learning-based stacking classifier," IET Renewable Power Generation, vol. 18, no. 3, pp. 384-397, 2024, doi: 10.1049/rpg2.12755.

[22] W. M. Shaban, "Detection and classification of photovoltaic module defects based on artificial intelligence," Neural Computing and Applications, vol. 36, no. 27, pp. 16769-16796, 2024, doi: 10.1007/s00521-024-10000-z.

[23] M. Chang, K.-H. Chen, Y.-S. Chen, C.-C. Hsu, and C.-C. Chu, "Developments of AI-assisted fault detection and failure mode diagnosis for operation and maintenance of photovoltaic power stations in Taiwan," IEEE Transactions on Industry Applications, 2024, doi: 10.1109/TIA.2024.3379319.

[24] N. Sabri, A. Tlemçani, A. Chouder, and W. Merrouche, "An Improved Fault Diagnosis in Stand-Alone Photovoltaic System Using Artificial Neural Network," Iranian Journal of Science and Technology, Transactions of Electrical Engineering, vol. 48, no. 1, pp. 325-336, 2024, doi: 10.1007/s40998-023-00671-0.

[25] K. He, X. Zhang, S. Ren, and J. Sun, "Deep residual learning for image recognition," in Proceedings of the IEEE conference on computer vision and pattern recognition, 2016, pp. 770-778, doi: 10.1109/CVPR.2016.90.

[26] A. E. Lazzaretti et al., "A monitoring system for online fault detection and classification in photovoltaic plants,"

Sensors, vol. 20, no. 17, p. 4688, 2020, doi: 10.3390/s20174688.

[27] S. A. Memon, Q. Javed, W.-G. Kim, Z. Mahmood, U. Khan, and M. Shahzad, "A machine-learning-based robust classification method for PV panel faults," Sensors, vol. 22, no. 21, p. 8515, 2022, doi: 10.3390/s22218515.

Sepehr Shakibi received the B.S. degree in electrical engineering from the University of Science and Culture, Tehran, Iran, in 2021, and the M.S. degree in electrical engineering from the University of Tehran, Tehran, Iran, in 2023. He is currently a Researcher with the Photovoltaic Systems Laboratory, the Department of Electrical and Electronics Engineering, University of Tehran, Tehran, Iran. His current research interests include photovoltaic systems and artificial-intelligence applications in this domain.

Amir Mohammad Farahani was born in Tehran, Iran. He received the B.S. degree in Electrical Engineering from the University of Science and Culture, Tehran, Iran, in 2019, and the M.S. degree in Digital Electronics Engineering from the Iran University of Science and Technology (IUST), Tehran, Iran. From 2019 to 2021, he was with GADA Group, Tehran, Iran. From 2021 to 2023, he was with Borna Electronics, Shahr-e Rey, Iran, as an Embedded Systems Developer. His current research interests include AI-based medical systems, natural language processing (NLP) and large language models (LLMs), and IoT-based edge devices.

Mohsen Hamzeh received the B.Sc. and M.Sc. degrees in Electrical Engineering from the University of Tehran, Tehran, Iran, in 2006 and 2008, respectively, and the Ph.D. degree in Electrical Engineering from Sharif University of Technology, Tehran, Iran, in 2012. From 2013 to 2018, he served as an Assistant Professor at Shahid Beheshti University, Tehran, Iran. In 2018, he joined the School of Electrical and Computer Engineering at the University of Tehran, where he is currently an Associate Professor. His research interests include photovoltaic systems, microgrid control, and the applications of power electronics in power distribution networks.

IECO

This page intentionally left blank.

IECO International Journal Of Industrial Electronics Control and Optimization
Print ISSN: 3517-2645
Online ISSN: 3568-2645
Homepage: https://ieco.usb.ac.ir/

An Improved Method for Capacitor Voltage Balancing Control and Capacitance Monitoring in Modular Multilevel Converter

Mohsen Rahmani-Haredasht[1] | Seyed-Masoud Barakati[2] | M. Bagheri Hashkavayi[3]
Faculty of Engineering, University of Sistan and Baluchestan, Zahedan, Iran.[1,2]
Taftan Power Development and Transmission Engineering Company, Mashhad, Iran[1]
Department of Electrical Engineering, Yuan Ze University, Taoyuan, 32003, Taiwan[3]
Corresponding author's email: smbaraka@ece.usb.ac.ir

Article Info

Article type:
Research Article

Article history:
Received: 16-November-2025
Received in revised form:
31-January-2026
Accepted: 08-February-2026
Published online: 22-June-2026

Keywords:Modular Multilevel Converter (MMC), Capacitor Voltages Balance,Half-bridge submodules(HB-SM), capacitance monitoring

ABSTRACT

The modular multilevel converter (MMC) has emerged as a leading topology for high-voltage and high-power applications, owing to its scalable modular structure, elimination of bulky output filters, and independence from multiple DC sources. Despite these advantages, the large number of capacitors in the MMC introduces substantial reliability challenges, particularly with respect to maintaining accurate voltage balance. Conventional balancing techniques typically rely on numerous voltage sensors, thereby increasing system cost and complexity while compromising reliability. This paper presents an improved capacitor voltage balancing strategy that significantly enhances the reliability of MMCs. The proposed approach employs a single voltage sensor shared between two half-bridge submodules (HB-SMs), thereby simplifying the sensing architecture and ensuring accurate capacitor voltage estimation with minimal hardware. Moreover, the strategic placement of the sensor enables an integrated capacitance monitoring scheme capable of assessing capacitor health in real time, further improving system robustness. The validity and effectiveness of the proposed method are demonstrated through comprehensive simulation and experimental results under a wide range of operating conditions.

I. Introduction

Recently, multi-level converters (MCs) have attracted the interest of many researchers [1], [2]. Compared to two-level converters, MCs have great advantages, such as producing high-quality AC voltages, low THD, reducing the voltage or current of semiconductors and switching frequency [3], [4]. Among the types of MCs, the modular multilevel converter (MMC) is recognized as one of the most important emerging developments for high voltage direct current (HVDC) systems [5], [6]. In industrial applications, half-bridge sub-modules are generally employed in MMC topology [7]. Thus, a large number of flying capacitors have been employed in the topology of MMCs based on HB-SM, and regulating the voltage balance of these capacitors is one of the main challenges of using MMC [8]. In order to balance the voltage of the capacitors, instantaneous information about the voltage of the capacitors is required, which necessitates the use of a large number of voltage sensors, where the number of voltage sensors is the same as HB-SMs [9], [10]. Using this number of voltage sensors affects the converter's expense, reliability, and complexity, mainly when a converter with a high number of levels is considered [11].

In recent years, numerous studies have concentrated on reducing the number of sensors in Modular Multilevel Converters (MMC). Table 1 presents a comparison of methods aimed at sensor reduction in MMC.

In references [12], [13], [14], techniques have been introduced to decrease the number of current sensors. However, these methods do not address the reduction of voltage sensors. Moreover, reducing current sensors causes the malfunction of open-circuit fault detection and circulation current-control systems in the MMC.

In [15], the concept of group measurement (GM) for capacitor voltage is introduced, necessitating a minimum of two voltage sensors in each arm. However, an advanced voltage balancing algorithm must be applied to the system, where activating and deactivating numerous SMs instantaneously may cause instability. Additionally, in the

Publisher: University of Sistan and Baluchestan

proposed technique, the update of capacitor voltage depends on the time when only one SM is active in the group, thereby compromising the accuracy of predicting capacitor voltage.

TABLE I Comparison of capacitor capacitance monitoring methods

Reference	**Method**	**Online /Offline**	**N. Voltage sensor**	**Low switching frequency**	**High switching frequency**	**Calculation burden**	**error**
[22]	RLS algorithm and second harmonic current injection	Online	N	NO	Yes	Low	1.3%>
[23]	KFA algorithm	Online	N	NO	Yes	High	*
[24]	RSUBM	Online	N	NO	Yes	Low	3%>
[25]	Using the MMC DC-Side Start-Up feature	Offline	N	*	*	*	1%>
[26]	Using the discharge curve of submodule capacitors and parallel resistors	Online	N	NO	Yes	Low	2%>
Proposed method	Ratio of estimated to measured voltage Increase	Online	N/2	Yes	Yes	Low	1% >

TABLE II Comparison of sensor reduction methods

Reference	Number of voltage sensors in the arm	Number of Current Sensors in the Arm	Calculation burden	Reliability	Capacitance monitoring	Voltage ripple of capacitors
[12-14]	N	0	Medium	Low	No	<5%
[15]	At least two	1	Medium	Medium	No	10%
[16]	0	1	Very high	Low	No	<4%
[17]	Number of groups	1	Very high	High	Yes	<10%
[18]	1	0	Very high	Low	No	<6%
[19]	N/2	1	Medium	High	NO	<5%
Proposed method	N/2	1	Low	High	Yes	<5%

The adaptive linear neuron (ADALINE) algorithm is used in [16] to track SM voltage dynamics. Despite the promising results, this method requires accurate arm inductor voltage measurement. In [17], a self-updating capacitor voltage method based on group measurement of SM output voltage is presented, which has raised the accuracy of capacitor voltage estimation. However, the estimation method is very complex, making it difficult to use in practical applications. In [18], an improved method for estimating capacitor voltage using Kirchhoff equations with only arm voltage sensors and output current sensors is presented. The system's reliability is decreased when the arm current sensors are removed, and updating the voltage of the capacitors depends on the forced activation algorithm. In [19], an optimized algorithm was introduced that reduces the number of voltage sensors by grouping submodules and simultaneously enables capacitor voltage balancing and fast open-circuit fault detection, validated through both simulations and experiments. The forced activation approach leads to system instability when using a high number of HB-SMs in actual applications. According to the above contents and the results of Table 1, the solutions to reduce the sensor have three major drawbacks:

a. the computational burden grows exponentially as the number of submodules rises, which makes the application of these methods challenging in MMCs with a large number of SMs;

b. the majority of these methods require high-voltage sensors or sensors with high galvanic isolation voltage;

c. most methods reduce the reliability of converter performance. Due to these three constraints, approaches for reducing the voltage of sensors in industrial applications have received little attention.

Furthermore, the MMC topology's large number of capacitors has harmed the converter's reliability, since capacitors with a 30% failure rate are among the most common sources of faults in power electronic systems [19]. In power electronics applications, three types of capacitors are often used [20]: electrolytic capacitors (E), metalized polypropylene film capacitors (MPPF), and multilayer ceramic capacitors (MLC). These capacitors are vulnerable due to internal or external variables, such as the aging effect, chemical reactions, and excessive threshold voltages. Capacitor failures decrease the MMC's availability and cause severe explosions and even loss of life [21]. Therefore, capacitance monitoring is essential to detect faulty capacitors as a solution. Table 2 compares the capacitor capacitance monitoring methods. The recursive least-squares (RLS) approach for capacitance estimate utilizing capacitor voltage, capacitor current, and submodule switching mode information is presented in reference [22]. In this approach, an AC current is injected into the circulating current, which increases the voltage ripple of the capacitors. As a result, the control process will be complicated, and the performance of the MMC will be affected. In [23], the Kalman-filter algorithm and instantaneous information of capacitor current and voltage are used for capacitance monitoring, but this algorithm complicates the capacitance estimation. Reference [24] describes a capacitance monitoring technique based on the reference submodule, in which the capacitance is estimated based on the capacitor voltage relationship between the reference submodule and other submodules. The most significant drawbacks of this method are the vast number of voltage sensors required and the requirement of a complicated sorting algorithm. An off-line capacitance monitoring method is presented in [25], which uses the relation between phase current and SM voltage at the stage of MMC startup to estimate the capacitance. However, this method has no online capacitance monitoring and only works at the stage of MMC startup. In [26], a method based on the characteristic of discharging capacitors is presented, that in each capacitance monitoring, a target sub-module is bypassed from each arm, to discharge the capacitors up to 0.368 times the rated capacitor voltage. Despite the realization of online monitoring in this method, the voltage stress in other capacitors increases, and the recharging process of the bypassed sub-modules causes the instability of the system. As a result, the reliability of MMC decreases. In [27], a capacitance health monitoring scheme for MMCs was introduced that minimizes the number of voltage sensors while maintaining a low computational burden. This approach enables

accurate and efficient assessment of capacitor conditions, and its effectiveness has been validated through both simulation and experimental studies.

This paper introduces an improved approach for regulating capacitor voltage balance, employing the GM methodology for capacitor voltage control. The proposed method employs the capacitor voltage and current equation to estimate capacitor voltage, ensuring heightened accuracy in estimation without incurring additional computational burden. Furthermore, leveraging the specific arrangement of voltage sensors, a novel Capacitance Monitoring Method is presented to enhance the reliability of the MMC. This monitoring method utilizes the ratio between estimated and measured increases in capacitor voltage. Within each operational cycle, an indicator meticulously assesses the health status of capacitors, issuing a fault warning promptly upon detecting any anomalies in capacitor performance. These advancements contribute not only to the precision of capacitor voltage control in MMC but also exemplify the commitment to enhancing the reliability and robustness of high-power applications.

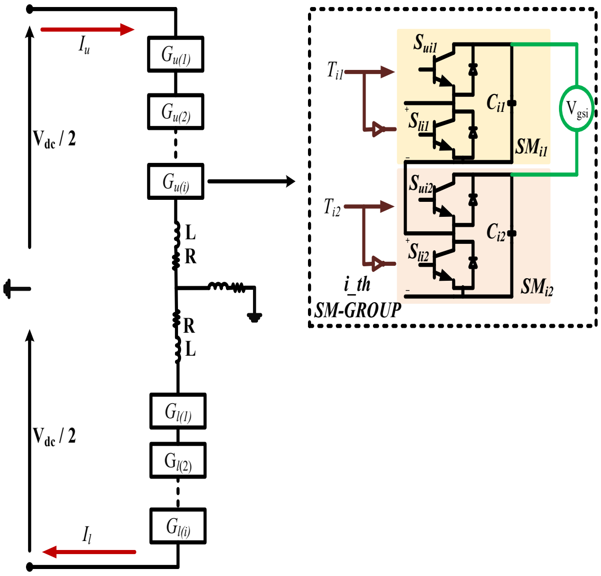

Fig. 1. Single-phase MMC arrangement based on GM

II. Configuration of GM

The schematic representation of the single-phase MMC configuration, featuring two arms (upper and lower arms), is illustrated in Fig.1. Each arm is constructed through the series connection of i (i=1, 2, ...N/2) groups, arm resistance (R), and arm inductor (L). Within each group, a voltage sensor (Vgsi) and two half-bridge submodules (SMij (j=1, 2)) are employed. The group voltage sensor is strategically positioned between the two positive poles of the submodule capacitors. The half-bridge submodule structure integrates two switches (Suij, Slij) and a capacitor (Cij). The switching state of the Half-Bridge Submodule (HB-SM), delineated in Table 3, is regulated by the switching function (Tij). When Tij=1, the capacitor is placed in the circuit; if Iarm>0, the capacitor's voltage (V_{cij}) increases; otherwise, the capacitor discharges. Also, if $T_{ij}=0$, the capacitor will be bypassed and the voltage of the capacitor will remain unchanged.

TABLE III HB-SM switching state

T_{ij}	Upper (S_{uij}) switch	Lower (S_{lij}) switch	I_{arm}	V_{cij}
1	ON	OFF	>0	Charge
			<0	Discharge
0	OFF	ON	>0	Unchanged
			<0	

III. Proposed estimation method of capacitor voltage

In typical MMC systems, each HB-SM has an individual sensor connected in parallel to the SM capacitor. To maintain the capacitors' voltage balance, these sensors must continuously accumulate information regarding the capacitors' voltage. Therefore, the data exchange rate between the processor and the power system increases significantly. In this paper, the number of sensors in the GM-based configuration is reduced by half, and it is necessary to estimate the capacitor voltage to maintain the capacitor voltage balance. In this way, a simple estimation method is proposed in two steps, which are described below.

Step 1: Voltage measurement of capacitors

Fig. 2 shows the current path of the arm in step 1 in the SMs of the group. According to Fig. 2, in step 1 of voltage estimation of capacitors, according to the switching state (T_{ij}), certain states occur in which the value measured by the group voltage sensor is equal to the voltage of each capacitor. These special states are as follows:

T_{i2} = 0: As shown in Fig 2 (a), in this case, the voltage sensor (V_{gsi}) is parallel to C_{i1}, and the capacitor voltage is measured directly by the group sensor:

$$V_{gsi}(t) = V_{Ci1}(t) \tag{1}$$

T_{i1} = 0 and, T_{i2} = 0: In this case, according to Fig. 2 (b), the voltage value measured by the group sensor is equal to the voltage difference of the group capacitors, so:

$$V_{gsi}(t) = V_{Ci1}(t) - V_{Ci2}(t) \Rightarrow V_{Ci2}(t) = V_{Ci1}(t) - V_{gsi}(t) \tag{2}$$

Step 2: Voltage estimation of capacitors

According to the above analysis, in certain switching conditions, the voltage value of the capacitors can be directly measured by the group voltage sensor. On the other hand, capacitor voltage balancing needs real-time voltage data. In this way, it is necessary to estimate the voltage of capacitors in various switching conditions. As a result, when the group voltage sensor cannot be used to directly measure the capacitor voltage, the following equation can be used to estimate the capacitor voltage:

$$\widehat{V}_{Cij}(t) = V_{Cmij} + \frac{1}{C_{ij}}\int_{t_0}^{t} i_{C_{ij}}(t)\ dt\ (t = t_0 + k_{ij}T_s < t_1) \tag{3}$$

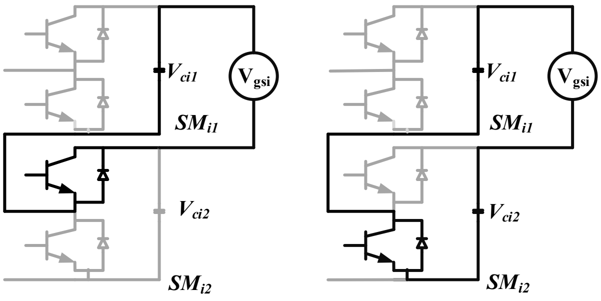

(a) **(b)**

Fig. 2. Block diagram for capacitor voltage measurement in the step 1 of the estimation method, (a) $T_{i2} = 0$, (b) $T_{i1} = 0$ and, $T_{i2} = 0$

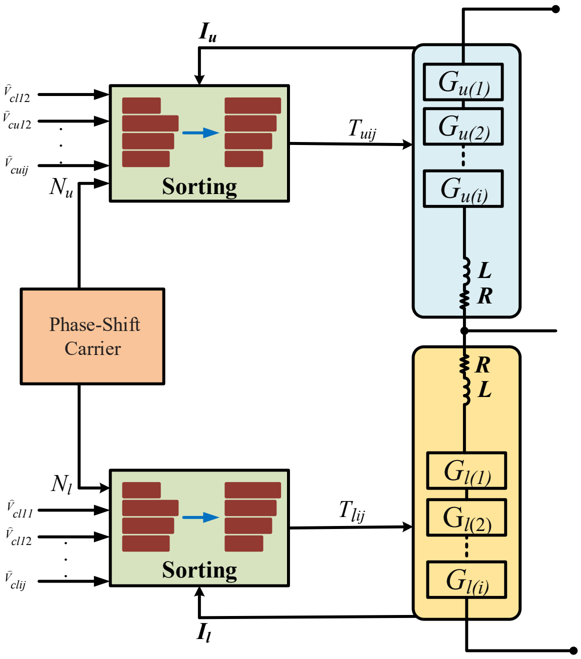

Fig. 3. Block diagram of MMC operation with the proposed estimation method

where $\widehat{V}_{Cij}(t)$ is the estimated capacitor voltage, C_{ij} is the capacitor's nominal capacitance, i_{Cij} is the current flowing through the capacitor, T_s is the sampling time, V_{Cmij} is the capacitor's most recent measured voltage, k_{ij} is the number of sampling times in the estimation step, and t_0 and t_1 are the beginning and stop of the estimation mode, respectively. Consequently, the voltage of the capacitors of each group can be obtained using (1) - (3). A block diagram of the converter's operation while using the proposed technique, which uses PSC-PWM modulation, is given in Fig. 3. Also, in Table 4, the pseudo-code of the method of estimating and sorting the voltage of capacitors is presented. The number of inserted

HB-SMs (N_u, N_l) in the upper and lower arms is determined by comparing the reference signals with triangular carriers and using the PSC-PWM algorithm. Then, the best HB-SMs are chosen for insertion using the sorting algorithm to preserve the capacitors' voltage balance, and the switching state of the SMs of each arm (T_{uij}, T_{lij}) is produced. The predicted voltage of the capacitors and the current of the arms serve as the sorting algorithm's input variables. In accordance with the arm current direction's sign, if the arm current direction is positive, the SM with the lowest capacitor voltage will be selected, and if the arm current direction is negative, the SM with the highest capacitor voltage will be selected.

TABLE IV Algorithm of the process of estimating and sorting the voltage of capacitors

```
1.  Start
2.    Check switching status
3.    if $T_{i2}$ == 0 then
        $V_{gsi}(t) = V_{Ci1}(t)$
      else if $T_{i1}$ == 0 and $T_{i2}$ == 0 then
        $V_{Ci2}(t) = V_{Ci1}(t) - \underline{V_{gsi}}(t)$
      else
        $\hat{V}_{Cij}(t) = V_{Cmij} + \frac{1}{C_{ij}}\int_{t_0}^{t} i_{C_{ij}}(t)\ dt\ (t = t_0 + k_{ij}T_s < t_1)$
4.    Calculate Nu and determine $T_{ij}$
5.    Nu = Calculate Nu ()
6.    if Nu == 0 then
        $T_{ij}(t) = T_{i1}(t-1)$
      else if Nu > 0 and $I_{arm}$ > 0 then
        Choose the SMs with the highest voltage
      else if Nu > 0 and $I_{arm}$ < 0 then
        Choose the SMs with the lowest voltage
7.  End of process
```

IV. The proposed capacitance monitoring method

The enormous number of capacitors in the MMC architecture decreases the system's reliability. According to the proposed configuration of the voltage sensors, an extreme decreasing the nominal value of the capacitance will result in a variance in the estimated voltage values of the capacitors. Therefore, capacitance continuous monitoring will be advantageous to raise the proposed configuration's reliability and improve its performance. Table 3 shows that if $I_{arm} > 0$, the capacitors' voltage rises. As a result, the proposed method uses the ratio of estimated to the measured capacitor voltage in $I_{arm} > 0$. According to section 3, the voltage of the capacitors can be measured directly by the group sensor in step (1). Thus, if $V_{m1(ij)}$ (the first capacitor voltage measured in the interval $I_{arm} > 0$) is the voltage measured at t_0 and $V_{m2(ij)}$ (the second voltage measured in the interval $I_{arm} > 0$) is the voltage measured at t_1, the measured voltage increase will be (For a better understanding, the pseudo-code of the proposed capacitance monitoring method is given in Table 5. Also, the block diagram of the capacitance monitoring process is shown in Fig. 4.):

$$\Delta V_{e1(ij)} = \frac{1}{C_{(ij)}}\int_{t_0}^{t_1} I_{arm}\, dt \tag{4}$$

where $\Delta V_{e1(ij)}$ is the estimated voltage increase value.
The voltage increase rate between the estimated capacitor voltage and the measured capacitor voltage can be determined using (4) and (5) as follows:

$$\frac{\Delta V_{e1(ij)}}{V_{m2(ij)} - V_{m1(ij)}} = \frac{C_{act(ij)}}{C_{(ij)}} = \frac{\Delta V_{e1(ij)}}{\Delta V_{m1(ij)}} \tag{5}$$

So, during the interval (t_0 - t_1), the actual value of the capacitance can be obtained through (6). Nevertheless, since the capacitance changes are not instantaneous, using (6) in small intervals, such as (t_0 - t_1) will increase the burden of calculations. Additionally, SMs switching frequency is higher than the arm's current frequency. Therefore, assuming that during the interval $I_{arm} > 0$ in an SM, there is k number of intervals like (t_0 - t_1) which causes the capacitor voltage to increase. Therefore, the equations (4) - (6) can be calculated in separate intervals, and applied as follows:

$$\Delta V_{m1(ij)} = V_{m2(ij)} - V_{m1(ij)} = \frac{1}{C_{act(ij)}}\int_{t_0}^{t_1} I_{arm}\, dt \tag{6}$$

In (4), $\Delta V_{m1(ij)}$ is the value of the voltage increase measured during the interval ($t_0 - t_1$), and $C_{act(ij)}$ is the actual value of the capacitance. The value of estimated voltage increases in the interval ($t_0 - t_1$) will be equal to:

$$\begin{aligned} \frac{\Delta V_{e1(ij)}}{\Delta V_{m1(ij)}} &= \frac{\Delta V_{e1(ij)}}{V_{m2(ij)} - V_{m1(ij)}} = \frac{C_{act(ij)}}{C_{ij}} \\ \frac{\Delta V_{e2(ij)}}{\Delta V_{m2(ij)}} &= \frac{\Delta V_{e2(ij)}}{V_{m3(ij)} - V_{m2(ij)}} = \frac{C_{act(ij)}}{C_{ij}} \\ \frac{\Delta V_{ek(ij)}}{\Delta V_{mk(ij)}} &= \frac{\Delta V_{ek(ij)}}{V_{mk(ij)} - V_{mk-1(ij)}} = \frac{C_{act(ij)}}{C_{ij}} \end{aligned} \tag{7}$$

It can be deduced from (7) that only the first and last voltage measured during the interval $I_{arm} > 0$ is required to calculate the actual capacitance. Therefore, (7) can be rewritten as follows:

$$\frac{\sum_{z=1}^{k} \Delta V_{ek(ij)}}{V_{mk(ij)} - V_{m1(ij)}} = \frac{C_{act(ij)}}{C_{(ij)}} \tag{8}$$

In (8), $V_{mk(ij)}$ and $V_{m1(ij)}$ are the maximum and minimum measured voltages during the interval $I_{arm} > 0$, respectively. As a result, the ratio of the sum of estimated to measured

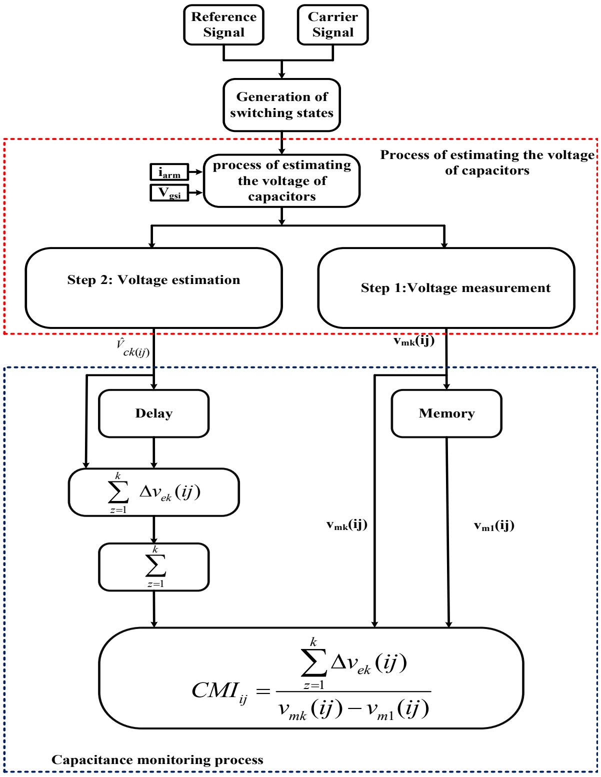

Fig. 4. Block diagram of the capacitance monitoring process

TABLE V CMI range for the failure of capacitor technology

Capacitor technology	CMI range for capacitor failure
E	CMI < 0.8
MPPF	CMI < 0.95
MLC	CMI < 0.9

voltage can be used to create a capacitance monitoring indicator (*CMI*):

$$\mathrm{CMI}_{(ij)} = \frac{\sum_{z=1}^{k} \Delta V_{ek(ij)}}{V_{mk(ij)} - V_{m1(ij)}} \tag{9}$$

The suggested indicator shows the ratio of the actual to nominal capacitance that is less than one. Depending on the type of capacitor technology of the MMC configuration, using the *CMI* index, there are different ranges for indicating failure in a capacitor, as shown in Table 6.

V. Simulation validation

A discrete-time validation of the proposed method has been performed using MATLAB/Simulink. The performance of the MMC operations with the proposed method was analyzed in different scenarios, such as steady state, transient state, switching frequency change, and abrupt input voltage change. Additionally, the proposed voltage estimation method was compared to the method introduced in [17], which will be referred to as the reference method from now on. Table 7 presents the parameters employed in the simulation.

TABLE VI Algorithm of the process of capacitance monitoring method

```
1.  Begin Procedure
2.  Monitor Capacitance
3.  Calculate voltage increase during the interval ($t_0$ - $t_k$)
        $\Delta V_m = V_{mk(ij)} - V_{m1(ij)}$
4.      Calculate estimated voltage increase
            $\Delta V_{e1(ij)}$
5.      Calculate capacitance monitoring indicator (CMI)
            $CMI_{(ij)} = \frac{\sum_{z=1}^{k} \Delta V_{ek(ij)}}{V_{mk(ij)} - V_{m1(ij)}}$
6.      Use CMI to assess capacitance health
            If $CMI_{ij}$ > (CMI range for capacitor failure) then
                Print ("Capacitance is within a healthy range.")
            else
        Print ("Fault Detection.")
    end If
7.  End Procedure
```

TABLE VII Critical parameters of the simulation and experimental evaluation

Items		Simulation values	Experimental values
DC terminal voltage (Vdc)		10 kV	120 V
Number of HB-SMs (N)		10	4
Nominal capacitance (C_{nam})		3200 µF	2200 µF
Nominal voltage of capacitors (V_{nam})		1 kV	30 V
Rated Modulation index (M_a)		0.87	0.9
Switching frequency (F_{sw})		1 kHz	500 Hz
Fundamental frequency (F_b)		50 HZ	50 Hz
Sampling time (Ts)		5e-5 s	2e-4 s
Arm inductance (L)		5 mH	5 mH
Output load	Resistance (Ro)	30 Ω	30 Ω
	Inductor (Lo)	17 mH	17 mH

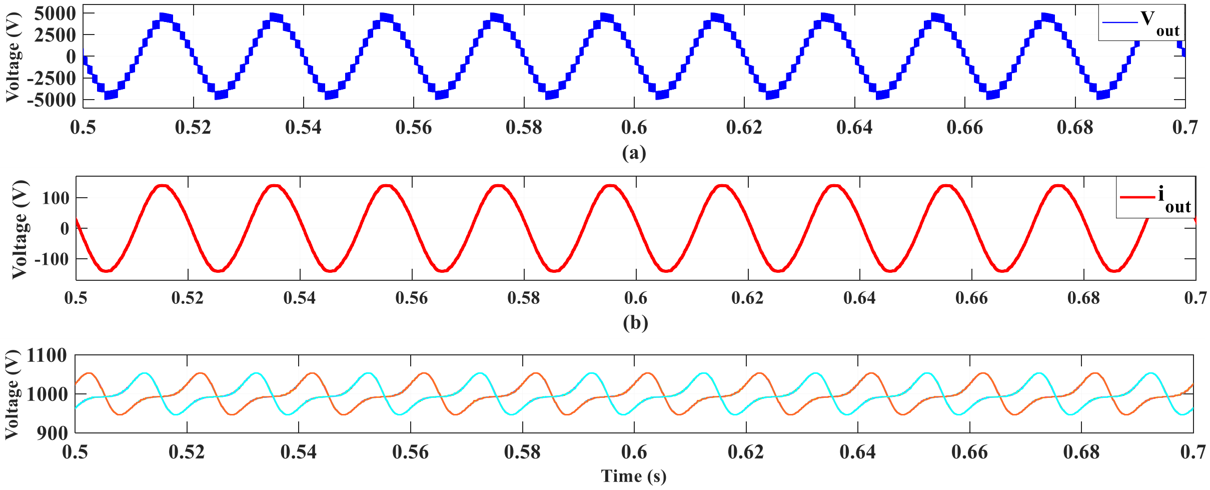

Fig. 5. Simulation results in steady-state conditions (proposed estimation method) (a) AC-side voltage, (b) AC-side current, (c) HB-SMs voltage

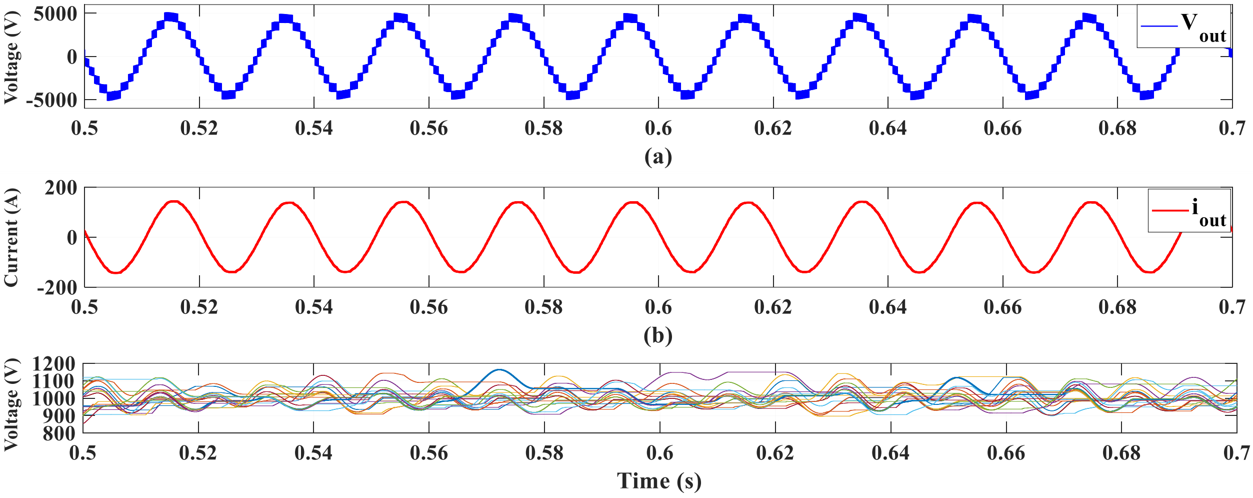

Fig. 6. Simulation results in steady-state conditions (Reference method) (a) AC-side voltage, (b) AC-side current, (c) HB-SMs voltage

A. Performance of steady-state conditions

In this section, the results of simulating the proposed estimation method are evaluated in steady-state conditions with RL constant load. First, the proposed estimated method is used to evaluate the capacitors' voltage balance method, and then the same test is run using the reference method. Fig. 5 and Fig. 6 displays the simulation results for this scenario using the proposed and reference method. The voltage and output current have the same performance as the proposed estimate (Fig 5 (a) and Fig 5 (b) and the reference method (Fig 6 (a) and Fig 6 (b)). However, the proposed estimating approach outperforms the reference method in terms of the capacitors' voltage balance. In the reference method, the ripple voltage of the capacitors is $10\%V_{nam}$, while the ripple

voltage of capacitors with the proposed method is $5\%V_{nam}$. This demonstrates the proposed estimation method's superiority to the reference method. Fig. 7 and Fig. 8 displays the estimated and measured capacitor voltages for HB-SM_{u11} and HB-SM_{u12}. Comparing the suggested technique to the reference method, it can be seen that the estimated values with the proposed method closely match the measured values. As a result, under steady-state operating conditions, the proposed method performs better than the reference method.

B. *Performance of transient conditions*

Fig. 9 – 12 show an evaluation of the performance of the proposed estimation method and reference method under transient situations, such as changing the DC side voltage and switching frequency. The conditions under which the DC side voltage is decreased by 25% V_{dc} in t = 0.6 s are shown in Fig. 9 and Fig. 10. The range of output current and voltage

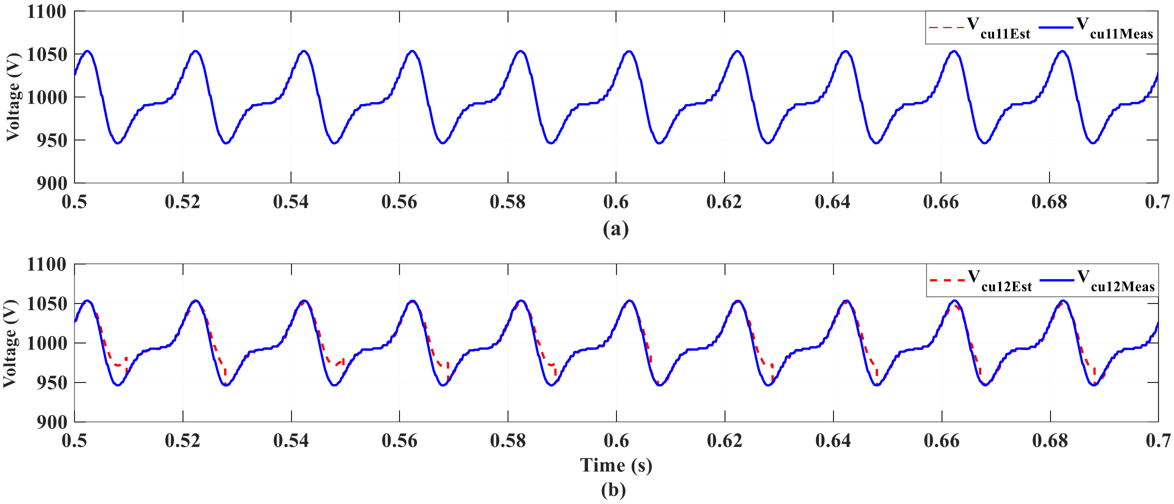

Fig. 7. Estimated and measured capacitor voltage (proposed estimation method) (a) HB-SM$_{u11}$ capacitor voltage, (b) HB-SM$_{u12}$ capacitor voltage

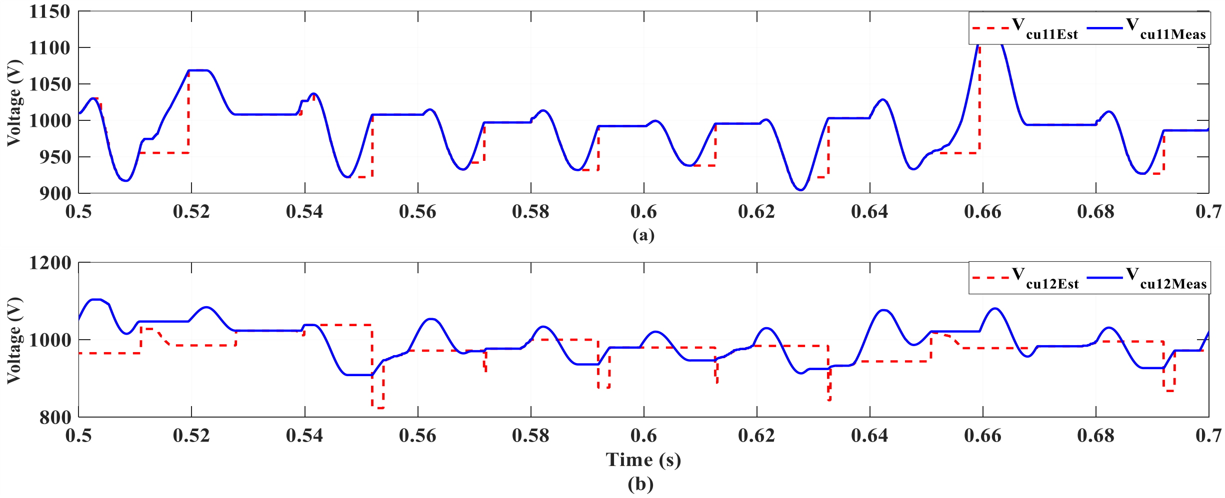

Fig. 8. Estimated and measured capacitor voltage (Reference method) (a) HB-SM$_{u11}$ capacitor voltage, (b) HB-SM$_{u12}$ capacitor voltage

have been decreased in both methods by reducing the DC side voltage, and the capacitors' voltages are now balanced at 7500V. However, the proposed method has a short transient period because the crossing of the transient conditions for the proposed and reference estimating procedures is 0.1s and 0.15s, respectively. In another scenario, the switching frequency is decreased from 1000Hz to 150Hz at t = 0.6s; Fig. 11 and Fig.12 compares the performance of the proposed method and the reference method. As expected, the disturbance in the current and voltage on the AC side has increased in both techniques after decreasing the switching frequency. However, the voltage ripple of the capacitors in the reference method has reached 20% V_{nam}, whereas it is only 6% V_{nam} in the proposed method. As a result, when compared to the reference method, the proposed voltage estimation method performs better at low switching frequencies.

C. Performance of the proposed monitoring method

The simulation results of the proposed monitoring approach when C_{u11} and C_{u12} are adjusted in their nominal value are shown in Fig. 13 and Fig. 14. Increasing the measured and estimated voltage for C_{u11} and C_{u12} are shown in Fig. 13 (a),

Fig. 13 (b), Fig. 14 (a) and Fig. 14 (b). The first and last measured voltages during each positive arm current cycle are denoted as $V_{m1}(ij)$ and $V_{mk}(ij)$, respectively. Fig. 13 (c) displays the capacitance monitoring indicator for C_{u11}, which is $CMI_{u11} = 1 \pm 0.2\%$ according to equation (13). Also, the capacitance monitoring indicator for C_{u12} is shown in Fig.13 (c), which for this capacitor is $CMI_{u12} = 1 \pm 0.4\%$. In another case, the capacitances of C_{u11} and C_{u12} are reduced by 25% and 20%, respectively, compared to the nominal capacitance, i.e., 2400 µF and 2560 µF, respectively. The simulation results of the proposed monitoring approach are shown in

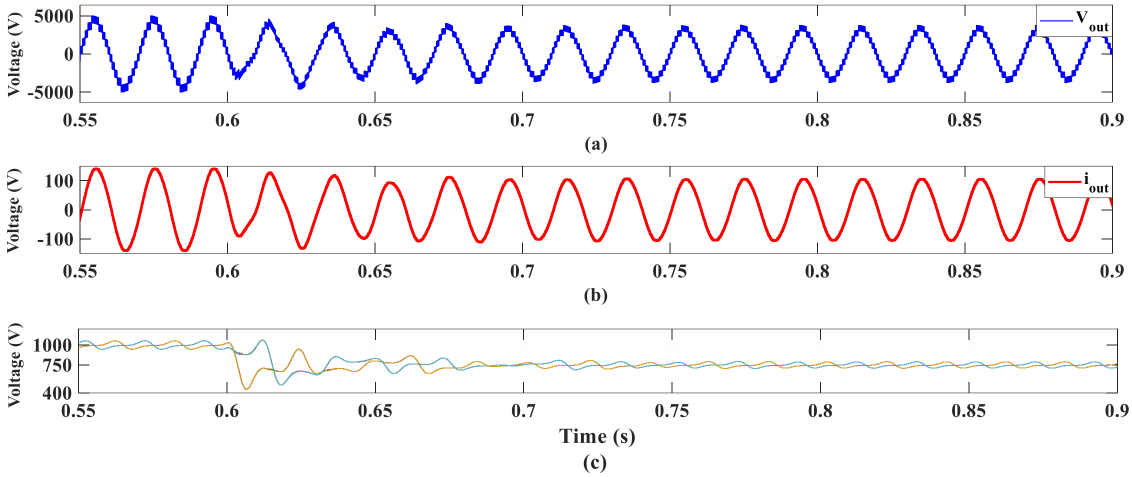

Fig. 9. Simulation results in DC side voltage changing conditions (proposed estimation method) (a) AC-side voltage, (b) AC-side current, (c) HB-SMs voltage

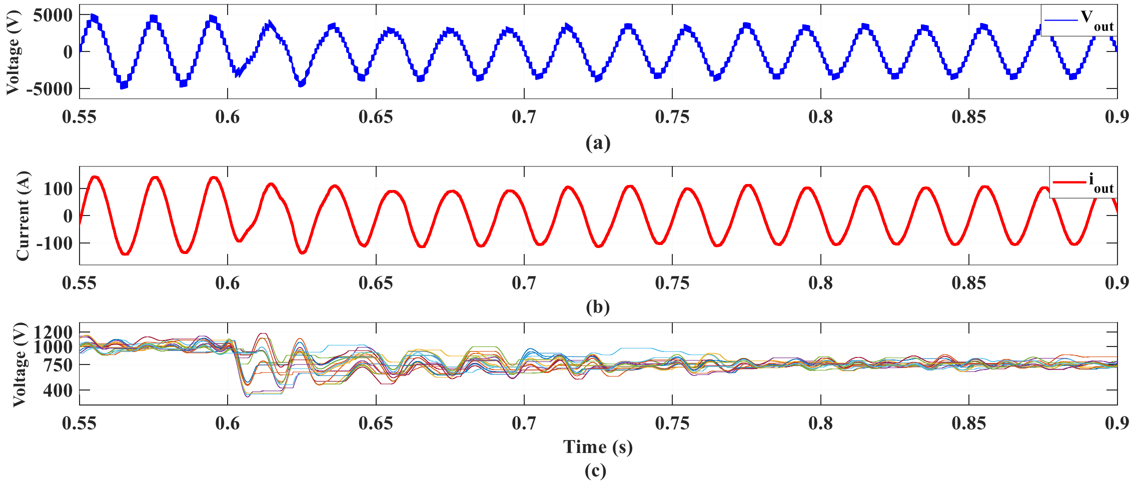

Fig. 10. Simulation results in DC side voltage changing conditions (Reference method) (a) AC-side voltage, (b) AC-side current, (c) HB-SMs voltage

Fig. 15. The measured capacitor voltage increase is shown in Fig. 15 (a), and it is greater due to the lower actual capacitance of the voltage ripple of C_{u11}. Fig. 15 (b) displays the estimated capacitor voltage increase, and Fig. 15 (c) displays the values of CMI_{ij} based on equation (13). The great accuracy of the suggested monitoring approach is demonstrated by the *CMI* values for C_{u11} and C_{u12}, which are $CMI_{u11}=0.75 \pm 0.2\%$ and $CMI_{u12}=0.8 \pm 0.4\%$, respectively. In this approach, if the damaged capacitor oscilloscope. Table 7 lists other critical parameters of the experimental setup. In this approach, if the damaged capacitor and keeps the MMC from further dangers. Additionally, the suggested monitoring technique ensures the capacitor voltage estimate method's excellent accuracy.

VI. Experimental evaluation

After the initial evaluation with different simulation scenarios, the proposed methods are implemented on a 5-level low-scale laboratory sample**.** Fig. 16 shows the experimental setup using four half-bridge sub-modules in each arm. According to the voltage sensor arrangement in this paper, two voltage sensors are required for each arm to manage the voltage balance of the capacitors. Also, the proposed methods and all MMC control algorithms have been implemented using Code Composer software and the JTAG interface on a TMS320F2812 DSP processor. Dual output drivers with IRF640N MOSFETs have been used in the laboratory setup structure for switching operations to increase the output signals sent from the microcontroller up to 15V. Also, all figures in experimental studies have been extracted to TIF format using a Tektronix DPO 5034 oscilloscope. Table 7 lists other critical parameters of the experimental setup.

A. Performance of steady-state conditions

Fig. 17 shows the experimental performance results of the proposed capacitor voltage estimation method under steady-state conditions. As shown in Fig. 17 (a), the output voltage is well produced at 5-level with the least disturbance. Fig.

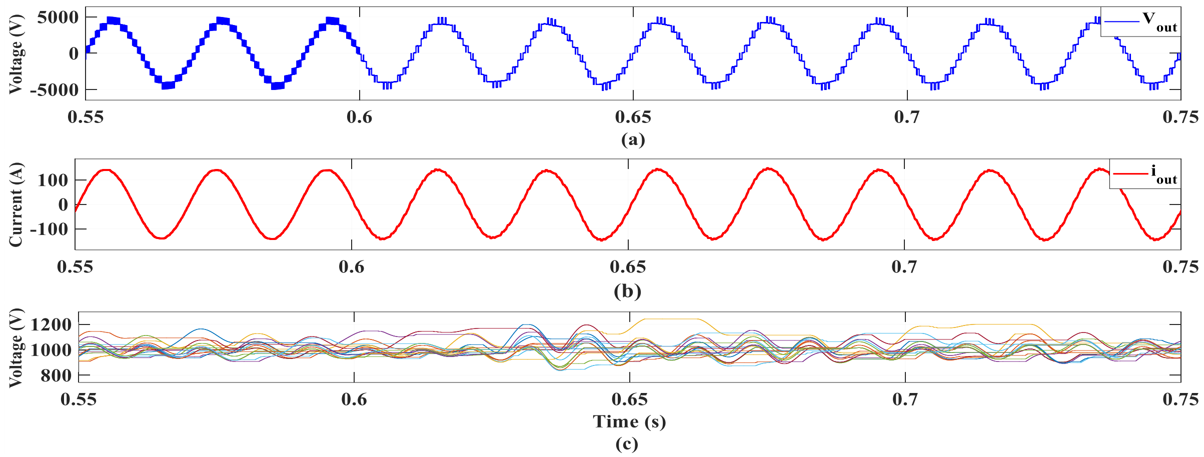

Fig. 11. Simulation results in transient conditions (Reference method) (a) AC-side voltage, (b) AC-side current, (c) HB-SMs voltage

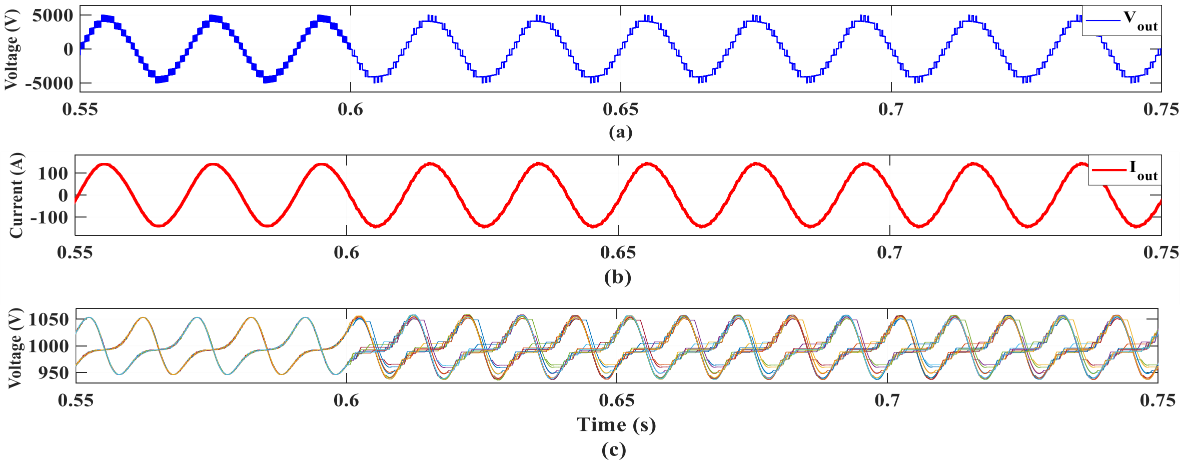

Fig. 12. Simulation results in transient conditions (proposed estimation method) (a) AC-side voltage, (b) AC-side current, (c) HB-SMs voltage

17 (b) also displays the current on the AC side, which oscillates with the least total harmonic distortion and in a sinusoidal pattern with a fundamental frequency of 50 Hz. Fig. 17 (c) depicts the capacitor voltage of the upper arm sub-modules, which oscillates at the capacitors' nominal voltage (30V) with a ripple of roughly 5% V_{nam}.

B. Performance by changing the modulation index

In this case, the converter is initially operating in a steady-state. At t = 1.08s, M_a decreases from 0.9 to 0.4; as shown in Fig. 18 (a) and Fig. 18 (b), the terminal voltage of the AC side is reduced from 5 to 4 levels, and the current range of the AC side is decreased from 1.9A to 0.8A. Despite the sudden change in M_a, the voltages of capacitors remain balanced (Fig. 18 (c)). Therefore, the proposed estimation method shows excellent performance. At t = 1.18s, the M_a changes once more to its steady-state value. Fig. 19 shows a scenario where the load impedance at t = 1.1s undergoes a sudden increase of 100%. Notably, notwithstanding the precipitous decline in the output current, the capacitors' voltage balance control is adeptly sustained. This observation attests to the efficacy of the employed estimation method, underscoring its capability to ensure proper system performance in the face of load impedance variations. To scrutinize the robustness of the proposed method, an examination was conducted under extreme conditions. Specifically, the intentional reduction of the DC link voltage from 120 V to 40 V is depicted in Fig. 20 within the experimental results for this scenario. Figures 20 (a) and 20 (b) vividly illustrate a sudden and substantial decline in both output voltage and current in response to the diminished DC link voltage. Nevertheless, the balance control and capacitors are well maintained.

C. Performance of the proposed monitoring method

Evaluation of the accuracy of the proposed monitoring method has been done by examining the capacitance of SM_{u12}. By using the LCR meter, the capacitance of C_{u12} is measured to be 1549 µF, instead of the nominal 2200 µF. As a result, CMI_{u12}=0.704 represents the capacitance monitoring index's true value. The experimental performance results of the method proposed are shown in Fig. 21. The measured voltage rise is equal to 1.91V, as shown in Fig. 21 (a). Also, by using the graph feature of processor, an estimated voltage increases of 1.35V is shown in Fig. 21 (b). The proposed capacitance monitoring index is equal to CMI_{u12}=0.706. As a result, the proposed monitoring method is able to accurately monitor the capacitance in MMC with an error of about 1%, which indicates the optimal performance of the proposed method despite the reduced number of sensors.

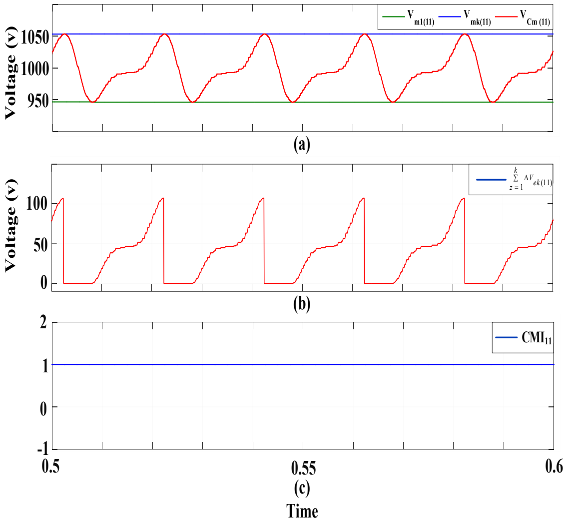

Fig. 13. Simulation results of the monitoring method for C_{u11} (a) Measured voltage increase, (b) Estimated capacitor voltage increase, (c) CMI_{u11} value.

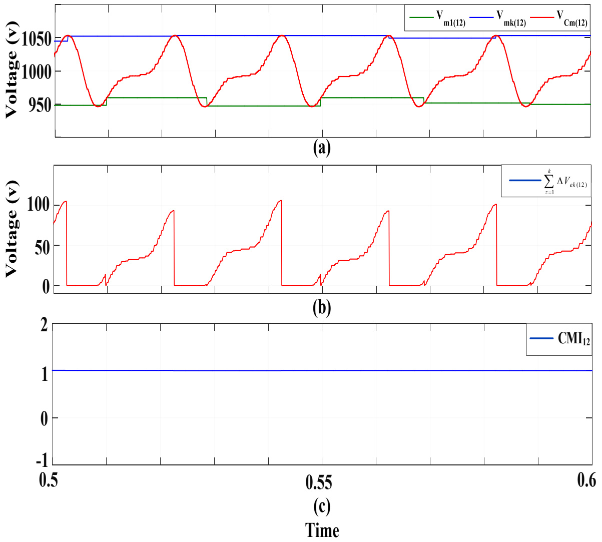

Fig. 14. Simulation results of the monitoring method for C_{u12} (a) Measured voltage increase, (b) Estimated capacitor voltage increase, (c) CMI_{u12} value.

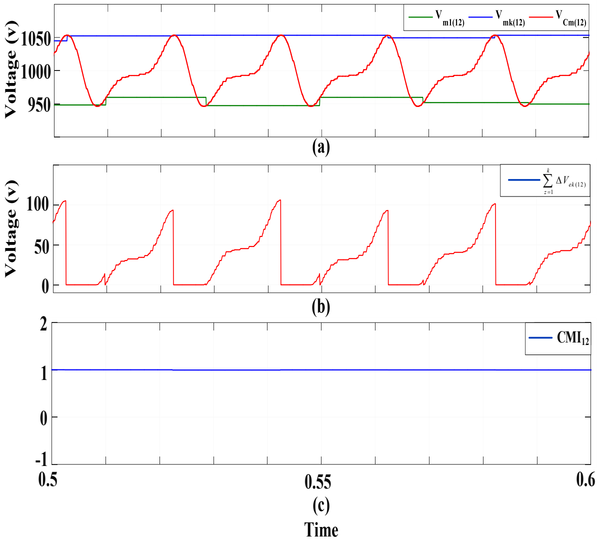

Fig. 15. Simulation results of the monitoring method for C_{u12} (a) Measured voltage increase, (b) Estimated capacitor voltage increase, (c) CMI_{u12} value.

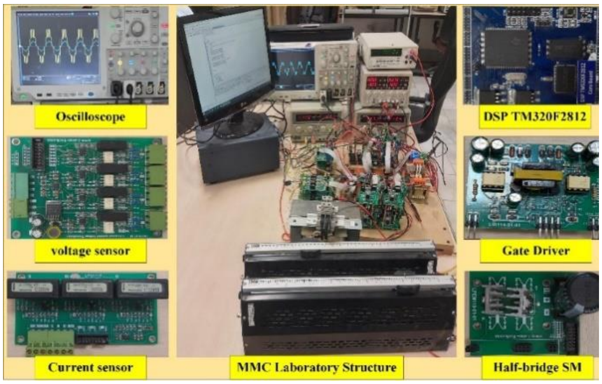

Fig. 16. MMC experimental-setup.

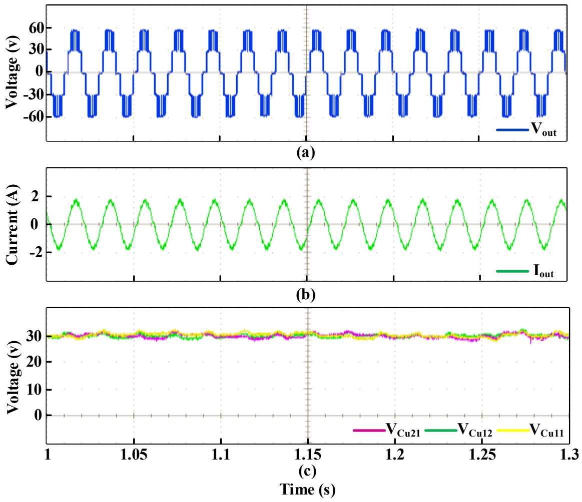

Fig. 17. Experimental results in steady-state conditions. (a) AC-side voltage, (b) AC-side current, (c) HB-SMs voltage.

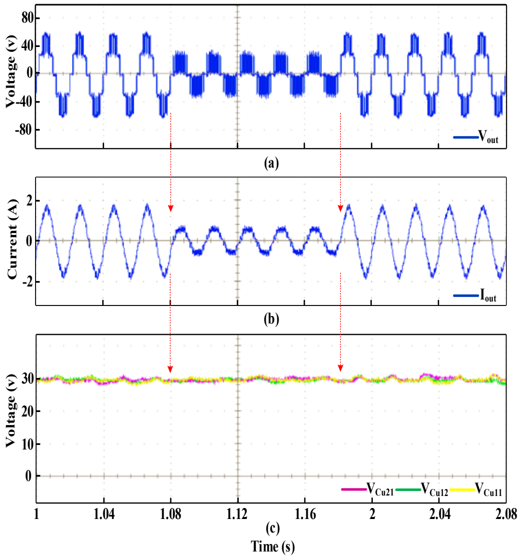

Fig. 18. Experimental results in transient state conditions (a) AC-side voltage, (b) AC-side current, (c) HB-SMs voltage.

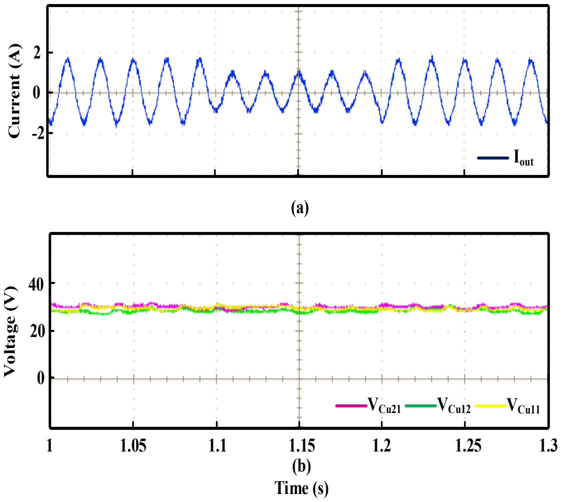

Fig. 19. Experimental results in transient state conditions (a) AC-side current, (b) HB-SMs voltage.

VII. Conclusion

This study presents an improved capacitor voltage balancing method that offers several key advantages for high-voltage and high-power MMC applications. The developed strategy effectively addresses the critical challenge of managing the large number of flying capacitors in the converter. Compared with conventional solutions, employing a single voltage sensor for two half-bridge submodules reduces the required sensor count while simultaneously improving computational efficiency and overall system reliability. The introduced estimation approach eliminates the need for forced activation algorithms or correction factors, making the control process simpler and more robust.

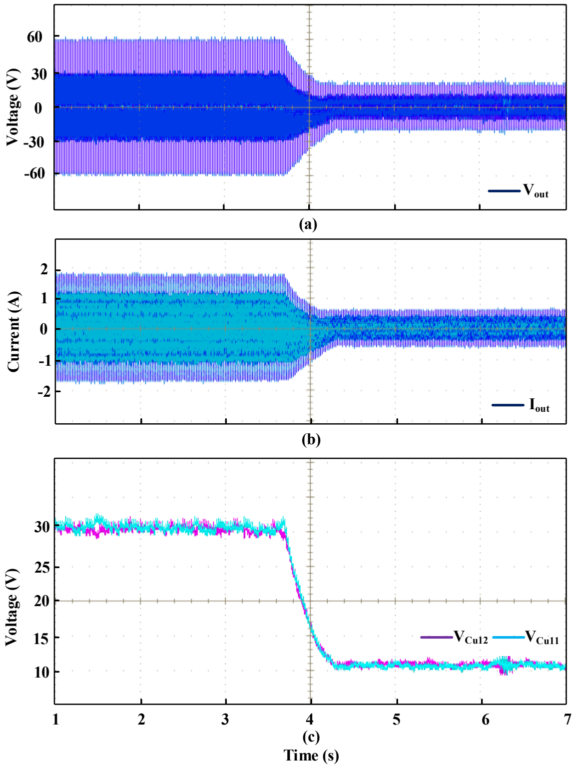

Fig. 20. Experimental results in transient state conditions (a) AC-side voltage, (b) AC-side current, (c) HB-SMs voltage.

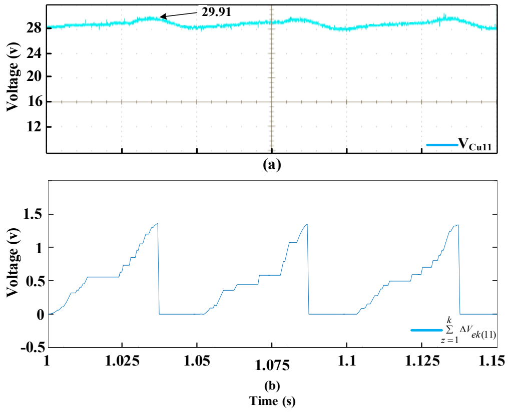

Fig. 21. Experimental results of the monitoring method for Cu12 (a) Measured voltage increase, (b) Estimated capacitor voltage increase.

In addition, a novel capacitance monitoring technique has been demonstrated, enabling accurate health assessment of capacitors once per cycle with less than 1% error. This capability significantly enhances the reliability and fault tolerance of the converter. Both simulation and experimental investigations confirm the effectiveness of the presented methods across steady-state and transient conditions. The results highlight that the developed approach is not only accurate and computationally efficient but also practical for real-world high-power and high-voltage applications.

REFERENCES

[1] L. Wu, J. Liu, S. Vazquez, and S. K. Mazumder, 'Sliding Mode Control in Power Converters and Drives: A Review', IEEE/CAA J. Autom. Sin., vol. 9, no. 3, pp. 392–406, Mar. 2022, doi: 10.1109/JAS.2021.1004380.

[2] V. Barahouei, S. M. Barakati, M. Rahmani Haredasht, and M. Bagheri Hashkavayi, 'Capacitor voltage balancing, capacitance monitoring, and fast fault detection in a nested neutral point clamped (NNPC) converter with the reduced number of sensors', Comput. Electr. Eng., vol. 119, p. 109543, Oct. 2024, doi: 10.1016/j.compeleceng.2024.109543.

[3] X. Shen et al., 'Adaptive Second-Order Sliding Mode Control for Grid-Connected NPC Converters With Enhanced Disturbance Rejection', IEEE Trans. Power Electron., vol. 37, no. 1, pp. 206–220, Jan. 2022, doi: 10.1109/TPEL.2021.3099844.

[4] M. R. Haredasht and S. M. Barakati, 'Fault-Tolerant Configuration for T-Type Nested Neutral Point Clamped (T-NNPC) Converter', in 2023 International Conference on Protection and Automation of Power Systems (IPAPS), IEEE, Jan. 2023, pp. 1–6. doi: 10.1109/IPAPS58344.2023.10123308.

[5] Z. Wang et al., 'A Review of EMI Research in Modular Multilevel Converter for HVDC Applications', IEEE Trans. Power Electron., vol. 37, no. 12, pp. 14482–14498, Dec. 2022, doi: 10.1109/TPEL.2022.3179234.

[6] D. D. Le, S. Hong, and D.-C. Lee, 'Fault detection and tolerant control for flying-capacitor modular multilevel converters feeding induction motor drives', J. Power Electron., vol. 22, no. 6, pp. 947–958, Jun. 2022, doi: 10.1007/s43236-022-00425-x.

[7] S. Debnath, J. Qin, B. Bahrani, M. Saeedifard, and P. Barbosa, 'Operation, Control, and Applications of the Modular Multilevel Converter: A Review', IEEE Trans. Power Electron., vol. 30, no. 1, pp. 37–53, Jan. 2015, doi: 10.1109/TPEL.2014.2309937.

[8] Y. Liu, Y. Liu, Y. Jin, and J. Chen, 'Novel submodule voltage balancing topology for hybrid modular multilevel converters', J. Power Electron., vol. 21, no. 10, pp. 1416–1426, Oct. 2021, doi: 10.1007/s43236-021-00285-x.

[9] J. Samantaray, R. Chakraborty, A. Dey, and S. Chakrabarty, 'Lyapunov-Based Capacitor Voltage Observation of Modular Multilevel Converters', IEEE Trans. Ind. Electron., vol. 70, no. 3, pp. 3024–3034, Mar. 2023, doi: 10.1109/TIE.2022.3172779.

[10] M. B. Hashkavayi, S. M. Barakati, M. R. Haredasht, V. Barahouei, and S. H. Torabi, 'Balancing of Capacitor Voltages with a Reduced Number of Voltage and Current Sensors in Alternate Arm Multilevel Converter (AAMC)', in 2023 14th Power Electronics, Drive Systems, and Technologies Conference (PEDSTC), IEEE, Jan. 2023, pp. 1–5. doi: 10.1109/PEDSTC57673.2023.10087151.

[11] W. Luo, Y. Ma, and C. Zheng, 'Selection-based capacitor voltage balancing control for modular multilevel converters', J. Power Electron., vol. 21, no. 10, pp. 1427–1438, Oct. 2021, doi: 10.1007/s43236-021-00288-8.

[12] P. Hu, R. Teodorescu, and J. M. Guerrero, 'State observer based capacitor-voltage-balancing method for modular multilevel converters without arm-current sensors', Int. J. Electr. Power Energy Syst., vol. 113, no. December 2018, pp. 188–196, Dec. 2019, doi: 10.1016/j.ijepes.2019.05.025.

[13] F. Deng, C. Liu, Q. Wang, R. Zhu, X. Cai, and Z. Chen, 'A Currentless submodule individual voltage balancing control for modular multilevel converters', IEEE Trans. Ind. Electron., vol. 67, no. 11, pp. 9370–9382, 2020, doi: 10.1109/TIE.2019.2952808.

[14] Z. Geng, M. Han, and W. Yan, 'Phase Delay Compensation and Average Capacitor Voltage Based Currentless Voltage Balancing Methods for Modular Multilevel Converters', IEEE Trans. Power Deliv., pp. 1–12, 2022, doi: 10.1109/TPWRD.2022.3199588.

[15] R. Picas, J. Zaragoza, J. Pou, S. Ceballos, and J. Balcells, 'New Measuring Technique for Reducing the Number of Voltage Sensors in Modular Multilevel Converters', IEEE Trans. Power Electron., vol. 31, no. 1, pp. 177–187, Jan. 2016, doi: 10.1109/TPEL.2015.2412658.

[16] M. Abdelsalam, M. Marei, S. Tennakoon, and A. Griffiths, 'Capacitor voltage balancing strategy based on sub-module capacitor voltage estimation for modular multilevel converters', CSEE J. Power Energy Syst., vol. 2, no. 1, pp. 65–73, Mar. 2016, doi: 10.17775/CSEEJPES.2016.00010.

[17] Z. Wang and L. Peng, 'Grouping Capacitor Voltage Estimation and Fault Diagnosis with Capacitance Self-Updating in Modular Multilevel Converters', IEEE Trans. Power Electron., vol. 36, no. 2, pp. 1532–1543, 2021, doi: 10.1109/TPEL.2020.3011131.

[18] M. Bagheri-Hashkavayi, S. M. Barakati, S. Yousofi-Darmian, and V. Barahouei, 'Improved Sensor Reduction Method in Modular Multilevel Converters Based on Energy Estimation', IEEE Trans. Power Deliv., vol. 8977, no. c, pp. 1–1, 2022, doi: 10.1109/TPWRD.2022.3165474.

[19] M. Rahmani, S. M. Barakati, S. Yousofi Darmian, V. Barahouei, and M. Bagheri Hashkavayi, 'Optimized Algorithm for Open-Circuit Fault Detection in Switches and Capacitor Voltage Balancing Control in Modular Multilevel Converters', Int. J. Ind. Electron. Control Optim., vol. 7, no. 1, pp. 15–27, 2024, doi: https://doi.org/10.22111/ieco.2024.47310.1509.

[20] H.-L. Dang and S. Kwak, 'Review of Health Monitoring Techniques for Capacitors Used in Power Electronics Converters', Sensors, vol. 20, no. 13, p. 3740, Jul. 2020, doi: 10.3390/s20133740.

[21] H. Xia et al., 'Capacitor ConditionMonitoring forModular Multilevel Converter Based on Charging Transient Voltage Analysis', vol. 38, no. 3, pp. 3847–3856, 2023.

[22] Y. J. Jo, T. H. Nguyen, and D. C. Lee, 'Condition monitoring of submodule capacitors in modular multilevel converters', 2014 IEEE Energy Convers. Congr. Expo. ECCE 2014, pp. 2121–2126, Nov. 2014, doi: 10.1109/ECCE.2014.6953683.

[23] O. Abushafa, S. Gadoue, M. Dahidah, and D. Atkinson, 'A new scheme for monitoring submodule capacitance in modular multilevel converter', IET Conf. Publ., vol. 2016, no. CP684, pp. 1–6, 2016, doi: 10.1049/cp.2016.0369.

[24] F. Deng, Q. Wang, D. Liu, Y. Wang, M. Cheng, and Z. Chen, 'Reference Submodule Based Capacitor Monitoring Strategy for Modular Multilevel Converters', IEEE Trans. Power Electron., vol. 34, no. 5, pp. 4711–4721, 2019, doi: 10.1109/TPEL.2018.2857832.

[25] Z. Wang, Y. Zhang, H. Wang, and F. Blaabjerg, 'Capacitor Condition Monitoring Based on the DC-Side Start-Up of Modular Multilevel Converters', IEEE Trans. Power Electron., vol. 35, no. 6, pp. 5589–5593, Jun. 2020, doi: 10.1109/TPEL.2019.2956808.

[26] H. Wang, H. Wang, Z. Wang, Y. Zhang, X. Pei, and Y. Kang, 'Condition Monitoring for Submodule Capacitors in Modular Multilevel Converters', IEEE Trans. Power

Electron., vol. 34, no. 11, pp. 10403–10407, Nov. 2019, doi: 10.1109/TPEL.2019.2917937.

[27] M. Zoraghi-Jedi, S. Barakati, M. Rahmani-Haredasht, V. Barahouei, and A. Yazdani, 'Capacitance health monitoring in the modular multilevel converter using a method with minimum number of sensors and computational burden', Int. J. Circuit Theory Appl., vol. 52, no. 12, pp. 6343–6361, Dec. 2024, doi: 10.1002/cta.4057.

Mohsen Rahmani-Haredasht received the B.Sc. degree in electrical engineering from the University of Velayat, Zahedan, Iran, in 2019, and the M.Sc. degree from the University of Sistan and Baluchestan, Zahedan, Iran, in 2021. As a researcher at the University of Sistan and Baluchestan, he has been participating in several research projects in the Power Electronics Laboratory since 2022. His research interests include multilevel converters, open circuit fault detection, fault tolerance of power electronics converters, and DC-DC converters. He has also been working as a relay and protection expert at Taftan Power Development and Transmission Engineering Company since 2023.

S.Masoud Barakati (Senior Member, IEEE) received the Ph.D. degree in electrical engineering from the University of Waterloo, Waterloo, ON, Canada, in 2008. He is currently an Associate Professor with the University of Sistan and Baluchestan, Zahedan, Iran. From 2008 to 2009, he was an Associate Researcher with the University of Wisconsin Madison, Madison, WI, USA. He was a Visiting Professor with the Universities of Ryerson, Toronto, ON, Canada, and Ecole Polytechnique de Montreal, Montreal, QC, Canada, in 2012 and 2014, respectively. His research interests include power electronic circuits, control systems, renewable energy, FACTS devices, matrix and multilevel converters, and mechatronic systems. He is the Editor-inChief of the International Journal of Industrial Electronics, Control, and Optimization.

Mohammad Bagheri-Hashkavayi was born in Rasht, Iran, in 1991. He received the B.Sc. degree in electrical engineering from the University of Guilan, Rasht, Iran, in 2015, and the M.Sc. degree from the University of Sistan and Baluchestan, Zahedan, Iran, in 2020. He specializes in the assembling and repairing of power electronics boards and the development of control systems. He is currently the Managing Director of the technical office and is also involved in several collaborative projects in the area of power electronics. His research interests include power electronics, power systems, control, renewable energy, and mechatronics.

IECO International Journal Of Industrial Electronics Control and Optimization
Print ISSN: 3517-2645
Online ISSN: 3568-2645
Homepage: https://ieco.usb.ac.ir/

Multi-Class Short-Term Voltage Stability Assessment Considering the Missing Data

Amir Hossein Babaali[1] | Mohammad Taghi Ameli[2]

Faculty of Electrical Engineering, Shahid Beheshti University, Tehran, Iran[1,2]
Corresponding author's email: mtameli@yahoo.com

Article Info

Article type:
Research Article

Article history:
Received: 21-June-2025
Received in revised form: 24-August-2025
Accepted: 01-September-2025
Published online: 22-June-2026

Keywords:
Gated recurrent unit,
Communication delay,
Missing data, short-term Voltage stability,
Multi-class classification.

ABSTRACT

Short-term voltage stability (STVS) varies with operating conditions of power networks, making its accurate assessment a critical challenge. This paper investigates a multi-class, data-driven approach to STVS assessment. A dynamic index is employed to categorize voltage magnitude variations into three classes: stable, alert, and unstable. A significant obstacle in data-driven methods is missing measurement data, typically caused by sensor failures or communication delays. To address this issue, we propose two complementary solutions. First, a Bidirectional Gated Recurrent Unit (Bi-GRU) network with an attention mechanism is designed to recover data loss due to sensor failures. This method leverages both temporal trends and historical system information to reconstruct missing values with high accuracy. Second, a variable-length sliding window (VLSW) algorithm combined with a Bi-GRU is introduced to mitigate data loss arising from communication delays. The VLSW algorithm enhances data diversity and enables fast recovery. Simulation results on IEEE 39-bus and IEEE 118-bus test systems demonstrate that the proposed framework effectively identifies multi-class STVSA under missing data conditions and remains robust against long-range data losses. Finally, validation on a real-world local network further confirms the practicality and robustness of the proposed approach.

I.Introduction

A. Motivation

Voltage stability has emerged as a critical concern in modern power systems characterized by high penetration of renewable energy sources (RESs) and the proliferation of microgrids. Unlike traditional synchronous generators, inverter-based RESs—such as solar photovoltaic (PV) and wind turbines—lack inherent inertia and reactive power support, compromising the system's ability to regulate voltage and maintain dynamic stability [1],[2]. Microgrids, capable of operating either connected to or islanded from the main grid, introduce additional complexity due to their limited voltage control mechanisms and heightened vulnerability to disturbances [3].

In this context, data-driven methods have gained considerable traction for real-time monitoring, stability assessment, and control, leveraging the widespread deployment of Phasor Measurement Units (PMUs) and advanced measurement infrastructure [4]. However, a persistent and significant challenge in these methods is missing data, which may arise from sensor malfunctions, communication failures, latency issues, or cyber-physical disruptions. Missing PMU measurements can severely impair the accuracy of voltage stability assessment models—particularly those based on dynamic, multi-class classification approaches [5].

The quality of PMU data severely restricts its various applications in the power system, in which a major factor affecting data quality is PMU data loss [6]. Due to communication congestion, hardware failures, data transmission/communication delays, cyber-attacks, and GPS-time synchronization issues, on-site PMUs typically experience different degrees of data quality issues[7]. Whenever data loss happens, the data-driven process of short-term voltage stability assessment (STVSA) cannot work correctly. Therefore, this paper focuses on the issue of STVSA considering missing data.

B. Literature Review

Many research efforts have been made to evaluate STVS online based on measurement data and machine learning (ML) algorithms Some promising ML-based data-driven solutions have been recently reported in the literature [8],[9]. Since STVS is generally driven by various fast-acting dynamic loads, such as induction motors and power electronically controlled devices[10], it often presents complicated stability patterns and characteristics in practical complex power systems.

Recently, deep learning-based neural network methods [11], [12],[13], [14], [15], [16] have been used with significant advantages in data-driven STVS assessment. The spatial-temporal features have been employed to learn a recurrent neural network (RNN) for STVSA[11], and the combination of graph convolutional network (GCN) and RNN is presented in [12]. Spatial-temporal GCN (STGCN) proposes to assess online STVS [13]. STGCN replaces the RNN module with the parallel-enabled 1-D Convolutional neural network (CNN). With the introduction of the attention mechanism, a gated recurrent graph attention network is utilized in [14] to perform spatial-temporal correlation learning, which results in adaptive STVSA against topological changes. A generative adversarial network (GAN) -based data augmentation in [15] and a data-driven approach to cyberattack conditions in [16] is presented to solve small data and bad data in STVS assessment.

Despite the efforts made, a serious gap is seen in the studies. Concretely [9],[12],[13] assumed that the measurement data are completely and continuously available. Some studies like [11] have investigated the impact of data loss but have not provided a solution.

To address this, data-driven approaches combining recovery and classification have been widely explored. For example, Long short-term memory (LSTM)-based imputation with Double Deep Q-Learning (DDQN) has been used to reconstruct missing data and classify voltage stability states under moderate data loss [17], while adaptive transient stability assessment frameworks explicitly considering PMU failures have demonstrated improved accuracy compared to mean imputation and tree-based classifiers [18]. A multi-task learning models [19] have been introduced to enhance robustness against incomplete or noisy measurements.

Ref.[20] presents an ensemble representation learning scheme (ERLS) to achieve data loss-tolerant online STVS assessment. It has focused on temporal missing data to recover lost data in different conditions. Attempts have been made to address the data loss issue in power system dynamic security assessment (DSA) [21]. These works focus mostly on network observability and cannot recover temporally lost data.

In practice, the power system operates at different operating points. Therefore, voltage stability should be monitored in several categories to create control measures appropriate to each operating situation. Some states may be alert but in binary classification, it recognizes unstable. So, the network can be brought to a stable state with limited instructions and low cost. Contrary to this insight, many studies including [13]-[20]. have assessed STVS in a binary class, which is a weakness. This paper attempts to fill this gap by examining multi-class STVS and modeling missing data in this framework.

PMU data recovery methods fall into two groups. The first uses correlations among PMUs, such as state estimation [22], tensor methods with historical data [23],[24], or correlation-based recovery[25]. While effective, these approaches degrade when multiple PMUs fail and tensor methods are too costly for real-time use; some variants also exploit past data [26].

The second group is prediction-based, relying mainly on historical PMU records [27], [28]. For example, [27] combines temporal patterns with spatial correlations from neighboring PMUs. These methods can handle wide data loss, but during sudden system events, short histories alone cannot capture future dynamics.

C. Innovations

A review of previous studies reveals that many studies ignored missing data. Moreover, most studies treated voltage stability as a binary problem, despite the fact that real measurement data are often affected by noise, communication interruptions, or PMU failures. Relying solely on a binary stable/unstable signal is insufficient for network monitoring and timely corrective actions. In contrast, this paper evaluates online voltage stability in a multi-class framework while explicitly considering missing data.

In this study, we address multi-class STVSA with missing measurements. A dynamic index is proposed to classify voltage stability levels, and a Bi-GRU network is developed to recover missing data and perform data-driven STVS assessment. Missing data caused by PMU failures and communication delays are studied in detail, and solutions are presented to reconstruct the data quickly and accurately.

Based on a thorough literature review and the limitations of existing approaches, the main contributions of this work are:

(1) Investigation of multi-class STVS under missing data conditions, accompanied by a dynamic index for accurate voltage stability classification.

(2) Integration of PMU data recovery with recent advances in artificial neural networks by developing a Bi-GRU network for both data reconstruction and voltage stability assessment.

(3) Detailed consideration of two types of missing data—PMU failure and communication delays—and presentation of solutions to ensure high-accuracy recovery.

(4) Analysis of the impact of recovered data on the accuracy of voltage stability predictions.
(5) Validation of the proposed model on a real power system, demonstrating its practical applicability.

The remainder of the paper is organized as follows: the proposed methodology is first introduced, followed by a description of the mathematical model, and finally, simulation results and discussions are presented.

II. Proposed model

This study aims to determine STVS based on measured data. The measurement data is considered in a time series format. Based on a dynamic index and behavior of the voltage magnitude, the database is classified into three classes: stable, alert, and unstable.

Measurement data may not be available due to PMU failures or communication delays during operation. The other part of the work deals with missing data. Measurement data is assumed to be unavailable for several seconds (PMU failure) or operating cycles (communication delays).

Time series data shows the dynamic behavior of the system well. One of the deep learning methods for data augmentation is a recurrent neural network (RNN), which is trained to process and convert a sequential data input into a specific sequential data output. GRU is an improved model of RNN, which can learn the dependency of past and future data simultaneously and thus predict future data with high accuracy. Among the recurrent neural networks, GRU has a simpler but more efficient model for the data of this paper, so a GRU model is developed for this study.

Fig. 1 shows the proposed framework for STVSA under missing data. On this basis, the lack of access to the data cannot be a problem in voltage stability assessment. Once access to the PMU data is interrupted, alternative data is predicted based on the behavior of previous data and the data sequence to determine the voltage stability.

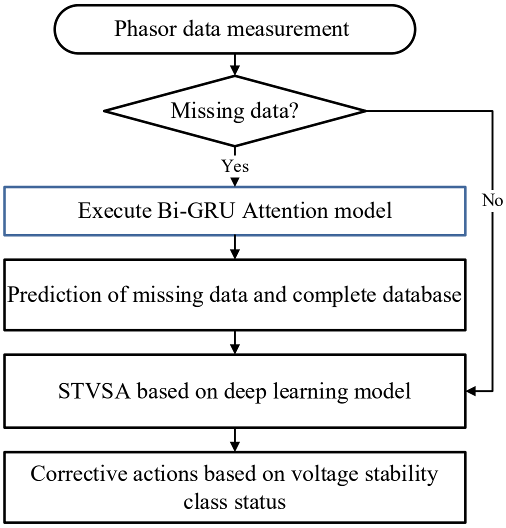

Fig. 1. STVSA with missing data in an overview

A. Failure of PMUs

One of the cases of data loss is the failure or out-of-service of PMUs. Fig. 2 shows that predicting missing data is based on a Bi-GRU and Attention layer learning process. In this structure, a masking layer is considered to remove null vectors in the input sequences. The Bi-GRU is compared in forward and backward forms.

A unidirectional GRU is included in the decoder stage. The dropout layer is used in both the encoder and decoder layers to avoid data overfitting. A dense layer is defined with a linear activation function to generate projections with continuous values. Missing data is retrieved using the previous measurement data through Bi-GRU in two stages: encoder and decoder. Past data samples are analyzed in the encoding phase.

As the data retrieval and training process progresses, decoding is performed, and new data is predicted. At this stage, the attention mechanism helps to focus on valuable data to increase the accuracy of data prediction.

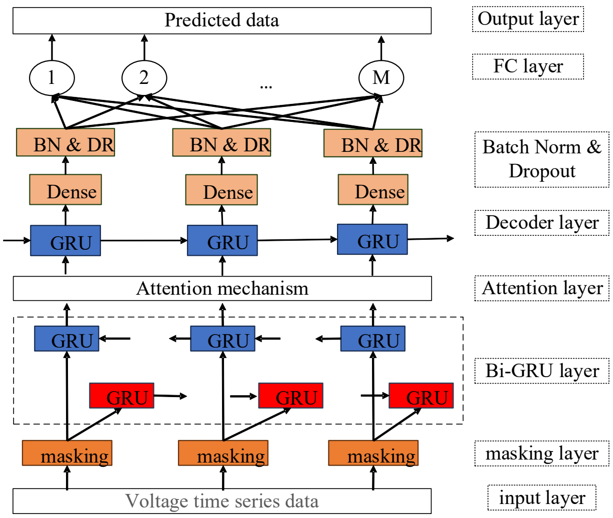

Fig. 2. The framework of the proposed method for recovering missing data in STVSA

B. Communication delay problem

We propose an attention-Bi-GRU approach to recover missing data caused by communication delays (see Fig. 2). In this section, we suggest the Variable-Length Sliding Window (VLSW) algorithm to recover limited data more accurately. The VLSW algorithm considers both past and future time indicators. Besides, it can generate a significantly greater number of samples by dynamically altering the input sequence length during the sampling process, which is crucial for implementing deep learning models.

The structure of Fig. 2 is based on the sequence-to-sequence method, where the encoder and decoder are two key functions. The encoder processes an input time series and maps it to a high-dimensional vector. The decoder takes the input from the vector and calculates the target data sequence. The attention mechanism also allows the decoder to learn how to focus on a particular region of the input sequence for different outputs.

III. Mathematical model

As **Error! Reference source not found.** shows that the recovery of the missing data is defined based on a Bi-GRU, whose model is presented in this section. The input for the problem is a sequence of variable length $x=\{x_1,x_2,...,x_n\}$, where *d* represents the features at a time index i. At each time index, the GRU maintains the hidden state h that leads to the hidden sequence $h=\{h_1,h_2,...,h_n\}$. The hidden vector at time index t is updated as follows.

$$i_t = \sigma\left(W_{xi}x_t + W_{hi}h_{t-1} + b_i\right) \quad (1)$$

$$f_t = \sigma\left(W_{xf}x_t + W_{hf}h_{t-1} + b_f\right) \quad (2)$$

$$c_t = f_t \otimes c_{t-1} + i_t \otimes \tanh\left(W_{xc}x_t + W_{hc}h_{t-1} + b_c\right) \quad (3)$$

$$O_t = \sigma\left(W_{xo}x_t + W_{ho}h_{t-1} + b_o\right) \quad (4)$$

$$h_t = o_t \otimes \tanh(c_t) \quad (5)$$

In the above relationships, i, f and o represent input, forgetting gates, and output. c, σ, and $\otimes$ are the cell vector, the sigmoid function, and the element-wise multiplication, respectively. In Bi-GRU, the input sequences are read not only from one sequence of h but from both the forward $\vec{h} = \{\overrightarrow{h_1}, \overrightarrow{h_2}, \dots, \overrightarrow{h_n}\}$ and backward $\overleftarrow{h} = \{\overleftarrow{h_1}, \overleftarrow{h_2}, \dots, \overleftarrow{h_n}\}$ directions to extract two sequences with hidden states, and then the hidden states are integrated into the time index i as follows:

$$h_i = \left[\overrightarrow{h_i}, \overleftarrow{h_i}\right] \quad (6)$$

The output of the Bi-GRU encoder is a sequence of hidden states of length *n* with input sequence *x*.

A. GRU decoder with an attention mechanism

The output recursive sequence $\mathrm{y} = \{\mathrm{y}_1, \mathrm{y}_2, \mathrm{y}_3, \dots, \mathrm{y}_\mathrm{m}\}$ is generated by the decoder. In this study, the GRU decoder is proposed with an attention mechanism similar to the attention structure in [29]. The attention mechanism allows the model to pay attention to certain parts of the data and give more weight to these parts when making predictions.

One issue with this model is the assignment of continuous values as output. Instead of calculating the probability distribution for the following possible outputs, a fully connected layer with a linear activation function is added to the GRU (Gated Recurrent Unit) layer. This modification allows the model to produce predictions in continuous values, which are used to estimate missing data. For the decoder, the estimate at time t is calculated as follows:

$$y_t = Linear(W\ [s_t; c_t] + b) \quad (7)$$

$$s_t = GRU\,(y_{t-1}, s_{t-1}, c_t) \quad (8)$$

where s_t is the hidden state of the decoder at time index t, c_t is the attention context vector (for each output y_t) and $[s_t, c_t]$ is a combination of the decoder's hidden state and the context vector. The parameters W and b map this combination to the size of the hidden states of the decoder and generate the final linear prediction layers y_t.

At each time sequence t, the attention context vector can be described as the weighted sum of the hidden states transmitted by the Bi-GRU encoder:

$$c_t = \sum_{i=1}^{n} \alpha_{ti} h_i \quad (1)$$

The weight of each hidden state α_{ti} is calculated as follows:

$$e_{ti} = a(s_{t-1}, h_i), \quad (2)$$

$$\alpha_{ti} = \mathrm{softmax}() \quad (3)$$

where e_{ti} expresses the dependency between the hidden states surrounding the h_i and the output in the sequence *t*. *a* is a feedforward network that can be jointly trained with other components of the GRU decoder. To ensure that the sum of all attention weights is normalized to 1, the softmax activation function is applied to e_{ti}.

As seen in Fig. 2, the masking layer is embedded after the input layer. The input layer includes a sequence of time series. The masking layer filters the vectors with a null layer in the input samples according to the input data and sends them to the Bi-GRU encoder. The encoder processes the data in future and past time sequences and generates a hidden output vector. Then the GRU decoder processes the hidden vector and the dense layer recursively generates the final target sequence. During this process, the decoder calculates the attention weights in each time sequence to focus on specific input parts and extract relevant information.

B. Variable length sliding window (VLSW) algorithm

During the data-driven STVSA process, the measurement data may arrive at the operation center with a delay or in a discrete form. In this section, assuming a communication delay in the measurement data, the variable length sliding window (VLSW) algorithm is used along with the proposed method (see Fig. 2). This way, alternative samples are produced quickly with only a few available samples.

One advantage of this method is the simultaneous use of past and future time sequences. In addition, dynamically changing the input sequence length in the sampling process generates more samples, which improves machine learning performance.

Fig. 3 shows how the VLSW algorithm works, using a dynamically changing range of input data to generate prediction patterns. In this algorithm, both the length of the left time series ($|IL|$) and the length of the right time series ($|IR|$) change during sampling. Assuming that the $|IL|$ varies dynamically between m and n and $|IR|$ varies dynamically between o and p, the sample number generated is Eq.(4).

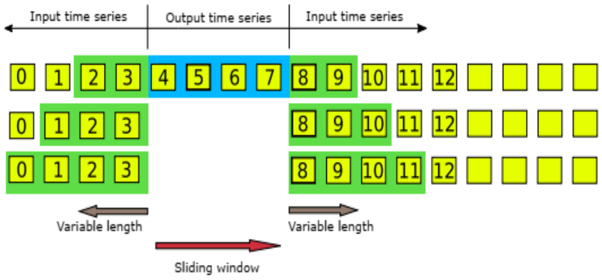

Fig. 3. Illustration of the VLSW algorithm

VLSW can generate more samples than the sliding window algorithm with future information [30], which can lead to higher accuracy in predicting missing data.

$$N = \sum_{i=m}^{n} \sum_{j=o}^{p} |T|-i-|O|-j+1$$

$$= \frac{(p-o+1)(n-m+1)\left[2\left(|T|-|O|+1\right)-\left(m+n+o+p\right)\right]}{2} \tag{4}$$

$$, n+p+|O| \le |T|$$

C. Model evaluation

Root Mean Square Error (RMSE), and Mean Absolute Error (MAE) are methods to evaluate the performance of missing data augmentation. The mathematical relationship between these methods is given below [7].

$$RMSE = \sqrt{\frac{1}{n}\sum_{i=1}^{n}\left(\left|f_i - f_i\right|\right)^2} \tag{5}$$

$$MAE = \frac{1}{n}\sum_{i=1}^{n}\left|f_i - f_i\right| \tag{6}$$

where f_i is the real value and $\widehat{f_i}$ is the estimated value of the monitored parameters. We use RMSE and MAE criteria because these can show the sensitivity of the proposed model to outlier data.

IV. Simulations and results

The investigated networks are IEEE 39-bus and 118-bus networks. The 39-bus network is used to recover the missing data caused by the PMU failure, and the 118-bus network is used to recover the missing data caused by the communication delay. According to [31], IEEE 39-bus and 118-bus have 8 and 21 buses connected to the PMU, respectively (TABLE I) to maintain the observability of the network.

According to the frequency of the 39-bus network (60 Hz) and the 118-bus network (50 Hz), the data sampling rates are assumed to be 30 ms and 20 ms, respectively. A time domain simulation is performed to generate operation scenarios and create a database in the DIgSILENT Power Factory 15.1.7-application environment and RMS mode [32]. The database is classified according to dynamic indices [32] in the MATLAB 2019b environment, and the learning and evaluation process is implemented in Python.

TABLE I. Selected buses connected to PMU in case studies

Case study	Selected buses (connected to PMU)
IEEE 39bus	3,8,10,16,20,23,25,29
IEEE 118bus	3,13,29,35,43,47,55,58,62,63,69,75,81,82,9 1,93,104,106,107,113,115

A. Classification of voltage time series data

In this study, the dynamic behavior of voltage is considered for the STVS assessment, so a database has been created based on time series. Static indicators to determine voltage stability only work from a certain operating point, so they are unsuitable for classifying voltage time series. To classify time series data, a dynamic index is needed to include all voltage change characteristics. Here, a dynamic voltage index is defined by considering the NERC operating voltage guidelines and the Lyapunov exponent (LE) [32].

a. Lyapunov exponent

LE is a fundamental concept of nonlinear dynamics that quantifies the local stability features of attractors and other invariant sets in state space. Positive LE indicates the exponential divergence of neighboring trajectories and is critical of chaotic attractors [32]. Assume a continuous dynamic system: $\dot{x} = f(x), x \in X \subset R^N$. If $\phi(t,x)$ is the answer to differential equations, the following restricted matrix is defined:

$$\Lambda(x) = \lim_{t\to\infty}\left[\frac{\partial\Phi(t,x)^T}{\partial x}\frac{\partial\Phi(t,x)}{\partial x}\right]^{1/2t} \tag{7}$$

Eq. (8) shows the LE per bus i for changes in the voltage magnitude. So that $\Lambda_i(x)$ is the eigenvalues of the bounded matrix $\Lambda(x)$. The LE $(\lambda_i(x))$ is defined as $\lambda_i(x) = log\Lambda_i(x)$.

In Eq. (8), $k = 1,2,\ldots,M$. Δt, M and N_b are the sampling rate, time window, and number of busses, respectively. For fixed and small values 0<ε1<ε2, N should be selected according to Eq. (8).

$$\lambda_i(k\Delta t):$$

$$= \frac{1}{Nk\Delta t} \times \sum_{m=1}^{N} log\frac{\left\|V_{(k+m)\Delta t} - V_{(k+m-1)\Delta t}\right\|}{\left\|V_{m\Delta t} - V_{(m-1)\Delta t}\right\|}, k > N \tag{8}$$

$$\forall i = 1,2,\ldots,N_b$$

$$\varepsilon_1 < \left\|V_{m\Delta t} - V_{(m-1)\Delta t}\right\| < \varepsilon_2, m = 1,2,\ldots,N \tag{9}$$

For each bus, λ_i specifies the trend of the voltage curves. λ_i will be positive for divergent oscillatory trends; otherwise, it will be negative.

b. Voltage Deviation (VD)

According to NERC, a voltage recovery problem occurs when the voltage deviation remains above 0.2 for 20 cycles [32]. VD is calculated using the following equations.

$$\Delta V_i^t = \frac{V_i^0 - V_i^t}{V_i^0}, i \in [1, N_b], t \in [t_{cl}, t_a] \quad (10)$$

$$VD_i = \min\left\{\Delta V_i^t\right\} \quad (11)$$

In Eq.(10), the voltage deviation per bus is calculated from the pre-fault value or steady-state, where V_i^0 is the pre-fault voltage in the i-th bus and t_a is equal to 20 cycles of the nominal frequency after clearing time (t_{cl}).

The voltage stability status is classified by combining VD and LE (or λ) into stable, alert, and unstable classes, according to TABLE II. If the oscillating behavior of the voltage is divergent (it means λ>0) and the voltage does not return within the defined time (VD>0.2), voltage instability has occurred (The red image in Fig. 4). In the alert mode, the voltage returned to an acceptable range after the fault clearing (VD<0.2), but voltage oscillating behavior resulted in a positive LE (The yellow image in Fig. 4). Moreover, a stable mode is shown by the green image in Fig. 4.

TABLE II. Database classification summary based on dynamic index and Lyapunov exponent

Lyapunov exponent (λ)	Voltage deviation (VD)	Stability class
0<	0.2<	Unstable
0>	0.2<	Alert
0<	0.2>	Alert
0>	0.2>	Stable

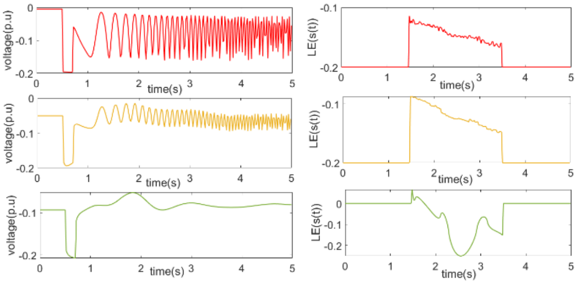

Fig. 4. Voltage magnitude curve and Lyapunov exponent in three-class STVS

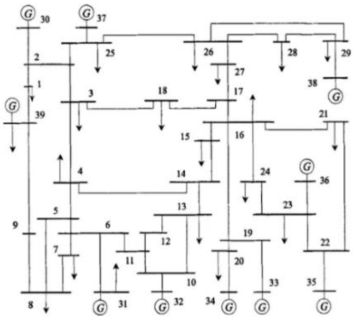

Fig. 5. One-line diagram of IEEE 39-bus network

B. Missing data due to PMU failure

To evaluate the performance of the proposed model in the 39-bus network (see Fig. 5).

We developed 1,000 operating scenarios that simulated three-phase faults occurring on the lines of the 39-bus system and generating unit failures. A database is created through time-domain simulations and classified into three classes: stable, alert, and unstable. This database is divided into training data (70%) and test data (30%). The parameters for the attention-Bi-GRU model are adjusted as detailed in TABLE III. Attention size represents the linear size of the attention weights.

TABLE III. Setting the main parameters of the attention-Bi-GRU model

Parameters	quantity/ type
Activator function	Tanh and ReLU
Learning rate	10e-5
Epochs	200
Batch size	128
Dropout	0.3
Attention size	16
hidden layer unit	128

Assuming we cannot access any of the PMUs, its data is predicted using the proposed method (Attention-Bi-GRU). The predicted data is compared with the actual data to evaluate the model, and MAE and RMSE criteria are formed. The results for a set of PMUs are shown in TABLE IV. It includes simulation results of the proposed method (Attention-Bi-GRU) and a generative adversarial network (GAN) with an attention mechanism.

In TABLE IV, voltage time-series is retrieved over 5 seconds. According to the results obtained, the proposed method predicted the missing data with higher accuracy than the GAN-attention method, so that for all PMUs, RMSE and MAE are less than 0.18 % and 0.16 %, respectively.

TABLE IV. The function of predicting missing data in each of the PMUs through the proposed model and GAN-attention model

PMU No.	RMSE		MAE	
	Att-Bi-GRU	GAN-Att	Att-Bi-GRU	GAN-Att
PMU#3	1.78E-03	1.86E-03	1.61E-03	1.74E-03
PMU#10	1.48E-03	1.59E-03	1.40E-03	1.44E-03
PMU#20	1.67E-03	1.78E-03	1.59E-03	1.69E-03
PMU#25	1.55E-03	1.68E-03	1.51E-03	1.60E-03
PMU#29	1.64E-03	1.76E-03	1.56E-03	1.66E-03

This paper proposes an approach that simultaneously recovers lost data and evaluates STVS. We compare our method with several state-of-the-art methods from various sources. Fig. 6 illustrates that the alternative data through the attention Bi-GRU resulted in a high accuracy of about 99% in the STVS assessment.

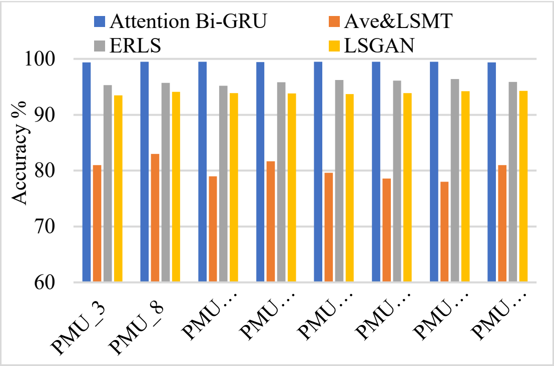

Fig. 6. Comparison of STVSA with recovering missing data due to PMU failure via various methods

As illustrated in Fig. 6, the use of LSTM with historical averaging achieves only about 80% accuracy in STVSA. In comparison, the least squares GAN (LSGAN)-based augmentation [15] and ERLS [20] improve performance to 94% and 95.8%, respectively. The proposed Attention Bi-GRU further advances this result, reaching 99.4% accuracy, which highlights its stronger capability in handling missing data and ensuring reliable stability assessment.

a. Hyperparameter tuning

The sensitivity analysis in Fig. 7 indicates that increasing the attention size and hidden units enhances performance until a saturation point, beyond which improvements are negligible. For dropout, no regularization (0.0) leads to overfitting with unstable recovery errors, while a high rate (0.6) causes underfitting and accuracy degradation. A moderate dropout value (0.3), together with attention size 16 and 128 hidden units, achieves the most stable balance, yielding low RMSE/MAE and consistently high classification accuracy.

C. Comparative Analysis with Existing Methods

To highlight the advantages of the proposed method, Fig. 8 provides a radar diagram comparing it with other ANN-based models. The proposed model demonstrates strong capability in recovering missing data and assessing multi-class STVS, whereas approaches such as LSGAN and ERLS fail to correctly identify multiple stability boundaries.

For further clarification, we assume the loss of PMU_3 data due to failure, and evaluate multi-class STVS using different methods across three categories: stable, alert, and unstable. Most alternative methods fail to detect the alert state effectively, mainly because their training datasets are limited to binary classification. Moreover, their assessment of stable and unstable conditions is inadequate, likely due to insufficient handling of missing data.

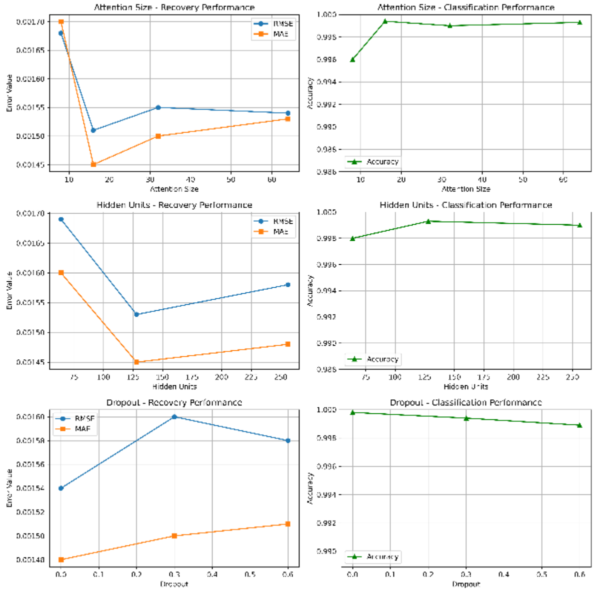

Fig. 7. Sensitivity analysis of key hyperparameters

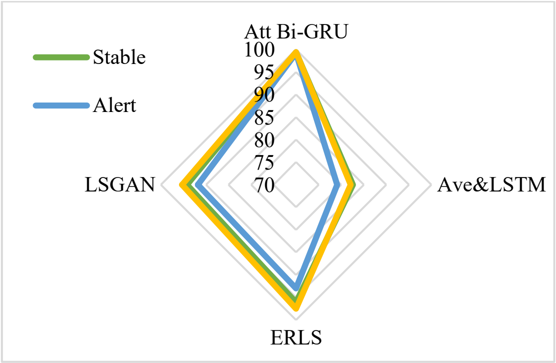

Fig. 8. Multi-class STVSA results through different methods with missing data in PMU_3

According to [33], this section considers 1000 operation scenarios in the IEEE 118-bus, including the failure of dense lines and the out-of-service of some power units, to generate the database. The database is divided into training and testing sets, in which training is based on the prediction model of Fig. 2.

D. Missing data due to communication delay

According to the IEEE C37.118.2-2011 standard, the communication delay between the PMU and PDC is typically between 0.02s and 0.05s [34]. The sampling rate consumed 20 ms in the IEEE 118-bus and the maximum permissible communication delay consumed 50 ms; three measurement data are missing for each delay. So, this study assumes three cases of communication delays with values of 50ms, 100ms, and 150ms, i.e., 3, 5, and 8 missing data samples. For each of these, the parameters setting of VLSW values are given in TABLE V.

In TABLE V, m, n, o, p, and q are the minimum and maximum length of the data before the missing data, the minimum and maximum length of the window after the missing data, and the output vector length, respectively, as shown in Fig. 3.

TABLE V. Setting the initial values of the parameters of the VLSW

parameters	**50 ms**		**100 ms**		**150 ms**		**200 ms**	
	w_1	w_2	w_1	w_2	w_1	w_2	w_1	w_2
M	3	3	3	3	3	3	4	4
N	5	5	6	6	8	8	9	9
O	3	3	3	3	3	3	4	4
P	5	5	6	6	8	8	9	9
q	3	5	5	8	8	10	10	11

In TABLE V, window 1 (w_1) shows that the length of the output vector at each delay is equal to the length of the missing data sequence. In w_2, it is assumed that the length of the output vector is longer, which means more data is lost.

Fig. 9-Fig. 11 present the performance of the proposed attention-based Bi-GRU model with VLSW across both training and test datasets. As shown in Fig. 9, the model successfully reconstructs missing data under a 50 ms communication delay (equivalent to three voltage magnitude samples at a 20 ms sampling rate). Despite the challenges introduced by this delay, the proposed framework achieves reliable convergence for both training and testing phases, reaching an accuracy of 98.5%.

The impact of increased communication delays is further demonstrated in Fig. 10, where the recovery accuracy decreases compared to Fig. 9. Specifically, with a longer delay leading to five consecutive missing data sequences, the reconstruction process becomes more complex. This results in reduced prediction speed and accuracy, highlighting that higher delays increase both the computational burden and the difficulty of maintaining high-fidelity recovery.

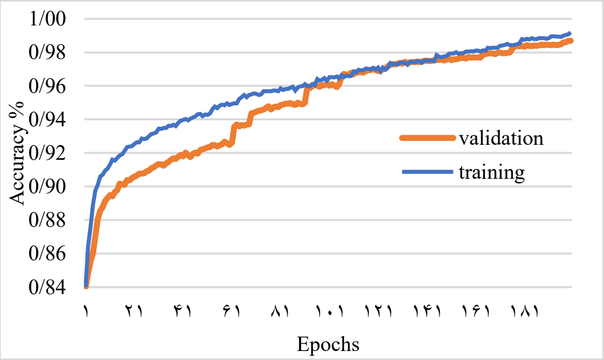

Fig. 9. The accuracy of training and testing the predicted data for a delay of 50 ms and w_1

Fig. 11 shows that the proposed model accurately predicted the alternative data, although the range of the missing data sequence increased. Thus, with the increased data required for prediction, the model's accuracy did not change significantly compared to a delay of 100 ms. The results indicate that attention Bi-GRU with the VLSW algorithm can accurately retrieve missing data due to communication delay. In this way, STVS can be assessed with complete information.

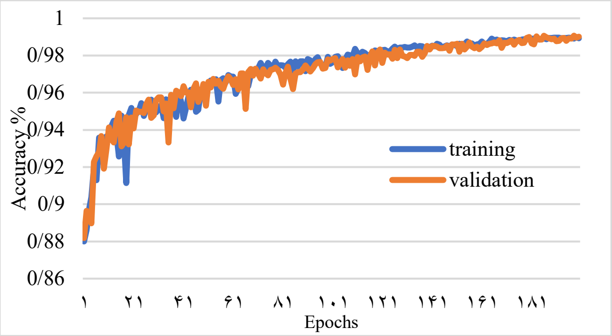

Fig. 10. The accuracy of training and testing the predicted data for a delay of 100 ms and w_1

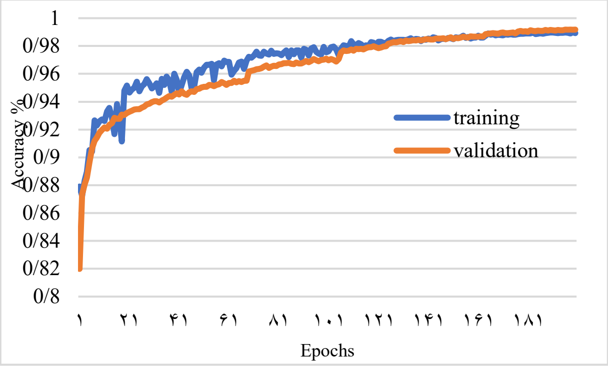

Fig. 11. The accuracy of training and testing the predicted data for a delay of 150 ms and w_1

Cases 1 to 3 represent communication delays of 50, 100, and 150 ms, respectively, while w1 and w2 correspond to different VLSW settings.

According to Fig. 12, the samples are recovered with an error of less than 0.2% across these scenarios, indicating that the estimated values remain very close to the actual missing data. Although the prediction error shows a slight upward trend as the delay increases, it consistently remains within an acceptable margin.

As illustrated in Fig. 12, when the delay is extended to Case 4 (200 ms), the error further increases, with RMSE reaching around 0.19 and MAE up to 0.184. This demonstrates that the model performance begins to degrade more noticeably at longer delays. Nevertheless, the overall error level remains relatively low, suggesting that the proposed approach is still reliable for delays up to 200 ms, beyond which the operational boundaries of the model may need to be carefully considered.

E. Robustness verification of method in noisy scenarios

To assess the robustness of the proposed framework, noisy PMU measurements with different signal-to-noise ratios (SNR = 20, 30, 40, and 50 dB) were evaluated, and the results are shown in Fig. 13. Even at severe noise levels (SNR = 20 dB), the model achieved 99.05% accuracy, with RMSE and MAE remaining on the order of 10^{-3}.

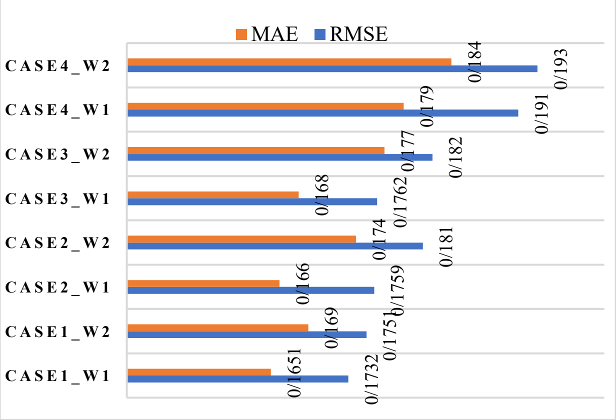

Fig. 12. Evaluation results of the proposed method for different modes of communication delay and sliding window

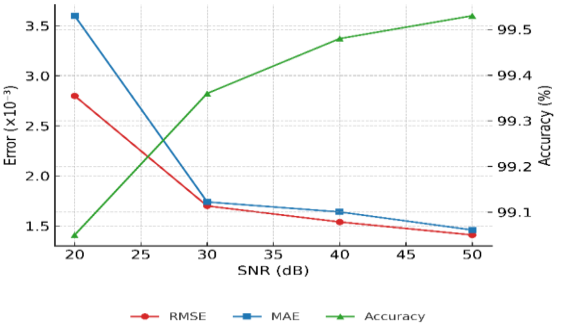

Fig. 13. Robustness of the proposed Attention Bi-GRU under different noise levels

As SNR increased, accuracy consistently exceeded 99%, while errors further decreased. These results demonstrate that the Attention Bi-GRU is not only effective for missing data recovery but also highly robust to measurement noise, confirming its practical applicability for real-world power grid monitoring.

F. Analysis of Computational Cost and Latency

In addition to accuracy and robustness, the computational efficiency of the proposed Attention Bi-GRU is evaluated to ensure suitability for real-time PMU applications. On a standard workstation (Intel i7 CPU, 16 GB RAM), the average inference time per PMU sequence is approximately 4 ms, which is significantly below the 20 ms reporting rate of conventional PMUs. The memory footprint remained modest (<250 MB during inference), and latency is negligible, confirming that the framework can operate under real-time constraints without imposing notable computational overhead. While training requires higher resources, this is performed offline and does not affect online deployment. These results indicate that the proposed model achieves a favorable trade-off between predictive accuracy and computational cost, ensuring practical scalability to large-scale power system monitoring.

G. Validation on Local network

A part of Iran Grid includes 72 buses, 47 transmission lines and 23 power units. We suppose 10 PMUs connected to 400 and 230 kV busses. Time domain simulations include 800 scenarios which consider N-1contingencies such as three-fault on lines and out-of-service of synchronous machines. TABLE VI shows average of RMSE and MAE as percentage in real power system. As shown, prediction of missing data in all of busses is done with high accuracy, so that, average of RMSE and MAE through proposed method (Att-Bi-GRU) are less than 0.14%.

TABLE VI. Results of missing data prediction in a Real

Method	RMSE	MAE
GAN-Att	0.174	0.171
Att-Bi-GRU	0.139	0.136

V. Conclusions

This paper introduces a data-driven framework for multi-class STVSA under conditions of missing data. By employing a dynamic index, STVS is categorized into three classes—stable, alert, and unstable—offering a more granular perspective compared to traditional binary approaches. To address the critical issue of incomplete measurements, two complementary strategies are proposed: (i) an attention-based Bi-GRU network for recovering data lost due to PMU failures, and (ii) a variable-length sliding window (VLSW) integrated with Bi-GRU to handle data loss caused by communication delays.

The proposed Attention Bi-GRU framework has demonstrated superior accuracy (over 99%) in short-term voltage stability assessment, even under challenging conditions of missing or noisy PMU data. Moreover, the method remains robust against severe communication delays (up to 200 ms) and noisy measurements (SNR as low as 20 dB), while maintaining RMSE and MAE in the order of 10^{-3}. These findings confirm the model's strong potential for real-time deployment in power system monitoring and control.

Validation on a real power system further confirmed its practicality, with both RMSE and MAE remaining under 0.14%. In addition to superior accuracy, the proposed framework benefits from reduced model complexity and faster operator response, making it suitable for real-time power system operations.

Recent studies have introduced multi-class stability assessment methods based on CNN-LSTM hybrids and transformer architectures. Although such approaches are not included in our benchmark analysis due to scope limitations, the superior accuracy of the proposed Attention Bi-GRU highlights its strong competitiveness with these state-of-the-art models.

Nevertheless, several limitations should be acknowledged. First, the framework relies on PMU placement quality, and suboptimal deployment may affect recovery performance. Second, although the model shows robustness to random noise and missing data, its resilience to adversarial or cyber-induced data losses was not explicitly investigated. Third, the threshold values for Lyapunov exponent and voltage deviation were based on NERC guidelines, without dataset-specific optimization.

Future research may therefore explore:

(1) Integration of graph-based or physics-informed priors to guide data recovery.
(2) Evaluation under adversarial or malicious missing data patterns for cybersecurity assurance.
(3) Optimization of thresholds to maximize classification accuracy across diverse systems.
(4) Exploring probabilistic deep learning techniques (e.g., Bayesian RNNs, MC-Dropout) to provide uncertainty bounds and confidence intervals for both data recovery and stability assessment.

References

[1] X. Liang, H. Chai, and J. Ravishankar, "Analytical Methods of Voltage Stability in Renewable Dominated Power Systems: A Review," Electricity, vol. 3, no. 1, pp. 75–107, Feb. 2022, doi: 10.3390/electricity3010006.

[2] P. Fakhrooeian, mehrdad Abedi, and peyman karimyan, "Optimal allocation and sizing of dynamic VAR support to improve short-term voltage stability considering wind farm and dynamic load model," IECO, vol. 1, no. 1, June 2018, doi: 10.22111/ieco.2018.24388.1024.

[3] N. Khosravi, D. Çelik, H. Bevrani, and S. Echalih, "Microgrid stability: A comprehensive review of challenges, trends, and emerging solutions," International Journal of Electrical Power & Energy Systems, vol. 170, p. 110829, Sept. 2025, doi: 10.1016/j.ijepes.2025.110829.

[4] J. Cao, M. Zhang, and Y. Li, "A Review of Data-Driven Short-Term Voltage Stability Assessment of Power Systems: Concept, Principle, and Challenges," Mathematical Problems in Engineering, vol. 2021, pp. 1–12, Dec. 2021, doi: 10.1155/2021/5920244.

[5] F. Boronuosi, S. Azad, M.-T. Ameli, and M. R. Shadi, "Dynamic Security Assessment of Power Systems Using a Deep Learning and GAIN-Based Approach for Addressing Missing Data," Results in Engineering, p. 106585, Aug. 2025, doi: 10.1016/j.rineng.2025.106585.

[6] A. Xue et al., "Method of amplitude data recovery in PMU measurements that considers synchronisation errors," IET Generation Trans & Dist, vol. 14, no. 24, pp. 5746–5755, Dec. 2020, doi: 10.1049/iet-gtd.2020.0785.

[7] Y. Cheng, B. Foggo, K. Yamashita, and N. Yu, "Missing Value Replacement for PMU Data via Deep Learning Model With Magnitude Trend Decoupling," IEEE Access, vol. 11, pp. 27450–27461, 2023, doi: 10.1109/ACCESS.2023.3254448.

[8] L. Zhu, C. Lu, I. Kamwa, and H. Zeng, "Spatial–Temporal Feature Learning in Smart Grids: A Case Study on Short-Term Voltage Stability Assessment," IEEE Transactions on Industrial Informatics, vol. 16, no. 3, pp. 1470–1482, 2020, doi: 10.1109/TII.2018.2873605.

[9] C. Ren, Y. Xu, Y. Zhang, and R. Zhang, "A Hybrid Randomized Learning System for Temporal-Adaptive Voltage Stability Assessment of Power Systems," IEEE Transactions on Industrial Informatics, vol. 16, no. 6, pp. 3672–3684, June 2020, doi: 10.1109/TII.2019.2940098.

[10] J. Zhang, Y. Luo, B. Wang, C. Lu, J. Si, and J. Song, "Deep Reinforcement Learning for Load Shedding Against Short-Term Voltage Instability in Large Power Systems," IEEE Transactions on Neural Networks and Learning Systems, vol. 34, no. 8, pp. 4249–4260, Aug. 2023, doi: 10.1109/TNNLS.2021.3121757.

[11] L. Zhu, D. J. Hill, and C. Lu, "Intelligent Short-Term Voltage Stability Assessment via Spatial Attention Rectified RNN Learning," IEEE Transactions on Industrial Informatics, vol. 17, no. 10, pp. 7005–7016, Oct. 2021, doi: 10.1109/TII.2020.3041300.

[12] G. Wang, Z. Zhang, Z. Bian, and Z. Xu, "A short-term voltage stability online prediction method based on graph convolutional networks and long short-term memory networks," International Journal of Electrical Power & Energy Systems, vol. 127, pp. 106647–106647, 2021, doi: 10.1016/j.ijepes.2020.106647.

[13] Y. Luo, C. Lu, L. Zhu, and J. Song, "Data-driven short-term voltage stability assessment based on spatial-temporal graph convolutional network," International Journal of Electrical Power & Energy Systems, vol. 130, pp. 106753–106753, Sept. 2021, doi: 10.1016/j.ijepes.2020.106753.

[14] H. Cai and D. J. Hill, "A data-driven distributed and easy-to-transfer method for short-term voltage stability assessment," International Journal of Electrical Power & Energy Systems, vol. 139, pp. 107960–107960, 2022, doi: 10.1016/j.ijepes.2022.107960.

[15] Y. Li, M. Zhang, and C. Chen, "A Deep-Learning intelligent system incorporating data augmentation for Short-Term voltage stability assessment of power systems," Applied Energy, vol. 308, pp. 118347–118347, 2022, doi: 10.1016/j.apenergy.2021.118347.

[16] C. Ren, X. Du, Y. Xu, Q. Song, Y. Liu, and R. Tan, "Vulnerability Analysis, Robustness Verification, and Mitigation Strategy for Machine Learning-Based Power System Stability Assessment Model Under Adversarial Examples," IEEE Transactions on Smart Grid, vol. 13, no. 2, pp. 1622–1632, 2022, doi: 10.1109/TSG.2021.3133604.

[17] A. Liu, X. Guan, D. Sun, H. Jiang, C. Cui, and D. Fang, "Short Term Voltage Stability Assessment with Incomplete Data Based on Deep Reinforcement Learning in the Internet of Energy," in Wireless Algorithms, Systems, and Applications, vol. 12938, Z. Liu, F. Wu, and S. K. Das, Eds., in Lecture Notes in Computer Science, vol. 12938. , Cham: Springer International Publishing, 2021, pp. 225–236. doi: 10.1007/978-3-030-86130-8_18.

[18] B. Ma, J. Yang, X. Peng, K. Jiang, D. Liu, and K. Cao, "An adaptive assessment method of power system transient stability considering PMU data loss," IET Generation Trans & Dist, vol. 18, no. 24, pp. 4116–4133, Dec. 2024, doi: 10.1049/gtd2.13340.

[19] T. Luo and X. Jiang, “A novel multi-task learning method for evaluating short-term voltage stability with incomplete PMU measurements,” Complex Intell. Syst., vol. 10, no. 2, pp. 1971–1983, Apr. 2024, doi: 10.1007/s40747-023-01252-8.

[20] L. Zhu et al., “Robust Representation Learning for Power System Short-Term Voltage Stability Assessment Under Diverse Data Loss Conditions,” IEEE Transactions on Neural Networks and Learning Systems, vol. 35, no. 5, pp. 6035–6047, May 2024, doi: 10.1109/TNNLS.2023.3325542.

[21] B. Tan et al., “Spatial-temporal adaptive transient stability assessment for power system under missing data,” International Journal of Electrical Power & Energy Systems, vol. 123, pp. 106237–106237, 2020, doi: 10.1016/j.ijepes.2020.106237.

[22] K. Sun, M. Huang, Z. Wei, and G. Sun, “High-Refresh-Rate Robust State Estimation Based on Recursive Correction for Large-Scale Power Systems,” IEEE Trans. Instrum. Meas., vol. 72, pp. 1–13, 2023, doi: 10.1109/TIM.2023.3277070.

[23] D. Osipov and J. H. Chow, “PMU Missing Data Recovery Using Tensor Decomposition,” IEEE Trans. Power Syst., vol. 35, no. 6, pp. 4554–4563, Nov. 2020, doi: 10.1109/TPWRS.2020.2991886.

[24] B. Foggo and N. Yu, “Online PMU Missing Value Replacement Via Event-Participation Decomposition,” IEEE Transactions on Power Systems, vol. 37, no. 1, pp. 488–496, Jan. 2022, doi: 10.1109/TPWRS.2021.3093521.

[25] Y. Cheng, B. Foggo, K. Yamashita, and N. Yu, “Missing Value Replacement for PMU Data via Deep Learning Model With Magnitude Trend Decoupling,” IEEE Access, vol. 11, pp. 27450–27461, 2023, doi: 10.1109/ACCESS.2023.3254448.

[26] Z. Yang, H. Liu, T. Bi, Z. Li, and Q. Yang, “An adaptive PMU missing data recovery method,” International Journal of Electrical Power & Energy Systems, vol. 116, pp. 105577–105577, 2020, doi: 10.1016/j.ijepes.2019.105577.

[27] J. Pei, Z. Wang, J. Wang, and D. Shi, “Robust fast PMU measurement recovery enhanced by randomized singular value and sequential Tucker decomposition,” IET Generation Trans & Dist, vol. 16, no. 16, pp. 3267–3281, Aug. 2022, doi: 10.1049/gtd2.12520.

[28] X. Deng et al., “Deep learning model to detect various synchrophasor data anomalies,” IET Generation Trans & Dist, vol. 14, no. 24, pp. 5739–5745, Dec. 2020, doi: 10.1049/iet-gtd.2020.0526.

[29] Z. Niu, G. Zhong, and H. Yu, “A review on the attention mechanism of deep learning,” Neurocomputing, vol. 452, pp. 48–62, Sept. 2021, doi: 10.1016/j.neucom.2021.03.091.

[30] Y.-F. Zhang, P. J. Thorburn, W. Xiang, and P. Fitch, “SSIM—A Deep Learning Approach for Recovering Missing Time Series Sensor Data,” IEEE Internet of Things Journal, vol. 6, no. 4, pp. 6618–6628, Aug. 2019, doi: 10.1109/JIOT.2019.2909038.

[31] M. M. Ahmed, M. Amjad, M. A. Qureshi, K. Imran, Z. M. Haider, and M. O. Khan, “A Critical Review of State-of-the-Art Optimal PMU Placement Techniques,” Energies, vol. 15, no. 6, p. 2125, Mar. 2022, doi: 10.3390/en15062125.

[32] A. H. Babaali and M. T. Ameli, “Weighted ensemble learning for real-time short-term voltage stability assessment with phasor measurements data,” IET Generation, Transmission & Distribution, Mar. 2023, doi: 10.1049/gtd2.12809.

[33] A. Babaali and M. T. Ameli, “Short-term voltage stability prediction based on a Bidirectional Gated Recurrent Unit neural network using phasor measurement data in power systems,” Computational Intelligence in Electrical Engineering, vol. 15, no. 1, pp. 1–16, 2024, doi: 10.22108/isee.2023.135273.1585.

[34] S. Shah, S. Koley, and F. Malandra, “Experimental End-To-End Delay Analysis of LTE cat-M With High-Rate Synchrophasor Communications,” July 11, 2022, arXiv: arXiv:2207.04847. doi: 10.48550/arXiv.2207.04847.

Amir Hossein Babaali received his B.Sc. degree from the University of Kashan, Isfahan, Iran, in 2012 and his M.Sc. degree from the Department of Electrical Engineering, Shahid Beheshti University, Tehran, Iran, in 2014. He is a Ph.D. student in the Department of Electrical Engineering at Shahid Beheshti University. His research interests include power system simulation, operation, planning, and machine learning applications in power systems.

Mohammad Taghi Ameli received his B.Sc. degree in electrical engineering from the Technical College of Osnabrueck, Osnabrueck, Germany, in 1988, and his M.Sc. and Ph.D. degrees from Technical University of Berlin, Berlin, Germany, in 1992 and 1997, respectively. He is a Professor of the Department of Electrical Engineering and Head of the Electrical Networks Institute at Shahid Beheshti University. He was the Iran Research and Technology Institute for Electric Machines General Director for three years. His research interests include power system simulation, operation, planning, and control of power systems, renewable energy in power systems, and smart grids.

IECO

This page intentionally left blank.

IECO International Journal Of Industrial Electronics Control and Optimization
Print ISSN: 3517-2645
Online ISSN: 3568-2645
Homepage: https://ieco.usb.ac.ir/

An Adaptive Robust Square Root Unscented Kalman Filter for State of Charge Estimation for Lithium-ion Batteries

Ramazan Havangi[1]| Fatemeh Karimi[2]

Faculty of Electrical Engineering and Computer, University of Birjand, Birjand, Iran.[1,2]
Corresponding author's email: Havangi@Birjand.ac.ir

Article Info

Article type:
Research Article

Article history:
Received: 25-March-2025
Received in revised form:
26-May-2025
Accepted: 09-June-2025
Published online: 22-June-2026

Keywords:
State of charge,
adaptive robust square root unscented Kalman filter,
lithium-ion batteries.

ABSTRACT

Accurate estimation of the State of Charge (SOC) is essential for effective Battery Management Systems (BMS), as it directly affects the performance, safety, and lifespan of battery-powered devices. However, precise SOC estimation remains challenging due to the nonlinear dynamics of batteries and unpredictable process and measurement noise. This paper proposes a novel hybrid approach that combines an Adaptive Robust Square Root Unscented Kalman Filter (ARSRUKF) with Recursive Least Squares (RLS) to improve the accuracy and robustness of SOC estimation. The ARSRUKF enhances numerical stability by maintaining the semi-positive definiteness of covariance matrices and enables direct computation of their square roots, which improves both symmetry and computational efficiency. Unlike conventional filters such as the Extended Kalman Filter (EKF) and Unscented Kalman Filter (UKF), the ARSRUKF does not require prior knowledge of noise statistics, making it suitable for real-world applications with unknown or non-Gaussian noise. To further enhance filter performance, an Adaptive Neuro-Fuzzy Inference System (ANFIS) is integrated for real-time adjustment of noise covariances, allowing dynamic tuning of filter parameters based on system behavior. Experimental results under diverse operating conditions, including temperature fluctuations and varying noise levels, demonstrate that the proposed method consistently outperforms EKF and UKF. The presented framework offers a robust and accurate solution for SOC estimation, with broad applicability in electric vehicles, renewable energy storage systems, and portable electronic devices.

I. Introduction

As the global concerns regarding energy consumption and environmental sustainability intensify, the need for cleaner, more efficient technologies has never been greater. The electric vehicle (EV) industry has emerged as a key player in addressing these concerns, experiencing substantial growth in recent years. The transition from traditional internal combustion engine vehicles to electric-powered alternatives is seen as a significant step toward reducing carbon emissions and minimizing dependence on fossil fuels. Central to the success and performance of electric vehicles is the battery technology employed, with lithium-ion batteries being the preferred choice in most applications. These batteries offer a combination of high energy density, long cycle life, and a relatively low self-discharge rate, making them ideal for storing and supplying energy in EVs as well as renewable energy applications, such as solar and wind power storage [1].

The integration of lithium-ion batteries into electric vehicles necessitates the development of advanced Battery Management Systems (BMS) to monitor and optimize battery performance. The BMS plays a critical role in ensuring the safe and efficient operation of the battery by continuously monitoring key parameters such as voltage, current, and temperature. In addition, it estimates the SOC, which represents the remaining energy capacity of the battery [2]. Accurate SOC estimation is essential for maintaining battery operation within safe limits and for preventing conditions such as overcharging or deep discharging-both of which can significantly degrade battery lifespan. Moreover, reliable SOC estimation contributes to more effective energy management, thereby enhancing the driving range and overall efficiency of electric vehicles [3]. In addition to estimation algorithms, several recent studies have explored robust control strategies at the power electronics level. For example, [2] presents an improved

Publisher: University of Sistan and Baluchestan

sliding mode controller for EV battery chargers designed to enhance voltage stability under input voltage fluctuations. While this approach effectively improves robustness at the power interface level, it does not address the challenges of internal battery state estimation. In contrast, the present study introduces an integrated filtering framework—ARSRUKF combined with RLS and ANFIS—that enhances the accuracy and robustness of SOC estimation under uncertain, nonlinear, and dynamic conditions. This methodology complements control-layer solutions by specifically targeting the estimation layer within battery management systems.

Over the years, various methods have been proposed for SOC estimation, each with its own strengths and limitations. These methods can generally be classified into three main categories: open-loop methods, model-free methods, and model-based methods [4-6]. Open-loop methods, such as ampere-hour (Ah) counting and open-circuit voltage (OCV) measurement, are commonly employed due to their simplicity and ease of implementation. The Ah counting method estimates SOC by integrating charge and discharge currents over time. However, this method is highly prone to cumulative errors, which can substantially impair estimation accuracy-particularly when the initial SOC is imprecisely known or when current measurement errors occur [8–9]. In contrast, the OCV method estimates SOC based on the well-established correlation between SOC and the open-circuit voltage of the battery. Although the OCV method can yield accurate results under controlled conditions, it requires the battery to remain at rest for a sufficient period to allow voltage stabilization, thereby rendering it unsuitable for real-time applications [10].

Model-free methods, which include techniques such as neural networks and fuzzy logic, represent an alternative approach to SOC estimation. These methods do not rely on predefined battery models but instead use machine learning algorithms to map battery parameters, such as voltage and current, directly to SOC values [11-12]. While model-free methods can achieve high accuracy, they require large amounts of training data and exhibit high computational complexity, making real-time implementation more challenging.

In contrast, model-based methods leverage mathematical models to describe the dynamics of the battery and use filtering techniques to estimate SOC. Among these, the EKF has become one of the most widely used techniques for SOC estimation. The EKF approximates nonlinear battery dynamics using a first-order Taylor series expansion and the Jacobian matrix [13]. However, the need for linearization introduces errors that can reduce the accuracy of the SOC estimation. To address this, the UKF was introduced as an alternative. The UKF provides a higher-order approximation of the nonlinear system dynamics and does not require linearization, offering improved estimation accuracy over the EKF [14].

While model-based approaches, such as EKF and UKF, provide valuable benefits, they face significant challenges, particularly when it comes to the estimation of noise characteristics, such as process and measurement noise covariances. In practical applications, noise characteristics are often not well-defined and may vary dynamically due to changing environmental conditions-such as temperature fluctuations-or the gradual degradation of battery components over time. If inaccurate assumptions are made regarding noise statistics, the performance of the filtering algorithm may deteriorate, resulting in reduced estimation accuracy and potential filter divergence [17]. To overcome this challenge, the Adaptive Unscented Kalman Filter (AUKF) has been developed. The AUKF addresses time-varying noise by continuously updating the process and measurement noise covariance matrices, thereby improving estimation accuracy and enhancing the robustness and stability of the filter in dynamic conditions [18–19]. However, the AUKF introduces additional computational complexity, particularly due to the need to repeatedly calculate the square root of the error covariance matrix at each time step, which can be inefficient for real-time applications [20-21].

To overcome these challenges and provide a more efficient solution for SOC estimation, this paper proposes a novel approach that combines the Adaptive Robust Square Root Unscented Kalman Filter (ARSRUKF) with RLS to handle scenarios where prior knowledge of noise statistics is unavailable. The ARSRUKF directly propagates and updates the square root of the state covariance matrix in its Cholesky factored form, significantly reducing the computational complexity associated with traditional filtering methods while improving numerical stability and estimation performance. Additionally, to optimize the performance of the filter further, ANFIS is integrated into the system to fine-tune the parameters of the square root UKF (SRUKF). This integration allows the ARSRUKF to adapt to changing operating conditions and handle non-Gaussian noise more effectively, making it particularly suitable for real-world applications where the system uncertainties are minimal and dynamic.

The remainder of this paper is organized as follows: Section 2 presents the equivalent circuit model (ECM) of the battery, which is used for simulating battery behavior. Section 3 introduces the RLS method for battery parameter estimation, highlighting its relevance to accurate SOC estimation. Section 4 discusses the implementation of the ARSRUKF for SOC estimation, detailing the filtering and adaptation processes involved. Section 5 presents the simulation and experimental results, comparing the performance of the proposed method with existing approaches. Finally, Section 6 concludes the paper, summarizing the key findings and suggesting directions for future research in SOC estimation and battery management systems.

II. Battery modeling

Lithium-ion battery modeling approaches can be broadly categorized into two main types: electrochemical models and equivalent circuit models (ECMs). Electrochemical models utilize nonlinear differential equations to characterize the intricate chemical and physical processes occurring within the battery. While these models offer a comprehensive and precise representation of battery behavior, their high computational complexity renders them unsuitable for real-time state-of-charge (SOC) estimation. Conversely, ECMs provide a more practical alternative by approximating battery dynamics through electrical components such as resistors, capacitors, and voltage sources[22-25]. These models require fewer parameters and do not explicitly account for complex internal electrochemical reactions, making them well-suited for implementation in BMS. Among various ECM structures, the second-order RC model has been widely recognized as a favorable trade-off between modeling accuracy and computational efficiency. Due to its capability to capture the battery's dynamic behavior while maintaining a manageable computational load, this model is chosen for simulating the electrical characteristics of the battery, as depicted in Fig. 1.

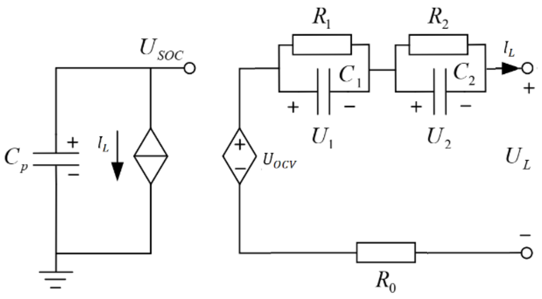

Fig 1. Second-order RC equivalent circuit model

The equivalent circuit model comprises a controlled voltage source (U_{SOC}) that models the nonlinear dependence of the battery's OCV on its SOC. A series resistance (R_0) is integrated to quantify the instantaneous ohmic losses during charge and discharge operations. To capture the transient dynamics of the battery, two distinct RC parallel networks (R_1, C_1, R_2 and C_2) are incorporated: the first network characterizes short-term polarization effects, while the second accounts for long-term diffusion processes. The voltage potentials across these RC elements, denoted as U_1, U_2 , describe the dynamic voltage deviations during operational cycles. Based on Kirchhoff's laws and transient circuit analysis, the system equations governing this model are expressed as follows [25]:

$$\dot{SOC}=-\frac{1}{Q_n}I_L$$

$$\dot{U}_1=-\frac{1}{R_1C_1}U_1+\frac{1}{C_1} \tag{1}$$

$$\dot{U}_2=-\frac{1}{R_2C_2}U_2+\frac{1}{C_2}$$

$$U_t=U_{OCV}-U_1-U_2-R_0I_L \tag{2}$$

where Q_n is the nominal capacity of the battery in ampere-hours (Ah), U_{OCV} Open-Circuit Voltage $I_L$is load current, and U_t represents is the terminal voltage of the battery. Based on Equation (1), the state-space representation of the system in discrete time is given by [23]:

$$SOC(K+1)=SOC(K)-\frac{T}{Q_n}I_L(K)$$

$$U_1(K+1)=\exp\left(-{}^{T}/_{\tau_1}\right)\times U_1(K)+\left[1-\exp\left(-{}^{T}/_{\tau_1}\right)\right]\times R_1I_L(K) \tag{3}$$

$$U_2(K+1)=\exp\left(-{}^{T}/_{\tau_2}\right)\times U_2(K)+\left[1-\exp\left(-{}^{T}/_{\tau_2}\right)\right]\times R_2I_L(K)$$

$$U_t(k)=U_{OCV}(k)-U_1(k)-U_2(k)-R_0(k)I_L(K) \tag{4}$$

where T denotes the sampling period, which defines the discrete-time step used in the state-space representation of the battery model, $\tau_1 = R_1C_1$ and $\tau_2=R_2C_2$are the time constants of the first and second RC branches, respectively.

III. Parameter identification

Parameter identification plays a crucial role in the process of battery modeling, ensuring that the battery model can accurately replicate the real-world behavior of the battery under various conditions. In this study, the least squares method is employed for parameter estimation, which is an efficient and widely used approach to minimize the difference between model outputs and observed data. The objective of this section is to estimate the parameters of the equivalent circuit model (ECM) that describe the behavior of the lithium-ion battery. In the equivalent circuit model, the battery voltage $U_t(s)$ in the Laplace domain is described as[22]:

$$U_t(s)=U_{OCV}(s)-\left(R_0+\frac{R_1}{1+R_1C_1s}+\frac{R_2}{1+R_2C_2s}\right)I_L(s) \tag{5}$$

where s is the frequency operator,and $I_L(s)$represents the load current in the Laplace domain. Next, we define the transfer function $G(s)$ of the system as [25]:

$$G(s)=\frac{U_{OCV}(s)-U_t(s)}{I_L(s)}=R_0+\frac{R_1}{1+R_1C_1s}+\frac{R_2}{1+R_2C_2s} \tag{6}$$

Defining the model parameters a and b as

$a=\tau_1\tau_2$, $b=\tau_1+\tau_2$,

G(s) can be written as

$$G(s)=\frac{R_0s^2+\frac{1}{a}(bR_0+R_1\tau_2+R_1\tau_2)+\frac{R_0+R_1+R_2}{a}}{s^2+\frac{b}{a}s+\frac{1}{a}} \tag{7}$$

To discretize the system, we apply a bilinear transformation with the substitution

$s=\frac{2}{T}\frac{1-z^{-1}}{1+z^{-1}}$ where T is the sampling period and z^{-1} represents the backward shift operator. This leads to the following discrete transfer function:

$$G(z^{-1})=\frac{k_3+k_4z^{-1}+k_5z^{-2}}{1-k_1z^{-1}-k_2z^{-2}} \quad (8)$$

where k_1, k_2, k_3, k_4 and k_5 are as follows:

$$k_1=\frac{8a-T^2}{2bT+4a+T^2}$$

$$k_2=\frac{2bT-4a-T^2}{2bTT+4a+T^2}$$

$$k_3=\frac{T^2(R_{0+}R_{1+}R_2)+2TR_0b+4R_0a+2T(R_1\tau_2+R_2\tau_1)}{2bT+4a+T^2}$$

$$k_4=\frac{2T^2(R_{0+}R_{1+}R_2)-8R_0a}{2bT+4a+T^2}$$

$$k_5=\frac{T^2(R_{0+}R_{1+}R_2)+4R_0a-2R_0T\tau_2-2T(R_1\tau_2+R_2\tau_{1+}R_0\tau_1)}{2bT+4a+T^2}$$

As a result, Equation (8) can be rewritten in the following difference equation form:

$$\begin{aligned}U_{OCV}(k)-U_t(k)&=-k_1(U_{OCV}(k-1)-U_t(k-1))\\&\quad-k_2(U_{OCV}(k-2)-U_t(k-2))\\&\quad+k_3I(k)+k_4I(k-1)+k_5I(k-2)\end{aligned} \quad (9)$$

Defining $U_d(k)$ as:

$$U_d(k)=U_{OCV}(k)-U_t(k) \quad (10)$$

$$U_d(k)=U_{OCV}(k)-U_t(k)$$

Equation (6) can be written as

$$\begin{aligned}U_d(k)&=k_1U_d(k-1)+k_2U_d(k-2)\\&\quad+k_3I_L(k)+k_4I_L(k\\&\quad-1)+k_5I_L(k-2)\end{aligned} \quad (11)$$

η(k)is set as the sampling error of the sensor at time k. Then, $U_d(k)$ can be written as:

$$U_d(k)=\emptyset(k)\theta(k)+\eta(k) \quad (12)$$

where the regressor vector $\emptyset(k)$ and parameter vector $\theta(k)$ are as follows:

$$\begin{aligned}&\emptyset(k)\\&=[U_d(k-1)\quad U_d(k-2)\quad I_L(k)\quad I_L(k-1)\quad I_L(k-2)]\end{aligned}$$

$$\theta(k)=[k_1\quad k_2\quad k_3\quad k_4\quad k_5]$$

To estimate the parameters, the RLS method is applied. The recursive estimation equation is given by:

$$\begin{aligned}\hat{\theta}(k)=\hat{\theta}(k-1)+K(k)(y(k)\\-\emptyset(k)\hat{\theta}(k-1))\end{aligned} \quad (13)$$

$$\hat{\theta}(k)=\hat{\theta}(k-1)+K(k)(y(k)-\emptyset(k)\hat{\theta}(k-1))$$

where $\hat{\theta}(k)$ is the estimated parameter vector, and $y(k)$ is the observed output. The gain vector $K(k)$ is calculated as:

$$\begin{aligned}K(k)=P(k-1)\emptyset(k)^T(\lambda\\+\emptyset(k)P(k-1)\emptyset(k)^T)^{-1}\end{aligned} \quad (14)$$

where $P(k-1)$ is the error covariance matrix and λ is a forgetting factor that determines how quickly past information is discarded. The updated error covariance matrix is given by:

$$P(k)=\frac{1}{\lambda}(P(k-1)-K(k)\emptyset(k)P(k-1)) \quad (15)$$

By using the recursive least squares method, the model parameters are iteratively adjusted to minimize the error between the predicted and observed voltage, thus improving the accuracy of the battery model over time. This approach provides an efficient way to estimate the parameters in real-time, making it suitable for use in Battery Management Systems.

IV. SOC estimation

To estimation SOC using ARSRUKF, the discrete state-space model of the battery is considered as follows:

$$\begin{aligned}&x_k=f(x_{k-1},U_k)+\\&w_k \qquad , \quad P(\omega_K)\sim N(0,Q_k)\\&z_k=h(x_k,U_k)+v_k \qquad , \quad P(v_K)\sim N(0,R_k)\end{aligned}$$

$$\begin{aligned}&f(x_{k-1},U_k)=\begin{bmatrix}e^{\frac{-T}{R_{1,k}C_{1,k}}} & 0 & 0\\ 0 & e^{\frac{-T}{R_{2,k}C_{2,k}}} & 0\\ 0 & 0 & 1\end{bmatrix}x_{k-1}+\\&\begin{bmatrix}R_{1,k}\cdot\left(1-e^{\frac{-T}{R_{1,k}C_{1,k}}}\right)\\ R_{2,k}\cdot\left(1-e^{\frac{-T}{R_{2,k}C_{2,k}}}\right)\\ \frac{-T}{C.3600}\end{bmatrix}I_{L,k}\end{aligned} \quad (16)$$

$$h(x_k,U_k)=U_{OC,k}-U_{1,k}-U_{2,k}-R_0I_{L,k}$$

A. H∞ extended filter

The H∞ filtering problem can be formulated based on game theory principles. In this approach, the performance measure is defined as follows [26]:

$$J=\frac{\sum_{k=0}^{k}\|x_k-\hat{x}_k\|_{S_k}^2}{\|x_0-\hat{x}_0\|_{P_0^{-1}}^2+\sum_{k=0}^{k}(\|w_k\|_{Q_k^{-1}}^2+\|v_k\|_{R_k^{-1}}^2)}<\gamma$$

where P_0^{-1} and S_k are weighting matrices, and $\hat{x}_k$ is determined such that $J<\gamma$. By selecting appropriate S_k, P_0, Q_k and R_k, prior knowledge about the influence of noise processes on the cost function can be incorporated into the estimation process. The H∞ extended filter is formulated as follows [26-27]:

$$\begin{aligned}&\hat{x}_k^-=f(x_{k-1},U_k)\\&P_k^-=F_kP_{k-1}F_k^T+Q_k\ ,\ F_k=\frac{\partial f}{\partial x}\end{aligned} \quad (17)$$

$$\begin{aligned}&K_k=P_k^-H_k^T(H_kP_k^-H_k^T+R_k)^{-1}\\&\hat{x}_k=\hat{x}_k^-+K_k(z_k-h(\hat{x}_k^-))\\&P_k=P_k^--P_k^-\begin{bmatrix}H_k^T & I\end{bmatrix}R_{e,k}^{-1}\begin{bmatrix}H_k\\ I\end{bmatrix}P_k^-\\&H_k=\frac{\partial h}{\partial x}\end{aligned} \quad (18)$$

where $R_{e,k}$ is as:

$$R_{e,k} = \begin{bmatrix} R_k & 0 \\ 0 & -\gamma I \end{bmatrix} + \begin{bmatrix} H_k \\ I \end{bmatrix} P_k^- \begin{bmatrix} H_k^T & I \end{bmatrix}$$

B. SOC estimation using ARSRUKF

The SOC estimation using ARSRUKF is initialized by the matrix square root of the state covariance via a cholesky factorization as follows:

$$\begin{aligned} \hat{x}_0 &= E[x_0] \\ S_0 &= chol\{E[(x_0 - \bar{x}_0)(x_0 - \bar{x}_0)^T]\} \end{aligned} \tag{19}$$

A set of sigma points are calculated as:

$$\begin{aligned} \chi_{k-1}^{[0]} &= \hat{x}_{k-1} \\ \chi_{k-1}^{[i]} &= \hat{x}_{k-1} + \sqrt{n+\lambda}(S_{k-1})_{\mathrm{i}} \qquad \text{i=1...n} \\ \chi_{k-1}^{[i]} &= \hat{x}_{k-1} - \sqrt{n+\lambda}(S_{k-1})_{\mathrm{i}} \qquad \text{i=n+1...2n} \end{aligned} \tag{20}$$

where $\lambda = n(\alpha^2 - 1)$ and the constant α is small positive value. These sigma points are then propagated through the nonlinear process model, given by:

$$\chi_k^{[i]} = f(\chi_{k-1}^{[i]}, U_k) \tag{21}$$

Subsequently, the transformed sigma points are used to estimate the state mean and square root of the covariance matrix:

$$\begin{aligned} \hat{x}_k^- &= \sum_{i=1}^{2n} \omega_i^{(m)} \chi_{k|k-1}^{[i]} \\ S_k^- &= qr(\sqrt{\omega_1^{(c)}}(\chi_k^{[1:2n]} - \hat{x}_k^-), \sqrt{Q_k}) \\ S_k^- &= cholupdate(S_k^-, (\chi_k^{[0]} - \hat{x}_k^-), \omega_1^{(c)}) \end{aligned} \tag{22}$$

where

$$\omega_0^{(c)} = \frac{\lambda}{n+\lambda} + (1 - \alpha^2 + \beta) \qquad \omega_0^{(m)} = \frac{\lambda}{n+\lambda}$$

$$\omega_i^{(m)} = \omega_i^{(c)} = \frac{\lambda}{2(n+\lambda)}$$

The square-root covariance matrix is updated using numerically stable orthogonal transformations. During the time update step, QR decomposition is employed to propagate the Cholesky factor of the covariance matrix, while rank-one updates are applied during the measurement update. This approach significantly enhances numerical stability by maintaining the positive definiteness of the covariance matrix and mitigating the accumulation of round-off errors that are often encountered in UKF. The transformed sigma points are then used to predict the measurements based on the measurement model, as follows:

$$\Im^{[i]} = h(\chi_k^{[i]}, U_k)$$

The expected measurement $\hat{z}_k^-$ is as:

$$\hat{z}_k^- = \sum_{i=0}^{2n} \omega_i^{(m)} \Im^{[i]}$$

The cross-correlation covariance P_k^{xz} and the measurement covariance P_k^{zz} can be approximated by:

$$\begin{aligned} P_k^{zz} \ @E[z_k - \hat{z}_k^-][z_k - \hat{z}_k^-]^T &= H_k P_k H_k^T \\ P_k^{xz} \ @E[x_k - \hat{x}_k][z_k - \hat{z}_k^-]^T &= P_k H_k^T \end{aligned} \tag{23}$$

On the other hand, using the predicted sigma points, P_k^{xz} and P_k^{zz} also determines as follows:

$$\begin{aligned} P_k^{xz} &= \sum_{i=0}^{2n} \omega_i^{(c)} (\chi_k^{[i]} - \hat{x}_k)(\Im^{[i]} - \hat{z}_k^-)^T \\ P_k^{zz} &= \sum_{i=0}^{2n} \omega_i^{(c)} (\Im^{[i]} - \hat{z}_k^-)(\Im^{[i]} - \hat{z}_k^-)^T + R_k \end{aligned} \tag{24}$$

Using extended H_∞ filter, the state mean and square root of covariance are updated using the actual measurement

$$\hat{x}_k = \hat{x}_k + P_k^{xz}[R + P_k^{xz}]^{-1}(z_k - \hat{z}_k) \tag{25}$$

$$S_k = chol(P_k)$$

$$\begin{aligned} P_k &= P_k^- - \\ &\begin{bmatrix} P_k^{xz} & P_k^- \end{bmatrix} \begin{bmatrix} R + P_k^{xz} & P_{k-1}^{xz\,T} \\ P_k^{xz} & -\gamma^2 I + P_k^- \end{bmatrix}^{-1} \begin{bmatrix} P_k^{xz} & P_k^- \end{bmatrix}^T \end{aligned} \tag{26}$$

To enhance the efficacy of the proposed methodology, the optimal selection of the weighting matrices $Q_k$and R_k is critical. This necessity arises from the asymptotic relationship between H_∞ and H_2 filtering frameworks: as the attenuation factor λ approaches infinity, the H_∞ filter converges to the extended H_2 filter (EKF) in behavior. Consequently, the weighting matrices $Q_k$and R_k in H_∞ filtering—and by extension, in the Robust Square-Root Unscented Kalman Filter (RSRUKF)—fulfill analogous roles to the process noise covariance matrix Q_k and measurement noise covariance matrix R_k in H_2-based filtering. Given this functional equivalence, adaptive estimation of $Q_k$and $R_k$represents a viable strategy to maintain filter robustness under dynamic operating conditions. A practical method for assessing the need for filter recalibration involves continuous observation of the residual signal, defined as the discrepancy between measured and predicted outputs. Deviations in residual statistics (e.g., magnitude or covariance) often indicate suboptimal tuning of $Q_k$and R_k necessitating real-time adjustments through adaptive algorithms. Such approaches ensure optimal noise suppression and state estimation accuracy, particularly in systems with time-varying noise characteristics or model uncertainties.

$$r_k = z_k - \hat{z}_k \tag{20}$$

Here, $\hat{z}_k$ denotes the *predicted measurement* at time step *k*, and z_k represents the *actual observed measurement*. When the filter operates under ideal conditions, the residual sequence r_k should exhibit properties of zero-mean white noise, indicating optimal noise suppression and unbiased estimation. To validate this behavior, the theoretical residual covariance P_k^{zz} (derived analytically in Equation 17) must align with the empirical residual covariance $\hat{C}_k$, computed from real-world data. The empirical covariance $\hat{C}_k$ can be estimated adaptively using a moving-average window of size *N*. This involves averaging the outer product of residuals over the most recent N_w time steps:

$$\hat{C}_k = \frac{1}{N} \sum_{i=k-N_w+1}^{k} (r_i^T r_i) \tag{21}$$

In this paper, ANFIS is employed to tune R_k and Q_k. The implemented ANFIS consists of a five-layer network, as illustrated in Fig. 2. The inputs to ANFIS are r_k and δr_k, where δr_k is defined as follows:

$$\delta r_k = r_k - r_{k-1}$$

The outputs are δR_k and δQ_k that employ to tune R_k and Q_k as follows:

$$Q_k = Q_k + \delta Q_k$$

$$R_k = R_k + \delta R_k$$

The ANFIS model comprises two inputs—innovation and its derivative—each represented by three Gaussian membership functions (Low, Medium, High), resulting in a total of nine fuzzy inference rules. The Gaussian membership functions corresponding to the input variables are shown in Fig. 3. A first-order Sugeno-type inference system is employed to perform the fuzzy reasoning. The ANFIS is trained online using a hybrid learning algorithm that combines least squares estimation for the consequent parameters with gradient descent for the optimization of membership function parameters. To maintain adaptability and numerical stability, training is conducted over a sliding window of recent data samples.

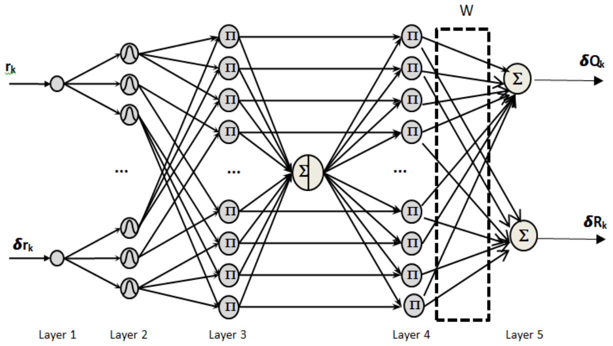

Fig.2. The ANFIS structure is used to tune R_k and Q_k

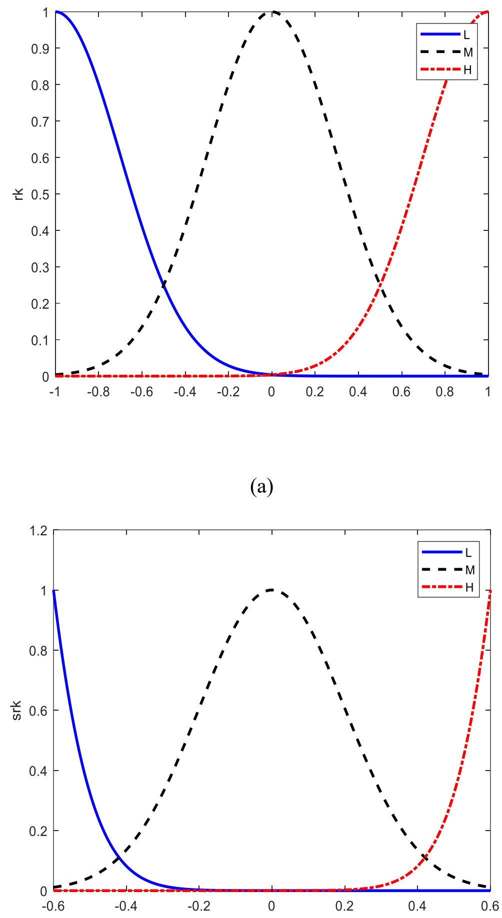

(a)

(b)

Fig.3. membership functions of ANFIS (a) r_k (b) δr_k

To describe the structure of ANFIS, assume that u_i^l and o_i^l represent the input and output of the i th node of the l th layer, respectively. The functioning of ANFIS is as follows:

Layer 1: Each node in this layer directly transmits its input values to the next layer

$$o_i^1 = u_i^1 \tag{27}$$

Layer2: In this layer, each node represents a membership function, and the output is computed as:

$$o_{ij}^2 = \mu_{ij}(u^2) = \exp\left\{-\frac{(u_{ij}^2 - m_{ij})^2}{(\delta_{ij})^2}\right\} \tag{28}$$

where m_{ij} and δ_{ij} are the mean and width of the Gaussian membership function, respectively.

Layer3: Each neuron in this layer represents a fuzzy AND operation, which combines the incoming signals from Layer 2 by multiplying the membership function values. The output of each node is given by:

$$o_l^3 = \prod_i u_i^3 \tag{29}$$

Layer4: The node in this layer performs the normalization of firing strengths from layer 3,

$$o_l^4 = \frac{u_l^4}{\sum_{l=1}^{9} u_l^4} \tag{30}$$

Layer5: This layer acts as a defuzzfier:

$$Output = \sum_{l=1}^{25} u_l^5 w_l \tag{31}$$

The weighting of ANFIS is tuned using the steep descent algorithm such that the objective function E_k is minimized:

$$E_k = \frac{1}{2}(P_k^{zz} - \hat{C}_k)^2$$

As a result, the weighting of ANFIS is updated as:

$$W_{k+1} = W_k - \eta \frac{\partial E_k}{\partial W_k}$$

Here η is learning rate of ANFIS. To maintain real-time model consistency, the RLS algorithm updates key battery parameters-such as internal resistance and RC pair values-at each time step using the most recent voltage and current measurements. These updated parameters are immediately integrated into the state-space model prior to ARSRUKF. This tightly coupled integration ensures synchronized model adaptation under dynamic operating conditions, including non-stationary behavior and rapid load variations. By continuously aligning the equivalent circuit model with real-time measurements, the RLS-enhanced framework ensures that both the prediction and correction phases of the ARSRUKF are based on the most accurate and up-to-date system representation. This real-time adaptability significantly improves estimation accuracy and filter robustness without relying on static model assumptions, enabling effective tracking of battery behavior in the presence of operating uncertainties.

V. Result

A test benchmark is performed to evaluate the proposed algorithms. The specifications of the test battery are summarized in Table I.

Table I Cell specification

Model	INR 18650-20R
Nominal Voltage(V)	3.6 V
Nominal Capacity (mAH)	2000mAh
Upper Cut-Off Voltage	4.2
Lower Cut-Off Voltage	2

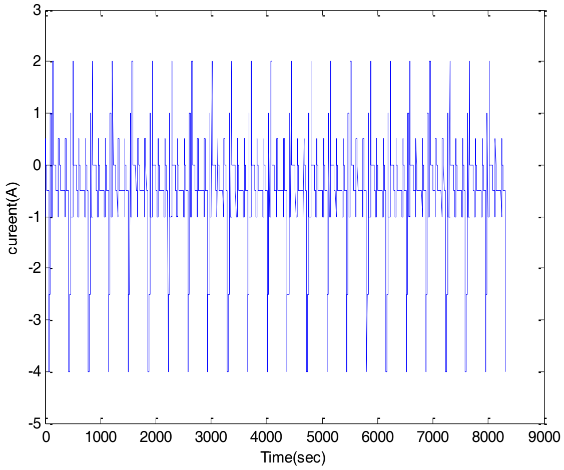

Fig. 4. Measured current

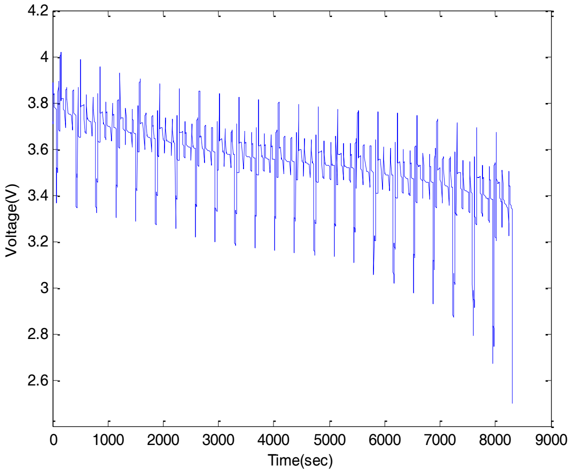

Fig.5. Measured voltage

A. *Parameter identification*

Accurate estimation of battery model parameters is essential for ensuring precise SOC estimation and improving the performance of BMS. To achieve this, a Dynamic Stress Test (DST) [28] is conducted, which is widely used for characterizing battery dynamics under realistic load conditions. The DST protocol involves applying a sequence of current pulses with varying amplitudes and durations while incorporating the effects of regenerative charging. This dynamic loading pattern is designed to capture the nonlinear behavior of the battery, including the impact of

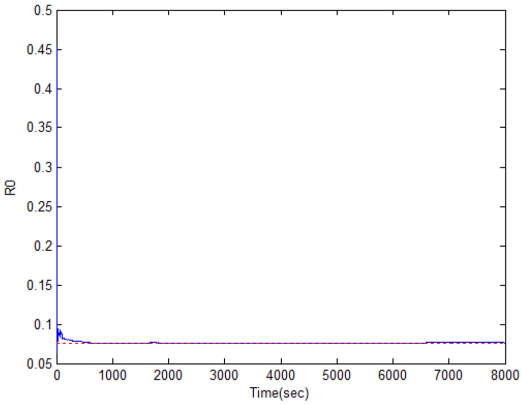

(a)

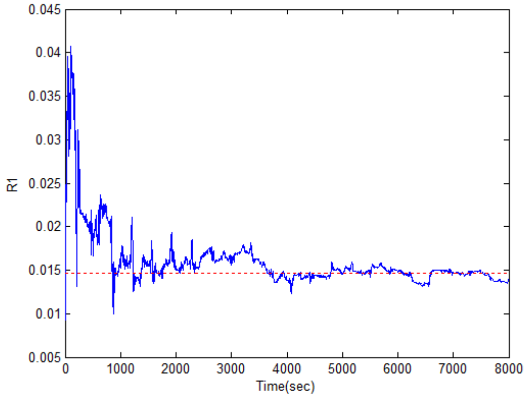

(b)

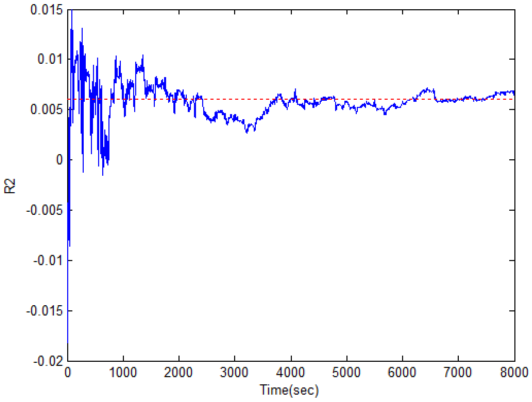

(c)

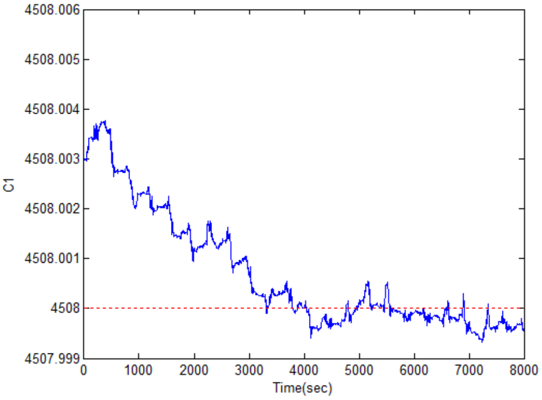

(d)

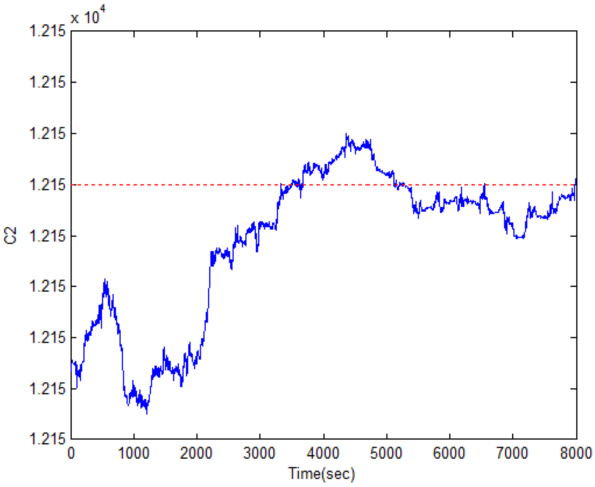

(e)

Fig.6. Battery parameter identification results

hysteresis, internal resistance variation, and transient response characteristics. The corresponding current profile and terminal voltage response of the battery under DST conditions are depicted in Figs. 4 and 5. By analyzing the battery's voltage response to the applied current steps, key parameters such as internal resistance, open-circuit voltage, and equivalent circuit elements (e.g., resistance-capacitance pairs) can be extracted. Although the DST does not fully replicate real-world operating conditions—where temperature fluctuations, aging effects, and complex load variations exist—it provides a well-structured and repeatable framework for parameter estimation. The parameter identification results, presented in Fig.6, indicate that the estimated parameters converge effectively to their true values. This convergence confirms the accuracy and reliability of the identification process, demonstrating that the selected modeling approach effectively captures the battery's electrical characteristics. The results also highlight the robustness of the estimation algorithm in handling variations in operating conditions, which is crucial for enhancing battery state estimation and predictive modeling in practical applications.Before proceeding with SOC estimation, it is crucial to validate the accuracy of the battery model. To achieve this, a model verification test is performed using the Federal Urban Driving Schedule (FUDS) [29], which serves as a standard benchmark for evaluating model performance. Fig. 7(a) presents the battery terminal voltage along with its estimation error during the FUDS test. As illustrated in Fig. 7(b), the discrepancy between the estimated and measured voltage remains minimal, confirming that the model provides a reliable representation of the battery's behavior.

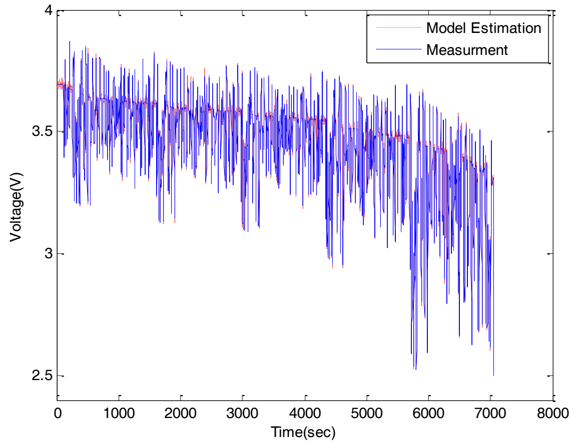

(a)

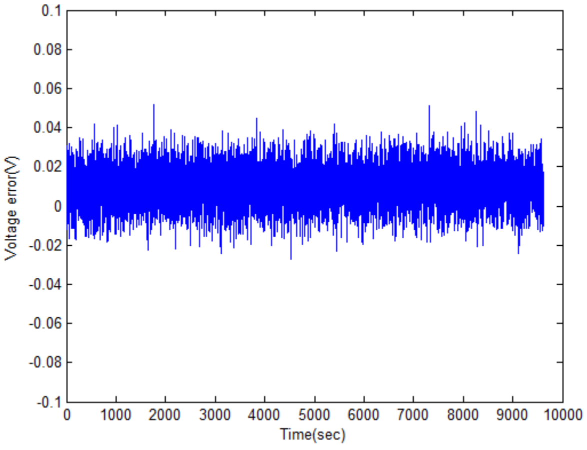

(b)

Fig.7. the results under FUDS: (a) Voltage comparison. (b) Voltage error.

B. SOC estimation

In this subsection, the accuracy and robustness of the proposed method are evaluated using standardized dynamic current profiles, including FUDS [29] and the US06 Highway Driving Schedule [30]. These profiles are more demanding than DST due to their highly variable charge and discharge rates, thereby offering a more rigorous assessment of estimation performance. The proposed method estimates SOC during both charging and discharging phases by incorporating bidirectional current flow into the state-space model. Specifically, the SOC update equation accounts for current polarity, with positive values indicating charging and negative values indicating discharging. To ensure accurate bidirectional behavior, model parameters were identified using RLS based on complete charge–discharge cycles. Experimental validation under the FUDS and US06 profiles—which include regenerative braking events—demonstrated robust SOC tracking performance. These results confirm the applicability of the proposed method in real-world battery management systems that require reliable SOC estimation under dynamic and bidirectional operating conditions. The corresponding current profiles used for testing are shown in Fig. 8.

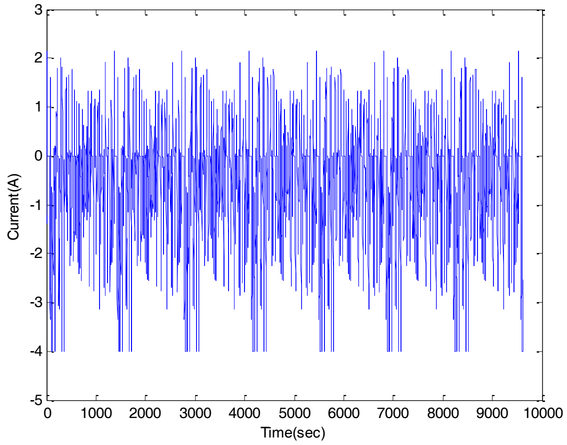

(a)

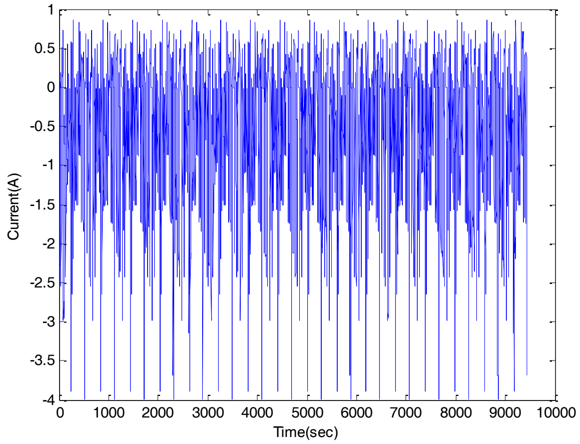

(b)

Fig.8. Battery test loading profiles: (a) Federal Urban Driving Schedule (FUDS) (c) US06 Highway Driving Schedule

First, the performance of the proposed method is evaluated and compared with existing approaches under the assumption that the statistical characteristics of noise are known a priori. To highlight proposed method advantages, the results are benchmarked against those obtained using UKF and EKF. Fig. 9 presents the SOC estimation results for the US06 and FUDS test profiles. Compared to the EKF and UKF, the SOC estimated by the proposed method exhibits a closer alignment with the actual SOC curves. Furthermore, the proposed method not only converges more accurately to the true SOC values but also maintains consistency in magnitude, demonstrating its superior accuracy and reliability in SOC estimation.

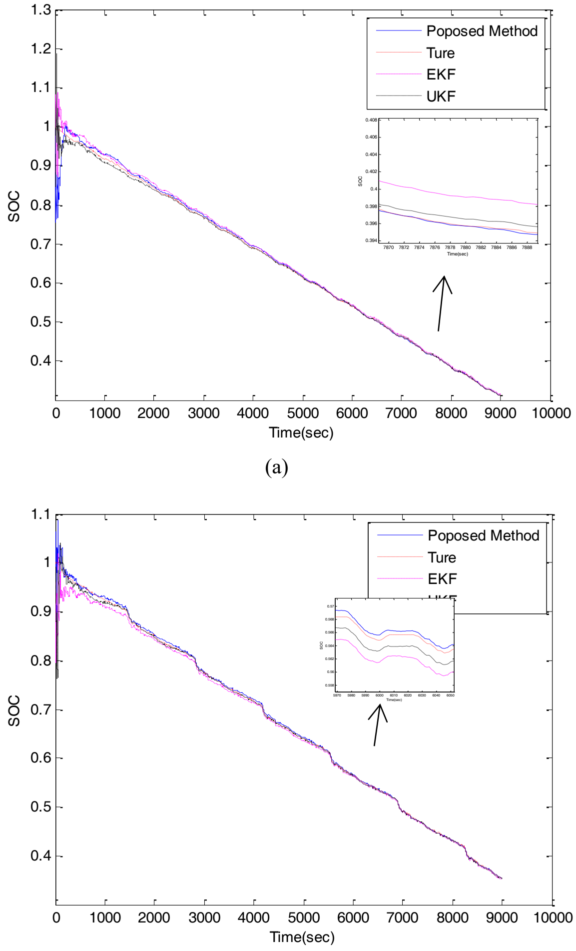

(a)

(b)

Fig.9. SOC estimation at 0 C (a) US06 (b) FUDS

Table II Sensitivity Analysis of ANFIS Parameters on SOC Estimation Performance

Parameter	Range	Observed Behavior	Optimal Value
Number of Membership Functions	2 – 4	<3 Underfitting; >3 negligible improvement, increased complexity	3
Learning Rate η	0.001 – 0.03	η > 0.02: minor oscillations η < 0.005: slow adaptation	0.01
Forgetting Factor λ	0.90 – 0.999	λ < 0.95 more adaptive, sensitive to noise λ > 0.995: sluggish adaptation	0.98
λ =0.94	-	Very fast adaptation, but noticeable increase in residual noise and RMSE spikes	-

The performance of SOC estimation using the proposed method is indeed affected by the choice of ANFIS parameters; however, the framework has been deliberately designed to minimize sensitivity and maintain robustness even in the presence of slight parameter mis-tuning. To assess this robustness, we performed a sensitivity analysis focusing on three key ANFIS parameters: the number of membership functions per input, the learning rate η, and the forgetting factor λ. The findings, summarized in the newly added Table II, demonstrate that using fewer than three membership functions leads to underfitting, while increasing the number beyond three results in negligible accuracy gains at the cost of increased computational complexity. Furthermore, the SOC estimation remains stable for learning rates within the range $\eta \in [0.005,0.02]$; higher values can introduce minor oscillations in the estimated covariance matrices. The forgetting factor also exhibits a wide robustness range, with stable behavior observed for $\lambda \in [0.95,0.995$. Although smaller λ values improve adaptability, they may also increase sensitivity to transient disturbances. Overall, the proposed method maintains reliable SOC estimation performance across a practical range of ANFIS parameter settings, underscoring the robustness of the proposed adaptive mechanism.

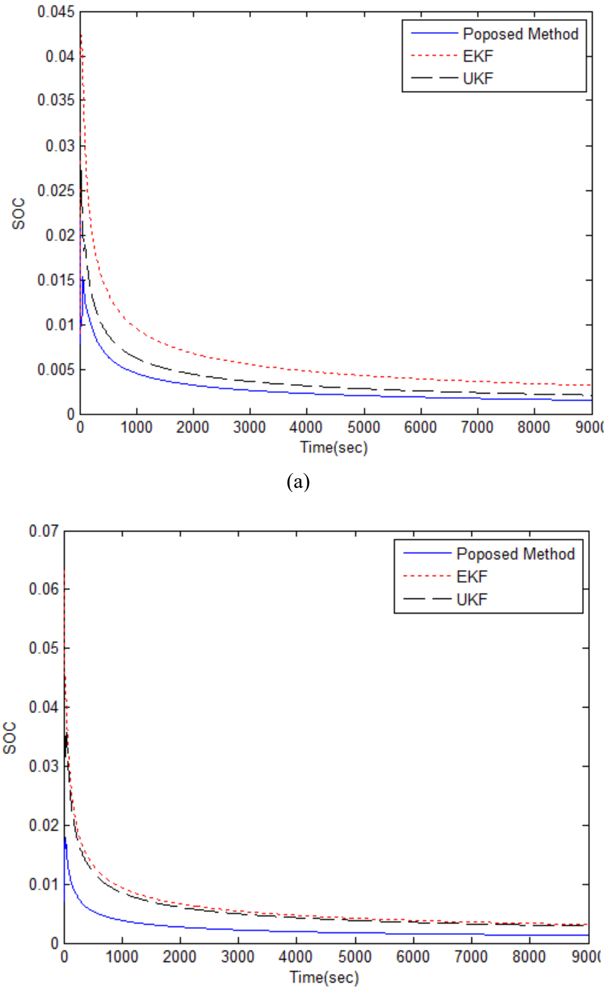

(a)

(b)

Fig.10. RMSE of SOC (a) US06 (b) FUDS

To further evaluate the estimation accuracy, the root mean square error (RMSE) is utilized as a performance metric. The RMSE is calculated over 50 Monte Carlo simulations for each estimation method. As shown in Fig. 10, the proposed method outperforms both the EKF and UKF in the FUDS and US06 test scenarios. This improvement can be attributed to the proposed method's enhanced capability in accurately estimating both the mean and covariance, leading to more precise SOC predictions compared to the UKF and EKF.

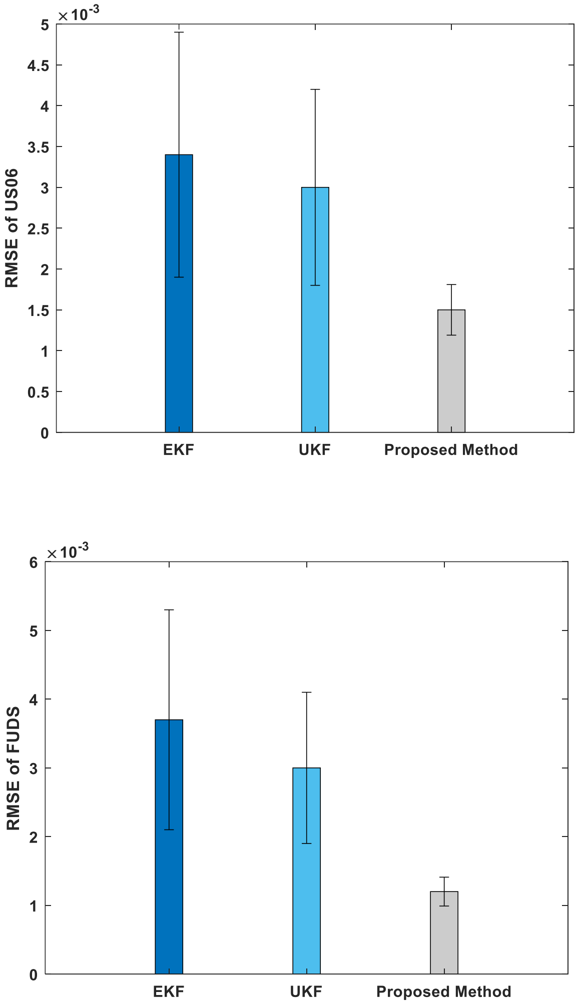

Fig.11. RMSE under known noise statistics

Fig.11 and Table III reports the mean RMSE, standard deviation, 95% confidence interval(CI) for pairwise comparisons. As shown, the proposed method achieves the lowest estimation error with significantly reduced variance. In the proposed method, several strategies have been employed to optimize performance on devices with limited computational resources. The use of a square-root formulation helps avoid matrix inversion, improving numerical stability and reducing computational complexity. Additionally, a compact ANFIS structure, consisting of only two inputs and nine fuzzy rules, minimizes the system's resource demands. The RLS algorithm is optimized with bounded updates to ensure efficient parameter estimation while keeping computational overhead low. To evaluate the computational efficiency of the proposed method, a detailed comparison with EKF and UKF implementations was conducted in Table IV. The findings under identical simulation settings MATLAB R2023a, Intel Core i7 @ 3.0 GHz, 16 GB RAM, single-threaded execution. As can be seen, the proposed method requires slightly higher runtime compared to EKF and UKF, but offers significantly improved accuracy and adaptive noise handling. This confirms that the added complexity due to ANFIS is marginal and feasible for real-time embedded implementation.

Table III RMSE under known noise statistics

Method	**FUDS**		**US06**	
	RMSE	**95% CI**	**RMSE**	**95% CI**
EKF	0.0037	0.0021–0.0053	0.0034	0.0019–0.0049
UKF	0.003	0.0019–0.0041	0.003	0.0018–0.0042
Proposed Method	0.0012	0.001–0.0014	0.0015	0.0012–0.0018

Table IV Computational Complexity

Method	**Computational Cost**	**Computational Complexity**
EKF	0.15	$O(2n^3+m^3)$
UKF	0.42	$O((2n+1)n^2+n^3)$
Proposed Method	0.47	$\mathrm{O}(\mathrm{n}^3+\mathrm{p})O(n^3+p)$

Here, p denotes the set of ANFIS parameters, while n and m represent the number of state variables and measurement variables, respectively. In this study, we consider n = 3 and m = 1.

Next, the robustness of the proposed method is evaluated under scenarios where the measurement noise statistics are incorrectly assumed. In the proposed framework, real-time adaptive tuning is triggered when a significant discrepancy is detected between the empirical residual covariance—computed over a sliding window—and the theoretical innovation covariance. This strategy ensures that recalibration is activated only when persistent deviations are identified. To avoid overfitting to transient noise variations, windowed averaging is employed to smooth short-term fluctuations, and the ANFIS training is regularized using a forgetting factor ($\lambda = 0.98$) and a small learning rate ($\eta = 0.01$), enabling gradual and stable adaptation. The initial process and measurement noise covariance matrices (Q_0 and R_0) are selected based on empirical data and sensor specifications. Small diagonal values are used for Q_0 to account for model uncertainty, while R_0 is initialized based on nominal sensor noise levels. Importantly, the adaptive mechanism of the filter—driven by innovation-based statistics and ANFIS tuning—progressively refines these covariance matrices during operation. As a result, the long-term accuracy of SOC estimation remains robust to the initial selection of Q_0 and R_0.

Figs.11–12 present a comparative analysis of the proposed method against alternative approaches. The results indicate that the proposed method achieves superior accuracy

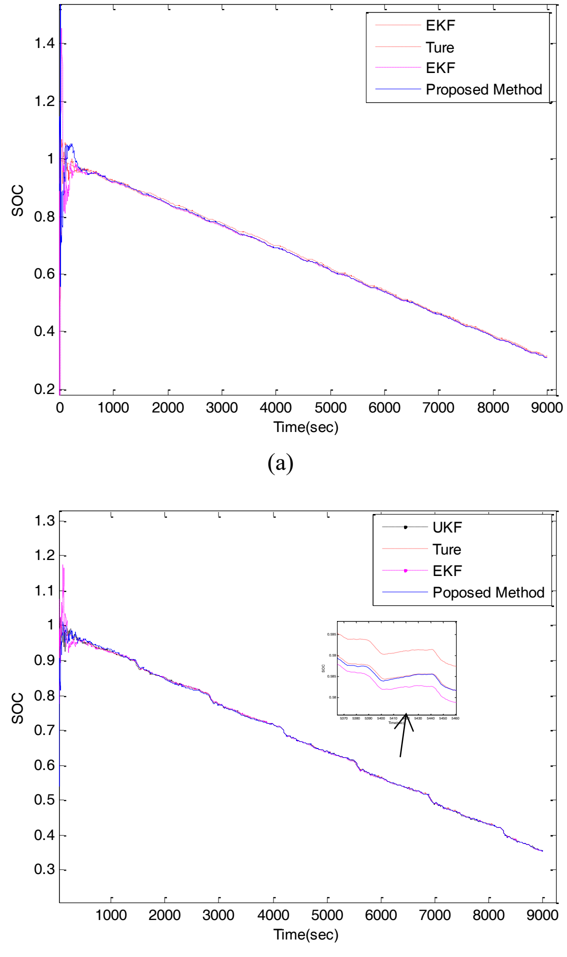

(a)

(b)

Fig.12. SOC estimation at 0 C (a) US06 (b) FUDS

compared to the EKF and UKF. Specifically, the SOC estimation results in Fig. 11 demonstrate that the proposed method rapidly converges to the actual SOC, highlighting its robustness even in the presence of unknown noise statistics. Furthermore, as shown in Figs. 11 and 13, the performance of the proposed method remains nearly unaffected compared to the previous case, whereas the performance of EKF and UKF degrades significantly. This resilience stems from the fact that the proposed approach does not rely on prior knowledge of noise statistics; instead, it operates under the assumption that the noise energy is bounded within a certain range. Additionally, the proposed method adaptively adjusts the process and measurement noise covariances, further enhancing its robustness.

To further demonstrate the advantages of the proposed approach over EKF and UKF, a quantitative comparison is conducted under identical simulation conditions. Fig. 12 illustrates the RMSE trajectories of SOC estimation over time, while Fig.14 the mean RMSE, standard deviation, 95% confidence interval for pairwise comparisons. Figs.13-14 and Table V present the RMSE results over 50 Monte Carlo simulations, confirming that the proposed method consistently outperforms the EKF and UKF by achieving more accurate mean and covariance estimates.

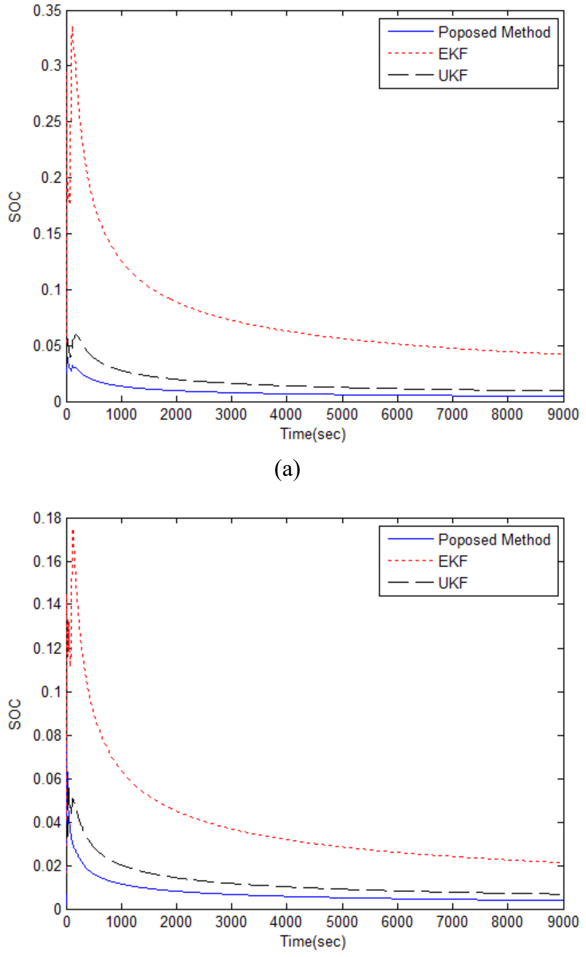

(a)

(b)

Fig.13. RMSE of SOC (a) US06 (b) FUDS

Table V RMSE under unknown noise statistics

Method	FUDS		US06	
	RMSE	95% CI	RMSE	95% CI
EKF	0.049	0.012-0.038	0.05	0.02-0.08
UKF	0.011	0.004-0.014	0.01	0.005-0.015
Proposed Method	0.003	0.0016-0.0026	0.003	0.0024-0.0036

Finally, the effectiveness of the proposed method is assessed under non-Gaussian noise conditions. In this evaluation, the measurement noise is modeled using a Gamma distribution, while the process noise is assumed to follow a Gaussian distribution. Although the proposed method is theoretically formulated under Gaussian noise assumptions, it demonstrates strong resilience to non-Gaussian disturbances due to its adaptive structure. By leveraging real-time innovation statistics and an ANFIS-based adjustment mechanism, the filter dynamically updates the noise covariance matrices (Q_k and R_k), thereby accommodating variations such as skewness, heavy tails, or

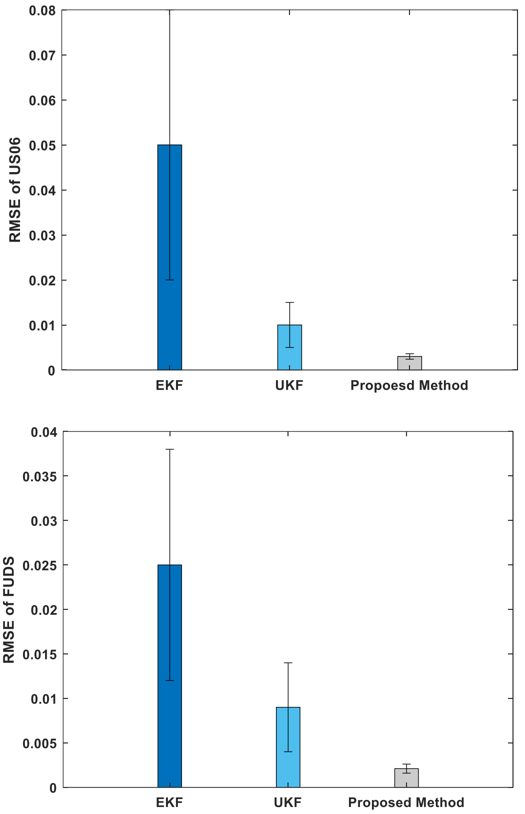

Fig.14. RMSE under unknown noise statistics

time-dependent noise profiles. This adaptive tuning enables the filter to maintain reliable performance without requiring explicit modeling of the noise distribution. The results, depicted in Fig.15, demonstrate that the proposed method outperforms both the EKF and UKF. For the EKF and UKF, the presence of non-Gaussian noise significantly impacts estimation accuracy, as these methods inherently rely on the assumption of Gaussian noise. In contrast, the proposed approach does not impose such a constraint, making it inherently more robust to variations in noise characteristics. This adaptability enhances its reliability in real-world applications, where noise distributions are often unknown or deviate from the Gaussian assumption.

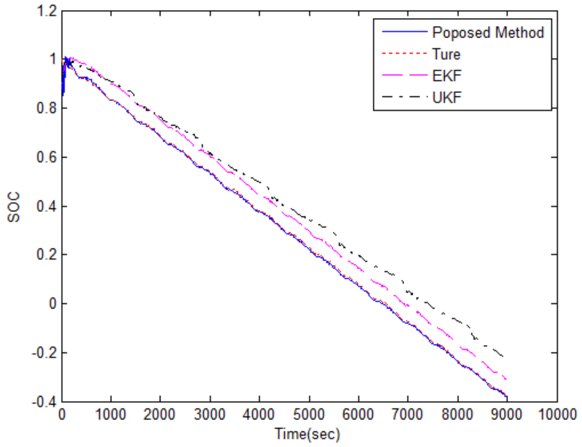

Fig.15 SOC estimation for US06 testing at 0 C

In a 10-cell configuration, each ARSRUKF estimator transmits state vectors (SOC, U_1, U_2) and Cholesky covariance factors at a nominal 100 Hz rate, resulting in a total data rate of 36 KB/s. ANFIS dynamically adjusts synchronization frequency to 10–200 Hz based on load dynamics, balancing accuracy and bus utilization. This approach ensures compatibility with automotive-grade CAN-FD networks (8 Mbps bandwidth), avoiding arbitration delays through prioritized alarm signaling.

VI. Conclusion

In this paper, we propose an advanced adaptive robust SR-UKF integrated with RLS for SOC estimation. The primary goal of this approach is to improve the robustness and accuracy of SOC estimation in the presence of uncertainties, especially when the statistical characteristics of process and measurement noise are unknown or variable. A key advantage of the proposed method is that it does not rely on prior knowledge of noise statistics, which are typically required in conventional filtering methods. Instead, covariance matrices for both process and measurement noise are dynamically adjusted in real-time using ANFIS. By combining the strengths of neural networks and fuzzy logic, ANFIS estimates optimal tuning parameters, enabling the filter to adaptively improve performance under varying operational conditions and environmental factors such as temperature changes and battery aging. The use of ANFIS allows effective modeling of nonlinear relationships and better handling of system uncertainties. By continuously adapting noise covariance parameters, the proposed method maintains high accuracy and stability even when noise characteristics are unknown or change over time. This makes the approach especially suitable for practical applications where accurate SOC estimation is critical, including EVs, renewable energy systems, and portable electronics. Experimental results demonstrate that the proposed SR-UKF with RLS and ANFIS-based tuning significantly outperforms traditional methods in both accuracy and robustness. Notably, the proposed method provides more precise SOC estimates under challenging scenarios involving high noise levels, battery behavior variations, and unknown environmental influences. The proposed SR-UKF with RLS offers a promising solution for SOC estimation in systems with uncertain noise statistics. Its adaptability and inherent robustness make it a valuable tool for reliable SOC estimation in real-world applications. Future work could focus on further refining the method and exploring its performance in other complex scenarios. Scaling the framework to multi-cell battery packs introduces challenges such as cell-to-cell variability, balancing operations, and communication overhead. To address these, parallel ARSRUKF filters can be deployed at the cell level for individualized state estimation. Balancing-induced transient currents can be compensated by integrating current compensation techniques or coupling the estimators with balancing control algorithms. Efficient communication and synchronization between estimators are crucial, and distributed filtering architectures may provide scalable solutions for large battery systems. Furthermore, as part of our future work, we plan to perform real-time Hardware-in-the-Loop (HIL) validation of the proposed method. Preliminary hardware specifications for the HIL platform include a Texas Instruments TMS320F28379D dual-core DSP or an equivalent ARM Cortex-M7 microcontroller (e.g., STM32H7 series), with a minimum clock speed of 200 MHz. The system will support real-time sampling at 100 Hz to accommodate battery dynamics and ANFIS-based adaptive filtering. Sensor inputs will include voltage, current, and temperature measurements acquired via high-precision ADCs. The HIL test bench will replicate real-world load profiles (e.g., US06, FUDS) using programmable power supplies and battery emulators. These efforts aim to evaluate the algorithm's robustness and computational feasibility in embedded platforms.

References

[1] Q. Ouyang, J. Chen, and J. Zheng, "State-of-charging observer design for batteries with online model parameter identification: A robust approach," IEEE Transactions on Power Electronics, vol. 35, no. 6, pp. 5820–5831, Jun.2020.

[2] G.Mohebalizadeh, H.Alipour,L.Mohammadian, M.Sabahi, "An Improved Sliding Mode Controller for DC/DC Boost Converters Used in EV Battery Chargers with Robustness against the Input Voltage Variations", International Journal of Industrial Electronics, Control and Optimization,vol.4, no.2, pp.257-266 , 2021.

[3] G. Mohebalizadeh, H. Alipour, L. Mohammadian, and M. Sabahi, "An Improved Sliding Mode Controller for DC/DC Boost Converters Used in EV Battery Chargers with Robustness Against Input Voltage Variations," Int. J. Ind. Electron. Control Optim., vol. 4, no. 2, pp. 257–266, 2021.

[4] W. Waag, C. Fleischer, and D. U. Sauer, "Critical review of the methods for monitoring of lithium-ion batteries in electric and hybrid vehicles," Journal of Power Sources, vol. 258, pp. 321-339, Mar. 2014

[5] Y. Yang, Z. Tan, and Y. Ren, "Research on factors that influence the fast charging behavior of private battery electric vehicles," Sustainability, vol. 12, no. 9, p. 3439, Sep. 2020.

[6] F. Wang, Z. Zhai, B. Liu, S. Zheng, Z. Zhao, and X. Chen, "Open access dataset, code library and benchmarking deep learning approaches for state-of-health estimation of lithium-ion batteries," Journal of Energy Storage, vol. 77, Article 109884, 2024, doi: 10.1016/j.est.2023.109884.

[7] E. D. Silva-Vera, J. E. Valdez-Resendiz, G. Escobar, D. Guillen, J. C. Rosas-Caro, and J. M. Sosa, ''Data-driven modeling and open-circuit voltage estimation of lithium-ion batteries,'' Mathematics, vol. 12, no. 18, p. 2880, 2024.

[8] W. Bao, H. Liu, Y. Sun, and Y. Zheng, ''A fast prediction of open-circuit voltage and a capacity estimation method of a lithium-ion battery based on a BP neural network,'' Batteries, vol. 8, no. 12, p. 289, Dec. 2022.

[9] Q. Shi, Z. Jiang, Z. Wang, X. Shao, and L. He, "State of charge estimation by joint approach with model-based and data-driven algorithm for lithium-ion battery," IEEE Transactions on Instrumentation and Measurement, vol. 71, pp. 1–10, 2022.

[10] U. Westerhoff, T. Kroker, K. Kurbach, and M. Kurrat, ''Electrochemical impedance spectroscopy based estimation of the state of charge of lithiumion batteries,'' J. Energy Storage, vol. 8, pp. 244–256, . 2016.

[11] S. Su, W. Li, J. Mou, A. Garg, L. Gao, and J. Liu, "A hybrid battery equivalent circuit model, deep learning, and transfer learning for battery state monitoring," IEEE Transactions on Transportation Electrification, vol. 9, no. 1, pp. 1113–1127, Mar. 2023.

[12] F. Wang, Z. Zhai, B. Liu, S. Zheng, Z. Zhao, and X. Chen, "Open access dataset, code library and benchmarking deep learning approaches for state-of-health estimation of lithium-ion batteries," J. Energy Storage, vol. 77, p. 108529, Apr. 2024.

[13] Z. Chen, Y. Fu, and C. C. Mi, ''State of charge estimation of lithium-ion batteries in electric drive vehicles using extended Kalman filtering,'' IEEE Trans. Veh. Technol., vol. 62, no. 3, pp. 1020–1030, Mar. 2013.

[14] J. Kim and B. H. Cho, "State-of-charge estimation and state-of-health prediction of a li-ion degraded battery based on an EKF combined with a per-unit system," IEEE Trans. Veh. Technol., vol. 60, pp. 4249-4260, 2011.

[15] Y. Tian, B. Xia, W. Sun, Z. Xu, and W. Zheng, ''A modified model based state of charge estimation of power lithium-ion batteries using unscented Kalman filter,'' J. Power Sources, vol. 270, pp. 619–626, Dec. 2014.

[16] Wang Qiuting, Lu Yunhao, JY, "State of health estimation for lithium-ion battery based on D-UKF", Int. J. Hybrid Inf. Technol., vol.8, no.16, 2015.

[17] J. Ma, Y. Hu, Q. Ma, S. Yang, J. Zheng, and S. Wang, ''Improved adaptive filter with unknown process and measurement noise covariance,'' in Proc. Chinese Intell. Syst. Conf., 2020, pp. 792–800.

[18] [19] B. Gao, S. Gao, G. Hu, Y. Zhong, and C. Gu, ''Maximum likelihood principle and moving horizon estimation based adaptive unscented Kalman filter,'' Aerospace Sci. Technol., vol. 73, pp. 184–196, Nov. 2024.

[19] J. Meng, G. Luo, and F. Gao, ''Lithium polymer battery state-of-charge estimation based on adaptive unscented Kalman filter and support vector machine,'' IEEE Trans.

Power Electron., vol. 31, no. 3, pp. 2226–2238,Mar. 2016.

[20] M. Partovibakhsh and G. Liu, “An Adaptive Unscented Kalman Filtering Approach for Online Estimation of Model Parameters and State-of-Charge of Lithium-Ion Batteries for Autonomous Mobile Robots,” IEEE Trans. Control Syst. Technol., vol. 23, no. 1, pp. 357-363, 2015.

[21] Q. Shi, Z. Jiang, Z. Wang, X. Shao, and L. He, "State of charge estimation by joint approach with model-based and data-driven algorithm for lithium-ion battery," IEEE Transactions on Instrumentation and Measurement, vol. 71, pp. 1–10, 2022.

[22] S. Su, W. Li, J. Mou, A. Garg, L. Gao, and J. Liu, "A hybrid battery equivalent circuit model, deep learning, and transfer learning for battery state monitoring," IEEE Transactions on Transportation Electrification, vol. 9, no. 1, pp. 1113–1127, Mar. 2023.

[23] J. Meng et al., “An Overview and Comparison of Online Implementable SOC Estimation Methods for Lithium-Ion Battery,” in IEEE Transactions on Industry Applications, 2018, vol. 54, no. 2, pp. 1583–1591.

[24] R. Xiong, J. Cao, Q. Yu, H. He, and F. Sun, “Critical Review on the Battery State of Charge Estimation Methods for Electric Vehicles,”IEEE Access, vol. 6, pp. 1832–1843, 2018.

[25] Jinhao Meng, Daniel-Ioan Stroe, Mattia Ricco, “A Simplified Model based State-of-Charge Estimation Approach for Lithium-ion Battery with Dynamic Linear Model”, IEEE Transactions on Industrial Electronics,vol.66,no.10,2018.

[26] Zhuang, Y., Wang, Z., Yu , H., Wang, W. , Lauria , S. “A robust extended H∞ filtering approach to multi-robot cooperative localization in dynamic indoor environments”, Control Engineering Practice ,vol.21, pp.953–961, 2013.

[27] P. Zhang, W. Wang, M. Gao, and Y. Wang, ‘‘Square-root cubature Kalman filter based on H∞ filter for attitude measurement of high-spinning aircraft,’’ Int. J. Aerosp. Eng., vol. 2021, Article ID 5589691, May 2021.

[27] T. Q. Duong, “USABC and PNGV test procedures,” Journal of Power Sources, vol. 89, no. 2, pp. 244–248, 2000.

[28] W. He, N. Williard, C. C. Chen, and M. Pecht, “Robust and adaptive estimation of state of charge for lithium-ion batteries,” International Journal of Power Electronics, vol. 62, pp. 783–791, 2014.

[29] Z. Ma, J. Jiang, W. Shi, W. Zhang, and C. C. Mi, “Investigation of path dependence in commercial lithium-ion cells for pure electric bus applications: aging mechanism identifcation,” Journal of Power Sources, vol. 274, pp. 29–40, 2015.

Ramazan Havangi received his M.S. and Ph.D. degrees from the K.N. Toosi University of Technology, Tehran, Iran, in 2003 and 2012, respectively. He is currently an Associate Professor of control systems with the Department of Electrical and Computer Engineering, University of Birjand, Birjand, Iran. His main research interests are inertial navigation, integrated navigation, estimation and filtering, evolutionary filtering, simultaneous localization and mapping, fuzzy, neural network, and soft computing.

Fatemeh Karimi was born in Borujerd, Iran. She received her associate degree in telecommunications, her B.Sc. degree in electronics engineering, and her M.Sc. degree in control engineering all from Islamic Azad University in 2003, 2008, and 2013, respectively. She is currently a Ph.D. candidate of control engineering at the state-run University of Birjand. Her research interests include function fields, active power filters, multi-agents, and Kalman filters.

IECO

This page intentionally left blank.

IECO
International Journal Of
Industrial Electronics Control and Optimization
Print ISSN: 3517-2645
Online ISSN: 3568-2645
Homepage: https://ieco.usb.ac.ir/

RSS Localization in the Presence of Byzantine Attacks using MAP Estimation

Mahdiye Mohammadi [1] | Hadi Zayyani [2] | Mehdi Bekrani [3]

Department of Electrical and Computer Engineering, Qom University of Technology, Qom, Iran [1,2,3]
Corresponding author's email: bekrani@qut.ac.ir

Article Info	ABSTRACT
Article type: Research Article **Article history:** Received: 21-February-2025 Received in revised form: 13-April-2025 Accepted: 10-May-2025 Published online: 22-June-2026 **Keywords**: Anchor node Fusion center (FC), MAP estimator, Target node.	Target localization in wireless sensor networks (WSNs) is essential for various applications. This study investigates received signal strength (RSS)-based localization in the presence of malicious anchor nodes that intentionally alter signal power levels to mislead the fusion center (FC) and degrade positioning accuracy. To address this challenge, we adopt a Maximum a Posteriori (MAP) estimator, which estimates the target location even when the path loss exponent is unknown. We show that the MAP estimation method can estimate the WSN unknown parameters, including the path loss exponent, the distance between the target node and anchor nodes, and the received signal strength. Simulation results demonstrate that the MAP method achieves lower localization errors than other competing approaches when the Signal-to-Noise Ratio (SNR) exceeds 10 dB, although it entails higher computational complexity in terms of simulation run time. The proposed approach is particularly efficient in applications in transportation, military operations, security, smart industries, and mapping.

I. Introductions

Wireless sensor networks (WSNs) have diverse applications, including tracking goods in supply chains, monitoring air quality, observing farm animal behavior, detecting landslides, and providing navigation assistance in environments like shopping malls and airports.

A WSN is composed of multiple sensor nodes that communicate and collaborate to achieve a common objective. Sensor nodes collect data and transmit it to a fusion center (FC) for further analysis. Radio frequency (RF)-based target localization is particularly valuable in military and industrial applications. Target localization can be achieved using various methods, including angle of arrival (AOA) [1], time of arrival (TOA) [2], and time difference of arrival (TDOA) [3]. However, among these techniques, the received signal strength (RSS) method is more cost-effective and does not require synchronization [4]. Moreover, some studies have explored hybrid localization techniques that combine methods such as RSS and AOA, as presented in [5] and [6].

Significant advancements have been made in RSS-based localization due to extensive research. Most studies assume that anchor nodes function reliably, but this may not always be the case, particularly in the presence of malicious attacks. During such attacks, compromised anchor nodes transmit incorrect measurements to the FC, thereby disrupting localization accuracy. As a result, the FC may fail to determine the precise location of the target node. Anchor nodes that intentionally provide false data and interfere with the localization process are referred to as Byzantine nodes. The presence of these nodes introduces significant challenges to accurate localization.

Several methods have been explored in the literature to enhance localization accuracy in the presence of malicious anchor nodes. One approach involves iterative gradient descent, as discussed in [7]. Triangulation and RF-based fingerprinting methods have also been investigated in [8], where an adaptive least squares (LS) technique and Least Median of Squares (LMdS) were proposed for triangulation, while a median-based distance metric was employed for RF fingerprinting. In [8] and [9], techniques were introduced to detect and eliminate malicious nodes, thereby mitigating their impact on the localization process. The study in [10] analyzed uncoordinated attacks, where malicious anchor

Publisher: University of Sistan and Baluchestan

nodes manipulate their transmission power following a Gaussian distribution to disrupt localization. Conversely, [11] assumed a uniform distribution for the transmission power, making the uncoordinated attack model more realistic.

Additionally, [11] examined both coordinated and uncoordinated attacks and proposed three localization techniques— Weighted LS (WLS), Secure WLS, and $l_1 - norm$ based (LN_1) localization—capable of identifying and mitigating the influence of malicious anchor nodes in the network. Localization in WSNs with unknown sensor positions has been explored in [12] and [13], offering a cost-effective solution that eliminates the need for time synchronization and extensive local processing.

Several approaches based on RSS have been proposed to address synchronization and computational challenges, utilizing LS or maximum likelihood (ML)-based source localization methods [14], [15]. Due to energy and bandwidth constraints, anchor nodes often rely on binary or multi-bit quantized data for communication. The problem of target node localization using quantized data has been investigated in various studies [16], [17]. In [18], an adversary is assumed to take control of certain sensors, compelling them to transmit false data to the FC.

A Byzantine identification scheme was introduced in [19] for distributed detection, where malicious nodes are adaptively identified, and their information is leveraged to enhance detection performance. The Byzantine problem has also been studied in the context of network coding and information theory [20], [21]. In [22], the ML estimation was employed for target localization in a WSN using binary quantized data, analyzing the impact of Byzantine attacks. In such a scenario, the performance metric is the Fisher information [23]. The work in [24] proposed an ML-based localization approach along with a Byzantine detection method and a dynamic non-uniform threshold design to mitigate malicious interference. Meanwhile, [25] examined target localization in the presence of malicious sensors using a Monte Carlo-based approach. This study assumed a random target location and evaluated the performance of the minimum mean square error (MMSE) estimator. The presence of malicious anchor nodes made performance evaluation more complex, with posterior Fisher information and the posterior Cramér-Rao lower bound (CRLB) serving as key performance measures.

In recent studies, one research effort reformulates the localization problem as a Generalized Trust Region Subproblem (GTRS) by applying specific approximations to enhance tractability [26]. However, these approximations can reduce the overall performance of the method. Additionally, the more recent work in RSS-based localization [27] proposes a cooperative localization approach in wireless sensor networks (WSNs) using biased RSS measurements, addressing a scenario with the presence of Byzantine nodes. This study employs semidefinite programming (SDP) with l_1 and l_2 norms to address the non-convexity of the maximum likelihood (ML) estimator, which is a notable advantage. Nonetheless, a key drawback of this method is its requirement to estimate both the biases and the distances/locations, which increases the computational complexity and may compromise localization accuracy.

In this study, we estimate the location of the target node using the Maximum A Posteriori (MAP) estimation method, which differs from the approach in [25] that employs the Minimum Mean Square Error (MMSE) estimator for the localization problem. In addition to the target node's location, denoted as Z, other unknown parameters include the Path Loss Exponent (PLE) (β), the distance between anchor nodes and the target node (d), and RSS. Each of these parameters is estimated using the MAP approach. We conduct a comprehensive analysis of the MAP method, detailing the estimation process for the path loss exponent, distances between non-malicious anchor nodes and the target node, RSS values, and the target node's location. The main contributions of this paper are as follows: (1) It computes the MAP estimator for all unknown variables, unlike other approaches such as the ML estimator, which does not consider prior distributions, and the MMSE estimator, which requires complex expectations and integral computations. (2) It employs an alternating maximization approach for estimating unknown variables, which simplifies the optimization process by updating one variable at a time instead of optimizing all variables jointly. (3) The study addresses RSS-based localization under Byzantine attacks in the case where the path loss exponent is also unknown, and estimates the PLE as part of the overall algorithm. Furthermore, we compare the MAP method with other state-of-the-art approaches to evaluate its performance. In the experimental results section, we present a detailed analysis of our MATLAB-based simulations, accurately reporting the estimation outcomes for all unknown parameters.

II. System model

We consider a network consisting of N anchor nodes with known locations and a single target node with an unknown location. It is assumed that all anchor nodes are within the communication range of the target node and transmit at a predefined power level. The target node extracts the RSS from packets transmitted by the anchor nodes and estimates its distance from each of them. Using these estimated distances and the known anchor node locations, a localization technique is applied to determine the target node's position.

The signal power loss is primarily influenced by the path loss exponent, which is modeled using the log-distance path loss model as follows:

$$P^r = P_0 - 10\beta \log_{10}(d) + \eta \quad (1)$$

where P^r represents the received power at the target, P_0 is the received power when the single anchor node is one meter away from the target node, β is the path loss exponent, d denotes the distance between the anchor node and the target node, and η is additive noise, assumed to be zero-mean, independently, and identically distributed (i.i.d) Gaussian.

The received power can be expressed as follows:

$$X_{i.j} = (p_i{}^r)_j = \begin{cases} P_0 - 10\beta \log_{10}(d_i) + \eta_{i.j}\,, i \text{ is non} - \text{malicious} \\ P_{0i} - 10\beta \log_{10}(d_i) + \eta_{i.j}, \;\; i \text{ is malicious} \end{cases} \quad (2)$$

where $(p_i{}^r)_j$ represents the received power from the i^{th} anchor node during the j^{th} observation, and P_{0i} represents the transmit power of the i^{th} malicious anchor node, while β is the path loss exponent, which follows a normal distribution with mean β_0 and variance σ_β^2. The power P_0 follows a normal distribution with mean $\overline{p_0}$ and variance $\sigma_{\varepsilon P}^2$. Similarly, P_{0i} follows a normal distribution with mean $\overline{p_{0\iota}}$ and variance $\sigma_{a,i}^2$. The additive noise $\eta_{i.j}$ is assumed to be normally distributed with zero mean and variance $\sigma_{\eta i}^2$. The target node is located at $\mathrm{Z} = [x_t \,.\, y_t]^T$. The distance between the target node and the i^{th} anchor node is given by:

$$d_i = \sqrt{(x_i - x_t)^2 + (y_i - y_t)^2} \quad (3)$$

The distance vector for all anchor nodes is:

$$d = [d_1 . d_2 \ldots d_N]^T \quad (4)$$

The number of observations or snapshots is P, where j ranges from 1 to P. The observation vector for the i^{th} anchor node is:

$$\boldsymbol{X}_i = [X_{i.1} . X_{i.2} \ldots X_{i.P}]^T \quad (5)$$

where $X_{i.j} = (p_i{}^r)_j$. The total observation matrix is:

$$\mathrm{X} = [X_1 . X_2 \ldots X_N]_{P \times N} \quad (6)$$

The vector of unknown parameters is:

$$\theta = [\beta, d, P_0^{'}, Z] \quad (7)$$

where

$$P_{0i}^{'} = \begin{cases} P_0 & i \text{ is non} - \text{malicious} \\ P_{0i} & i \text{ is malicious} \end{cases} \quad (8)$$

III. Estimation of the target location

Figure 1 illustrates the typical placement of sensors in the network. In this figure, the target node, located at [20,10], is represented by a green circle. The anchor nodes are positioned at [−50,−50], [−50,50], [50,−50], [50,50], [−30,−30], [−30,30], [30,−30], and [30,30].

Among these anchor nodes, we assume that the nodes at [−50,−50] and [50,50] are Byzantine, meaning they introduce false information to disrupt the localization process. In Figure 1, non-malicious anchor nodes are depicted in blue, while malicious anchor nodes are shown in red.

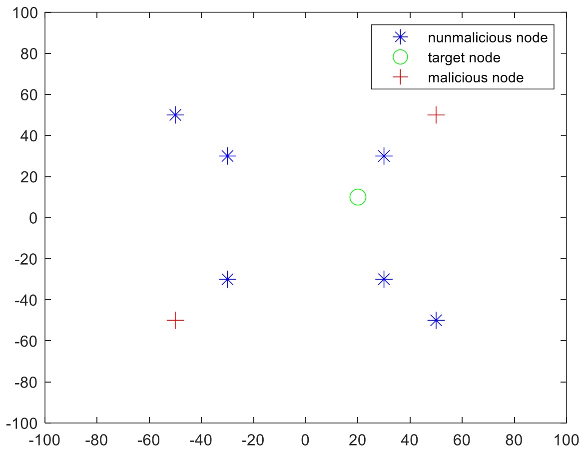

Fig. 1. Location of sensors in the network.

For target localization, the known locations of the sensors in the network are used to estimate the target's position based on RSS from these sensors. To achieve this, we employ the LS, WLS, and the proposed MAP methods. We then compare the performance of the MAP method against the LS and WLS methods to evaluate its effectiveness in target localization.

A. Estimating the location of the target node using the Linear LS (LLS) method

In [28], the LLS method is proposed for target node localization. In this approach, the target location is estimated using LLS estimation based on the received signal power from surrounding anchor nodes. To implement the LLS method, we first need to define a range variable that converts the RSS measurements into a linear model for estimating the target location.

Let the i^{th} anchor node be located at $[x_i . y_i]^T$. The range variable, R, is defined as follows:

$$R = x^2 + y^2 \quad (9)$$

The distance d_i between the target node and the i^{th} anchor node is given by:

$$d_i = \sqrt{(x_t - x_i)^2 + (y_t - y_i)^2} \quad (10)$$

Squaring both sides of equation (50) yields:

$$-2x_i x_t - 2y_i y_t + R = d_i{}^2 - x_i{}^2 - y_i{}^2 \quad (11)$$

To express this problem in matrix form, we get the following system:

$$A\lambda = b \quad (12)$$

where λ represents the unknowns to be estimated. The matrix A is:

$$A = \begin{bmatrix} -2x_1 & -2y_1 & 1 \\ -2x_2 & -2y_2 & 1 \\ \vdots & \vdots & \vdots \\ -2x_N & -2y_N & 1 \end{bmatrix} \quad (13)$$

The vector λ is:

$$\lambda = [x\ y\ R]^2 \quad (14)$$

and the observation vector b is:

$$b = \begin{bmatrix} {d_1}^2 - {x_1}^2 - {y_1}^2 \\ {d_2}^2 - {x_2}^2 - {y_2}^2 \\ \vdots \\ {d_N}^2 - {x_N}^2 - {y_N}^2 \end{bmatrix} \quad (15)$$

In this formulation, A is a known matrix, λ is the parameter vector to be estimated, and b is the observation vector.

The solution to the LLS optimization problem is given by:

$$\hat{\lambda} = (A^T A)^{-1} A^T b \quad (16)$$

B. Estimating the target location using the WLS method

The WLS method for localization is introduced in [11]. This method assigns weights to anchor nodes based on their distance from the target node. The target node receives P packets from anchor nodes and computes the mean received power. Using this power measurement, the target node estimates its distance from each anchor node. The WLS model is a refined version of the LS method.

The measurement model can be expressed as:

$$b = A\theta + w \quad (17)$$

where w is the noise vector, b is the measurement vector, A is the coefficient matrix, and θ is the vector of unknown parameters.

Without assuming a specific probability distribution for w, the target node's estimated location can be obtained by solving the WLS problem. The WLS estimate minimizes the weighted error:

$$\hat{\theta} = \underset{\theta}{\operatorname{argmin}} (b - A\theta)^T W (b - A\theta) \quad (18)$$

where W is a weight matrix that accounts for variations in measurement confidence, typically set as the inverse of the noise covariance matrix. In [11], a weighted diagonal matrix is considered whose elements are the inverse of the variance $\sigma_{d_i}^2$ of the estimated distance between the i^{th} anchor node and the actual target node as follows:

$$W = \operatorname{diag}\left\{\frac{1}{\sigma_{d_1}^2}, \cdots, \frac{1}{\sigma_{d_N}^2}\right\} \quad (19)$$

The solution to this optimization problem is given by:

$$\hat{\theta} = (A^T W A)^{-1} A^T W b \quad (20)$$

where A and b are as defined in (13) and (15), respectively. This approach refines the target location estimate by reducing the influence of measurements with higher uncertainty.

In the WLS method, greater weight is assigned to anchor nodes that are closer to the target node, and specific weights are applied to the received signal strength based on the distance between each sensor and the target node. Since RSS-based localization methods also estimate the distances, these estimated distances are used to determine which anchor nodes are closer to the target, allowing greater weights to be assigned accordingly. While this approach improves accuracy, it increases the cost function, leading to longer computation times to determine the exact location of the target node, causing delays in reaching the goal in comparison to the LS method. However, due to its weighting of the received signal strength, the WLS method can localize the target node with lower error, making it more accurate in estimating the target's position despite the higher computational cost in comparison to the LS method.

IV. The proposed target localization

In this paper, we employ the MAP estimation method to determine the location of the target node [29]. In the MAP method, the target node location is estimated by maximizing the posterior distribution $P(\theta|X)$ [29], where θ represents the vector of unknown parameters, which includes the target location $Z = [x_t, y_t]^T$, the path loss parameter β, the received signal strength d, and a model parameter P_0. The posterior distribution is typically expressed as:

$$\max P(\theta|X) = \max\{\log P(\theta) + \log P(X|\theta)\} \quad (21)$$

The prior distribution $P(\theta)$ is defined as:

$$\log P(\theta) = \log\{P(Z)P(\beta|Z)P(d|\beta, Z)P\left(P_0^{'}\middle|d, \beta, Z\right)\} \quad (22)$$

This can be expanded as:

$$\log P(\theta) = \log P(\beta) + \log P\left(P_0^{'}\right) + \log P(d|\beta, Z) = -\frac{(\beta-\beta_0)^2}{2\sigma_\beta^2} + \sum_{i=1}^{N} \log P\left(P_{0.i}^{'}\right) + \sum_{i=1}^{N} \log P(d_i|\beta, Z) \quad (23)$$

We assume that $P(z)$ has a uniform distribution, while $P(d_i|\beta, z)$ is normally distributed with mean $\overline{d_\iota}$ and variance $\sigma_{\varepsilon_d}^2$. We note that

$$\mathrm{P}(P_{0.i}^{'}) = P_a \mathcal{N}\left(\overline{p_{0\iota}}, \sigma_{a,i}^2\right) + (1 - P_a)\mathcal{N}(\overline{p_0}, \sigma_{\varepsilon_P}^2) \quad (24)$$

where P_a is the probability that i^{th} sensor is malicious and $(1 - P_a)$ probability that i^{th} sensor is non-malicious.

The likelihood of the observed measurements $x_{i.j}$ is given by:

$$x_{i.j} = P'_{0.i} - 10\beta\log(d_i) + \eta_{i.j} \tag{25}$$

where $\eta_{i.j}$ is the noise term. To compute (32), we note that the likelihood function is:

$$\begin{aligned}\log\{P(X|\theta)\} &= \sum_{i=1}^{N}\sum_{j=1}^{P}\log P\left(x_{i.j}|\theta\right)\\ &= c + \sum_{i=1}^{N}\sum_{j=1}^{P}\frac{-\left(x_{i.j} - P'_{0i} - 10\beta\log d_i\right)^2}{2\sigma_{\eta_i}^2}\end{aligned} \tag{26}$$

Thus, the objective function to maximize for the MAP estimation is:

$$\begin{aligned}&J_{MAP}(\theta)\\ &= -\frac{(\beta-\beta_0)^2}{2\sigma_\beta^2}\\ &+ \sum_{i=1}^{N}\sum_{j=1}^{P}\frac{-\left(x_{i.j} - P'_{0i} - 10\beta\log d_i\right)^2}{2\sigma_{\eta_i}^2}\\ &+ \sum_{i=1}^{N}\log\Bigg(P_a\frac{1}{\sigma_{a,i}\sqrt{2\pi}}e^{\frac{-\left(P'_{0i}-\overline{p_{0\iota}}\right)^2}{2\sigma_{a,i}^2}}\\ &+ (1-P_a)\frac{1}{\sigma_{\varepsilon_P}\sqrt{2\pi}}e^{\frac{-\left(P'_{0i}-\overline{p_0}\right)^2}{2\sigma_{\varepsilon_P}^2}}\Bigg)\\ &+ \sum_{i=1}^{N}\frac{-(d_i - \sqrt{(x_i-x_t)^2+(y_i-y_t)^2})^2}{2\sigma_{\varepsilon_d}^2}\end{aligned} \tag{27}$$

Next, to estimate the unknown parameters θ, we maximize the function $J_{MAP}(\theta)$. Given that there are $2N + 1$ unknowns and PN known parameters, the estimation procedure proceeds by calculating the unknown parameters one by one, assuming the others are known.

For the first step, we solve for β by considering the values of d, P'_0, and Z as known, and we maximize $J_1(\beta)$, which is given by:

$$J_1(\beta) = \frac{-1}{2\sigma_\beta^2}(\beta-\beta_0)^2 + \sum_{i=1}^{N}\sum_{j=1}^{P} -a_i\left(k_{ij} - \beta r_i\right)^2 \tag{28}$$

TABLE 1: Localization error with respect to variance of biases of two Byzantine nodes in the network in SNR equal to 20 dB.

Methods	$\sigma_a^2 = 0.2$	$\sigma_a^2 = 0.5$	$\sigma_a^2 = 1$	$\sigma_a^2 = 5$
LS	7.0	8.4	9.5	12.2
WLS	2.6	3.3	4.0	7.2
SDP	2.9	3.7	4.2	6.9
BFLA	2.0	2.9	3.3	5.7
Proposed MAP	1.3	1.9	2.4	4.6

Expanding and simplifying, we get:

$$\begin{aligned}J_1(\beta) &= \frac{-1}{2\sigma_\beta^2}\beta^2 + \frac{\beta_0}{\sigma_\beta^2}\beta - \frac{{\beta_0}^2}{2\sigma_\beta^2}\\ &+ \sum_{i=1}^{N}\sum_{j=1}^{P} -a_i\left({k_{ij}}^2 + \beta^2{r_i}^2\right.\\ &\left.- 2k_{ij}\beta r_i\right)\\ &= \beta^2\left[\frac{-1}{2\sigma_\beta^2} - \sum_{i=1}^{N}\sum_{j=1}^{P}a_i{r_i}^2\right]\\ &+ \beta\left[\frac{\beta_0}{\sigma_\beta^2} + 2\sum_{i=1}^{N}\sum_{j=1}^{P}a_i r_i\,k_{ij}\right]\\ &- \frac{{\beta_0}^2}{2\sigma_\beta^2} - \sum_{i=1}^{N}\sum_{j=1}^{P}a_i{k_{ij}}^2\end{aligned} \tag{29}$$

where $a_i \triangleq \frac{1}{2\sigma_{\eta_i}^2}$, $k_{ij} \triangleq x_{i.j} - P'_{0i}$, and $r_i \triangleq 10\log d_i$. This leads to a quadratic equation in β, and solving for β gives:

$$\frac{\partial J_1(\beta)}{\partial\beta} = 0 \rightarrow \beta = \frac{\frac{\beta_0}{\sigma_\beta^2} + 2\sum_{i=1}^{N}\sum_{j=1}^{P}a_i r_i\,k_{ij}}{\frac{1}{\sigma_\beta^2} + 2\sum_{i=1}^{N}\sum_{j=1}^{P}a_i{r_i}^2} \tag{30}$$

This equation provides the MAP estimate for β. The process can be repeated to estimate the other unknowns, including d, P'_0, and Z.

For the second step, we calculate P'_0 by assuming the values of d, β, and Z are known and then maximizing the function $J_2(P'_0)$, which is given by:

$$\begin{aligned}&J_2(P'_0)\\ &= \sum_{i=1}^{N}\sum_{j=1}^{P}\frac{-1}{2\sigma_{\eta_i}^2}\left(x_{i.j} - P'_{0i} - 10\beta\log d_i\right)^2\\ &+ \sum_{i=1}^{N}\log\Bigg(P_a\frac{1}{\sigma_{a,i}\sqrt{2\pi}}e^{\frac{-\left(P'_{0i}-\overline{p_{0\iota}}\right)^2}{2\sigma_{a,i}^2}}\\ &+ (1-P_a)\frac{1}{\sigma_{\varepsilon_P}\sqrt{2\pi}}e^{\frac{-\left(P'_{0i}-\overline{p_0}\right)^2}{2\sigma_{\varepsilon_P}^2}}\Bigg)\end{aligned} \tag{31}$$

Using the steepest ascent (SA) method, we update P'_0 as:

$$\begin{aligned}&P'_0\\ &\leftarrow P'_0 + \mu_P\sum_{j=1}^{P}\frac{1}{\sigma_{\eta_i}^2}\left(x_{kj} - P'_{0k} - 10\beta\log d_k\right)\\ &+ \mu_P\frac{\frac{-\left(P'_{0k}-\overline{p_{0\iota}}\right)}{\sigma_{a,i}^2}\cdot P_a\frac{1}{\sigma_{a,i}\sqrt{2\pi}}e^{\frac{-\left(P'_{0k}-\overline{p_{0\iota}}\right)^2}{2\sigma_{a,i}^2}}}{C}\\ &- \frac{\frac{\left(P'_{0k}-\overline{p_0}\right)}{\sigma_{\varepsilon_P}^2}\frac{1-P_a}{\sigma_{\varepsilon_P}\sqrt{2\pi}}e^{\frac{-\left(P'_{0k}-\overline{p_0}\right)^2}{2\sigma_{\varepsilon_P}^2}}}{C}\end{aligned} \tag{32}$$

where μ_P is the step-size that control the convergence of P'_0 and

$$C = \frac{P_a}{\sigma_{a,i}\sqrt{2\pi}} e^{\frac{-\left(P'_{0k}-\overline{p_{0\iota}}\right)^2}{2\sigma^2_{a,i}}} + \frac{1-P_a}{\sigma_{\varepsilon_P}\sqrt{2\pi}} e^{\frac{-\left(P'_{0k}-\overline{p_0}\right)^2}{2\sigma^2_{\varepsilon_P}}} \tag{33}$$

For the third step, we solve for d by assuming P'_0, β, and Z are known, and maximizing $J_2(d)$, which is:

$$J_3(d) = \sum_{i=1}^{N}\sum_{j=1}^{P} \frac{-1}{2\sigma^2_{\eta_i}} \left(x_{i.j} - P'_{0i} - 10\beta \log d_i\right)^2 + \sum_{i=1}^{N} \frac{-1}{2\sigma^2_{\varepsilon_d}} (d_i - \sqrt{(x_i - x_t)^2 + (y_i - y_t)^2})^2 \tag{34}$$

Using the SA method, we derive the following update rule for d:

$$d_k = d_k + \mu_d \sum_{j=1}^{P} \frac{-1}{2\sigma^2_{\eta_k}} \left(\frac{-10\beta}{d_k}\right) \times 2\left(x_{kj} - P'_{0,k} - 10\beta \log d_k\right) + \mu_d\left(\frac{-1}{2\sigma^2_{\varepsilon_d}}\right)(2)\left(d_k - \sqrt{(x_k - x_t)^2 + (y_k - y_t)^2}\right) \tag{35}$$

where μ_d is the step-size that controls the convergence of SA method. This is further simplified to:

$$d_k = d_k + \frac{10\beta\mu_d}{d_k\sigma^2_{\eta_k}} \sum_{j=1}^{P} \left(x_{kj} - P'_{0.k} - 10\beta \log d_k\right) - \left(\frac{\mu_d}{\sigma^2_{\varepsilon_d}}\right)\left(d_k - \sqrt{(x_k - x_t)^2 + (y_k - y_t)^2}\right) \tag{36}$$

Finally, for the Z value, we solve by assuming P'_0, β, and d are known and maximizing $J_4(Z)$, which is:

$$J_4(Z) = \sum_{i=1}^{N}\sum_{j=1}^{P} \frac{-\left(x_{i.j} - P'_{0i} - 10\beta \log d_i\right)^2}{2\sigma^2_{\eta_i}} + \sum_{i=1}^{N} \frac{-1}{2\sigma^2_{\varepsilon_d}} (d_i - \sqrt{(x_i - x_t)^2 + (y_i - y_t)^2})^2 \tag{37}$$

We consider two strategies for solving this, as follows:

A. Strategy 1: SA method

$$x_t \leftarrow x_t + \mu_x \frac{\partial J_4}{\partial x_t} \tag{38}$$

$$y_t \leftarrow y_t + \mu_y \frac{\partial J_4}{\partial y_t} \tag{39}$$

where μ_x and μ_y are step-sizes that control the convergence of Z to its final value. We then derive:

$$\begin{aligned} x_t &\leftarrow x_t + \mu_x \sum_{i=1}^{N}\sum_{j=1}^{P} \frac{-\left(x_{i.j} - P'_{0i} - 10\beta \log d_i\right)\left[-10\beta \frac{\partial}{\partial x_t} \log d_i\right]}{\sigma^2_{\eta_i}} \\ &+ \mu_x \sum_{i=1}^{N} \frac{-1}{\sigma^2_{\varepsilon_d}} (d_i - \sqrt{(x_i - x_t)^2 + (y_i - y_t)^2})^2 \cdot \frac{-2x_i - x_t}{2\sqrt{(x_i - x_t)^2 + (y_i - y_t)^2}} \\ &= x_t + \mu_x \sum_{i=1}^{N}\sum_{j=1}^{P} \frac{10\beta\left(x_{i.j} - P'_{0i} - 10\beta \log d_i\right)}{\sigma^2_{\eta_i}} \frac{\frac{\partial d_{i_1}}{\partial x_t}}{d_i} \\ &- \mu_x \sum_{i=1}^{N} \frac{1}{\sigma^2_{\varepsilon_d}} \left(d_i - d_{i_1}\right) \frac{\partial d_{i_1}}{\partial x_t} = \frac{-(x_i - x_t)}{\sqrt{(x_i - x_t)^2 + (y_i - y_t)^2}} \end{aligned} \tag{40}$$

$$\begin{aligned} y_t &\leftarrow y_t + \mu_y \sum_{i=1}^{N}\sum_{j=1}^{P} \frac{10\beta\left(x_{i.j} - P'_{0i} - 10\beta \log d_i\right)}{\sigma^2_{\eta_i}} \frac{\partial d_{i_1}}{\partial y_t} \\ &+ \mu_y \sum_{i=1}^{N} \frac{1}{\sigma^2_{\varepsilon_d}} \left(d_i - d_{i_1}\right) \frac{\partial d_{i_1}}{\partial y_t} = \frac{-(y_i - y_t)}{\sqrt{(x_i - x_t)^2 + (y_i - y_t)^2}} \end{aligned} \tag{41}$$

B. Strategy 2: LS method

Assuming that d_i is known, we can write:

$$d_i{}^2 = (x_i - x_t)^2 + (y_i - y_t)^2 \tag{42}$$

Then, we derive

$$d_i{}^2 - x_i{}^2 - y_i{}^2 = -2x_i x_t - 2y_i y_t + x_t{}^2 + y_t{}^2 \tag{43}$$

$$R_t{}^2 = x_t{}^2 + y_t{}^2 \tag{44}$$

In the matrix form, we have:

$$\underline{b} = \begin{bmatrix} d_1{}^2 - x_1{}^2 - y_1{}^2 \\ \vdots \end{bmatrix} = \begin{bmatrix} -2x_1 & -2y_1 & 1 \\ -2x_2 & -2y_2 & 1 \\ \vdots & \vdots & \vdots \end{bmatrix} \begin{bmatrix} x_t \\ y_t \\ R_t \end{bmatrix} \tag{45}$$

$$A = \begin{bmatrix} -2x_1 & -2y_1 & 1 \\ -2x_2 & -2y_2 & 1 \\ \vdots & \vdots & \vdots \end{bmatrix} \tag{46}$$

$$\theta' = \begin{bmatrix} x_t \\ y_t \\ R_t \end{bmatrix} \tag{47}$$

$$\widehat{\theta'} = A^{\dagger} b \tag{48}$$

The first two elements of $\widehat{\theta'}$ gives the estimated values of x_t and y_t.

V. Simulation Results

This section presents the simulation results demonstrating the enhanced system performance achieved using the proposed MAP method. We assume the true location of the target is $x = 20$, $y = 10$, with $P_0 = 10$ for eight sensors randomly distributed across the network in a 100 x 100 square region. The actual path loss exponent (β) is 3, with $\sigma_\beta = 0.2$, $\sigma_{\varepsilon_P}^2 = 0.01$, $\sigma_{a,i}^2 = \sigma_a^2 = 1$, and the signal-to-noise ratio (SNR) is 20 dB. Based on this setup, the results from the MATLAB simulation are provided below.

Figure 2 shows the actual value of PLE (β) and the estimated β using the MAP method after 30 iterations. The initial value of PLE is set to 2. The figure demonstrates the convergence of the estimated PLE, with the final estimation error of 5.2%.

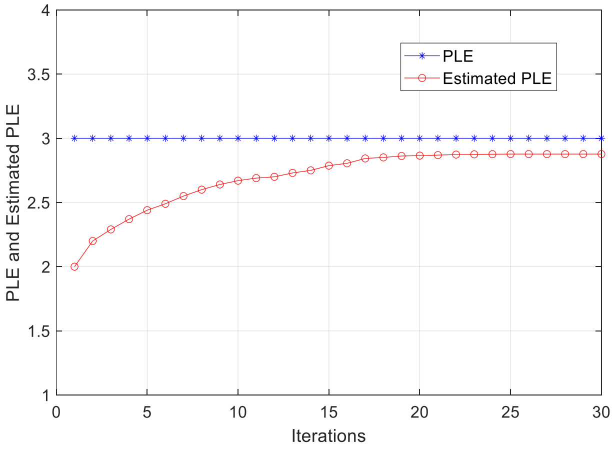

Fig. 2. Estimated β by MAP method with 30 iterations.

Figure 3 displays the estimated distances between the anchor nodes and the target node. The distance estimation is a close approximation to the actual values, with an average error of 16.05%.

Figure 4 shows the actual values of power $P_0^{'} = 10$ for each anchor node along with their estimated values of $P_0^{'}$ using the MAP method. As observed, the estimates converge well, with a final estimation error of approximately 2%.

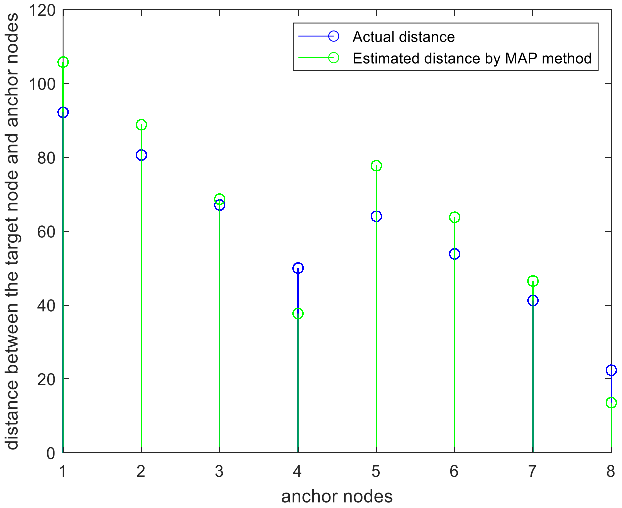

Fig. 3. Estimated distance between the target node and anchor nodes by MAP method

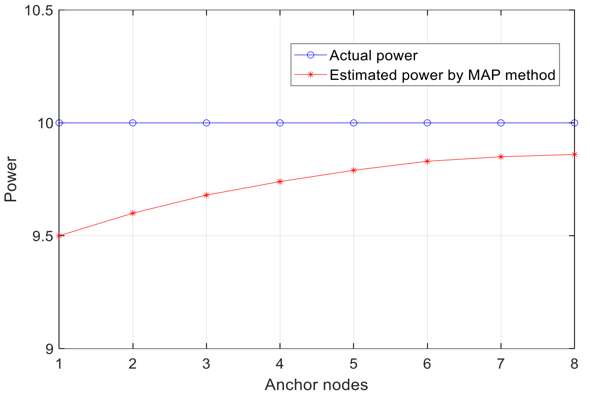

Fig. 4. Estimated power by MAP method

For comparison of the proposed MAP estimation method with the LS, WLS, Semidefinite Programming (SDP) method [27], and the Byzantine Fault-Tolerant Localization Algorithm (BFLA) [26], Figure 5 presents the target localization error as a function of SNR, along with the Cramér-Rao Bound (CRB) calculated in [25]. The graph shows that as the SNR increases, the error decreases. As shown, in the LS method graph, the error decreases slightly with increasing SNR, and it does not achieve optimal efficiency. The WLS method estimates the target location with considerably greater precision. Our proposed MAP estimation method effectively minimizes the impact of malicious anchor nodes, regardless of their number.

Moreover, the figure indicates that the proposed MAP method outperforms other methods when the SNR exceeds 10 dB, while for SNR values below 10 dB, its performance is comparable to that of the BFLA method. Additionally, as the SNR increases, the localization accuracy of both the WLS and the proposed MAP method approaches the CRB.

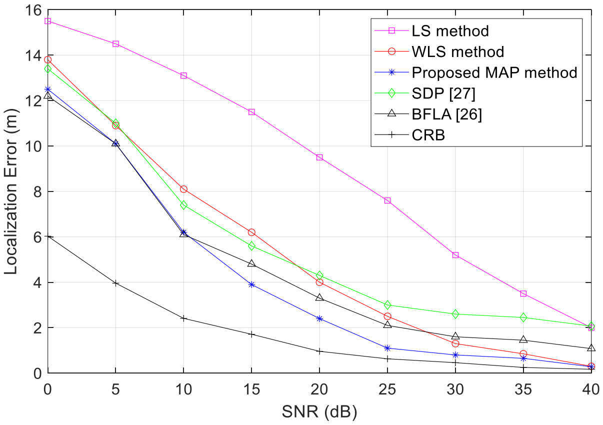

Fig. 5. Localization error in term of SNR for LS, WLS, SDP, BFLA and MAP methods in addition to CRB.

To investigate the effect of bias variance, denoted as σ_a^2 (where $\sigma_{a,i}^2 = \sigma_a^2$), we present Table 1 that illustrates the localization error as a function of σ_a^2 under an SNR of 20 dB. The results show that as the variance of biases introduced by Byzantine nodes increases, the localization error also increases. Among the evaluated methods, the proposed MAP algorithm consistently achieves the lowest localization error, demonstrating its robustness to bias variance.

To evaluate the computational complexity of the methods, we calculated the average simulation run time over 200 Monte Carlo runs. Table 2 presents the simulation run times for all algorithms, indicating that the proposed MAP method exhibits the highest computational complexity in terms of average run time.

TABLE 2: Average Simulation run times of various algorithms in SNR equal to 20dB.

Methods	Simulation run time (s)
LS	0.06
WLS	0.51
Proposed MAP	2.12
SDP	0.89
BFLA	1.56

Referring to the target location in Figure 2, the WLS method is capable of accurately estimating the target location in certain scenarios. However, its accuracy is dependent on the target's position within the network. For instance, if the target is located at the edge of the network or far from the anchor nodes, the likelihood of error increases. However, as previously noted, the WLS method has higher computational complexity and is less time-efficient compared to the LS and MAP methods, which are more efficient.

VI. Conclusion

In this paper, we addressed the localization problem in the presence of malicious anchor nodes and proposed the use of the MAP method to overcome this challenge. We examined scenarios where the path loss exponent, the distance between the target node and anchor nodes, received signal strength, and the target node location were all unknown. This approach enables the fusion center to estimate the target node's location with minimal error. Simulations were carried out in MATLAB, and the corresponding graphs were generated. The MAP method effectively estimates unknown parameters, such as the path loss exponent, the distance between the target node and anchor nodes, and received signal strength. Simulations demonstrated that the MAP method effectively estimates all unknown parameters and achieves the lowest localization error among the evaluated methods. However, this improved accuracy comes at the cost of increased computational complexity due to the iterative calculation of complex likelihoods and gradients. It is also worth noting that all prior distributions were assumed to be Gaussian, which is a simplifying assumption. Future work could explore the use of non-Gaussian priors, such as impulsive noise models or non-Gaussian biases, to enhance robustness in more challenging environments.

REFERENCES

[1] Q. Yan, H. M. Wang, Y. Chen, and C. Gao, “Robust 3-D AOA Localization Against Malicious Attacks in Non-Gaussian Noise,” IEEE Sens. J., vol. 24, no. 9, pp. 14573-14585, 2024.

[2] C. Si, R. Fan, Y. Yang, and Y. Sun, “Improved TOA Localization Using Modified Polar Representation,” IEEE Commun. Lett., vol. 28, no. 9, pp. 2051-2055, 2024.

[3] Y. Liu, C. Chen, Y. Wang, and C. Liu, “Range-Independent TDOA Localization Using Stepwise Accuracy Enhancement Under Speed Uncertainty,” IEEE Signal Process. Lett., vol. 30, pp. 1372-1376, 2023.

[4] R. Sari and H. Zayyani, “RSS Localization Using Unknown Statistical Path Loss Exponent Model,” IEEE Commun. Lett., vol. 22, no. 9, pp. 1830-1833, 2018.

[5] S. Haidari, H. Moradi, and S. M. M. Dehghan, “RF Source Localization Using Obstacles Map and Reflections,” International Journal of Industrial Electronics, Control and Optimization, vol. 4, no. 2, pp. 181-190, 2021.

[6] M. H. Arabsorkhi, H. Zayyani, and M. Korki, “3-D Hybrid RSS-AoA Passive Source Localization with Unknown Path Loss Exponent,” IEEE Sens. Lett., vol. 7, no. 6, pp. 1372-1376, 2023.

[7] R. Garg, A. L. Varna, and M. Wu, “An Efficient Gradient Descent Approach to Secure Localization in Resource Constrained Wireless Sensor Networks,” IEEE Trans. Inf. Forensics Security, vol. 7, no. 2, pp. 717-730, 2012.

[8] Z. Li, W. Trappe, Y. Zhang, and B. Nath, “Robust Statistical Methods for Securing Wireless Localization in Sensor Networks,” in Fourth Int. Symposium Inf. Process. Sensor Netw, pp. 91-98, 2005.

[9] J. Won and E. Bertino, “Robust Sensor Localization Against Known Sensor Position Attacks,” IEEE Trans, Mobile Comput, vol. 18, no. 12, pp. 2954-2967, 2019.

[10] B. Mukhopadhyay, S. Srirangarajan, and S. Kar, “Robust Range-Based Secure Localization in Wireless Sensor Networks,” in IEEE Global Commun. Conf. (GLOBECOM), pp. 1-6, 2018.

[11] B. Mukhopadhyay, S. Srirangarajan, and S. Kar, “RSS-Based Localization in the Presence of Malicious Nodes in Sensor Networks,” IEEE Trans. Instrum. Meas., vol. 70, pp. 1-16, 2021.

[12] S. Marano, V. Matta, P. Willett, and L. Tong, “DOA Estimation Via a Network of Dump Sensors Under the SENMA Parading,” IEEE Signal Process. Lett., vol. 12, no. 10, pp. 709-712, 2005.

[13] S. Marano, V. Matta, P. Willett, and L. Tong, “Support-Based and ML Approaches to DOA Estimation in a Dumb Sensor Network,” IEEE Trans. Signal Process., vol. 54, no. 4. pp. 1563-1567, 2006.

[14] D. Li and Y. H. Hu, “Energy-Based Collaborative Source Localization Using Acoustic Micro-Sensor Array,”' EURASIP J. Appl. Signal Process, pp. 321-337, 2003.

[15] X. Sheng and Y. H. Hu, “Maximum Likelihood Multiple-Source Localization Using Acoustic Energy Measurements with Wireless Sensor Networks,” IEEE Trans. Signal Process., vol. 53, no. 1. pp. 44-53, 2005.

[16] N. Patwari and A. Hero, “Using Proximity and Quantized RSS For Sensor Localization in Wireless Networks,” in Proc. 2nd Int. ACM Workshop Wireless Sens. Netw. Appl., San Diego, CA, USA, pp. 20-29, 2003.

[17] R. Niu and P. K. Varshney, “Target Location Estimation in Sensor Networks with Quantized Data,” IEEE Trans. Signal Process., vol. 54, no. 12, pp. 4519-4528, 2006.

[18] S. Marano, V. Matta, and L. Tong, “Distributed Detection in the Presence of Byzantine Attacks,” IEEE Trans. Signal Process., vol. 7, no. 1, pp. 16-29, 2009.

[19] A. Vempaty, K. Agrawal, H. Chen, and P. K. Varshney, “Adaptive Learning of Byzantines Behavior in Cooperative Spectrum Sensing,” in Proc. IEEE Wireless Commun. Netw. Conf. (WCNC), Cancun, Mexico, pp. 1310-1315, 2011.

[20] O. Kosut and L. Tong, “Distributed Source Coding in the Presence of Byzantine Sensors,” IEEE Trans. Inf. Theory, vol. 54, no. 6, pp. 2550-2565, 2008.

[21] O. Kosut, L. Tong, and D. Tse, “Nonlinear Network Coding is Necessary to Combat General Byzantine Attacks,” in Proc. 47th Ann. Allerton Conj. Commun. Contr. Comput., Urbana, IL, USA, pp. 593-599, 2009,.

[22] K. Agrawal, A. Vempaty, H. Chen, and P. K. Varshney, “Target Localization in Sensor Networks with Quantized Data in the Presence of Byzantine Attacks,” in Proc. Asilomar Conf. Signals, Syst. Comp., Pacific Grove, CA, USA, pp. 1669-1673, 2011.

[23] H. L. V. Trees and K. L. Bell, Bayesian Bounds for Parameter Estimation and Nonlinear Filtering/Tracking, Wiley IEEE press, Hoboken, NJ, USA, 2007.

[24] A. Vempaty, O. Ozdemir, and P. Varshney, “Mitigation of Byzantine Attacks for Target Location Estimation in Wireless Sensor Networks,” in Proc. 46th Ann. Conf. on Inf. Sci. Syst. (CISS), Princeton, NJ, USA, 2012.

[25] A. Vempaty, O. Ozdemir, K. Agrawal, H. Chen, and P. K. Varshney, “Localization in Wireless Sensor Networks Byzantines and Mitigation Techniques,” IEEE Trans. Signal Process., vol. 61, no. 6, pp. 1495-1508, 2013.

[26] X. Mei, H. Wu, J. Xian, and B. Chen, “RSS-Based Byzantine Fault-Tolerant Localization Algorithm Under NLOS Environment,” IEEE Commun. Lett., vol. 25, no. 2, pp. 474-478, 2021.

[27] Q. Wang, Z. Duan, and F. Li, “Semidefinite Programming for Wireless Cooperative Localization Using Biased RSS Measurements,” IEEE Commun. Lett., vol. 26, no. 6, pp. 1278-1282, 2022.

[28] H. C. So and L. Lin, “Linear Least Squares Approach for Accurate Received Signal Strength Based Source Localization,” IEEE Trans. Signal Process., vol. 59, no. 8, pp. 4035-4040, 2011.

[29] S. Kay, Fundamentals of Statistical Signal Processing: Estimation Theory, Prentice Hall, 1993.

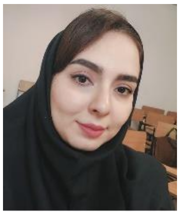

Mahdiye Mohammadi was born in Qom, Iran. She received her B.Sc. degree in Telecommunication Engineering from Qom University, Qom, Iran, in 2022. She is currently pursuing her M.Sc. degree in Telecommunication Systems Engineering at Qom University of Technology, Qom, Iran. Her current research interests include localization in wireless sensor networks and pattern recognition.

Hadi Zayyani received his B.Sc., M.Sc., and Ph.D. degrees in Electrical Engineering, all with a focus on communications, from Sharif University of Technology. Since 2012, he has been a faculty member at Qom University of Technology, where he was promoted to full professor in 2024. He was recognized among the top 2% of scientists worldwide by Stanford University in 2021, 2022, and 2023. Dr. Zayyani has published over 70 journal papers and 35 conference papers, with approximately half appearing in IEEE venues. He serves as an editor for the Iranian Journal of Science and Technology and as a reviewer for several high-impact journals published by IEEE and Elsevier. His research interests include statistical and sparse signal processing, adaptive filtering, radar signal processing, graph signal processing, and distributed signal processing.

Mehdi Bekrani received his B.Sc. degree in Electrical Engineering from Ferdowsi University of Mashhad, Iran, in 2002, and earned his M.Sc. and Ph.D. degrees in Electrical Engineering from Tarbiat Modares University, Tehran, Iran, in 2004 and 2010, respectively. From 2010 to 2012, he was a Research Fellow at Nanyang Technological University, Singapore. He joined the Department of Electrical and Computer Engineering at Qom University of Technology, Qom, Iran, in 2012, and is currently an Associate Professor at the same university. His research interests include acoustic and ultrasonic signal processing, with a focus on source localization, beamforming, channel equalization, and noise cancellation.

IECO

This page intentionally left blank.

International Journal Of
Industrial Electronics Control and Optimization
Print ISSN: 3517-2645
Online ISSN: 3568-2645
Homepage: https://ieco.usb.ac.ir/

A Novel Cascade Control Strategy for Robust Fuel Cell Systems Using Variable Gain Sliding Technique

Violet Farhad[1] | Seyed Mehdi Mirhosseini-Alizamini[2]

Department of Mathematics, Payame Noor University (PNU), Tehran, Iran[1-2]
Corresponding author's email: m_mihosseini@pnu.ac.ir

Article Info

Article type:
Research Article

Article history:
Received: 23-April-2025
Received in revised form: 23-June-2025
Accepted: 18-July-2025

Keywords:
PEM fuel cell,
Oxygen excess ratio,
Variable gain super-twisting algorithm,
Lyapunov stability analysis,
Cascade structure.

ABSTRACT

This paper introduces a new application of variable gain sliding mode control (VGST) to the air supply system of a proton exchange membrane fuel cell (PEMFC), which is crucial for its performance and longevity. The air supply system comprises a centrifugal compressor, a DC-DC converter, and a fuel cell stack, forming a complex and nonlinear system with multiple inputs and outputs. The VGST method adjusts the control gain based on the system state and the sliding level and employs a cascade structure to regulate the excess oxygen ratio and the compressor airflow. The main goals of VGST are to control the PEMFC output voltage and power under various load conditions and uncertainties and to optimize the excess oxygen ratio (λ_{O_2}) to avoid oxygen depletion and membrane damage. The stability and robustness of the proposed controller are verified by Lyapunov theory and its performance is superior compared to other controllers such as variable gain closed-loop control and constant gain sliding mode control (single loop and cascade). The controller is validated by simulation and experimental data and demonstrates that it can enhance the efficiency and reliability of the PEMFC system. The variable gain controller of the cascade structure was also tested under noisy and uncertain conditions to further confirm its desired performance and showed that it could cope well with adverse situations and achieve the control objectives.

I. Introduction

Fuel cells are electrochemical devices that convert the chemical energy of a fuel and an oxidant into electrical energy, with high efficiency and low emissions [1]. Among different types of fuel cells, proton exchange membrane fuel cells (PEMFCs) are widely used for various applications, such as electric vehicles, portable devices, and stationary power generation [2]. However, PEMFCs have some challenges, such as nonlinear dynamics, uncertain parameters, and varying load conditions that affect their performance and durability [3]. Therefore, effective control strategies are needed to regulate the output voltage and power of PEMFCs under different operating scenarios.

A crucial Proton Exchange Membrane Fuel Cell (PEMFC) subsystem is the air-feed system, which supplies pressurized air to the cathode side of the fuel cell stack. This system comprises a centrifugal compressor, a DC-DC converter, and the fuel cell stack, creating a complex nonlinear system with multiple inputs and outputs. Effective management of the air-feed system is essential for maintaining the oxygen excess ratio (λ_{O_2}) at an optimal level, which is a key parameter affecting the performance and lifespan of the PEMFC. The λ_{O_2} is defined as the ratio between the actual and the stoichiometric oxygen flow rates, and it should be kept between 2 and 3 to prevent oxygen starvation and membrane degradation [4]. However, the λ_{O_2} is affected by the load variations, the compressor dynamics, the converter efficiency, and the fuel cell characteristics, which introduce uncertainties, and nonlinearities in the system [5].

In recent years, many control strategies have been proposed to regulate the performance of polymer electrolyte membrane fuel cells, each with its specific objective. These include pressure differential control, compressor motor control, net output power control, and air stoichiometry ratio control, as well as sensor reduction [6], among others. One of the promising control techniques for the air-feed system is sliding mode control (SMC), which is a robust nonlinear control method that can handle uncertainties, disturbances,

Publisher: University of Sistan and Baluchestan

and model mismatch [7]. SMC works by driving the system state to a predefined sliding surface and keeping it there by applying a discontinuous control input. However, SMC has some drawbacks, such as chattering, high control effort, and sensitivity to noise [8]. To address these limitations, Variable Gain Sliding Mode Control (VGSMC) has been introduced. This modified version of SMC adjusts the control gain based on the system state and the sliding surface [9]. To comprehensive study of sliding mode controllers, interested readers may refer to [10-16], to name a few.

In 2012, Gonzalez [17], implemented variable gain control method on spring-mass system by providing a new technique for measuring the noise bounds. They compared three classic Super Twisting Algorithm, variable gain STA and first order sliding mode and after implementation of these systems, they found out that the first order sliding mode control had little chattering and it was significantly decreased by both STA algorithm including the variable gain and the constant gain. Also the result showed that compared to the classic STA, the STA variable gain was able to compensate for the larger class of perturbation and to reduce the chattering in a higher degree. The authors in [5] have presented the management and control strategies of a distributed generation system powered by a PEM fuel cell. The aim of their control strategy is to reduce the current and voltage oscillations of the fuel cell and improve its lifetime. Aguiar et al. have compared two control strategies: one with the direct control of the fuel flow and another with the management of an energy storage system. The experimental results show that the second strategy can achieve better performance and stability. Chen et al. [18] proposed strategies utilizing second-order sliding mode control to achieve improved transient response during rapid stack changes. They introduced a second-order sliding mode control law based on a nonlinear optimization method to mitigate chattering, stabilize excess oxygen levels, and address the optimization problem of net power in fuel cells. The authors also suggested a cascade configuration with a super-twisting algorithm to enhance net power output by maintaining oxygen stoichiometry between 2 and 2.4 and employed a reduced three-state model for controller design.

The adoption of a cascade control architecture (outer loop: oxygen excess ratio λ_{O2}; inner loop: air flow rate) is grounded in recent advancements in fuel cell system optimization. As demonstrated by Kart et al. [19], this hierarchical structure—when integrated with intelligent techniques like fuzzy-PID coordination—reduces steady-state error and accelerates dynamic response under load current step changes, significantly outperforming single-loop configurations. Crucially, the decoupled loop design effectively isolates disturbance propagation: empirical data from Du et al. [20] confirms the superiority of cascade systems in disturbance rejection (e.g., pressure fluctuations, temperature spikes) compared to centralized multivariable controllers. Furthermore, thermodynamic stability analysis by Luo et al. [21] validates that staged control inherently mitigates oscillation risk under aggressive disturbances—addressing instability concerns in our design. This synergy of precision, robustness, and computational efficiency makes cascade control uniquely suited for proton exchange membrane fuel cell (PEMFC) applications. In 2018 [22] and in 2022 [23], Mirrashid et al. have used the VGSMC method to optimize fuel cell system and upper limb rehabilitees robot, achieving desirable results such as robustness against various internal and external disturbances, model uncertainties, and precision in tuning, regulation, and tracking of variables with finite-time convergence. Furthermore, by comparing VGSMC with standard sliding mode strategies, it was found that mechanical stresses are minimized (preventing mechanical wear), and chattering in the output is significantly reduced.

Incremona et al. in 2020 [24] introduces a general framework for the design and tuning of higher order sliding mode controllers with switched and variable gain. The framework can accommodate any order sliding mode controller and both continuous and discrete variation of the controller parameters. The authors have analyzed the properties of the closed-loop system and demonstrate the method on some examples of switched and variable gain higher order sliding mode controllers. In 2021 Ma et al. [25] have presented an adaptive variable gain sliding mode control method for a class of uncertain nonlinear systems. The method can estimate the system uncertainties and adjust the controller gain accordingly. They have proved the finite-time convergence and stability of the proposed method and have showed its superiority over the conventional sliding mode control and the fixed gain sliding mode control.

Tang et al. in 2022 [7] have investigated a cascade control strategy of sliding mode and PID for the air supply system of a PEM fuel cell. The authors have developed an expansion state observer to estimate the cathode pressure and reconstruct the oxygen excess ratio. The simulation results demonstrate that the proposed method has a faster response time and less overshoot than other methods.

Moré et al. [26] have presented the development of multiple input/multiple output sliding mode controllers for a fuel cell-super capacitor module in hybrid generation applications. The objective is to satisfy the demand and regulate the DC bus voltage, even in the presence of model uncertainties and varying operating conditions. The authors have used two design approaches: variable-gains first-order sliding mode and super-twisting second-order sliding mode control. The stability of the nonlinear controlled system is formally analyzed and the performance of the proposed controllers is compared with classic linear PID controllers.

This paper develops a nonlinear dynamic model of a PEM fuel cell. Traditional sliding mode control (SMC) induces chattering and high-frequency switching due to the sign function in the control signal or instability. To resolve this, a high-order sliding mode (HOSM) control is proposed, ensuring stability, robustness, and chattering suppression. While the standard super-twisting algorithm (STA) with fixed gains fails to compensate for severe nonlinearities and large perturbations in the fuel cell system, this work introduces a variable-gain STA (VGST). The VGST adapts gains online to disturbances, reducing chattering while guaranteeing finite-time convergence, robustness, and stability. Crucially, the proposed continuous control law maintains accurate and robust stability under all conditions—unlike discontinuous alternatives. Time-varying gains further accelerate convergence and relax the need for precise perturbation bounds. Stability is proven via a quadratic Lyapunov function, and convergence time is analytically estimated. Beyond these contributions, this work breaks new ground by implementing the variable-gain controller within a cascaded architecture - a novel departure from existing literature. The cascaded implementation demonstrates three key operational advantages: substantial reduction of power fluctuations, enhanced stability against dynamic disturbances, and improved robustness to parametric uncertainties when compared to traditional single-loop configurations. These advancements are particularly valuable for practical fuel cell applications where system reliability and dynamic response are critical.

The rest of the paper is organized as follows. Section 2 is devoted to the dynamic modeling of a fuel cell system. Section 3 deals with a variable gain controller design based on Lyapunov stability and Section 4 is related to the design of the cascaded controller. The simulation results are given in Section 5. Finally, section 6 concludes the paper.

II. The fuel cell system dynamics model

The Fig. 1 shows the structure of the fuel cell system, which consists of the stack and its peripheral equipment. The model used in this study is based on the reference [27], but with some modifications. Instead of using tabular data to describe the relationship between some system states, the model uses continuous equations to interpolate the values between the data points. This eliminates the need for table lookup and simplifies the model. Following RakhtAla & Eini [28] and Tang et al. [29], properly validated continuous interpolation functions can maintain sufficient accuracy while offering computational advantages. Moreover, our choice of pressure over mass as state variables (as suggested by Oladosu et al. [30].) provides direct correlation with measurable quantities in real systems, simplifies physical interpretation, and yields more controller-friendly state equations. The model proposed in this study is a nonlinear dynamic model with six states: $X = [\omega_{cp}, P_{sm}, m_{sm}, P_{O_2}, P_{N_2}, P_{rm}]^T$. The states represent the compressor speed (ω_{cp}), the supply manifold pressure (P_{sm}), the supply manifold mass (m_{sm}), the oxygen partial pressure (P_{O_2}), the nitrogen partial pressure (P_{N_2}), and the return manifold pressure (P_{rm}). The model assumes that the air is composed of only oxygen and nitrogen, with 21% oxygen and 79% nitrogen by volume.

The dynamic model of the fuel cell is a mathematical representation of the behavior of the fuel cell over time, taking into account the physical and chemical processes that occur inside the fuel cell. There are different types of dynamic models for fuel cells, depending on the level of detail, the type of fuel cell, and the purpose of the model. Table 1 presents the states and their definitions for better understanding

Table 1. States and their definitions.

States	Descriptions
$\mathbf{x_1 = \omega_{cp}}$ **(rad/s)**	Motor angular speed
$\mathbf{x_2 = P_{sm}}$ **(atm)**	Supply manifold pressure
$\mathbf{x_3 = m_{sm}}$ **(kg)**	Air mass in the supply manifold
$\mathbf{x_4 = P_{O_2}}$ **(atm)**	Oxygen pressure at cathode side
$\mathbf{x_5 = P_{N_2}}$ **(atm)**	Nitrogen pressure at cathode side
$\mathbf{x_6 = P_{rm}}$ **(atm)**	Return manifold pressure

The dynamic model of the fuel cell considered in the paper is:

$$\dot{x}_1 = \frac{\eta_{cm}}{J_{cp}}\frac{k_t}{R_{cm}}(v_{cm} - k_v x_1) - \frac{C_p}{J_{cp}}\frac{T_{atm}}{\eta_{cp}}(\left(\frac{x_2}{P_{atm}}\right)^{\frac{\gamma-1}{\gamma}} - 1)\frac{W_{cp}}{x_1}, \tag{1}$$

$$\begin{aligned}\dot{x}_2 = \frac{\gamma R_a}{V_{sm}}(&-K_{sm,out}x_2 + K_{sm,out}P_{v,ca} \\ &+K_{sm,out}\frac{x_5}{M_{N2}} + K_{sm,out}\frac{x_4}{M_{O2}})\frac{\gamma x_2}{x_3} \\ &+W_{cp}(T_{atm} + \frac{T_{atm}}{\eta_{cp}}\left(\left(\frac{x_2}{P_{atm}}\right)^{\frac{\gamma-1}{\gamma}} - 1\right),\end{aligned} \tag{2}$$

$$\begin{aligned}\dot{x}_3 = W_{cp} - K_{sm,out}x_2 + K_{sm,out}P_{v,ca} + \\ K_{sm,out}\frac{x_5}{M_{N2}} + K_{sm,out}\frac{x_4}{M_{O2}},\end{aligned} \tag{3}$$

$$\begin{aligned}\dot{x}_4 = &-\frac{x_4}{m_{O2} + m_{N2} + \frac{P_{v,ca}V_{ca}M_v}{R_v T_{st}}} \\ &\times K_{ca,out}\left(-x_6 + P_{v,ca} + \frac{x_5}{M_{N2}} + \frac{x_4}{M_{O2}}\right) \\ &+ y_{O2,in}K_{sm,out}\frac{(R_{O2}T_{st})}{V_{ca}} \\ &\times\left(x_2 - \frac{x_4}{M_{O2}} - P_{v,ca} - \frac{x_5}{M_{N2}}\right) \\ &-n\frac{(R_{O2}T_{st})}{V_{ca}}\frac{M_{O2}}{4\ F}I_{st},\end{aligned} \tag{4}$$

$$\begin{aligned}\dot{x}_5 = &(1 - X_{O_2})(1 + \Omega_{atm})^{-1}K_{sm,out} \\ &\times\frac{R_{N2}T_{st}}{V_{ca}}(x_2 - \frac{x_4}{M_{O2}} - \frac{x_5}{M_{N2}} - P_{v,ca}) \\ &-\frac{x_5}{m_{O2} + m_{N2} + \frac{P_{v,ca}V_{ca}M_v}{R_v T_{st}}}K_{ca,out} \\ &\times\left(-x_6 + \frac{x_4}{M_{O2}} + \frac{x_5}{M_{N2}} + P_{v,ca}\right),\end{aligned} \tag{5}$$

$$\dot{x}_6 = \frac{R_a T_{rm}}{V_{rm}} \times \left(K_{ca,out}\left(\frac{x_4}{M_{O2}} + \frac{x_5}{M_{N2}} + P_{v,ca} - x_6\right) - \left(P_{a_6}x_6^5 + P_{a_5}x_6^4 + P_{a_4}x_6^3 + P_{a_3}x_6^2 + P_{a_2}x_6 + P_{a_1}\right)\right). \tag{6}$$

The model uses the compressor motor voltage ($u=V_{cm}$ (V)) as the input control variable, and the fuel cell stack current ($d=I_{st}$ (A)) as the measured disturbance variable. The model parameters are given in Appendix A. The compressor air flow rate (W_{cp}) is a function of x_1, and x_2 [27].

The output voltage of the fuel cell depends on the stack current, the partial pressure of the reactants, the temperature of the fuel cell, and the humidity of the membrane. The output voltage is lower than the standard potential of the fuel cell due to various losses, such as ohmic losses, activation losses, and concentration losses. These losses are nonlinear functions of the fuel cell current, temperature, pressure, and chemical reactions. The thermodynamic potential, E, is given by the Nernst equation in its extended form.

$$E = N\left(E_0 + \frac{R\,T}{2\,F}\left\{\frac{P_{H2}\left(\frac{P_{O2}}{P_{OP}}\right)^{\frac{0}{5}}}{P_{H_2O_C}}\right\}\right) \tag{7}$$

So, it can be written:

$$v_{cell} = E - v_{act} - v_{ohm} - v_{conc}\,, \tag{8}$$

$$v_{stack} = N\ v_{cell}\,, \tag{9}$$

$$P_{net} = P_{Stack} - P_{auxiliary}. \tag{10}$$

where symbols and parameters are given in Appendix A. Eq. (12) shows that the requested current (I_{st}) depends on the air flow $W_{o2,reacted}$, which causes a significant decrease in λ_{O_2}. As λ_{O_2} increases, the partial pressure of oxygen and the stack voltage (P_{st}) also increase. However, increasing λ_{O_2} also increases the compressor power demand and the losses. Therefore, the inlet air flow needs to be regulated and adjusted to match λ_{O_2} with the load variations. This is the main objective of the control system design.

$$\lambda_{O_2} = \frac{\text{Oxygen Supplied}}{\text{Oxygen reacted}} = \frac{W_{O2,in}}{W_{o2,reacted}}, \tag{11}$$

where

$$W_{o2,reacted} = M_{o2}\frac{n.\,I_{st}}{4.\,F}, \tag{12}$$

$$W_{O2,in} = X_{O_2,in}\frac{1}{(1+\Omega_{atm})}K_{sm,out} \times \left(x_2 - \frac{x_4}{M_{O2}}\frac{R_{O2}T_{st}}{V_{ca}} - \frac{x_5}{M_{N2}}\frac{R_{N2}T_{st}}{V_{ca}} - P_{v,ca}\right). \tag{13}$$

The polarization curve shows how the voltage and current of a fuel cell are related. The model of the polarization curve includes the ideal voltage and the different voltage drops in the fuel cell. The voltage drops are caused by activation, ohmic, and concentration effects. Fig. 2 illustrates how the fuel cell voltage decreases as the current increases because of these effects. (N_{cell}=260).

III. Lyapunov-Based Design of Variable Gain Super Twisting Algorithm for PEM Fuel Cell

This section proposes a Lyapunov function for designing a variable gain super twisting algorithm for PEM fuel cell. This design can be applied to the system with relative degree one. The oxygen excess ratio in the closed loop system converges in finite time, even with model uncertainty. The adaptive controller gains ensure robust regulation of the oxygen excess ratio despite severe uncertainty. The control signal is smooth and continuous, and the convergence time is bounded.

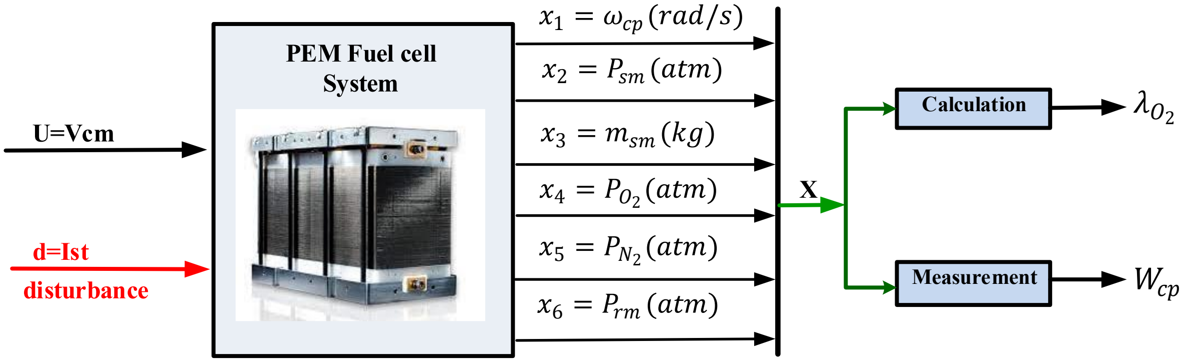

Fig. 1. Block diagram of the fuel cell system with state representation.

where x and $u = v_{cm}$ are the system states and control input, respectively, f and g are the unknown functions, and $d(t) = I_{st}$ indicates external perturbation and uncertainty of system parameters.

Before presenting the main finding of the paper, the following concept must be defined.

Definition 1. The sliding surfaces $s_1(t)$ and $s_2(t)$ are functions of the errors, $e_1(t)$, and $e_2(t)$, which $e_1(t)$ and $e_2(t)$ are the deviations of oxygen stoichiometry and compressor air flow from their desired value, respectively. The sliding surface $s_1(t)$ can be expressed as:

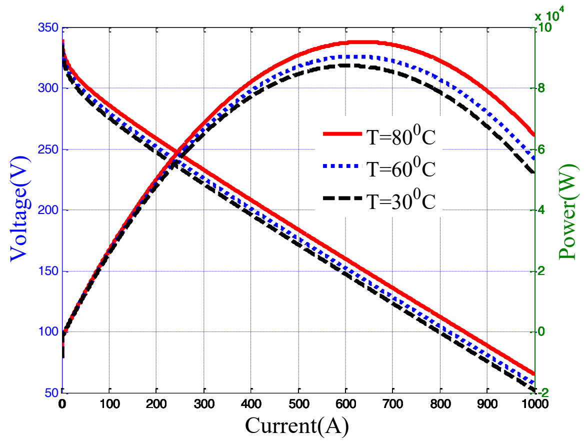

Fig. 2. Fuel cell characteristics for various values of temperature.

A dynamic model of the system can be expressed as follows:

$$\dot{x}=\begin{bmatrix}\dot{x}_1\\ \dot{x}_2\\ \dot{x}_3\\ \dot{x}_4\\ \dot{x}_5\\ \dot{x}_6\end{bmatrix}=f(x,t)+g(x,t)u+\varphi(x,t)d(t)\,, \tag{14}$$

with

$$\mathrm{f(x,t)}=\begin{bmatrix}\mathrm{f_1(x_1\,,x_2)}\\ \mathrm{f_2(x_1\,,x_2,x_3,x_4,x_5)}\\ \mathrm{f_3(x_2,x_4,x_5)}\\ \mathrm{f_4(x_2,x_4,x_5,x_6)}\\ \mathrm{f_5(x_2,x_4,x_5,x_6)}\\ \mathrm{f_6(x_4,x_5,x_6)}\end{bmatrix}, \tag{15}$$

$$\mathrm{g(x,t)}=\begin{bmatrix}\eta_{\mathrm{cm}}\dfrac{\mathrm{k_t}}{\mathrm{J_{cp}R_{cm}}}\\ 0\\ 0\\ 0\\ 0\\ 0\end{bmatrix},$$

$$\varphi(\mathrm{x,t})=\begin{bmatrix}0\\ 0\\ 0\\ -\mathrm{n}\dfrac{\mathrm{M_{O2}}}{4\ \mathrm{F}}\times\dfrac{\mathrm{R_{O_2}\ T_{st}}}{\mathrm{V_{ca}}}\\ 0\\ 0\end{bmatrix}, \tag{16}$$

$$s_1(t)=\lambda_{\mathrm{O_2}}-\lambda_{\mathrm{O_{2,ref}}}\,.$$

Thus, the derivate of s_1 is:

$$\dot{s_1}(t)=\dot{\lambda}_{\mathrm{O_2}}-\dot{\lambda}_{\mathrm{O}_{2,ref}}\ \rightarrow\dot{s_1}(t)=\dot{\lambda}_{\mathrm{O_2}}\,, \tag{17}$$

where:

$$\dot{\lambda}_{\mathrm{O_2}}=\frac{X_{O_{2,in}}\dfrac{1}{1+\Omega_{atm}}.K_{SM,OUT}}{\dfrac{\mathrm{nM_{O_2}}}{\mathrm{4F}}\mathrm{I_{st}}}\left[\dot{\mathrm{x}}_2-\frac{\dot{\mathrm{x}}_4}{\mathrm{M_{O_2}}}-\frac{\dot{\mathrm{x}}_5}{\mathrm{M_{N_2}}}\right] \tag{18}$$

$$=\mathrm{A}\,\frac{\gamma\,\mathrm{R_a\,T_{atm}}}{\mathrm{V_{sm}}}\left[1+\left(\left(\frac{\mathrm{x_2}}{\mathrm{P_{atm}}}\right)^4-1\right)\mathrm{n_{cp}^{-1}}\right]\mathrm{W_{cp}}$$

$$+A\left[\frac{\gamma x_2}{x_3}(-x_2B_{12}+B_{13}+B_{14}x_5+B_{15}x_4)-\frac{\dot{x_4}}{m_{O_2}}-\frac{\dot{x_5}}{m_{n_2}}\right],$$

in which:

$$A=\frac{X_{O_{2,in}}\frac{1}{1+\Omega_{atm}}.K_{SM,OUT}}{\frac{\mathrm{nM_{O_2}}}{\mathrm{4F}}\mathrm{I_{st}}}\,, \tag{19}$$

The sliding surface $s_2(t)$ can be expressed as:

$$s_2(t)=\mathrm{W_{cp}}-\mathrm{W_{cp,ref}}\,.$$

We can write the derivative of s_2 as:

$$\dot{s_2}(t)=\dot{\mathrm{W}}_{\mathrm{cp}}-\dot{\mathrm{W}}_{\mathrm{cp,ref}}\ \rightarrow$$

$$\dot{s_2}(t)=[\mathrm{B_{10}+B_{11}x_{02}+2B_{02}x_1}]\dot{\mathrm{x}}_1+[\mathrm{B_{10}+2B_{20}x_2+B_{11}x_1}]\dot{\mathrm{x}}_2-\dot{\mathrm{W}}_{\mathrm{cp,ref}}\,. \tag{20}$$

By substituting the relation $\dot{\mathrm{x}}_1$ (Eq. (1)) in Eq. (20), and considering $D=[B_{10}+B_{11}x_{02}+2B_{02}x_1]$, we have:

$$\dot{s_2}(t)=\mathrm{D\times B_1K_tV_{cm}}+[\mathrm{B_{10}+2B_{20}x_2+B_{11}x_1}]\dot{\mathrm{x}_2}+\mathrm{D}\left(-\left[\frac{\mathrm{c_p\times T_{atm}}}{\mathrm{n_{cp}\times J_{cp}\times x_1}}\times\mathrm{W_{cp}}\times\left(\left(\frac{\mathrm{x_2}}{\mathrm{P_{atm}}}\right)^{\mathrm{B_4}}-1\right)\right]+(-\mathrm{B_2x_1k_t})\right)-\dot{\mathrm{W}}_{\mathrm{cp,ref}}\,. \tag{21}$$

A. Super twisting algorithm sliding mode controller (ST)

Definition 2. The sliding surface $s_2(t)$ by considering the error as $e=\mathrm{W_{cp}}-\mathrm{W_{cp,ref}}$ can be defined as follows:

$$s_2(t)=\lambda\,e+\dot{e}=\lambda(\mathrm{W_{cp}}-\mathrm{W_{cp,ref}})+(\dot{\mathrm{W}}_{\mathrm{cp}}-\dot{\mathrm{W}}_{\mathrm{cp,ref}})\,,$$

where λ is a positive constant.

Theorem 1. If we consider the following control law,

$$\mathrm{u=u_1+u_2} \tag{22}$$

where

$$\begin{aligned}\mathrm{u_1}&=-\mathrm{k_1}\phi_1(\mathrm{s})+\rho_1(\mathrm{t,x})\,,\\ \dot{\mathrm{u}}_2&=-\mathrm{k_2}\phi_2(\mathrm{s})+\rho_2(\mathrm{t,x})\,,\end{aligned} \tag{23}$$

then the Lyapunov function $L(s)=v^TP\,v$ is strong and robust, and the origin is exactly robust, in which $\mathrm{k_1}$, and $\mathrm{k_2}$ are constant gains.

Proof. The first derivative of ST surface is:

$$\dot{\mathrm{s}}(\mathrm{t,x,u})=\frac{\partial}{\partial\mathrm{t}}\mathrm{s(t,x)}+\frac{\partial}{\partial\mathrm{x}}[\mathrm{s(t,x)}][\mathrm{f(x)+g(x)u}]\,, \tag{24}$$

Taking the second derivative of ST surface results in

$$\ddot{\mathrm{s}}(\mathrm{t,x,u})=\tfrac{\partial}{\partial\mathrm{t}}\dot{\mathrm{s}}(\mathrm{t,x,u})+\tfrac{\partial}{\partial\mathrm{x}}[\dot{\mathrm{s}}(\mathrm{t,x,u})][\mathrm{f(x)+g(x)u}]+\tfrac{\partial}{\partial\mathrm{u}}\dot{\mathrm{s}}(\mathrm{t,x,u})\dot{\mathrm{u}}=\varphi(\mathrm{t,x,u})+\emptyset(\mathrm{t,x,u})\dot{\mathrm{u}}\,,$$

where

$$\varphi(t,x,u)=\left[\frac{\partial \dot{s}}{\partial x_1}\ \frac{\partial \dot{s}}{\partial x_2}\frac{\partial \dot{s}}{\partial x_3}\frac{\partial \dot{s}}{\partial x_4}\frac{\partial \dot{s}}{\partial x_5}\frac{\partial \dot{s}}{\partial x_6}\right]\times\left(f(x)+g(x)u\right), \tag{25}$$

$$\emptyset(t,x,u)=\frac{\partial}{\partial u}\dot{s}(t,x,u).$$

Thus

$$\dot{s}=\phi_2(t,x)+\gamma_2(t,x)u-\dot{W}_{cp,ref}.$$

By considering Eq. (25), One can write:

$$\emptyset(t,x,u)=\frac{\partial}{\partial u}\dot{s}(t,x,u)=\gamma_2(t,x)=D\times B_1K_1,$$

$$\varphi(t,x,u)=\frac{\partial \dot{s}}{\partial x_1}\dot{x}_1+\frac{\partial \dot{s}}{\partial x_2}\dot{x}_2+\frac{\partial \dot{s}}{\partial x_3}\dot{x}_3+\frac{\partial \dot{s}}{\partial x_4}\dot{x}_4+\frac{\partial \dot{s}}{\partial x_5}\dot{x}_5+\frac{\partial \dot{s}}{\partial x_6}\dot{x}_6.$$

We can write Lyapunov's function as a quadratic form:

$$L(s)=v^TP\,v,$$

with

$$A^TP+PA=-Q,$$

where $v^T=\Phi^T(s)=[\phi_1(s),u_2]$, in which $\phi_1(s)=|s|^{\frac{1}{2}}sign(s)$, $\phi_2(s)=sign(s)$, P is a symmetric matrix that is positive definite and unique, $A=\begin{bmatrix}-k_1 & 1\\ -k_2 & 0\end{bmatrix}$ and $Q=Q^T>0$ is a positive definite matrix that is equal to its transpose. The controller coefficients have to satisfy the following condition [22] to guarantee finite-time convergence and Lyapunov stability:

$$k_1^2\geq\frac{4\ g\ d_M(k_2+g)}{d_m^3(k_2-g)},\ k_2>\frac{g}{d_m}, \tag{26}$$

where for all $u\in U$ and, $x\in X$:we have , $|\frac{\delta}{\delta x}s|\leq g$, $0<d_m<\frac{\delta}{\delta x}\dot{s}<d_M$.

Fig. 3 shows the super twisting controller (ST) block diagram.

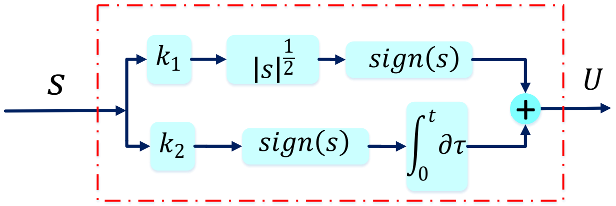

Fig. 3. Block diagram of the ST controller.

A. Variable gain super twisting sliding mode controller

The following expression [31] shows the VGST adaptive control law:

$$u=u_1+u_2, \tag{27}$$

with

$$u_1=-k_1(t)\phi_1(s)+\rho_1(t,x),$$
$$\dot{u}_2=-k_2(t)\phi_2(s)+\rho_2(t,x),$$

where $k_1(t)$, and $k_2(t)$ are variable adaptive gains, $\rho_1(t,x)$ and $\rho_2(t,x)$ are perturbations, and $\phi_1(s)=|s|^{\frac{1}{2}}sign(s)$, $\phi_2(s)=sign(s)$. We assume that the perturbations are limited, and they follow these equations:

$$\begin{aligned}\rho_1(t,x)&=r_1(t,x)\phi_1(s),\\ &|r_1(t,x)|\leq|c_1(t,x)|,\\ \rho_2(t,x)&=r_2(t,x)\phi_2(s),\\ &|r_2(t,x)|\leq|c_2(t,x)|,\end{aligned} \tag{28}$$

where $c_1(t,x)\geq 0$, $c_2(t,x)\geq 0$ are continuous functions that are known. Using Lyapunov stability analysis, we derive the gains of the VGST controller in the next theorem.

Theorem 2. Let the gains of the control law Eq. (27) with the perturbation conditions Eq. (28) be

$$k_1(t,x,s)=\delta+\frac{1}{\beta}\left\{\frac{1}{4\eta}[2\eta c_1+c_2]^2+2\eta c_2+\eta+[2\eta+c_1(t,x)](\beta+4\eta^2)\right\}, \tag{29}$$

$$k_2(t,x,s)=\beta+4\eta^2+2\eta k_1(t,x,s).$$

Then:

a) The Lyapunov function $L(s)=v^TP\,v$ is strong and robust, and the origin is exactly robust, where $v^T=\Phi^T(s)=[\phi_1(s),u_2]$, and P is a unique positive definite symmetric matrix.

b) The sliding surface s(t) tends to the origin in the following finite time T:

$$T=\frac{2}{\vartheta_1}L^{\frac{1}{2}}(0) \tag{30}$$

Proof.

a) Let's look at the following quadratic Lyapunov function:

$$\begin{aligned}&L(s)=v^TP\,v,\\ &A^TP+PA=-Q,\end{aligned} \tag{31}$$

where $A=\begin{bmatrix}-k_1 & 1\\ -k_2 & 0\end{bmatrix}$ and $Q=Q^T>0$ is a symmetric positive definite matrix.

One can write $\phi_2(s)=\phi'_1(s)\phi_1(s)$, and $\phi'_1(s)=\frac{1}{2}|s|^{-\frac{1}{2}}$. Thus

$$\dot{v}=\begin{bmatrix}\phi'_1(s)\{-k_1\ \phi_1(s)+s\}\\ -k_2\ \phi_2(s)\end{bmatrix}=\phi'_1(s)\begin{bmatrix}-k_1, 1\\ -k_2, 0\end{bmatrix}v=\phi'_1(s)\,A\,v,$$

The derivative of the Lyapunov function is:

$$\dot{L}(s)=\dot{v}^TPv+v^TP\dot{v}=\phi'_1(s)v^T(A^TP+PA)v=-\phi'_1(s)v^TQv \tag{32}$$

where Q can be obtained from the equation ALE Eq. (31). From [31], one obtain:

$$|\rho_1(t,x)|\leq k_c|s|^{\frac{1}{2}}c_1(t,x), \tag{33}$$

$$\left|\frac{d}{dt}\rho_2(t,x)\right|\leq\frac{{k_c}^2}{2}c_2(t,x). \tag{34}$$

From Eq. (31), we can write:

$$Q(t,x)=\begin{bmatrix}2\big(k_1(t,)-r_1(t,x)\big)p_1 & * \\ +2\big(k_2(t,x)-r_2(t,x)\big)p_3 & \\ \big(k_1(t,x)-r_1(t,x)\big)p_3 & -2p_3 \\ +\big(k_2(t,x)-r_2(t,x)\big)p_2-p_1 & \end{bmatrix},$$

where * denotes the transpose of the corresponding element below the main diagonal of the matrix Q(t,x). Now, if we consider

$$P=\begin{bmatrix}p_1 & p_3\\ p_3 & p_2\end{bmatrix}=\begin{bmatrix}\beta+4\eta^2 & -2\eta\\ -2\eta & 1\end{bmatrix},$$

then, by substituting p_1, p_2, and p_3 in $Q(t,x)$ and setting $k_2=2\eta k_1+\beta+4\eta^2$.

We have

$$Q-2\eta I=\begin{bmatrix}2\beta k_1+4\eta(2\eta k_1-k_2) & * \\ -2(\beta+4\eta^2)r_1+4\eta r_2-2\eta & \\ k_2-2\eta k_1-(\beta+4\eta^2)+2\eta r_1 & 2\eta\end{bmatrix}$$
$$=\begin{bmatrix}2\beta k_1-(\beta+4\eta^2)(4\eta+2r_1) & * \\ +4\eta r_2-2\eta & \\ 2\eta r_1-r_2 & 2\eta\end{bmatrix},$$

The Q-matrix is positive for all values of (t, x) if:

$$k_1>\frac{2\eta r_2+(\beta+4\eta^2)(2\eta+r_1)+\eta}{\beta}.$$

Now, we need to show that $\dot{L}(s)$ is negative definite. We know that

$$\lambda_{\min}\{P\}\|v\|_2^2\le v^{T}Pv\le\lambda_{\max}\{P\}\|v\|_2^2,$$

where $\|v\|_2^2=\phi_1^2(s)+u_2^2=|s|+u_2^2$, and note that the inequality $|s|^{-\frac{1}{2}}\le|\phi_1(s)|\le\|v\|_2\le\frac{L^{\frac{1}{2}}(s)}{\lambda_{\min}^{\frac{1}{2}}\{P\}}$ holds.

Therefore, $-|s|^{-\frac{1}{2}}\le-\frac{L^{\frac{1}{2}}(s)}{\lambda_{\min}^{\frac{1}{2}}\{P\}}$. Consequently

$$\begin{aligned}\dot{L}(s)&=-\phi'_1(s)v^{T}Q(t,x)v\le-2\eta\phi'_1(s)v^{T}v\\ &\le-\vartheta L^{\frac{1}{2}},\end{aligned}\tag{35}$$

where

$$\vartheta=\frac{\eta\left(\lambda_{\min}^{\frac{1}{2}}\{P\}\right)^{-1}}{\lambda_{\max}\{P\}}.$$

b) Solving the following differential equation gives the convergence time T:

$$\dot{L}(s)=-\vartheta L^{\frac{1}{2}},\quad L(0)=L_0\ge0.$$

So, we have

$$L(t)=\left(L_0^{\frac{1}{2}}-\frac{1}{2}\vartheta t\right)^2\quad\text{if}\ \ \gamma>0.$$

As a result, all system trajectories of Eq. (27) converge in finite time for all perturbations with the following convergence time T:

$$T=\frac{2}{\gamma_1}L^{\frac{1}{2}}(0).$$

Therefore L decreases uniformly and has a stable asymptotic origin. This means that L is a strong Lyapunov function.

To ensure finite-time convergence and to establish Lyapunov stability conditions, the controller coefficients have to be determined as follows [22]:

$$\begin{aligned}k_1(t,x,s)=\delta+\frac{1}{\beta}\Big\{&\frac{1}{4\eta}[2\eta c_1+c_2]^2+2\eta c_2\\ &+\eta\\ &+[2\eta+c_1(t,x)](\beta+4\eta^2)\Big\}\end{aligned}\tag{36}$$

$$k_2(t,x,s)=\beta+4\eta^2+2\eta k_1(t,x,s),$$

where β> 0, η> 0 , and δ> 0 are arbitrary positive constants. This completes the proof.

Fig. 4 depicts the variable gain super twisting controller (VGST) controller block diagram.

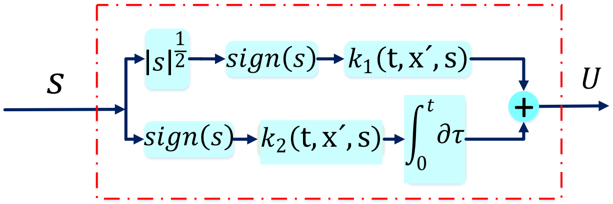

Fig. 4. Block diagram of the VGST controller.

IV. Robust cascade control of fuel cell systems using variable gain sliding mode

Eqs. 1-6. describe the dynamics of the simplified system. A cascade structure is designed using the second order sliding mode control technique, which is shown in the block diagram in Fig. 5. This control method is robust to disturbances and parametric uncertainties.

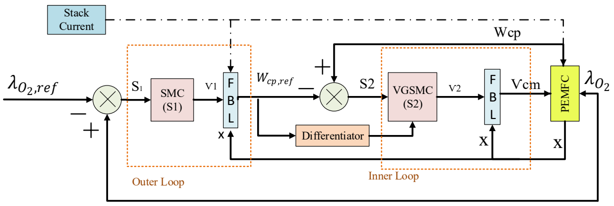

Fig. 5. Schematic of control system with cascade structure.

The control goal is to keep the excess oxygen (λ_{O_2}) at 2.5. The control system has two loops: External loop and internal loop. The External loop uses a second-order sliding mode controller (2-SMC) with a fixed gain super twisting algorithm to control the excess oxygen ratio, which has the excess oxygen error as the input. The controller output, $W_{cp,ref}$, is the target air flow for the compressor. The internal loop uses a feedback controller and variable gain super twisting algorithm to control the compressor air flow, which produces the compressor motor voltage, V_{cm}, to be applied to the fuel cell. Two sliding surfaces are selected to guide λ_{O_2} and W_{cp} to their target values, $\lambda_{O_{2,ref}}$, and $W_{cp,ref}$.

A. External loop

The sliding surface of external loop is defined as follows:

$$s_1(t)=\lambda_{O_2}-\lambda_{O_{2,ref}}.$$

Another way to write Equation (18) is:

$$\dot{s_1} = \dot{\lambda}_{O_2} = \gamma_1 W_{cp} + \phi_1 \,, \tag{37}$$

where

$$\begin{aligned} \phi_1(t,x) = A \Bigg[\frac{\gamma x_2}{x_3} (-x_2 B_{12} + B_{13} + B_{14} x_5 \\ + B_{15} x_4) - \frac{\dot{x_4}}{m_{O_2}} - \frac{\dot{x_5}}{m_{n_2}} \Bigg], \\ \gamma_1(t,x) = A \frac{\gamma\, R_a\, T_{atm}}{V_{sm}} \Bigg[1 \\ + \left(\left(\frac{x_2}{P_{atm}} \right)^4 - 1 \right) n_{cp}^{-1} \Bigg] \,. \end{aligned} \tag{38}$$

Using linearization feedback technique, we will have:

$$W_{cp,ref} = \gamma_1(t,x)^{-1} \big(v_1 - \phi_1(t,x) \big) \,, \tag{39}$$

v_1 results to integral $\dot{s_1} = v_1$ which is designed to stabilize this new system.

$$\begin{aligned} & v_1 = v_{11} + v_{12} \,, \\ & \dot{v_{11}} = -\beta_1 \mathrm{sign}(s_1) \,, \\ & v_{12} = -\alpha_1 |s_1|^{\frac{1}{2}} \mathrm{sign}(s_1) \,, \\ & \alpha_1 = -0.5 \ ; \ \beta_1 = 0.5 \,. \end{aligned} \tag{40}$$

α_1, and β_1 are obtained according to the described terms in Eq. (26). For this purpose, the limits of the maximum and minimum values of $\phi_1(t,x)$, $\gamma_1(t,x)$ were obtained by programming with MATLAB based on the limits of system state changes.

B. Internal Loop

The sliding surface $s_2(t)$ can be expressed as:

$s_2(t) = W_{cp} - W_{cp,ref}$.

Another way to write Eq. (20) is:

$$\dot{s_2} = \phi_2(t,x) + \gamma_2(t,x) v_{cm} - \dot{W}_{cp,ref} \,. \tag{41}$$

where

$$\begin{aligned} & \gamma_2(t,x) = \frac{\partial s}{\partial v_{cm}} = D \times B_1 K_1 \\ & \phi_2(t,x) = \frac{\partial s}{\partial x_2} \dot{x}_2 + \frac{\partial s}{\partial x_1} \dot{x}_1 = \\ & D \left(- \left[\frac{c_p \times T_{atm}}{n_{cp} \times J_{cp} \times x_1} W_{cp} \left(\left(\frac{x_2}{P_{atm}} \right)^{B_4} - 1 \right) \right] + \right. \\ & \left. (-B_2 x_1 k_t) \right) + [B_{10} + 2B_{20} x_2 + B_{11} x_1] \dot{x_2} \,. \end{aligned} \tag{42}$$

Using linearization feedback technique:

$$v_{cm} = \gamma_2(t,x)^{-1} \big(v_2 - \phi_2\,(t,x) + \dot{W}_{cp,ref} \big) \,, \tag{43}$$

where v_2 results to an integrator $\dot{s_2} = v_2$ which is designed to stabilize this new system. V_2 equal to u in Eq. (27).

For obtained perturbation bounds and so v_2, we need to define the sliding variable as a new variable. So, the S variable becomes part of the new set of variables as follows:

$$s_2(t) = W_{cp} - W_{cp,ref} \tag{44}$$

This implies:

$$\begin{aligned} s_2 = B_{00} + B_{10}(x_2) + B_{20} x_2^2 + B_{10} x_1 \\ + B_{11} x_2 x_1 + B_{02} x_1^2 \\ - W_{cp,ref} \end{aligned} \tag{45}$$

Therefore, we can compute the new value of x_1 as follows:

$$\begin{aligned} -s_2 + B_{00} + B_{10}(x_2) + B_{20} x_2^2 + B_{10} x_1 + \\ B_{11} x_2 x_1 + B_{02} x_1^2 - W_{cp,ref} = 0 \end{aligned} \tag{46}$$

As a result:

$$\begin{aligned} & x_1 = \frac{-(B_{11} x_2 + B_{10})}{2\, B_{02}} \mp \\ & \frac{\sqrt{(B_{11} x_2 + B_{10})^2 + 4 B_{02} (s_2 + W_{cp,ref} - B_{00} - B_{10} x_2 - B_{20} {x_2}^2)}}{2\, B_{02}} \end{aligned} \tag{47}$$

Now, we have a new set of conditions for $x_{new} = \{x_2, x_3, x_4, x_5, x_6\}$. Let $x_1 = a(t, x_{new}, s) = B_{106}\, x_2 - B_{107} \mp \sqrt{B_{104}\, {x_2}^2 + B_{103}\, x_2 + B_{105} + \frac{s_2 + W_{cp,ref}}{B_{02}}}$, now, with substitute the value of $\dot{x_1}$ in the Eq. (21) we have:

$$\begin{aligned} \dot{W}_{cp} = [B_{10} + B_{11} x_{02} + 2B_{02} a(t, x_{new}, s)] \dot{x}_1 \\ + [B_{10} + 2B_{20} x_2 \\ + B_{11} a(t, x_{new}, s)] \dot{x}_2 \end{aligned} \tag{48}$$

Let $D = [B_{10} + B_{11} x_2 + 2B_{02} a(t, x_{new}, s)]$ and substitute the value of $\dot{x_1}$ in the following:

$$\begin{aligned} & \dot{W}_{cp} = D \times B_1 K_1 V_{cm} \\ & +D \left(- \left[\frac{c_p \times T_{atm}}{n_{cp} \times J_{cp} \times a(t, x_{new}, s)} \times W_{cp} \times \right. \right. \\ & \left. \left. \left(\left(\frac{x_2}{P_{atm}} \right)^{B_4} - 1 \right) \right] + (-B_2 a(t, x_{new}, s) k_t) \right) + \\ & [B_{10} + 2B_{20} x_2 + B_{11} a(t, x_{new}, s)] \dot{x_2} \,. \end{aligned} \tag{49}$$

This results in:

$$\dot{s}_2 = f_s(t, x_{new}, s) + g_s(x_{new}, s) V_{cm} \,, \tag{50}$$

where

$$\begin{aligned} & g_s(x_{new}, s) = \frac{\partial s}{\partial v_{cm}} = D \times B_1 K_1 \\ & f_s(t, x_{new}, s) = \frac{\partial s}{\partial x_2} \dot{x}_2 + \frac{\partial s}{\partial x_1} \dot{x}_1 = \\ & D \left(- \left[\frac{c_p \times T_{atm}}{n_{cp} \times J_{cp} \times a(t, x_{new}, s)} W_{cp} \left(\left(\frac{x_2}{P_{atm}} \right)^{B_4} - 1 \right) \right] + \right. \\ & \left. (-B_2 a(t, x_{new}, s) k_t) \right) + [B_{10} + \\ & 2B_{20} x_2 + B_{11} a(t, x_{new}, s)] \dot{x_2} - \dot{W}_{cp,ref} \,. \end{aligned}$$

To find the boundaries, we extract the functions $\rho_1(x\,)$ and $\rho_2(x)$ as follows:

$$\begin{aligned} & \dot{s} = f_s(t, x_{new}, s) + u \\ & = \underbrace{f_s(t, x_{new}, 0)}_{\rho_2(t, x_{new})} \\ & + \underbrace{[f_s(t, x_{new}, s) - f_s(t, x_{new}, 0)]}_{\rho_1(t, x_{new}, s)} + u \,, \end{aligned} \tag{51}$$

$$\begin{aligned} & \rho_1(t, x_{new}, s) = \\ & D(t, x_{new}, s) \left(- \left[\frac{c_p \times T_{atm}}{n_{cp} \times J_{cp} \times h} W_{cp} \left(\left(\frac{x_2}{P_{atm}} \right)^{B_4} - \right. \right. \right. \\ & \left. \left. \left. 1 \right) \right] + (-B_2 a(t, x_{new}, s) k_t) \right) + [B_{10} + \\ & 2B_{20} x_2 + B_{11} a(t, x_{new}, s)] \dot{x_2} - \dot{W}_{cp,ref} - \\ & \rho_2(x_{new}, t) \,, \end{aligned} \tag{52}$$

$$\begin{aligned}&\rho_2(x_{new},\mathrm{t})\\&=\mathrm{D}(\mathrm{t},x_{new},0)\left(-\left[\frac{\mathrm{c_p}\times \mathrm{T_{atm}}}{\mathrm{n_{cp}}\times \mathrm{J_{cp}}\times \mathrm{h}}\,\mathrm{W_{cp}}\left(\left(\frac{\mathrm{x_2}}{\mathrm{P_{atm}}}\right)^{\mathrm{B_4}}\right.\right.\right.\\&\left.\left.\left.-1\right)\right]+(-\mathrm{B_2}a(\mathrm{t},x_{new},0)\mathrm{k_t})\right)\\&+[\mathrm{B_{10}}+2\mathrm{B_{20}x_2}+\mathrm{B_{11}h}(\mathrm{t},x_{new},0)]\dot{\mathrm{x}}_2-\dot{\mathrm{W}}_{\mathrm{cp,ref}}\end{aligned} \tag{53}$$

Then, we obtain $\dot{\rho}_2$ and ρ_1 from the extension of Eq. (51), and we can calculate $c_2(t,x)$, $c_1(t,x)$. Due to the complexity of the equations, these calculations were done by MATLAB software. The proposed control scheme integrates a high-precision robust differentiator for real-time estimation of $\dot{W}_{cp,ref}$Error! Bookmark not defined. [32]. The differentiator implements the following second-order sliding mode algorithm:

$$\begin{cases}\dot{z}_0=-\gamma_1 L^{\frac{1}{2}}|z_0-s|^{\frac{1}{2}}\mathrm{sign}(z_0-s)+z_1\\ \dot{z}_1=-\gamma_1 L\,\mathrm{sign}(z_1-\dot{z}_0)\end{cases} \tag{54}$$

where z_0 is finite-time convergent estimate, z_1 is derivative estimate, γ = [1.10, 1.5] are the fixed gain parameters per [32], and $L > |\ddot{W}_{cp,ref}|$ is the sole tuning parameter (bounded acceleration condition).

V. Results and Discussions

Fig. 6 displays the stack current that acts as a disturbance to the system.

The simulation of the model has been done and then the net power output (P_{net}), the excess oxygen ratio λ_{O_2}, and the compressor flow ratio (W_{cp}) values have been calculated using the equations of the previous section. We used the difference between W_{cp} and $W_{cp,ref}$ as the sliding surface for the controller input. Finally, we obtained the k_1, and k_2 gains and the control system input based on the relations mentioned above. Fig. 7 shows the corresponding simulation in MATLAB environment:

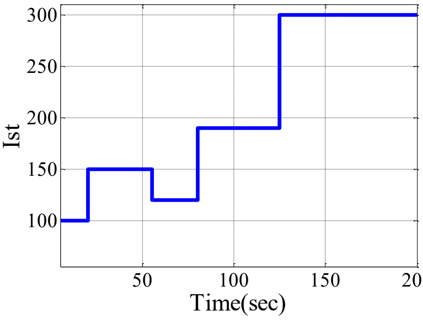

Fig. 6. The load current variation profile as disturbances current

The implementation details of the model and control system simulation in MATLAB are illustrated in Fig. 8. Fig. 9 displays the system states under the variable gain conditions. We can see from the Fig. 9 that the state x_1 or the engine angular velocity, varies between 7000 and 15000 rad/sec, which is a reasonable range. The air mass in the supply manifold changes between 0.03 and 0.06 kg depending on the load current value. The pressure values of the states x_2, x_4, x_5 and x_6 are within the acceptable pressure limits, which indicates that the state control is effective. According to Fig. 10 the compressor voltage or the control input ranges from 100 to 350V. To validate the performance of the cascade controller with variable gain, this controller has been compared with three other controllers, i.e. single loop constant gain ($ST_{C\text{-loop}}$), single loop variable gain ($VGST_{C\text{-loop}}$) and cascaded constant gain ($ST_{Cascade}$). It is also clear from the Fig. 10 that the compressor voltage has much less fluctuations in the conditions of using the cascaded variable gain controller and the cascaded variable gain controller shows better performance than other controllers. The variable gains k_1 and k_2 are shown in Fig. 11 and we can see from the figure that $5 < k_1 < 25$, and $2 < k_2 < 6$.

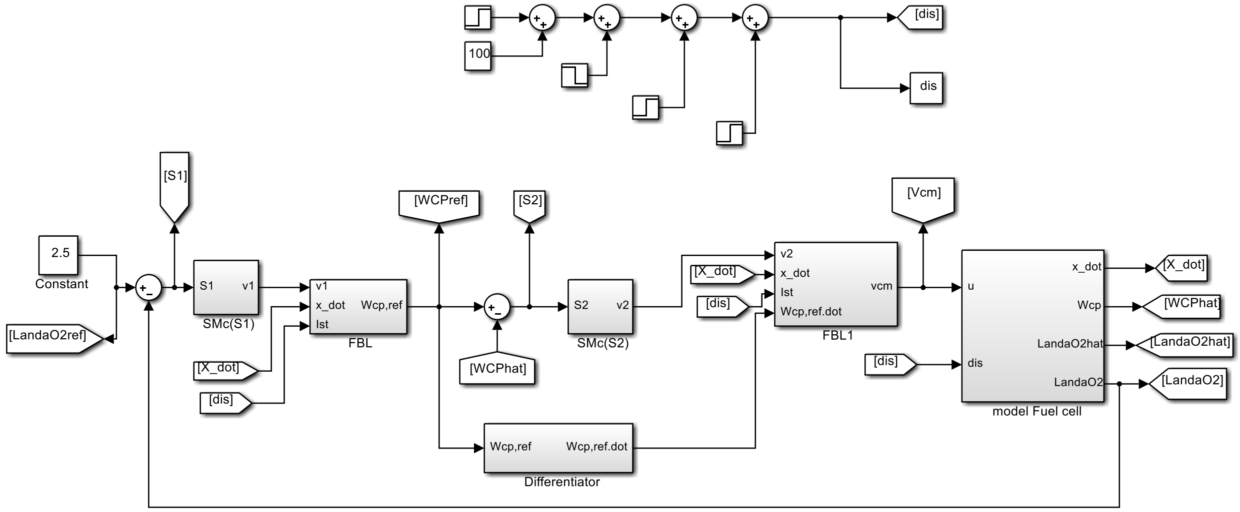

Fig. 7. Block diagram of the control system in Matlab/Simulink environment

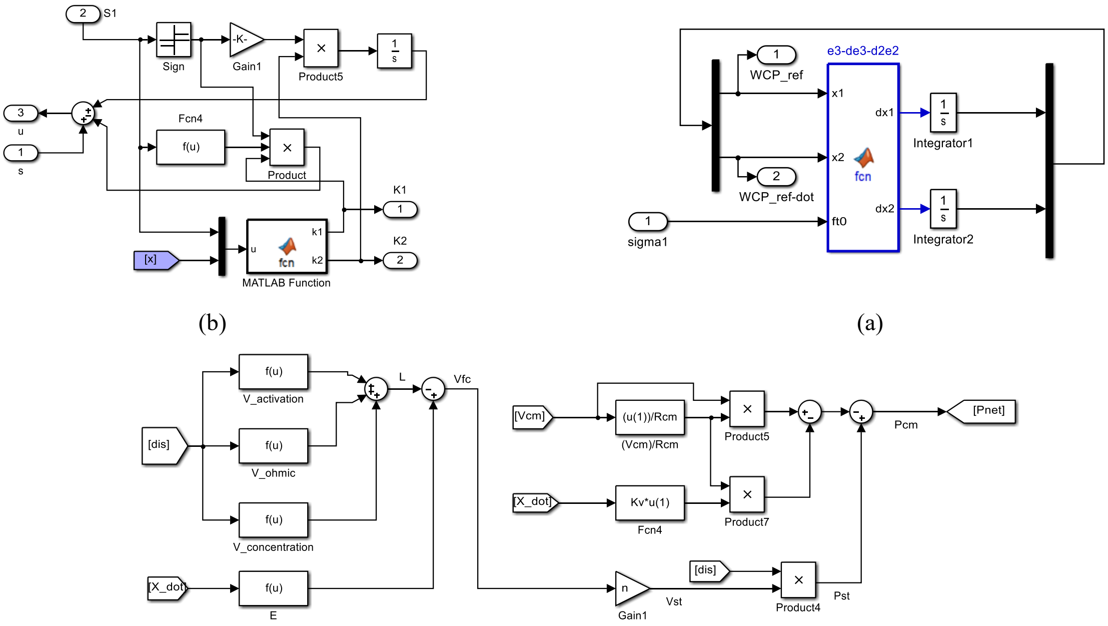

(b)

(a)

(c)

Fig. 8. Simulation framework detailing (a) Levant differentiator implementation, (b) variable-gain control logic with real-time adaptation, and (c) power calculation blocks.

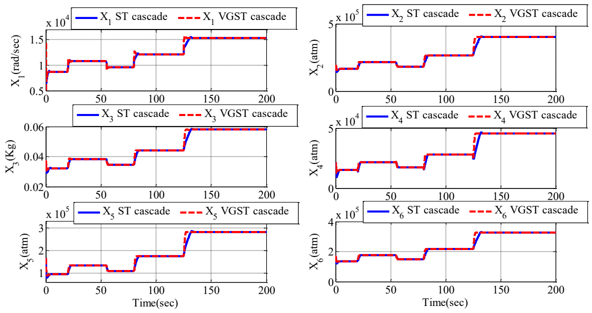

Fig. 9. System States Under Variable vs. Constant Gain Control

Fig. 12 shows the excess oxygen ratio for different controllers. As it is clear from the Fig. 12, the cascade structure variable gain controller performs better than the other three controllers.

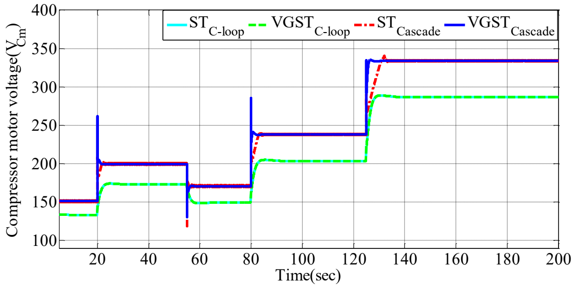

Fig. 10. Compressor voltage and performance comparison of cascade variable-gain vs. constant-gain/single-loop controllers

Fig. 13 shows a comparison between the net output power in the variable gain second-order sliding mode and the constant gain mode in statuses cascade and single close loop.

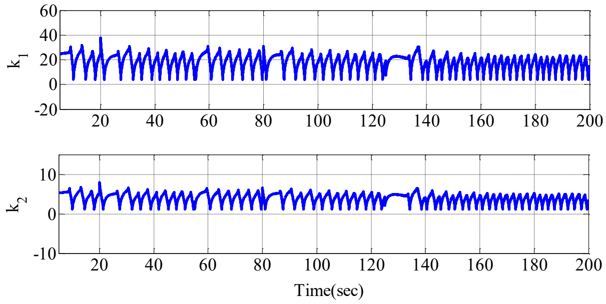

Fig. 11. Variable gains

We can infer from this Fig. 13 that the net output power is higher in the cascade variable gain mode and also, the fuel cell produces a power of about 60 KW at the maximum current. Therefore, there is a significant saving in the total power. Fig. 13 clearly proves the superiority of the variable gain controller of the cascade structure compared to the other three controllers, so that the maximum power value in the cascade variable gain mode is about 10 kW compared to the single loop variable gain and compared to the constant gain mode (single loop and cascade) is about 20 kW more. Fig. 13 in the zoomed mode shows a significant reduction in chattering and a high convergence speed in the variable gain mode, which have better performance in both the cascade mode and the single loop mode compared to the constant gain controllers. Fig. 14 shows the compressor airflow in both cases of applying fixed-gain sliding mode control and variable-gain sliding mode control, and indicates that the proposed cascade variable-gain controller reduces chattering.

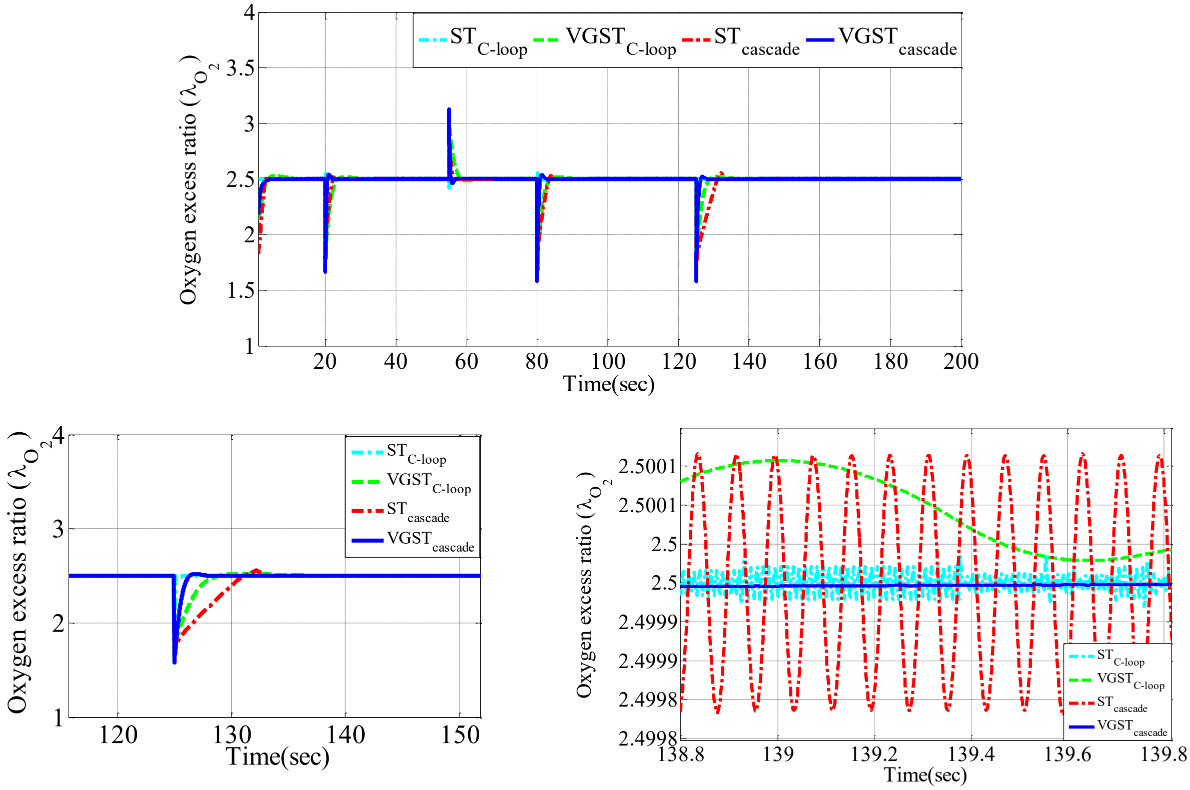

Fig. 12. Excess oxygen ratio under four controllers, demonstrating superior performance of the cascade variable-gain structure.

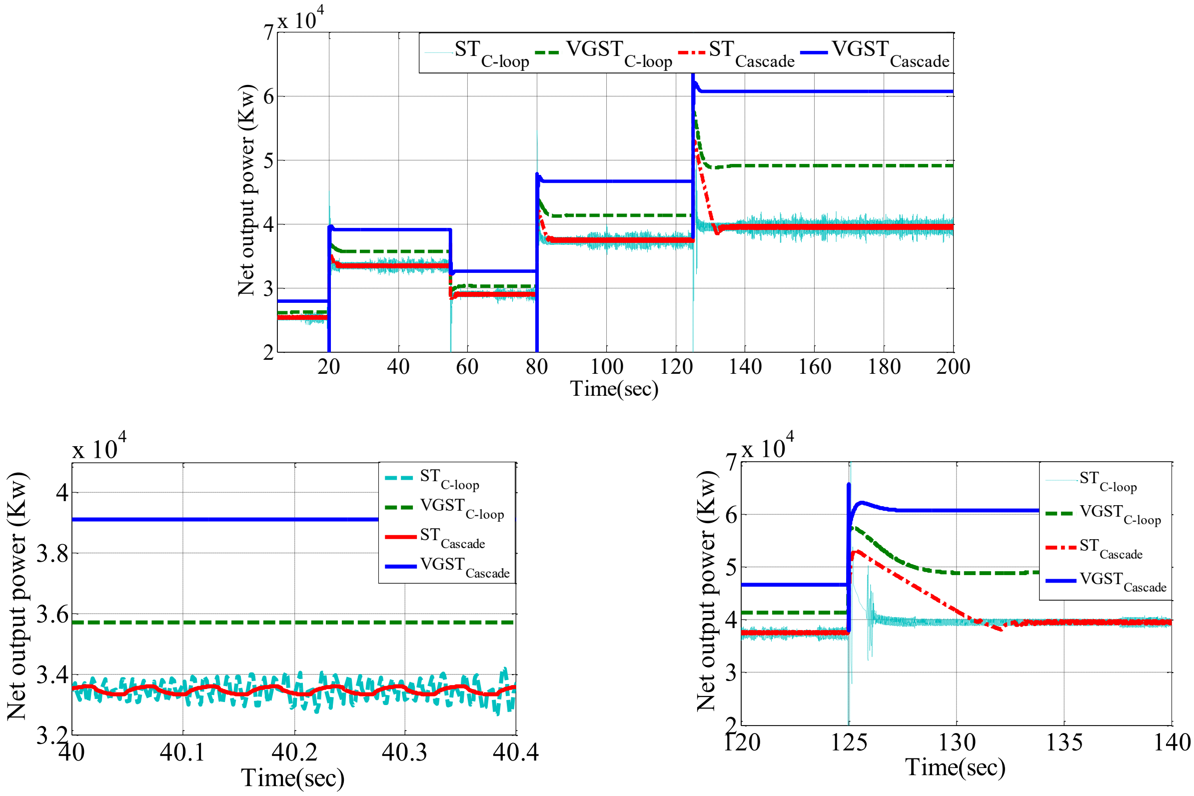

Fig. 13. Net output power comparison of variable-gain vs. constant-gain second-order sliding mode controllers in cascade/single-loop configurations.

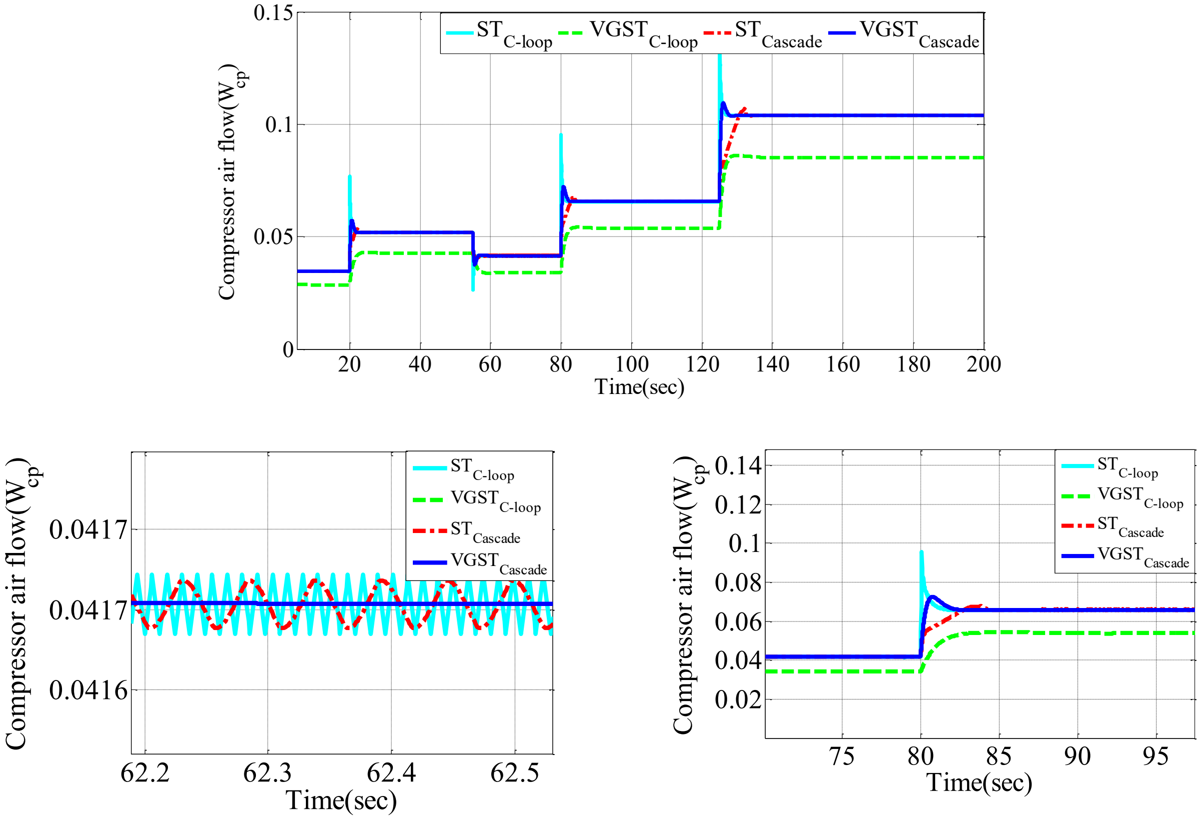

Fig. 14. Compressor airflow comparison: Fixed-gain vs. variable-gain sliding mode control

A. Variations of System Parameters

The parameters of the PEMFC system are difficult to estimate precisely in real conditions. This is because they depend on the environmental factors (e.g., temperature, pressure) and the structural features (e.g., manifolds volumes, rotor inertia, motor resistance, motor inductance, etc.). Sensitivity analysis to model uncertainties was conducted by varying key parameters following Table 2. The controller's robustness was evaluated under parametric variations.

Table 2. Parameter variations applied to simulate model uncertainty and assess controller robustness [22]

parameters	**Volatility and uncertainty**
Temperature of the stack(T_{st})	+10%
Single stack cathode (V_{ca}) volume	+5%
Motor constant(k_v)	-10%
Electrical resistance of (R_{cm}) motor	+5%
Diameter Compressor(d_c)	+10%
Motor inertia(J_{cp})	+10%
Atmospheric pressure(P_{atm})	+10%
Supply manifold volume(V_{sm})	-10%
Return manifold volume(V_{rm})	-10%

The resulting performance degradation is shown in Fig. 15, and Fig. 16. Fig. 15 is depicted under parametric uncertainty conditions and shows the desired performance of net output power that is between 25 and 50 Kw. It also implies that the closed-loop system is robust against severe parametric uncertainty. Fig. 16 shows that the excess oxygen ratio remains at a value of 2.5 even under conditions of parametric uncertainty. The Fig. 15 and Fig. 16 indicates that the proposed controller effectively handles parametric uncertainty. According to Fig. 17 the compressor voltage or the control input ranges from 100 to 300V. As evident from Fig. 17, the compressor voltage (or controller input) remains bounded despite applied parametric uncertainties and step disturbances (stack current (I_{st})). This demonstrates the system's robustness and the satisfactory performance of the VGST controller.

B. The Noisy Conditions

To evaluate the performance of the proposed controller, Rakhtala et al. [27] have conducted some tests with realistic measurement noise. They also have used the Data Acquisition Card (DAQ) of Advantech USB-4711A as a real application with the LabViewTM to match the simulation data and tests with the experimental system, and have utilized the MatlabTM for extracting the features of the

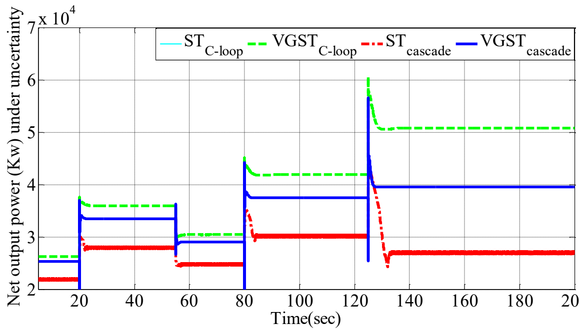

Fig. 15. Robust net output power (25–50 kW) under severe parametric uncertainty.

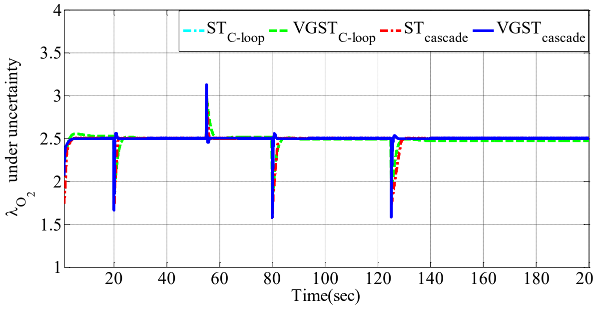

Fig. 16. Robust regulation of excess oxygen ratio ($\lambda_{O_2} = 2.5$) under parametric uncertainty

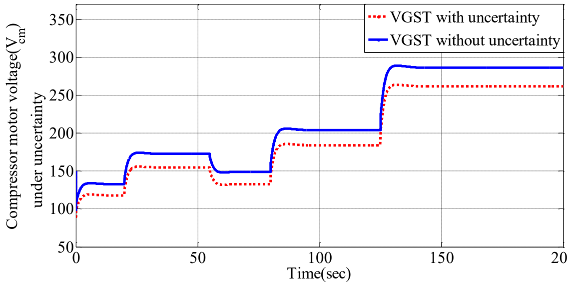

Fig. 17. Compressor voltage (100–300 kW) under severe parametric uncertainty.

measured noise, which are as follows:

Mean=0.0023	Variance=0.13362	Co-variance = 0.0179
PSD=0.22	Signal/noise(SNR)=28dB	Distribution: Gaussian

We added similar noise to the measured signals of the compressor output flow (W_{cp}), which passed through a 2nd-order Butterworth low pass filter with a cut off frequency of 30Hz. The implementation details of the noise generation and injection simulation in MATLAB are illustrated in Fig. 18.

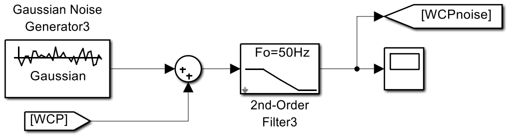

Fig. 18. Simulink block diagram for noise generation and injection.

Fig. 19, Fig. 20, and Fig. 21 show the results of the controlled output under the noisy conditions. One can see from the figures that the control achieved good convergence within a limited time and followed the desired value. Even with the noise, the proposed controller reached the desired value of 2.5, showing a satisfactory tracking and behavior. The net output power also increased in the noisy mode. As evident from Fig. 20, the system states remain bounded under applied noise and step disturbances (stack current (I_{st})), demonstrating the system's robustness and the effective performance of the variable-gain controller.

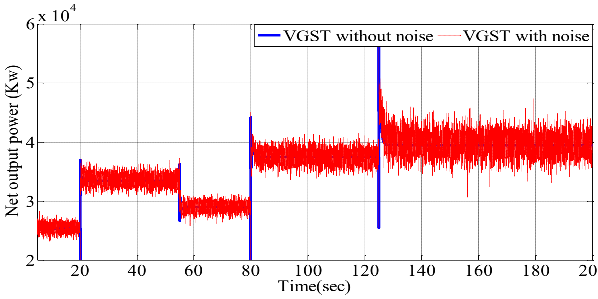

Fig. 19. Net power output under realistic noise condition

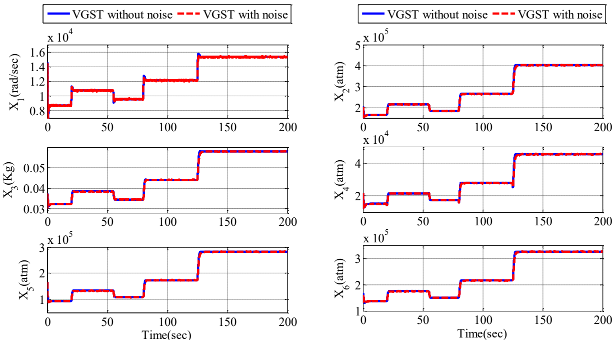

Fig. 20. States profile in the case of variable gain controller under realistic noise condition

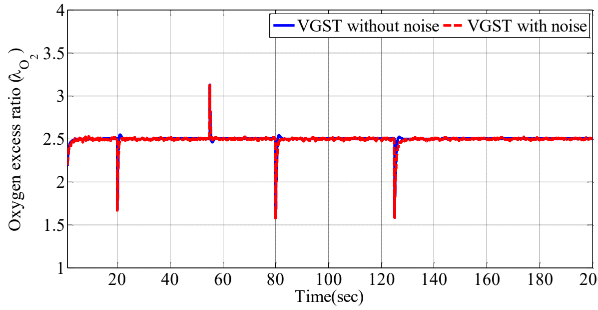

Fig. 21. Oxygen excess ratio under realistic noise condition

The performance of the controllers has been compared from a statistical point view. In this regard, we have used four famous statistical indices: mean square error (MSE), the root-mean-square error (RMS), mean absolute error (MAE), and standard deviation (Sd). To better understand, we have depicted the value of the statistical indices for the error of oxygen excess ratio. As can be seen from Fig. 22, the VGST_Cascade controller has a better performance than the other controllers because it has the smallest mentioned statistical indices.

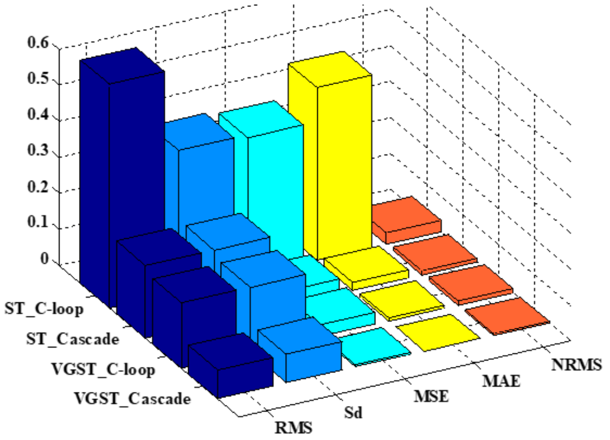

Fig. 22. Comparative evaluation of controller performance using statistical error indices (MSE, RMSE, MAE, SD) for oxygen excess ratio

For better comparison of statistical metrics, the data from Fig. 22 have been tabulated in Table 3.

Table 3. Comparative evaluation of controller performance using statistical error indices for oxygen excess ratio

	RMS	sd	MSE	MAE	NRMS
ST_C-loop	0.520	0.3931	0.3845	0.4795	0.0328
ST_Cascade	0.202	0.2003	0.0406	0.0226	0.011
VGST_C-loop	0.181	0.181	0.0328	0.0089	0.0105
VGST_Cascade	0.079	0.0793	0.0063	4.32E-04	0.0045

Table 4 benchmarks our method against published results for MPC and PID [33].

Table 4. RMS, MSE, and MAE of controllers.

	Error Integral Criterion		
	RMS	**MSE**	**MAE**
VGST_C-loop	0.1812	0.0328	0.0089
VGST_Cascade	0.0793	0.0063	4.32E-04
PID	0.114	0.013	0.0091
MPC	0.190	0.0363	0.046

VI. Conclusion

This paper presents a cascade variable gain super-twisting second-order sliding mode control for the air-feed system of the PEM fuel cell. The PEMFC model is nonlinear and has 6 states, which is adequate for the controller design. The controller was designed using Lyapunov theory and tested using simulation and experimental methods. Also, for further validation, uncertainty and noise in the system were considered and the results were confirmed. Finally, it was shown that the proposed controller performs better and more accurately than the constant gain and closed loop controller. This design method reduces the online calculations by avoiding the computation of chaos and confusion for the controller design and operation. The controller tracks the oxygen stoichiometry precisely and improves the net power output. For the maximum current condition (300A), the net power output is 60 KW, which is 20 KW higher than the constant gain controller. The controller also has the advantages of being robust to noise and uncertainty, reducing chattering, being easy to implement, and having a short convergence time. While VGST exhibits minor tracking errors and strong robustness, its computational load, chattering at UHF, and model dependency remain inherent trade-offs. These are offset by its unique capability to prevent oxygen starvation –a critical safety requirement in PEMFC systems. Future research will extend this controller to hydrogen flow regulation and thermal dynamics integration, enhancing operational stability under load transients. Additionally, hybrid fuel cell-battery system implementation will be explored to optimize power management. These extensions address critical limitations while advancing toward real-world multi-physics control solutions.

Appendix A:

Table 5. Value of parameters [22].

Symbol	**Parameter**	**Value**
P_{atm}	Atmospheric pressure (Pa)	101.325
$P_{sat,Tatm}$	Saturation pressure in ambient temperature (Pa)	3.14×10^3
$P_{sat,Tst}$	Saturation pressure in stack temperature (Pa)	4.09×10^4
$\emptyset_{atm}$	Average ambient air relative humidity	0.5
$\emptyset_{ca,in}^{des}$	Relative humidity in cathode inlet	1
T_{atm}	Atmospheric temperature (K)	298.15
γ	Air-specific heat ratio	1.4
C_p	Air density (J/kg/K)	1004
R	Universal gas constant (J/mol/K)	8.31
ρ_a	Air density (kg/m^3)	1.23
R_a	Air gas constant (J/mol/K)	286.9
R_{O_2}	Oxygen gas constant (J/kg/K)	259.8
R_{N_2}	Nitrogen gas constant (J/kg/K)	296.8
R_v	Vapor gas constant (J/kg/K)	461.5
Ma	Molar mass of air (kg/mol)	28.9×10^{-3}
M_{o_2}	Molar mass of oxygen (kg/mol)	30×10^{-3}
M_{n_2}	Molar mass of nitrogen (kg/mol)	28×10^{-3}
Mv	Molar mass of vapor (kg/mol)	18.0×10^{-3}
$m_{v,ca,max}$	Maximum molar mass of vapor in cathode (kg/mol)	3×10^{-3}
F	Faraday's constant (C/mol)	96,487
T_{st}	Temperature of the stack (K)	353
Kt	Motor constant (N m/A)	0.0153
Rcm	Motor constant (ohm)	0.82
Kv	Motor constant (V/(rad/s))	0.0153

η_{cp}	Compressor efficiency	0.8
η_{cm}	Compressor motor mechanical efficiency	0.98
n	Number of cells in fuel cell stack	381
A_{fc}	Fuel cell active area (m^2)	280×10^{-4}
V_{sm}	Supply manifold volume (m^3)	0.02
V_{ca}	Single stack cathode volume (m^3)	0.005
V_{rm}	Return manifold volume (m^3)	0.005
$K_{\mathrm{sm,out}}$	Supply manifold outlet orifice constant (kg/s/Pa)	0.363×10^{-5}
$K_{\mathrm{c\ a,out}}$	Cathode outlet orifice constant (kg/s/Pa)	0.22×10^{-5}
dc	Compressor diameter (m)	0.2286
$y_{\mathrm{O_2,in}}$	Oxygen mole fraction at cathode inlet	0.21

References

[1] J. Kuang, J. Lv, W. Hao, X. Lin, D. Zhao, I. Matraji, *et al.*, "Oxygen excess ratio control of PEM fuel cell systems with prescribed regulation time," *ISA transactions,* vol. 142, pp. 683-692, 2023.

[2] R. Y. Dahham, H. Wei, and J. Pan, "Improving thermal efficiency of internal combustion engines: recent progress and remaining challenges," Energies, vol. 15, p. 6222, 2022.

[3] D. Wu, C. Peng, C. Yin, and H. Tang, "Review of system integration and control of proton exchange membrane fuel cells," Electrochemical Energy Reviews, vol. 3, pp. 466-505, 2020.

[4] Q. Li, W. Yang, L. Yin, and W. Chen, "Real-time implementation of maximum net power strategy based on sliding mode variable structure control for proton-exchange membrane fuel cell system," IEEE Transactions on Transportation Electrification, vol. 6, pp. 288-297, 2020.

[5] C. R. d. Aguiar, K. M. d. Aguiar, R. F. Bastos, W. C. Leal, M. O. Godinho, G. H. Fuzato, et al., "Energy management and operation control of fuel cells in grid-tied operation," Journal of Control, Automation and Electrical Systems, pp. 1-12, 2021.

[6] Y. Nagao, "Proton-Conducting Polymers: Key to Next-Generation Fuel Cells, Electrolyzers, Batteries, Actuators, and Sensors," ChemElectroChem, p. e202300846, 2024.

[7] A. Tang, L. Yang, T. Zeng, and Q. Yu, "Cascade Control Method of Sliding Mode and PID for PEMFC Air Supply System," Energies, vol. 16, p. 228, 2022.

[8] Y. Mousavi, G. Bevan, I. B. Kucukdemiral, and A. Fekih, "Sliding mode control of wind energy conversion systems: Trends and applications," Renewable and Sustainable Energy Reviews, vol. 167, p. 112734, 2022.

[9] K. R. Palepogu and S. Mahapatra, "Design of sliding mode control with state varying gains for a Benchmark Twin Rotor MIMO System in Horizontal Motion," European Journal of Control, vol. 75, p. 100909, 2024.

[10] M. Ebrahimipour and S. M. Mirhosseini-Alizamini, "Optimal Adaptive Sliding Mode Control for a Class of Nonlinear Affine Systems," Control and Optimization in Applied Mathematics, vol. 9, pp. 123-138, 2024.

[11] M. Ghamgosar, S. M. Mirhosseini-Alizamini, and M. Dadkhah, "Design of optimal sliding mode control based on linear matrix inequality for fractional time-varying delay systems," International Journal of Industrial Electronics Control and Optimization, vol. 5, pp. 317-325, 2022.

[12] M. Gholami, S. Mirhosseini-Alizamini, and A. Heidari, "Designing a sliding mode controller for a class of multi-controller COVID-19 disease model," Iranian Journal of Numerical Analysis and Optimization, vol. 15, pp. 27-53, 2025.

[13] G. Khaledi, S. M. Mirhosseini-Alizamini, and S. Khaleghizadeh, "Sliding mode control design for a class of uncertain time-delay conic nonlinear systems," Iranian Journal of Science and Technology, Transactions A: Science, vol. 46, pp. 583-593, 2022.

[14] A. Rezaie, "Sliding Mode Control for Chaotic Systems with Unknown Uncertainties," International Journal of Industrial Electronics Control and Optimization, vol. 7, pp. 53-60, 2024.

[15] F. Roshanravan and A. Heydari, "Sliding Mode Control Design for a Class of Nonlinear Fractional Systems with Application to Glucose-Insulin Systems," International Journal of Industrial Electronics Control and Optimization, vol. 5, pp. 337-347, 2022.

[16] G. R. Shahabadi and M. R. Naseh, "Novel Sliding Mode Control Approach for Quasi-Z-Source Converters with Improved Performance," International Journal of Industrial Electronics Control and Optimization, vol. 7, pp. 213-224, 2024.

[17] T. Gonzalez, J. Moreno, and L. Fridman, "Variable gain super-twisting sliding mode control," Automatic Control, IEEE Transactions on, vol. 57, pp. 2100-2105, 2012.

[18] F. Chen, J. Jiao, Z. Hou, W. Cheng, J. Cai, Z. Xia, et al., "Robust polymer electrolyte membrane fuel cell temperature tracking control based on cascade internal model control," Journal of Power Sources, vol. 479, p. 229008, 2020.

[19] S. Kart, F. Demir, İ. Kocaarslan, and N. Genc, "Increasing PEM fuel cell performance via fuzzy-logic controlled cascaded DC-DC boost converter," International Journal of Hydrogen Energy, vol. 54, pp. 84-95, 2024.

[20] Y. Du, Y. Zhang, J. Lou, J. Wang, and P. Zhao, "Conception and thermo-economic performance investigation of a novel solid oxide fuel cell/gas turbine/Kalina cycle cascade system using ammonia-water as fuel," Applied Thermal Engineering, vol. 239, p. 122118, 2024.

[21] H. Luo, J. Xiao, P. Bénard, C. Yuan, L. Tong, R. Chahine, et al., "Thermodynamic modeling and analysis of cascade hydrogen refuelling with three-stage pressure and temperature for heavy-duty fuel cell vehicles," International Journal of Hydrogen Energy, vol. 63, pp. 103-113, 2024.

[22] N. Mirrashid, S. M. Rakhtala, and M. Ghanbari, "Robust control design for air breathing proton exchange membrane fuel cell system via variable gain second-order sliding mode," Energy Science & Engineering, vol. 6, pp. 126-143, 2018.

[23] N. Mirrashid, E. Alibeiki, and S. M. Rakhtala, "Nonlinear robust controller design for an upper limb rehabilitation robot via variable gain super twisting sliding mode," International Journal of Dynamics and Control, vol. 10, pp. 1996-2010, 2022.

[24] G. P. Incremona, M. Rubagotti, M. Tanelli, and A. Ferrara, "A general framework for switched and variable gain higher order sliding mode control," IEEE Transactions on Automatic Control, vol. 66, pp. 1718-1724, 2020.

[25] R. Ma, Y. Han, and W. Pan, "Variable-gain super-twisting sliding mode damping control of series-compensated

DFIG-based wind power system for SSCI mitigation," Energies, vol. 14, p. 382, 2021.

[26] J. J. Moré, P. F. Puleston, E. Fossas, and C. Kunusch, "Decoupled inputs sliding mode controllers for a fuel cell-supercapacitor module in hybrid generation applications," International Journal of Energy and Environmental Engineering, vol. 10, pp. 257-269, 2019.

[27] S. M. Rakhtala, A. R. Noei, R. Ghaderi, and E. Usai, "Design of finite-time high-order sliding mode state observer: A practical insight to PEM fuel cell system," Journal of Process Control, vol. 24, pp. 203-224, 2014.

[28] S. M. RakhtAla and R. Eini, "Nonlinear modeling of a PEM fuel cell system; a practical study with experimental validation," arXiv preprint arXiv:2501.08420, 2025.

[29] X. Tang, M. Yang, L. Shi, Z. Hou, S. Xu, and C. Sun, "Adaptive state-of-health temperature sensitivity characteristics for durability improvement of PEM fuel cells," Chemical Engineering Journal, vol. 491, p. 151951, 2024.

[30] T. L. Oladosu, J. Pasupuleti, T. S. Kiong, S. P. J. Koh, and T. Yusaf, "Energy management strategies, control systems, and artificial intelligence-based algorithms development for hydrogen fuel cell-powered vehicles: A review," International Journal of Hydrogen Energy, vol. 61, pp. 1380-1404, 2024.

[31] H. Obeid, S. Laghrouche, L. Fridman, Y. Chitour, and M. Harmouche, "Barrier function-based adaptive super-twisting controller," IEEE Transactions on Automatic Control, vol. 65, pp. 4928-4933, 2020.

[32] A. Levant, "Robust exact filtering differentiators," European Journal of Control, pp. 6-29, 2019.

[33] Y. Wang, H. Li, H. Feng, K. Han, S. He, and M. Gao, "Simulation study on the PEMFC oxygen starvation based on the coupling algorithm of model predictive control and PID," Energy Conversion and Management, vol. 249, p. 114851, 2021.

Violet Farhad received his B.S. degree in Applied Mathematics from Mazandaran University, Babolsar in 1996, her M.S. degree in Applied Mathematics from Islamic Azad University ,Karaj in 2001. She is currently a PhD candidate in Applied Mathematics (Control & Optimization) from PNU, Tehran, Iran. Her current research interests include Advanced Cotrol Systems, Cascade Control Design, Fuel Cell Systems (PEMFC), Optimal and Nonlinear Control Methods, Applied Mathematics in Control Engineering, Higher Education and Interdisciplinary Research.

Seyed Mehdi Mirhosseini-Alizamini received his b.s. Degree in applied Mathematics from damghan university, damghan in 2004, his m.s. Degree in appiled mathematics (control & optimization) from isfahan university of technology, isfahan in 2006, and his ph.d. In applied mathematics (control & optimization) from pnu, tehran in 2015 under the supervision of professor sohrab effati at the ferdowsi university of mashhad, mashhad, iran. Currently he is an associate professor at department of mathematics of payame noor university, iran.his research interests are time daily systems, optimal control, fractional optimal control problems and numerical methods

IECO International Journal Of Industrial Electronics Control and Optimization
Print ISSN: 3517-2645
Online ISSN: 3568-2645
Homepage: https://ieco.usb.ac.ir/

Numerical Assessment of Optimal Control Problems with Variable-Order Fractional Integro-Differential Equation Based on Laguerre Wavelets Functions

Maryam Alipour[1]| Samaneh Soradi-Zeid[2]

Faculty of Mathematics, University of Sistan and Baluchestan, Zahedan, Iran.[1]
Faculty of Industry and Mining (khash), University of Sistan and Baluchestan, Zahedan, Iran.[2]
Corresponding author's email: soradizeid@eng.usb.ac.ir

Article Info

Article type:
Research Article

Article history:
Received: 02-June-2025
Received in revised form: 10-July-2025
Accepted: 15-July-2025
Published online:22-June-2026

Keywords:
Collocation method,
Integro-differential equation,
Laguerre wavelet,
Optimal control problem,
Variable-order calculus.

ABSTRACT

This paper deals with a general form of fractional optimal control problems involving variable-order fractional integro-differential equation using orthonormal Laguerre wavelets expansions. By effectively employing these functions, product variable-order operational matrices have been obtained. By using these fractional operational matrices and collocation points, the study transforms the original continuous-time optimal control problems of variable-order fractional integro-differential equations into a system of linear or non-linear algebraic equations. Attempts have been made to use the collocation method with a joint application of Lagrange multiplier technique, to obtain the approximate cost function based on determining the state and control functions. The main components for applying these wavelets is to have viable solutions due to their orthogonality. In addition, the convergence analysis is presented with respect to the operational matrices of this scheme. Simulation results indicate that the proposed method works well and provides satisfactory results with regard to accuracy and computational effort.

I. Introduction

Variable-order fractional differential equations (V-FDEs) are considered as a growing research field which have extensive action on interactive inhibitor, application of electric circuit analysis and development of excitatory neurons models [1, 37]. The V-FDEs provide a flexible framework for modeling and analyzing signals with varying degrees of regularity and complexity [38]. Due to the significant increase of nonlinear mixed V-FDEs and optimal control problems (OCPs) [25, 26], in the last decades, many approximation techniques are developed for these types of problems. Zheng and Wang [39] proved the well-possedness and smoothing property of an OCP governed by a hidden-memory V-FDE. Cardinal functions based on Chebyshev polynomials have been used in [14] for a common type of OCPs generated by nonlinear dynamical systems involved with V-FDE. Transcendental Bernstein functions were proposed in [15, 16] for the numerical solutions of these problems. Authors in [2] applied a robust method for nonlinear variable-order fractional systems to obtain the approximate values of optimal control. Wavelet method used for some type of OCPs governed by V-FDEs in [12,32].

Integral equations have attracted extensive research in the field of applicable models [8,18]. To obtain the approximate solutions of these equations, the wavelet and spectral methods have been applied in [24]. In the modeling of many non-linear physical phenomena and engineering applications [5], a generalization of OCPs has been presented, whose dynamic system is described by an integro-differential equation [19]. Considerable researches have been done on developing the valid and efficient techniques for solving these problems [3, 33]. Fractional frameworks make it possible to tackle the challenges associated with environmental changes which is favorable in physical scenarios [31], where the objects are subject to dynamic changes. Researchers and practitioners in fields like engineering, physics, economics, and applied mathematics often study and address fractional integro-differential

Publisher: University of Sistan and Baluchestan

equations to analyze and control complex systems with fractional dynamics. Touchard wavelets are employed to obtain approximation values of OCPs involving Volterra integral equation with fractional derivative [27]. A direct method based on piece-wise Bernoulli functions is applied to find the optimal control of these Volterra equations [17]. Authors in [10] design the Gegenbauer approach for evaluating the approximate outputs of OCP with fractional integro-differential equation. A robust method has been used in [20] to obtain the optimal control of fractional Volterra integro-differential equation. A generalized fractiona Chebyshevl wavelets [13], Fibonacci wavelets [28] and Lucas wavelets [29] have been suggested to solve variable-order fractional OCPs. Some approaches for these problems can be found in [34, 35].

An OCP governed by variable-order fractional integro-differential equations (V-FIDEs), refer to a class of mathematical models that involve both fractional calculus and control theory. Although various type of fractional OCPs have been solved by many researchers [40], but to the best of our knowledge, the literature dealing with OCPs influenced by nonlinear V-FIDEs is seemingly lacking and has not yet been employed. Here, we want to determine an optimal control strategy that optimizes a given performance index governed by V-FIDEs in the sense of Volterra-Fredholm integro-differential equations and manage the computational complexity associated with analytical solutions. By generalizing these concepts, an approximation scheme is here proposed to solve the following OCP:

$$Min_u\ J(x,u) = \int_{t_0}^{t_f} Q(t,x(t),u(t))dt, \tag{1}$$

$$s.t.\ {}_0D_t^{\beta(t)}x(t) = \int_{t_0}^{t} G(t,s,x(s),u(s))ds$$

$$+\int_{t_0}^{t_f} K(t,s,x(s),u(s))ds + g(t), \tag{2}$$

$$x(t_0) = x_0,\quad u(t) \in U, \tag{3}$$

in which $t \in [0,1]$, $x_0 \in \mathbb{R}$, Q, G, K and g are continuously differentiable, (x,u) is the couple of state and control variables, respectively. The set $U \subset \mathbb{R}^m$ indicates the allowed inputs that are continuous functions, and ${}_0D_t^{\beta(t)}$ is the variable-order fractional derivative with the arbitrary order $\beta(t)$ in the sense of variable-order Liouville-Caputo derivative. Throughout this paper, we assume that the optimal control problem is well-posed. In particular, in this case, $0 < \beta(t) \leq 1$ is continuous and bounded, ensuring the existence and uniqueness of the solution to the integral constraint. We want to acquire the control function $u^*(t)$ that optimizes the outlay of the controlling effort (1) by extracting the differential system (2) through conditions (3). This necessitates the development of efficient numerical methods to address these equations and manage the computational complexity associated with analytical solutions. To assess this concept, an approximate idea is here proposed based on the Laguerre polynomials and Laguerre wavelets functions [30]. The prominent feature of this approximation is the expression of functions as series expansion using orthogonal polynomials. Orthogonality significantly reduces the complexity of the problem by re-scaling the variable-order fractional OCP (1)-(3) up to a simpler system that reveals the important characteristics of fractional OCPs and, comes from the direct methods for solving OCPs. Indeed, the investigated method performed very well when employing some algebraic equations for detecting the solution of OCP (1)-(3). Throughout the paper, we will build upon the existing body of knowledge while introducing novel methodologies and insights. By structuring our paper into the following main sections, we will provide readers with a cohesive and logically organized presentation of our research on V-FIDEs and their applications in optimal control problems. We continue the discussion as described in follow. The essential concepts of fractional calculus and also, the major specifications of the Laguerre wavelets functions and their properties are introduced in Section II. The proposed method for the expressed problem and its convergence analysis are investigated in Section III and Section IV, respectively. The validity of this technique is investigated by solving several examples in Section V. Furthermore, Section VI includes a brief conclusion.

II. Preliminary Tools

In the last section, we provided a thorough overview of the topic, including the fundamental concepts and key theories related to V-FIDEs and their applications. This background will serve as a foundation for understanding the subsequent sections of the paper. In the second section, some preparations regarding fractional calculus and Laguerre wavelets functions are provided.

A. Variable-order fractional calculus

The characteristic of fractional operators is the conquest of memory and scale transformations. However, if there is a permanent (or static) order in the fractional models, it can be potentially caused the heterogeneity of the system to be neglected over time [11]. Accordingly, to cover this shortcoming, models are introduced with variable-order derivatives that potentially capture time-dependent system properties [4]. Regarding this pivotal characteristic, the operators of these calculations can be expressed as follows.

Definition 1 The variable-order fractional Riemann-Liouville integral of order $\beta(t) > 0$ for a given function $x(t)$ is determined as:

$$I^{\beta(t)}x(t) = \frac{1}{\Gamma(\beta(t))}\int_0^t (t-\tau)^{\beta(t)-1}x(\tau)d\tau,$$

and satisfies the following useful property:

$$I^{\beta(t)}t^{b} = \begin{cases} \dfrac{\Gamma(b+1)}{\Gamma(b+1+\beta(t))}t^{b+\beta(t)}, & b > -1, \\ 0, & \text{elsewhere.} \end{cases}$$

Definition 2 Riemann-Liouville fractional derivatives of order $\beta(t) > 0$, $n-1 < \beta(t) \le n$, $n \in \mathbb{N}$, are given by:

$${}_0^{RL}D_t^{\beta(t)}x(t) = \frac{1}{\Gamma(n-\beta(t))}\left(\frac{d}{dt}\right)^n \int_0^t (t-\tau)^{n-\beta(t)-1}x(\tau)d\tau,$$

and

$${}_t^{RL}D_{t_f}^{\beta(t)}x(t) = \frac{(-1)^n}{\Gamma(n-\beta(t))}\left(\frac{d}{dt}\right)^n \int_t^{t_f} (\tau-t)^{n-\beta(t)-1}x(\tau)d\tau.$$

Definition 3 Liouville-Caputo fractional derivatives of order $\beta(t) > 0$, $n-1 < \beta(t) \le n$, are given by:

$${}_0D_t^{\beta(t)}x(t) = \frac{1}{\Gamma(n-\beta(t))}\int_0^t (t-\tau)^{n-\beta(t)-1}x^{(n)}(\tau)d\tau,$$

and

$${}_tD_{t_f}^{\beta(t)}x(t) = \frac{(-1)^n}{\Gamma(n-\beta(t))}\int_t^{t_f} (\tau-t)^{n-\beta(t)-1}x^{(n)}(\tau)d\tau.$$

Since, Liouville-Caputo's definition has some useful properties in dealing with initial value problems, specially in tackling natural models, we selected it in this work. This operator also holds the linearity property as follows:

$${}_0D_t^{\beta(t)}(\sigma g(t) + \kappa f(t)) = \sigma\, {}_0D_t^{\beta(t)}g(t) + \kappa\, {}_0D_t^{\beta(t)}f(t),$$

when σ and κ are constants. Besides, for $n \le b \in \mathbb{N}$, it has the following property:

$${}_0D_t^{\beta(t)}t^{b} = \begin{cases} \dfrac{\Gamma(b+1)}{\Gamma(b+1-\beta(t))}t^{b-\beta(t)}, & n-1 < \beta(t) \le n, \\ 0, & \text{elsewhere,} \end{cases}$$

and ${}_0D_t^{\beta(t)}C = 0$, when C is a constant.

B. Properties of Laguerre wavelets

Consider the following differential equation in $(0,\infty)$:

$$tx'' + (\alpha + 1 - t)x' + nx = 0,$$

or

$$(t^{\alpha+1}\exp(-t)x')' + nt^{\alpha}\exp(-t)x = 0,$$

in which $\alpha > -1$. The polynomial solutions of these equations are known as Laguerre polynomials [23] and, introduced as follows:

$$\mathbf{L}_0^{\alpha}(t) = 1,$$

$$\mathbf{L}_1^{\alpha}(t) = 1 + \alpha - t,$$

and for any $k \ge 1$, we have:

$$\mathbf{L}_{k+1}^{\alpha}(t) = \frac{2k+1+\alpha-t}{k+1}\mathbf{L}_k^{\alpha}(t) - \frac{k+\alpha}{k+1}\mathbf{L}_{k-1}^{\alpha}(t),$$

in which $\mathbf{L}_0^{\alpha}(t) = 1$ and $\mathbf{L}_1^{\alpha}(t) = \alpha + 1 - t$. The Rodriguez formula for them is:

$$\mathbf{L}_k^{\alpha}(t) = \exp(t)\frac{t^{-\alpha}}{k!}\frac{d^k}{dt^k}(t^{k+\alpha}\exp(-t)).$$

Furthermore,

$$\mathbf{L}_k^{\alpha}(t) = \sum_{i=0}^{k}\binom{\alpha-\gamma+k-i}{k-i}\mathbf{L}_i^{\gamma}(t), \quad \alpha,\gamma \in \mathbb{R}.$$

Also, by differentiation of these polynomials we obtain:

$$\frac{d^n}{dt^n}\mathbf{L}_k^{\alpha}(t) = (-1)^k\mathbf{L}_{k-n}^{\alpha+n}(t), \quad k \ge n.$$

Moreover, the following equation holds:

$$\frac{1}{n!}\frac{d^n}{dt^n}(t^{\alpha}\mathbf{L}_k^{\alpha}(t)) = \binom{k+\alpha}{n}t^{\alpha-n}\mathbf{L}_k^{\alpha-n}(t).$$

Considering the weighting function $t^{\alpha}\exp(-t)$, we have:

$$\int_0^{\infty} t^{\alpha}\exp(-t)\mathbf{L}_m^{\alpha}(t)\mathbf{L}_k^{\alpha}(t)dt = \frac{(k+\alpha)!}{k!}\delta_{m,k},$$

that means the orthogonality of Laguerre polynomials in $[0,\infty)$, in which $\delta_{m,k}$ is the Dirac delta function [23]. Particularly, for $\alpha = 0$, it is true that

$$\mathbf{L}_k(t) = \sum_{i=0}^{k}\frac{(-1)^i}{i!}\frac{k!}{i!\,(k-i)!}t^{i},$$

in which the Laguerre polynomials $\mathbf{L}_k^{0}(t) = \mathbf{L}_k(t)$ satisfy $\mathbf{L}_k(0) = 1$ and are orthogonal in $[0,\infty)$. Also, there is a well-known classical global uniform for Laguerre polynomials that estimates by [23]:

$$|\mathbf{L}_k^{\alpha}(t)| \le \exp\left(\frac{t}{2}\right)\frac{(\alpha+1)k}{k!}, \alpha \ge 0,$$
$$t \ge 0, k = 0,1,2,\cdots.$$

Therefore, the Laguerre wavelets are defined as follows in interval [0,1):

$$\phi_{n,m}(x) = \begin{cases} \dfrac{2^{\frac{k}{2}}}{m!}\mathbf{L}_m^{\alpha}(2^k t - 2n + 1), \dfrac{n-1}{2^{k-1}} \le t < \dfrac{n}{2^{k-1}}, \\ \qquad n = 1,\cdots,2^{k-1}, k \in \mathbb{Z}^+, \\ 0, \qquad \text{elsewhere.} \end{cases} \tag{4}$$

III. Method of Solution

In this paper, we aim to address the shortcomings of the previous researches and highlight the significance of our study. In the comprehensive background section we emphasized the significance of our study by discussing the limitations and gaps in the existing literature. We identified the specific challenges and unresolved issues in the field of V-FIDEs and OCPs, highlighting the need for novel approaches and techniques. By doing so, we will establish the rationale for our research and demonstrate its potential contributions to the field. Finally, we will explicitly state the aim of our study, which is to propose a novel approximation method for solving OCPs governed by V-FIDEs. We will outline the key objectives and research questions that will guide our investigation. By developing an efficient and accurate numerical method, we aim to provide a valuable tool for analyzing and solving complex optimal control problems in diverse applications.

Herein, the fractional derivative of variable-order $\beta(t)$ is extracted to an operational matrix by employing the Laguerre wavelet expansions. They provide strong interpolation properties and achieve higher accuracy with fewer collocation points. It is observed that the proposed method is fully compatible with the complexity of such problems and is very user-friendly. Accordingly, to evaluate the dynamical system (2), we consider the introduced operational matrix. The desired method with the help of the collocation method is present to solve problem (1)-(3). Next, the collocation points should be considered to generate some algebraic equations. Additionally, the initial condition (3) is utilized to extract an algebraic equation. After applying the Lagrange multipliers algorithm for this system, the constrained extremum method was employed to obtain the best-fitted parameters for state and control variables.

A function $f(t) \in C[0,1]$ can be expanded in terms of Laguerre wavelets as follows:

$$f(t) = \sum_{n=1}^{\infty} \sum_{m=0}^{\infty} \gamma_{n,m} \phi_{n,m}(t),$$

where $\gamma_{n,m} =< f(t), \phi_{n,m}(t) >$, $\phi_{n,m}(t)$ for $n = 1,2,\cdots$, $m = 0,1,2,\cdots$ are the Laguerre wavelets which has been defined in Equation (4) (in which for simplicity we assumed that $\alpha = 0$) and $<.,.>$ signifies the inner produce in $L^2[0,1]$. If these infinite series are truncated, then we have:

$$f(t) \cong \sum_{n=1}^{2^{k-1}} \sum_{m=0}^{M-1} \gamma_{n,m} \phi_{n,m}(t) = \sigma^T \Phi(t), \tag{5}$$

where $\Phi(t)$ and σ are two $2^{k-1}M$ column vectors, given by$[\phi_{1,0}(t), \phi_{1,1}(t), \cdots, \phi_{2^{k-1},(M-1)}(t)]$, and σ is $[\gamma_{1,0}, \gamma_{1,1}, \cdots, \gamma_{1,(M-1)}, \gamma_{2,0}, \cdots, \gamma_{2^{k-1},(M-1)}]^T$, in which $\gamma_{n,m} = \int_0^1 \phi_{n,m}(t) f(t) dt$. For solving our problem, by attention to relation (4) and considering the collocation points $t_s = \frac{s}{q-1}$, $s = 0,1,\cdots,q-1$, $q = 2^{k-1}(M-1)$, we obtain:

$$\mathbf{L}_{q\times q} = [\Phi(0), \Phi(\frac{1}{q-1}), \cdots, \Phi(1)],$$

which is called the Laguerre wavelets matrix. Accordingly, the Liouville-Caputo variable-order fractional derivative of Laguerre polynomials is given by:

$$ {}_0D_t^{\beta(t)} \mathbf{L}_n(t) = \sum_{k=\lceil \beta(t) \rceil}^{n} \frac{(-1)^k}{k!} \frac{n!}{(n-k)!} \frac{t^{k-\beta(t)}}{\Gamma(k-\beta(t)+1)}.$$

So, for ${}_0D_t^{\beta(t)}\Phi(t)$ we get:

$$({}_0D_t^{\beta(t)}\Phi)(t) \cong (\mathbf{L}_{q\times q} B^{\beta(t)} \mathbf{L}_{q\times q}^{-1})\Phi(t), \tag{6}$$

wherein B^{α} is obtained as follows:

$$\frac{1}{(q-1)^{\beta(t)}\Gamma(\beta(t)+2)} \times \begin{bmatrix} 0 & b_{1,1} & \binom{1}{0} b_{1,2} + \binom{2}{0} b_{2,2} & \cdots & \sum_{j=1}^{q} \binom{j}{0} b_{j,q} \\ 0 & -b_{1,1} & -[\binom{1}{1} b_{1,2} + \binom{2}{1} b_{2,2}] & \cdots & -\sum_{j=2}^{q} \binom{j}{1} b_{j,q} \\ 0 & 0 & \binom{2}{2} b_{2,2} & \cdots & \sum_{j=3}^{q} \binom{j}{2} b_{j,q} \\ \vdots & \vdots & \vdots & \ddots & \vdots \\ 0 & 0 & 0 & \cdots & (-1)^q \binom{q}{q} b_{q,q} \end{bmatrix},$$

in which:

$$b_{r,s} = \begin{cases} (-1)^r \dfrac{r!}{\Gamma(r+1-\beta(t))} \dbinom{s}{r}, & \text{if } s \geq r \geq \lceil \beta(t) \rceil \\ 0, & \text{otherwise.} \end{cases}$$

Now, we want to solve the OCP (1)-(3). Utilizing this approach, we first expand the state and the control variables as follows:

$$x(t) \cong \sum_{n=1}^{2^{k-1}} \sum_{m=0}^{M-1} \phi_{n,m}(t) x_{n,m} = X^T \Phi(t), \tag{7}$$

$$u(t) \cong \sum_{n=1}^{2^{k-1}} \sum_{m=0}^{M-1} \phi_{n,m}(t) u_{n,m} = U^T \Phi(t),$$

in which

$$X = [x_{1,0}, x_{1,1}, \cdots, x_{2^{k-1},(M-1)}]^T,$$

$$U = [u_{1,0}, u_{1,1}, \cdots, u_{2^{k-1},(M-1)}]^T.$$

Substitution Equations (7) into the performance index (1), holds approximately the subsequent relation:

$$J(X,U) = \int_{t_0}^{t_f} Q(t, X^T\Phi(t), U^T\Phi(t)) dt, \tag{8}$$

where X and U are the same as before. Accordingly, Mathematica software can be computed the integral in Equation (8). Therefore, it can be approximated by $J(X,U) \cong \tilde{F}(X,U)$. In a similar way, substituting from Equations (7) and (6) into the variable-order fractional system (2) yields:

$$\begin{aligned} &(t-t_0)^{-\beta(t)} X^T S^{\beta(t)} \Phi(t) - g(t) \\ &- \int_{t_0}^{t} G(t,s,X^T\Phi(s),U^T\Phi(s)) ds \\ &- \int_{t_0}^{t_f} K(t,s,X^T\Phi(s),U^T\Phi(s)) ds \\ &\cong E(t,X,U) \simeq 0. \end{aligned} \tag{9}$$

The algebraic system of equations are generated by the following scheme. First, we approximate the dynamical system (9) with the above operational matrix (7). Applying the introduced points t_s, Equation (9) can be easily implemented to obtain a system of nonlinear algebraic equations. Then, we get:

$$\Lambda_s \cong E(t_s, X, U) = 0, \tag{10}$$

for $s = 1, \dots, q-1$. Meanwhile, from the initial condition (3) and using approximation (7), we get an algebraic equation as follows:

$$\Lambda_0 \cong X^T \Phi(t_0) - \mathbf{x}_0 = 0. \qquad (11)$$

Now, in order to acquire the solutions of the generated algebraic system, we need to optimize the behavior of cost function (8) in the presence of conditions (10)-(11). So, we pursue the Lagrange multipliers method as follows:

$$J^*(X,U,\lambda) = J(X,U) + \Lambda\lambda,$$

in which $\lambda = [\lambda_0 \ \lambda_1 \ \dots \ \lambda_{2^{k-1}(M-1)}]^T$ are the unknown Lagrange multipliers and $\Lambda = [\Lambda_0 \ \Lambda_1 \ \dots \ \Lambda_{2^{k-1}(M-1)}]$. Thus, in order to assess an extremum for problem (1)-(3), we employed the modified Newton's method to solve the following necessary optimality conditions:

$$\frac{\partial J^*}{\partial X} = 0, \quad \frac{\partial J^*}{\partial U} = 0, \quad \frac{\partial J^*}{\partial \lambda} = 0. \qquad (12)$$

Accordingly, X and U should be successfully computed from Equation (12) to obtain an approximate solution of problem (1)-(3) using Laguerre wavelet functions.

A. The Iterative Algorithm

To combine the scheme developed in the previous section, here we apply an iterative algorithm.

Step 1. Take a positive pre assigned error bound $\epsilon > 0$ and set $i = 1$.

Step 2. Consider positive integer values for the constants k and M, and determine the collocation points.

Step 3. Approximate $x(t)$ and $u(t)$ using Equation (7) and compute the approximation of ${}_0D_t^{\beta(t)}x(t)$ from the method developed in Section 3.

Step 4. Use the approximated values in step 3 and decompose problem (1)-(3) using relations (8)-(11).

Step 5. Construc the system of linear or nonlinear equations given in (12) using the Lagrange multipliers technique. By determining X and U via the modified Newton's method, we have determined the approximated values of the state and control functions.

Step 6. Terminate the algorithm if the expression $e_i = |\frac{J_i - J_{i-1}}{J_i}|$ satisfies $e_i < \epsilon$, else, replace i by $i+1$ and go to step 2.

IV. Convergence Analysis and Error Estimate

Here, we perform the error analysis of the Laguerre wavelet expansion. For this purpose, we assume $|f(t)| \leq C$ in which C is a real positive number.

Theorem 1 If $f(t) \in L^2[0,1]$ is an arbitrary function which can be approximated by an infinite series of Laguerre wavelet functions, then this series converges uniformly to $f(t)$.

Proof. We know, $f(t)$ can be defined as Equation (5) in such a way that $\gamma_{n,m} = \langle f(t), \phi_{n,m} \rangle$. Hence, we have for $n, m > 0$ we have $\gamma_{n,m} = \langle f(t), \phi_{n,m} \rangle = \int_0^1 \phi_{n,m} f(t) dt = \frac{2^{\frac{k}{2}}}{m!} \int_{I_{nk}} f(t) \mathbf{L}_m(2^k t - 2n + 1) dt$, in which $I_{nk} = [\frac{n-1}{2^{k-1}}, \frac{n}{2^{k-1}})$. Upon assigning the change of variable $2^k t - 2n + 1 = p$, yields to:

$$\gamma_{n,m} = \frac{2^{\frac{-k}{2}}}{m!} \int_{-1}^{1} f(\frac{p-1+2n}{2^k}) \mathbf{L}_m(p) dp.$$

Then we will have $|\gamma_{n,m}| \leq \frac{1}{2^{\frac{k}{2}} m!} \int_{-1}^{1} |f(\frac{p-1+2n}{2^k})| \, |\mathbf{L}_m(p)| dp \leq \frac{C}{2^{\frac{k}{2}} m!} \int_{-1}^{1} |\mathbf{L}_m(p)| dp$. According to the properties of continuity and integrability of $\mathbf{L}_m(.)$ on $(-1,1)$, let $\int_{-1}^{1} |\mathbf{L}_m(p)| dp = A$. Then, we get: $|\gamma_{n,m}| \leq \frac{CA}{2^{\frac{k}{2}} m!}$. So, the series $\sum_{n=1}^{2^{k-1}} \sum_{m=0}^{M-1} \gamma_{n,m}$ is absolutely convergent. This means that the presented series in relation (5) is uniformly convergent. Suppose that $P_{nm} = \{\phi_{1,0}, \cdots, \phi_{2^{k-1},(M-1)}\}$ is the set of Laguerre wavelets of nm degree and $\Upsilon = span(P_{nm})$ in which $n = 2^{k-1}$ and $m = M - 1$.

Theorem 2 Let $\tilde{f}(t) = \sigma^T \Phi(t)$ be the best approximation of $f(t)$ from Υ. We will have:

$$\| f - \tilde{f} \|_2 \leq \frac{R}{M! \sqrt{2M+1}},$$

in which $R = max_{\tau \in [0,1]} |f^{(M)}(\tau)|$.

Proof. We know that $\{1, t, t^2, \cdots, t^{M-1}\}$ is a basis set for polynomials space with $M - 1$ degree. Applying Taylor's formula we have $\hat{f}(t) = f(\tau) + f'(\tau)(t-\tau) + \frac{f''(\tau)}{2!}(t-\tau)^2 + \cdots + \frac{f^{(M-1)}(\tau)}{(M-1)!}(t-\tau)^{M-1} + R_{M-1}(t), \quad \tau \in [0,1]$, in which $R_{M-1} = \frac{f^{(M)}(\tau)}{M!}(t-\tau)^M$, $\tau \in [0,1]$. Hence, it is clear that $\left| f(t) - \hat{f}(t) \right| = \frac{t^M f^{(M)}(\tau)}{M!}, \quad \tau \in [0,1]$. Now, due to the error of the Taylor expansion, and using the best approximation concept we obtain $\| f(t) - \tilde{f}(t) \|_2^2 = \| f(t) - \sigma^T \Phi(t) \|_2^2 \leq \sum_{n=1}^{2^{k-1}} \| f(t) - \hat{f}(t) \|_{I_{n,k}}^2 \leq \sum_{n=1}^{2^{k-1}} \int_{I_{n,k}} (f(t) - \hat{f}(t))^2 dt \leq \sum_{n=1}^{2^{k-1}} \int_{I_{n,k}} (\frac{t^M max_{\tau \in I_{n,k}} |f^{(M)}(\tau)|}{M!})^2 dt \leq \int_0^1 (\frac{t^M R}{M!})^2 dt = \frac{R^2}{(M!)^2 (2M+1)}$. According to the computing procedure, we have the absolute error function for this case as follows:

$$E(t) = |f(t) - \sum_{n=1}^{2^{k-1}} \sum_{m=0}^{M-1} \gamma_{n,m} \phi_{n,m}(t)|,$$

wherein $f(t)$ is a continuous bounded function defined on interval $[0,1]$ which can be approximated by the Laguerre wavelet expansion defined in Equation (5). Therefore, based on the above analysis, when M approaches to ∞, the obtained approximate solution with this method converges to the exact solution of problem (1)-(3).

V. Applications

Three examples of OCPs governed by V-FIDE are considered in this section. The calculations related to the examples were done using Mathematica 14.1 from a 2.30 MHz Core i7 PC with 16 GB RAM. Also, we used the default number of digits in Mathematica, that this digit is equal to 10^{-16}. Also, we have been used the following notations:

$$\| E_u \|_2^2 = \| u(t) - u^*(t) \|_2^2 = \int_{t_0}^{t_f} (u(t) - u^*(t))^2 dt,$$

$$\| E_x \|_2^2 = \| x(t) - x^*(t) \|_2^2 = \int_{t_0}^{t_f} (x(t) - x^*(t))^2 dt,$$

to get a fair comparison of performances in which (x, u) and (x^*, u^*) are the couples of approximate and exact solutions, respectively.

Example 1 Consider the following OCP:

$$\underset{u}{\text{Min}} J(x, u) = \int_0^1 (u(t) - t^2)^2 + (x(t) - \text{sin}t)^2 dt,$$

subject to the following Volterra integro-differential equation:

$$ {}_0D_t^{\beta(t)} x(t) =$$

$$g(t) + t^2 x^3(t) + t^2 u^2(t) + \int_0^t s x^3(s) ds,$$

where $x(0) = 0$ and, $g(t) = -t^6 + \text{cos}t + \frac{2}{3} t\text{cos}t - \frac{2}{3}\text{sin}t - \frac{2}{3} t^2 \text{sin}t + \frac{2}{3} t^2 \text{cos}^2 t\text{sin}t + \frac{1}{3} t\text{cos}t\text{sin}^2 t - \frac{1}{9}\text{sin}^3 t - \frac{1}{3} t^2 \text{sin}^3 t$. The analytical solution for this problem is $(x^*(t), u^*(t)) = (\text{sin}t, t^2)$. The Laguerre wavelet polynomials approximation are given as $x(t) \cong \sum_{n=1}^{2^{k-1}} \sum_{m=0}^{M-1} \phi_{n,m}(t) x_{n,m}$, and $u(t) \cong \sum_{n=1}^{2^{k-1}} \sum_{m=0}^{M-1} \phi_{n,m}(t) u_{n,m}$. Considering $\alpha = 0$, $k = 1$ and $M = 4$, we have:

$$\phi_{1,0}(t) = 2\sqrt{2},$$

$$\phi_{2,0}(t) = 2\sqrt{2},$$

$$\phi_{1,1}(t) = 4\sqrt{2} - 16\sqrt{2}t,$$

$$\phi_{2,1}(t) = 8\sqrt{2} - 16\sqrt{2}t,$$

$$\phi_{1,2}(t) = \frac{11}{\sqrt{2}} - 32\sqrt{2}t + 32\sqrt{2}t^2,$$

$$\phi_{1,3}(t) = \frac{40\sqrt{2}}{9} - \frac{284\sqrt{2}t}{9} t + \frac{512\sqrt{2}t^2}{9} - \frac{256\sqrt{2}t^3}{9}.$$

By taking the collocation points $\{t_0 = 0, t_1 = \frac{1}{6}, \dots, t_6 = 1\}$ and following the proposed approximation method, the generated algebraic system for deriving the extremum of J^* can be derived. In order to perform the proposed method, the first stage is executed. The results of this stage, which has been shown in Table 1, are the evolution of J_M^* for different choices of $\beta(t)$ and M, and the values of CPU time required by the proposed scheme for $M = 6$. Detected errors of approximate solutions with $\beta(t) = 1$ are reported in Fig. 1 and Table 2. Also, these results are compared with the presented approach in [36]. With this comparison, we also want to verify the incremental performance of the Laguerre wavelet polynomials in contrast of other literature. These results allow our approach to reach more accurate behaviors than the other literature by selecting fewer iteration.

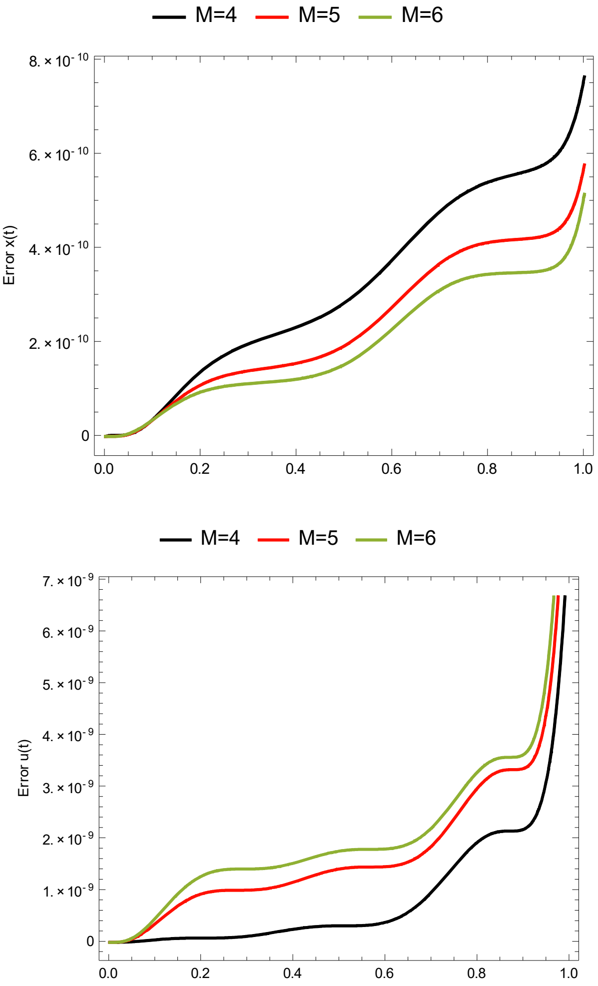

Fig. 1. Absolute errors with $k = 1, \beta(t) = 1$ for Example 1.

TABLE I Evaluated results of J_M^* with $k = 1$ for Example 1.

This study	$\beta(t)$				
	1	$1 - 0.001t$	$1 - 0.05t$	$1 - \text{sin}0.001t$	$1 - \text{sin}0.05t$
$M = 3, k = 1$	8.03644×10^{-7}	7.51393×10^{-7}	1.06269×10^{-5}	7.51393×10^{-7}	1.06193×10^{-5}
$M = 4, k = 1$	9.30188×10^{-9}	8.54271×10^{-9}	1.20137×10^{-5}	8.54255×10^{-9}	1.20053×10^{-5}
$M = 5, k = 1$	1.21444×10^{-8}	1.15061×10^{-8}	1.15228×10^{-5}	1.15063×10^{-8}	1.14577×10^{-5}
$M = 6, k = 1$	1.46575×10^{-8}	1.30573×10^{-8}	1.20035×10^{-5}	1.33206×10^{-8}	1.1949×10^{-5}
CPU Time	31.0781	32.0938	30.7969	31.7031	31.1281

TABLE II Absolute errors with $\beta(t) = 1$ for Example 1.

Method	Number of basis functions	$\parallel E_x \parallel_2^2$	$\parallel E_u \parallel_2^2$
This study	$M = 3, k = 1$	1.37303×10^{-8}	7.89914×10^{-7}
	$M = 4, k = 1$	7.64273×10^{-10}	8.53761×10^{-9}
	$M = 5, k = 1$	5.76936×10^{-10}	1.15675×10^{-8}
Legendre polynomials [36]	$M = 4$	9.5×10^{-7}	1.2×10^{-7}

Example 2 Consider the OCP:

$$\underset{u}{\text{Min}}\ J(x,u) = \int_0^1 ((u(t) - e^t)^2 + (x(t) - e^t)^2)dt,$$

subject to the following Volterra integro-differential equation:

$${}_0D_t^{\beta(t)}x(t) = e^t(1 - t - \frac{e^t}{2}) - e^t(\frac{e^t}{2} + 1) + 1 + \big(t + x(t)\big)u(t) + \int_0^t u(s)ds,$$

where $x(0) = 1$. It should be noted that the analytical solution for this problem is $(x^*(t), u^*(t)) = (e^t, e^t)$. The behavior of cost functional J_M^* using different choices of $\beta(t)$ and M have been shown in Table 3. Also, this table shows we achieve the accurate values with the small number of M in comparision with Haar wavelet and hat functions methods [21, 22]. Also, we obtain the reasonable CPU time for $M = 5$ in this table. Further, we present the absolute errors of control function and optimal trajectory for $\beta(t) = 1$ in Table 4 and Fig. 2. Moreover, Fig. 3 explores the best-fitted evolution results for different choices of $\beta(t)$, $k = 1$ and $M = 5$. This behavior indicates an agreement between the exact and approximate solutions. In addition, this figure illustrates the convergence pattern with depicting solutions for various choices of $\beta(t)$ using a small number of M. This accurate behavior can be improved by increasing the number of M. These excellent evaluations allow us to claim that the variable-order fractional derivatives have been used as benchmark performances in dynamical models.

TABLE III Evaluated results of J_M^* for Example 2.

Number of basis function	$\beta(t)$				
	1	$1 - 0.001t$	$1 - 0.05t$	$1 - \sin 0.001t$	$1 - \sin 0.05t$
$M = 3, k = 1$	1.57744×10^{-4}	1.57154×10^{-4}	1.60185×10^{-4}	1.57154×10^{-4}	1.60173×10^{-4}
$M = 4, k = 1$	1.57939×10^{-6}	1.66966×10^{-6}	3.6558×10^{-5}	1.66967×10^{-6}	3.65479×10^{-5}
$M = 5, k = 1$	3.42939×10^{-7}	7.23057×10^{-7}	3.07637×10^{-5}	7.23057×10^{-7}	3.0768×10^{-5}
$M = 6, k = 1$	3.3273×10^{-7}	3.38541×10^{-7}	3.06707×10^{-5}	3.38541×10^{-7}	3.06618×10^{-5}
$M = 32$ [21]	4.4380×10^{-4}	---	---	---	---
$M = 32$ [22]	1.168×10^{-7}	---	---	---	---
CPU Time	12.0156	13.1406	12.7188	13.5	11.7969

TABLE IV Absolute errors with $\beta(t) = 1$ for Example 2.

Number of basis functions	$\parallel E_x \parallel_2^2$	$\parallel E_u \parallel_2^2$
$M = 2, k = 1$	7.22747×10^{-5}	8.54695×10^{-5}
$M = 3, k = 1$	1.57554×10^{-7}	1.42184×10^{-6}
$M = 4, k = 1$	1.69442×10^{-8}	3.25995×10^{-7}
$M = 5, k = 1$	1.7371×10^{-8}	3.15359×10^{-7}

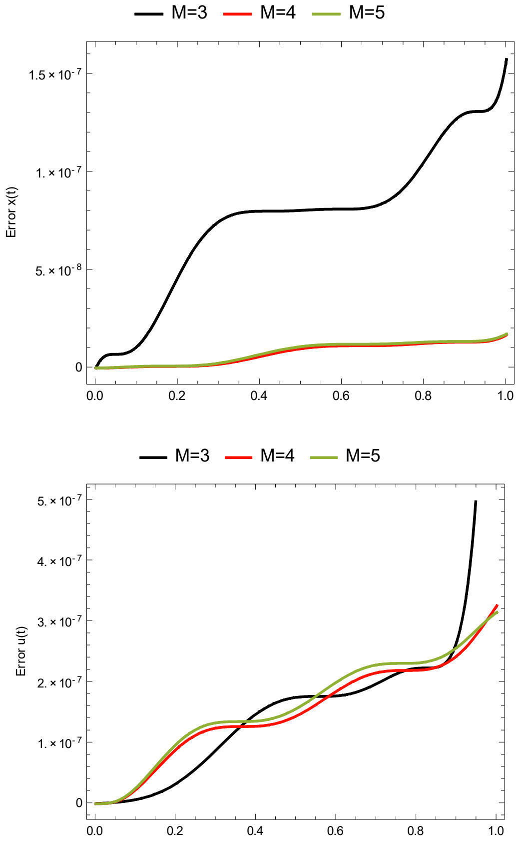

Fig. 2. Evaluated errors with $\beta(t) = 1$ and $k = 1$ for Example 2.

Example 3 Consider the following performance index:

$$\underset{u}{\text{Min}} J(x,u) = \int_0^1 (u(t) - x(t))^2 dt,$$

subject to the following Fredholm integro-differential equation with variable-order fractional derivative:

$${}_0D_t^{\beta(t)}x(t) = e^t - \frac{1}{3}t + \int_0^1 (e^{-2s}s^2tu(s)x'(s))ds,$$

and condition $x(0) = 1$. The behavior of J_M^* using different choices of $\beta(t)$ and M in comparison with other literature have been listed in Table 5. Comparing the results utilize that the Laguerre wavelet functions create good conditions to receive more accurate approaches in the presence of CPU time for $M = 6$. The analytical solutions of this problem are $u^*(t) = e^t$ and $x^*(t) = e^t$. Thus, we present the absolute errors of control function and optimal trajectory for $\beta(t) = 1$ in Fig. 4 and Table 6. In addition, a comparison has been made with the obtained results in [36] in this table. The presented results in Table 6 demonstrate a good agreement with the reported results in other literature. The Evaluated results of $x(t)$ and $u(t)$ for $\beta(t) = 1$ and various choices of M with $k = 1$ are depicted in Fig. 5. This behavior indicates that variable-order models have the capacity to attract the attention of researchers.

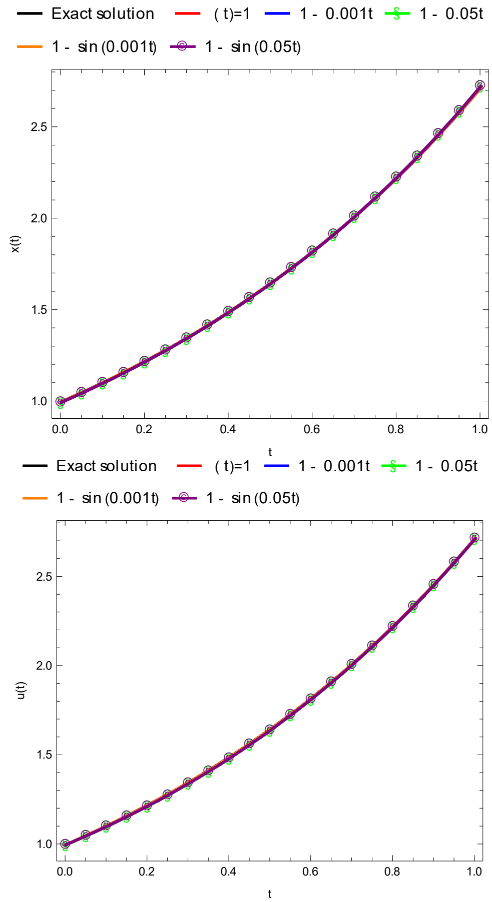

Fig. 3. The state and control functions with some variable-orders $\beta(t)$ and $M = 5$ for Example 2.

Example 4 In this example, we consider the variable-order fractional model of population growth in the form below:

$$ {}_0D_t^{\beta(t)}x(t) = rx(t)\left(1 - \frac{x(t)}{K}\right) - \int_0^t M(t - s)x(s)ds - u(t)x(t), \qquad (13)$$

TABLE V Evaluated results of J_M^* with various choices of $\beta(t)$ for Example 3.

This study	$\beta(t)$				
	1	$1 - 0.001t$	$1 - 0.05t$	$1 - \sin 0.001t$	$1 - \sin 0.05t$
$M = 4, k = 1$	3.77958×10^{-7}	3.78572×10^{-7}	3.78573×10^{-7}	3.73113×10^{-7}	8.032×10^{-3}
$M = 5, k = 1$	4.90204×10^{-7}	4.90968×10^{-7}	4.90969×10^{-7}	4.8358×10^{-7}	9.5512×10^{-3}
$M = 6, k = 1$	5.92307×10^{-9}	5.12684×10^{-7}	6.10464×10^{-9}	7.08212×10^{-9}	1.09014×10^{-2}
VIMP with $M = 2, k = 3$ [6]	4.0135×10^{-4}	---	---	---	---
HAM with $M = 2, k = 3$ [7]	1.09746×10^{-7}	---	---	---	---
PMP with $M = 2, k = 3$ [9]	1.09746×10^{-7}	---	---	---	---
CPU Time	11.4219	11.2969	11.2188	12.3594	10.7969

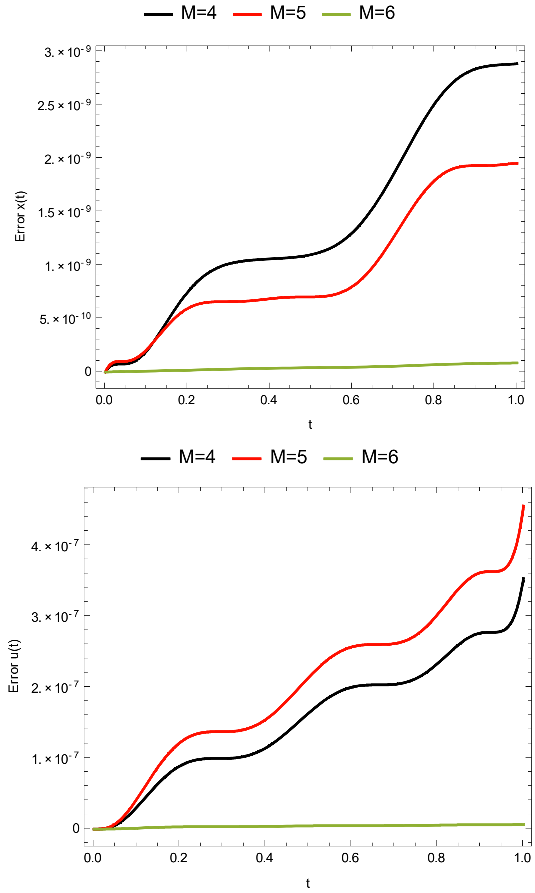

Fig. 4. Absolute errors with $\beta(t) = 1$ and $k = 1$ for Example 3.

TABLE VI Absolute errors with $\beta(t) = 1$ for Example 3.

Method	Number of basis functions	$\parallel E_x \parallel_2^2$	$\parallel E_u \parallel_2^2$
This study	$M = 4, k = 1$	2.88592×10^{-9}	3.534×10^{-7}
	$M = 5, k = 1$	1.95403×10^{-9}	4.55891×10^{-7}
	$M = 6, k = 1$	8.58198×10^{-11}	6.39124×10^{-9}
Legendre polynomials [36]	$M = 2, k = 3$	8.88256×10^{-8}	1.98494×10^{-7}

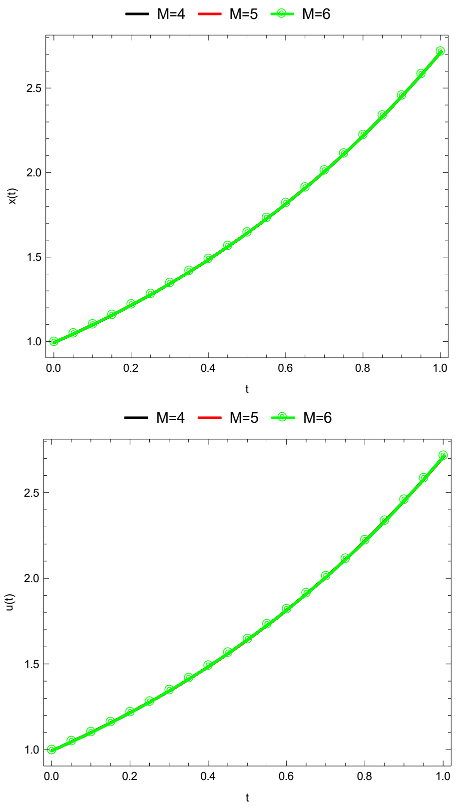

Fig. 5. The Evaluated results of $x(t)$ and $u(t)$ for $\beta(t) = 1$ and various choices of M for Example 3.

in which, $x(t)$ and $u(t)$ signify, respectively, the population biomass and the harvesting effort (or control variable) at time t and the parameters r and K are the intrinsic growth rate and the environmental carrying capacity, respectively. In addition, $M(.)$ is the delayed effects in memory core modeling (e.g. diseases, maturation delay). The harvest rate can be controlled to maximize the total harvested biomass while avoiding population collapse as follows:

$$J(\mathrm{x}, u) = \int_0^T [pu(t)x(t) - cu^2(t)]dt, \tag{14}$$

wherein p and c are the price per unit biomass harvested and the cost coefficient for harvesting effort, respectively. The objective is to design the optimal tracking control $u^*(t)$ which moves the system (13) from the initial population $x(0) = x_0 > 0$ and harvesting effort limits $u(t) \leq u_{\max}$ to maximize (14) over time T. In order to solve the optimal tracking control problem, here we consider the mentioned parameters take the values $r = 0.5$(per year), $K = 1000$(tons), $M(t) = 0.1e^{-0.3t}$, $p = 10$ (price per ton), $c = 1$, $u_{\max} = 2$ and $T = 5$ (years). Simulation results including the cost values are summarized in Table 7. This table indicates that for different values of $\beta(t)$, the numerical achievements decrease as the value of M increases. Fig. 6 shows the plots of $x(t)$ and $u(t)$ after different iterations for $\beta(t) = 1 - 0.001t$ and $k = 1$. The perspective view of this figure confirms that the proposed approach works well to solve the optimal tracking control problem (13)-(14).

TABLE VII Evaluated results of J_M^* with various choices of $\beta(t)$ for Example 4.

Number of basis function	$\beta(t)$		
	1	$1 - 0.001t$	$1 - \sin 0.01t$
$M = 4, k = 1$	22.1772	22.1722	22.1269
$M = 5, k = 1$	18.8498	18.8459	18.8113
$M = 6, k = 1$	17.0781	17.0747	17.0452
CPU Time for $M = 6$	4.42188	4.70313	4.75

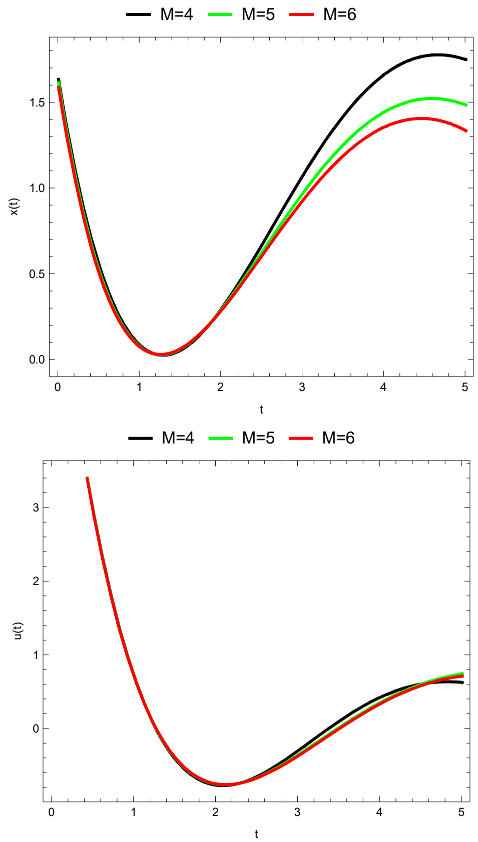

Fig. 6. The Evaluated results of $x(t)$ and $u(t)$ for $\beta(t) = 1 - 0.001t$ and various choices of M for Example 4.

VI. Conclusion

A joint application of variable-order fractional calculus and optimal control theory was presented to obtain the efficient control of V-FIDE. Through using Laguerre wavelets, the state and control variables are expanded. Also, the operational matrix of Liouville-Caputo variable-order fractional derivative is deduced for the mentioned polynomials. Consequently, the procedure of the constrained extremum problem supported by the collocation method is utilized to convert this OCP into some nonlinear algebraic equations that can be solved via any arbitrary iteration method. Approximate solutions utilize a high accuracy with a small number of iterations. Simulations with various costs of variable-order $\beta(t)$ and iteration M, support the effectiveness of this method.

Since each wavelet component is actually a differently scaled bandpass filter in the frequency domain, the signal analysis capability of the wavelet transform is limited in the time frequency plane and, therefore, the wavelet transform is inefficient for processing signals whose energy is not well concentrated in the frequency domain.

The study of variable-order fractional-integro OCPs represents an advanced frontier in fractional calculus. Continued research and development in this area hold the promise of significantly enhancing the effectiveness and applicability of optimal control strategies across various scientific and engineering domains. The results of this paper present an encouraging view for future discussion. Indeed, for the recently developed of fractional equations, the theoretical justification on the merit of this method will enhance the engineers, physicists and other scientists to use these results for their practical objectives.

REFERENCES

[1] H. Alrabaiah, I. Ahmad, R. Amin and K. Shah, "A numerical method for fractional variable order pantograph differential equations based on Haar wavelet," *Eng. Comput.*, 38 (2022) 2655-2668.

[2] J. António Tenreiro Machado and B. Parsa Moghaddam, "A robust algorithm for nonlinear variable-order fractional control systems with delay," *Int. J. Nonlinear Sci. Numer. Simul.*, 19 (3-4) (2018) 231-238.

[3] M. Alipour and S. Soradi Zeid, "Optimal control of Volterra integro-differential equations based on interpolation polynomials and collocation method," *Comput. Methods Differ. Equ.*, 11(1) (2023) 52-64.

[4] R. Almeida, D. Tavares and D.F. Torres, "The Variable-Order Fractional Calculus of Variations," Cham, Switzerland: *Springer International Publishing*, 2019.

[5] S. Ahmed, S. Jahan, K. Shah and T. Abdeljawad, "On computational analysis via fibonacci wavelet method for investigating some physical problems," *J. Appl. Math. Comput.*, 71(1) (2025) 531-550.

[6] M. Alipour, M.A. Vali, "Approximate optimal control of Volterra-Fredholm integral equations based on parametrization and variational iteration method," *Math. Commun.* 26 (2021) 107-119.

[7] M. Alipour, M.A. Vali, A.H. Borzabadi, "A direct approach for approximate optimal control of integro-differential equations based on homotopy analysis and parametrization method," *IMA J. Math. Control. Inf.* 34 (2) (2017) 611-630.

[8] M. Bilal, A. Ghafoor, M. Hussain, K. Shah and T. Abdeljawad, "Numerical Scheme for the Computational Study of Two Dimensional Diffusion and Burgers' Systems with Stability and Error Estimate," J. Nonlinear Math. Phys., 32(1) (2025) 1-23.

[9] A. H. Borzabadi, M. Azizsefat, "Numerically solution of optimal control problems governed by integro-differential equation via a hybrid iterative scheme," WASJ, 10 (2010) 538-543.

[10] H. Dehestani and Y. Ordokhani, "A numerical study on fractional optimal control problems described by Caputo-Fabrizio fractional integro-differential equation," Optim. Control. Appl. Methods., 44(4) (2023) 1873-1892.

[11] M. Du, Z. Wang and H. Hu, "Measuring memory with the order of fractional derivative," Sci. Rep., 3 (1) (2013) 3431.

[12] G. Dewangan, A. Singh and A. Kanaujiya, "Generalized distributed-order fractional optimal control problem using Laguerre wavelet method," J. Math. Modell., (2025) 707-725.

[13] G. Ghanbari and M. Razzaghi, "Numerical solutions for distributed-order fractional optimal control problems by using generalized fractional-order Chebyshev wavelets," Nonlinear Dyn., 108(1) (2022) 265-277.

[14] M.H. Heydari and Z. Avazzadeh, " A direct computational method for nonlinear variable-order fractional delay optimal control problems," Asian J. Control., 23 (6) (2021) 2709-2718.

[15] H. Hassani and Z. Avazzadeh, "Transcendental Bernstein series for solving nonlinear variable order fractional optimal control problems," Appl. Math. Comput., 362 (2019) 124563.

[16] H. Hassani, Z. Avazzadeh and J.A.T. Machado, "Solving two-dimensional variable-order fractional optimal control problems with transcendental Bernstein series," J. Comput. Nonlinear Dyn., 14 (6) (2019) 061001.

[17] M.H. Heydari, M. Razzaghi and Z. Avazzadehm, "Orthonormal piecewise Bernoulli functions: Application for optimal control problems generated using fractional integro-differential equations," J. Vib. Control., 29 (5-6) (2023) 1164-1175.

[18] M. Izadi and H. M. Srivastava, "A novel matrix technique for multi-order pantograph differential equations of fractional order," Proc. R. Soc. A, 477(2253) (2021) 20210321.

[19] A. Keimer and L. Pflug, "Modeling infectious diseases using integro-differential equations: Optimal control strategies for policy decisions and Applications in COVID-19," Res Gate., (2020) 10.13140/RG.2.2.10845.44000.

[20] R. Khanduzi, A. Ebrahimzadeh and S.P.A. Beik, "Optimal control of fractional integro-differential systems based on a spectral method and grey wolf optimizer," Int. J. Optim. Control: Theor. Appl., (IJOCTA). 10 (1) (2020) 55-65.

[21] K. Maleknejad and A. Ebrahimzadeh, "The use of rationalized Haar wavelet collocation method for solving optimal control of Volterra integral equations," J. Vib. Control., 21 (2015) 1958-1967.

[22] F. Mirzaee, E. Hadadiya, "Numerical solution of optimal control problem of the non-linear Volterra integral

equations via generalized hat functions," IMA J. Math. Control Inf. 34(3) (2017) 889-904.

[23] M. Michalska and J. Szynal, "A new bound for the Laguerre polynomials," J. Comput. Appl. Math., 133 (1-2) (2001) 489-493.

[24] S.S. Ray and S. Behera, 'Two-dimensional wavelets operational method for solving Volterra weakly singular partial integro-differential equations," J. Comput. Appl. Math., 366 (2020) 112411.

[25] N. Sweilam, S. Mahyoub Al-Mekhlafi, O. Albalawi and J. Tenreiro Machado, "Optimal control of variable-order fractional model for delay cancer," App. Math. Modell., 89 (2021) 1557-1574.

[26] S. Soradi-Zeid, H. Jahanshahi, A. Yousefpour and S. Bekiros, "King algorithm: A novel optimization approach based on variable-order fractional calculus with application in chaotic financial systems," Chaos Solit. Fract., 132 (2020) 109569.

[27] S. Sabermahani, Y. Ordokhani, K. Rabiei and M. Razzaghi, "Solution of optimal control problems governed by volterra integral and fractional integro-differential equations," J. Vib. Control., 29(15-16) (2023) 3796-3808.

[28] S. Sabermahani and Y. Ordokhani, "Solving distributed-order fractional optimal control problems via the Fibonacci wavelet method," J. Vib. Control, 30(1-2) (2024), 418-432.

[29] S. Sabermahani, Y. Ordokhani and P. Rahimkhani, "Application of generalized Lucas wavelet method for solving nonlinear fractal-fractional optimal control problems," Chaos Solit. Fract., 170 (2023) 113348.

[30] S. Soradi-Zeid and M. Alipour, "A collocation method using generalized Laguerre polynomials for solving nonlinear optimal control problems governed by integro-differential equations," J. Comput. Appl. Math., 436 (2024) 115410.

[31] K. Shah, M. Sarwar and T. Abdeljawad, "Modeling Virus Mutation Dynamics Using Piecewise Fractional Derivatives," Eur. J. Pure Appl. Math., 18(2) (2025) 6053-6053.

[32] A. Singh, A. Kanaujiya and J. Mohapatra, "Chelyshkov wavelet method for solving multidimensional variable order fractional optimal control problem," J. Appl. Math. Comput., 70(4) (2024) 3135-3160.

[33] A. Singh, A. Kanaujiya and J. Mohapatra, "Euler wavelets method for optimal control problems of fractional integro-differential equations," J. Comput. Appl. Math., 454 (2025) 116178.

[34] A. Singh, A. Kanaujiya and J. Mohapatra, "An efficient generalized Lucas wavelet operational matrix method for optimal control problems," J. Comput. Appl. Math., (2025) 116749.

[35] F. Soufivand, F. Soltanian and K. Mamehrashi, "An operational matrix method based on the Gegenbauer polynomials for solving a class of fractional optimal control problems," Int. J. Ind. Electron. Control Optim., 4(4) (2021) 475-484.

[36] E. Tohidi and O.R.N. Samadi, "Optimal control of nonlinear Volterra integral equations via Legendre polynomials," IMA J. Math. Control Inf., 30(1) (2013) 67-83.

[37] C.A. Valentim, J.A. Rabi, S.A. David and J.A.T. Machado. "On multistep tumor growth models of fractional variable-order," Biosystems, 199 (2021) 104294.

[38] Q. Yu, V. Vegh, F. Liu and I. Turner, "A variable order fractional differential-based texture enhancement algorithm with application in medical imaging," PLOS ONE, 10(7) (2015) e0132952.

[39] X. Zheng, H. Wang, "A hidden-memory of variable-order time-fractional optimal control model: Analysis and approximation," SIAM J. Control Optim., 59 (3) (2021) 1851-1880.

[40] S.S. Zeid, S, Effati and A.V. Kamyad, "Approximation methods for solving fractional optimal control problems," Comput. Appl. Math., 37(2018) 158-182.

Maryam Alipour was born in Mazandaran, Iran. She received her M.Sc. degree in Applied Mathematics from the University of Mazandaran, Iran, in 2010. She earned her Ph.D. in Applied Mathematics from Shahid Bahonar University of Kerman, Iran in 2016. She is currently an Assistant Professor at the University of Sistan and Baluchestan, Zahedan, Iran. Her current research interests include numerical analysis, optimal control, and iterative methods.

Samaneh Soradi-Zeid received his B.S. degree in Apllied Mathematics fom National University of Birjand, Iran, in 2010, and his M.S. degree in Operation Research from Sharif University of Tehran, Iran, in 2012 and his Ph.D. degree in Optimal Control and Optimization from Ferdowsi University of Mashhad, Iran, in 2017. From September 2018 she works at the Faculty of Industry and Mining (khash), University of Sistan and Baluchestan, Zahedan. Iran. Her current research interests include Fractional Optimal control, Delay differential Equations, Nonlinear Optimization, Collocation and Spectral Methods.

IECO

This page intentionally left blank.

IECO International Journal Of Industrial Electronics Control and Optimization
Print ISSN: 3517-2645
Online ISSN: 3568-2645
Homepage: https://ieco.usb.ac.ir/

State-of-Charge Fusion Estimation of Lithium-Ion Batteries based on the Mathematical Models of the Open Circuit Voltage Curve

Mohammad Moodi[1] | Mohammad Reza Ramezani-al[2]

Department of Electrical Engineering, Faculty of Electrical and Computer Engineering, Quchan University of Technology, Quchan, Iran.[1,2]
Corresponding author's email: m-ramezani@qiet.ac.ir

Article Info

Article type:
Research Article

Article history:
Received: 23-June-2025
Received in revised form:
24-August-2025
Accepted: 14-September-2025

Keywords:
Fusion estimation,
Lithium-Ion battery,
OCV-SOC curve,
State-of-charge.

ABSTRACT

Accurate state-of-charge (SOC) estimation is essential for the safe and efficient operation of lithium-ion batteries in electric vehicles and energy storage systems. This paper proposes a fusion-based SOC estimation method that integrates two extended Kalman filters (EKFs), each paired with a distinct open-circuit voltage (OCV)–SOC model. The fusion strategy, grounded in Bayesian probability and residual error analysis, dynamically assigns weights to each model's output, ensuring that the most appropriate model contributes predominantly to the final SOC estimate at any given moment. The proposed framework utilized a second-order equivalent circuit model (ECM) and estimates parameters online via a variable forgetting factor recursive least squares (VFFRLS) algorithm. Simulation results under LA92 and UDDS driving cycles demonstrate that the method achieves superior accuracy and robustness, reducing the maximum estimation error by up to 26% and RMSE by over 10% compared to conventional EKF approaches. These findings highlight the method's effectiveness and adaptability for real-time battery management applications.

I. Introduction

In response to global energy constraints and the accelerating shift toward low-carbon technologies, lithium-ion batteries have become indispensable across a wide range of applications, including electric vehicles (EVs), consumer electronics, and renewable energy systems [1], [2]. Their high energy density, long cycle life, and rapid charging capabilities make them ideal for modern energy storage [3], [4]. Central to effective battery management is accurate estimation of the SOC, which reflects the remaining capacity of a battery relative to its full charge. SOC estimation is critical for ensuring safety, optimizing performance, and extending battery lifespan [5], [6].

Recent literature classifies SOC estimation techniques into two categories: direct and indirect. Among direct methods, the Coulomb Counting (CC) approach is widely adopted for its simplicity [7]. However, its reliance on the initial SOC value and open-loop design often causes error accumulation [8]. To address these issues, indirect methods have gained prominence and are further divided into adaptive filters and artificial intelligence (AI) techniques. AI approaches, such as recurrent neural networks (RNN) [9], feed-forward neural networks (FNN) [10], and support vector machines (SVM) [11], leverage experimental data to model the nonlinear relationship between SOC and external parameters. Despite their accuracy, AI methods require extensive data and computational resources, which limits their practical applicability. On the other hand, adaptive filter-based techniques strike a balance between simplicity and accuracy, making them cost-effective and suitable for resource-limited embedded systems. These methods involve selecting a battery model and determining its parameters, deriving the OCV-SOC relationship, and designing a state estimation algorithm.

Over the past decade, researchers have developed a range of adaptive filter algorithms to improve the accuracy and robustness of battery state estimation. Among these, the Kalman filter (KF) family—including the EKF, unscented Kalman filter (UKF), and cubature Kalman filter (CKF)—has been widely adopted due to its balance of computational

Publisher: University of Sistan and Baluchestan

efficiency and estimation performance [5], [12], [13]. Other methods, such as H∞ filters and RLS, have also been explored. While RLS is effective for parameter identification in ECM, it struggles with divergence in nonlinear systems [12]. The H∞ filter offers robustness under uncertainty[14], but introduces significant computational complexity, making it less suitable for embedded applications with limited resources. Among these, EKF remains a preferred choice for SOC estimation due to its simplicity and adaptability to nonlinear battery dynamics [15]. However, even the most refined filtering algorithms face limitations when applied uniformly across different operating conditions.

To address these limitations, fusion techniques have emerged as a powerful solution for enhancing SOC estimation accuracy and robustness. Battery behavior is inherently nonlinear and varies across discharge intervals due to electrochemical dynamics, temperature effects, and aging. A single model or algorithm may perform well in one interval but poorly in others. Fusion methods allow the integration of multiple models and algorithms, each selected based on its performance in specific operating conditions. This approach not only improves estimation accuracy but also enhances generalizability across battery types and environments. Moreover, fusion techniques can mitigate noise sensitivity and provide smoother outputs, making them particularly valuable for real-world applications such as electric vehicles and energy storage systems.

In recent years, fusion-based SOC estimation techniques have gained prominence for their ability to combine the strengths of multiple models and algorithms. For instance, Wu et al. [16] proposed a multidimensional element space mapping architecture (MESMA) that integrates an ECM with convolutional neural networks (CNN) and XGBoost, achieving high adaptability across temperatures but introducing computational complexity. Cheng et al. [17] introduced a three-interval fusion approach for SOC estimation, leveraging fitness-based model-algorithm selection to enhance accuracy. Zhou et al. [18] presented a hybrid MIEKPF-EKPF algorithm for SOC and state of health (SOH) estimation in Lithium-ion batteries, integrating multi-innovation theory with extended Kalman particle filtering. By compensating for aging effects and leveraging past observations, it achieves high accuracy. Li et al. [19] introduced a multi-model fusion framework using Thevenin and second-order ECMs, UKF, and Bayesian weighting, achieving SOC estimation errors within 1% and incorporating fault diagnosis via residual innovation sequences. Chen et al. [20] developed a multi-task learning network for simultaneous SOC and state of energy (SOE) estimation using multi-layer feature extraction and expert layers, offering high fusion accuracy but remaining sensitive to input noise. Collectively, these studies underscore the potential of fusion-based SOC estimation to enhance precision, fault tolerance, and adaptability. Despite these advancements, fusion methods often face challenges related to computational complexity, model transparency, and real-time applicability.

The OCV-SOC relationship in lithium-ion batteries is influenced by several factors, including temperature, aging, and discharge rate. Accurate SOC estimation hinges on the ability to model this nonlinear curve effectively, as it directly impacts the reliability of model-based predictions. Consequently, the mathematical formulation used to represent the OCV-SOC relationship plays a critical role in determining estimation accuracy. In most existing literature, this curve is approximated using polynomial, exponential, or piecewise functions [13], [21], [22]. However, a single model often fails to capture the full spectrum of nonlinear behavior across varying operating conditions, limiting its generalizability and precision.

To address this issue, this paper introduces a fusion estimation method based on the EKF to enhance the accuracy of SOC estimation under diverse operating conditions. The proposed algorithm significantly improves robustness, effectiveness, and reliability while maintaining computational simplicity—unlike conventional fusion strategies that often involve complex switching logic and high processing demands. In this method, two optimal mathematical models are independently selected from a set of seven well-established OCV-SOC models in the literature, based on error analysis. These models are embedded into two separate ECMs, each integrated with its own EKF algorithm, resulting in two distinct SOC estimations at each time step. Additionally, the RLS algorithm with a variable forgetting factor is employed to estimate ECM parameters online. The final SOC value is obtained by fusing the two estimations, with fusion weights determined by the statistical characteristics of the residual error in terminal voltage (RETV), thereby enhancing overall accuracy and reliability.

The remainder of the paper is organized as follows: Section 2 introduces the selected ECM and derives the governing equations for its parameters. Section 3 presents the proposed fusion algorithm in detail. Section 4 provides simulation results and evaluates the performance of the proposed method alongside benchmark algorithms. Finally, Section 5 concludes the paper with final remarks and potential directions for future research.

II. Battery modeling and parameter identification algorithm

A. Battery model

The accuracy of the battery model significantly affects the precision of SOC estimation algorithms, but computational constraints in industrial applications necessitate a balance between simplicity and accuracy [23]. Lithium-ion battery models are generally categorized into ECMs[24], data-driven AI models [25], and electrochemical models [26]. ECMs are widely used due to their ease of implementation

[27], reasonable computational burden [2], and adequate accuracy, making them suitable for online applications. A review of eleven ECMs identifies first-order (1RC) and second-order (2RC) RC models as the most reliable and accurate [28]. The 1RC model, while less complex, struggles in dynamic situations, whereas the 2RC model performs better under varying currents and C-rates, making it ideal for applications such as laptops and electric vehicles [29]. Based on this, the proposed algorithm in this paper was tested under highly dynamic scenarios, with the 2RC model selected to effectively represent battery behavior.

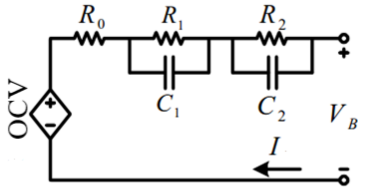

Fig. 1. The 2RC model of the lithium-ion battery

In the 2RC model, the OCV represents the battery's terminal voltage when it reaches internal equilibrium with zero load current. The internal resistance (R_0), terminal voltage ($V_B(t)$), and polarization states (R_1, C_1, R_2, C_2) are parameters used to describe the battery's internal electrochemical behavior. Based on Fig. 1 and basic circuit principles, the mathematical expressions for the 2RC model are derived as follows:

$$\begin{cases} C_1 \dfrac{dV_1(t)}{dt} + \dfrac{V_1(t)}{R_1} = I(t) \\ C_2 \dfrac{dV_2(t)}{dt} + \dfrac{V_2(t)}{R_2} = I(t) \end{cases} \tag{1}$$

So, we have:

$$\begin{cases} \dot{V}_1(t) = -\dfrac{V_1(t)}{R_1C_1} + \dfrac{I(t)}{C_1} \\ \dot{V}_2(t) = -\dfrac{V_2(t)}{R_2C_2} + \dfrac{I(t)}{C_2} \\ V_B(t) = OCV(t) - R_0I(t) - V_1(t) - V_2(t) \end{cases} \tag{2}$$

The discretized form of the 2RC model is given by:

$$\begin{cases} V_1(k+1) = V_1(k)e^{-\frac{T_s}{R_1C_1}} + I(k)R_1\left(1 - e^{-\frac{T_s}{R_1C_1}}\right) \\ V_2(k+1) = V_2(k)e^{-\frac{T_s}{R_2C_2}} + I(k)R_1\left(1 - e^{-\frac{T_s}{R_2C_2}}\right) \\ V_B(k) = OCV(k) - R_0I(k) - V_1(k) - V_2(k) \end{cases} \tag{3}$$

where, T_s is the sampling time and k and $k+1$ represent the consequence times.

B. Parameter identification

Model parameters can be estimated online or offline, with online estimation being more precise due to variations in temperature, SOC, and other factors. The RLS algorithm is a well-known method for estimating battery parameters and is easy to implement online [30], [31]. However, its accuracy diminishes with increasing data volumes. To address this, a forgetting factor (FF) is used to prioritize new data, but a constant FF is unsuitable for varying conditions. Therefore, the variable forgetting factor RLS (VFFRLS) algorithm is applied in this paper to estimate the 2RC model's parameters online, accommodating time-varying conditions. Suppose at sampling time k, system output is written as:

$$Y(k) = \phi(k)\theta(k)^T + \varepsilon(k) \tag{4}$$

Where $\phi(k)$ represents the vector of known information, $\theta(k)$ denotes the vector of unknown parameters, $Y(k)$ is the system's output, and $\varepsilon(k)$ is random noise. The primary equations of the RLS algorithm with a forgetting factor are:

$$\begin{cases} K(k) = -\dfrac{P(k-1)\phi(k)}{\lambda + \phi(k)^T P(k-1)\phi(k)} \\ e(k) = Y(k) - \phi(k)^T\theta(k-1) \\ \theta(k) = \theta(k-1) + K(k)e(k) \\ P(k) = \dfrac{1}{\lambda}\left(I - K(k)\phi(k)^T\right)P(k-1) \end{cases} \tag{5}$$

where $K(k)$ is the estimator gain, $P(k)$ is the covariance matrix, $e(k)$ is the error vector, and λ is the forgetting factor. The variable forgetting factor λ(k) is selected at each sampling time using the following rule [32]:

$$\lambda(k) = \begin{cases} \lambda_{max};\ (0 < |e(k)| < 0.005) \\ \lambda_{max} - (\lambda_{max} - \lambda_{min})\left(\dfrac{|e(k)|}{e_{max}}\right)^2;\ (0.005 < |e(k)| < 0.05) \\ \lambda_{min} = V_B(k);\ \text{for } |e(k)| \geq 0.05 \end{cases} \tag{6}$$

The value of e_{max} is considered 0.01 and generally $0.95 < \lambda < 1$. Using measured data at each sampling time and the VFFRLS algorithm, all model parameters are identified online.

C. OCV-SOC Curve's Mathematical Models

The relationship between OCV and SOC in lithium-ion batteries is inherently nonlinear and is typically characterized through offline experimental measurements. To model this behavior, a variety of mathematical functions including high-order polynomials (commonly 7th), logarithmic, exponential, and hybrid formulations have been proposed, each offering distinct advantages and limitations [13]. Table I summarizes representative OCV–SOC models frequently cited in the literature, reflecting a range of strategies for capturing this nonlinear behavior.

Rational and logarithmic models (e.g., Models 1 and 6) are particularly effective near SOC boundaries but may introduce singularities at low SOC values. High-order polynomial models (Model 2) provide strong curve-fitting capabilities; however they are prone to overfitting and can become unstable outside the calibration range. Exponential models (Model 3) can represent steep voltage transitions, though they require careful parameter tuning. Sinusoidal models (Model 4) may capture subtle voltage oscillations, though they lack physical interpretability in battery systems. Gaussian-like models (Model 5) provide localized fitting and smooth transitions, but their performance can be sensitive to the choice of initial parameters. Ultimately, the accuracy and suitability of each model depend on the specific battery chemistry, design, desired precision, computational constraints, and application context. These models are further evaluated based on their accuracy in Section 4.

TABLE I OCV-SOC Mathematical models in literature

num	Mathematical Model	Reference
1	$OCV = K_0 + K_1 SOC + \frac{K_2}{SOC} + K_3 \ln(SOC) + K_4 \ln(1 - SOC)$	[33]
2	$OCV = K_1 SOC^7 + K_2 SOC^6 + K_3 SOC^5 + K_4 SOC^4 + K_5 SOC^3 + K_6 SOC^2 + K_7 SOC + K_8$	[13]
3	$OCV = K_1 e^{\alpha 1.SOC} + K_2 e^{\alpha 2.SOC} + K_3 SOC^2$	[22]
4	$OCV = K_1 \sin(\alpha_1 SOC + \beta_1) + K_2 \sin(\alpha_2 SOC + \beta_2) + K_3 \sin(\alpha_3 SOC + \beta_3)$	[21]
5	$OCV = K_1 e^{\left(\frac{SOC-\alpha_1}{\beta_1}\right)^2} + K_2 e^{\left(\frac{SOC-\alpha_2}{\beta_2}\right)^2} + K_3 e^{\left(\frac{SOC-\alpha_3}{\beta_3}\right)^2}$	[21]
6	$OCV = K_0 + \frac{K_1}{SOC} + \frac{K_2}{SOC^2} + \frac{K_3}{SOC^3} + \frac{K_4}{SOC^4} + K_5 SOC + K_6 \ln(SOC)$	[34]

III. SOC estimation algorithms

A. SOC estimation by EKF method

The KF is a commonly used tool for estimating dynamic system states across various industries. Its nonlinear variant, the EKF, is widely utilized for battery SOC estimation. The EKF algorithm is implemented using the discrete state equations of the battery model, which are provided in Eq. 7.

$$\begin{cases} \begin{bmatrix} SOC(k+1) \\ V_1(k+1) \\ V_2(k+1) \end{bmatrix} = \begin{bmatrix} 1 & 0 & 0 \\ 0 & e^{\frac{-\Delta t}{R_1 C_1}} & 0 \\ 0 & 0 & e^{\frac{-\Delta t}{R_2 C_2}} \end{bmatrix} \begin{bmatrix} SOC(k) \\ V_1(k) \\ V_2(k) \end{bmatrix} + \begin{bmatrix} \frac{\Delta t}{C_{bat}} \\ R_1\left(1 - e^{\frac{-\Delta t}{R_1 C_1}}\right) \\ R_2\left(1 - e^{\frac{-\Delta t}{R_2 C_2}}\right) \end{bmatrix} . I(k) + \omega(k) \\ V_B(k) = \begin{bmatrix} \frac{dOCV(soc(k))}{dSOC(k)} & -1 & -1 \end{bmatrix} \begin{bmatrix} SOC(k) \\ V_1(k) \\ V_2(k) \end{bmatrix} - R_0 I(k) + \nu(k) \end{cases} \tag{7}$$

In Eq. (7), the battery current $I(k)$ and terminal voltage $V_B(k)$ are considered as the input and output of the system, respectively. The state vector is defined as $[SOC, V_1, V_2]$, where V_1 and V_1 represent the voltages across the RC blocks. The term $\omega(k)$ denotes the stochastic process noise, which is unmeasurable and affects the system states, while $\nu(k)$ represents the measurement noise. Also, Δt is the sampling interval, and C_{bat} is the battery capacity. Fig. 2 demonstrates the SOC estimation process using the EKF algorithm.

At each sampling interval, battery voltage and current are measured, and battery parameters are determined via the VFFRLS technique and battery equations. Then, the SOC is estimated using the EKF algorithm and the OCV-SOC model (Eq. 7). Finally, accuracy is verified by comparing the estimated SOC with experimental values obtained through the CC method.

B. SOC estimation with proposed fusion method

Model-based SOC estimation of lithium-ion batteries requires the mathematical representation of the OCV-SOC curve and its variation with respect to SOC, i.e., $\frac{\mathrm{dOCV(soc(k))}}{\mathrm{dSOC(k)}}$, as described in the state space equations (Eq. 7). Although polynomial functions are commonly used in the literature to model this curve, they cannot account for all situations and working conditions. This paper proposes a fusion SOC estimation process that employs two EKF algorithms simultaneously, each utilizing a different mathematical model from Table 1 to represent the OCV-SOC curve. The final SOC is calculated as a linear combination of the two SOC estimates at each sampling time, as shown in Eq. 8.

$$\begin{cases} SOC_f(k) = W_1(k) SOC_1(k) + W_2(k) SOC_2(k) \\ W_1(k) + W_2(k) = 1 \end{cases} \tag{8}$$

where, $SOC_1(k)$ and $SOC_2(k)$ are the estimated SOCs using each EKF, $W_1(k)$ and $W_2(k)$ are the weights of each estimation, and $SOC_f(k)$ is the final fusion estimation value. Fig. 3 illustrates SOC estimation in the proposed fusion method.

In the proposed fusion estimation method, determining the weight of each SoC estimate at every sampling time is essential. The RETV serves as a key metric for evaluating the accuracy of SoC estimations produced by each EKF estimator [33], [35]. The weight assigned to each estimate is inversely related to its RETV (higher error leads to lower weight, and vice versa). This relationship is expressed as:

$$r_i(k) = V_B(k) - \hat{V}_{Bi}(k) \tag{9}$$

where $V_B(k)$ is the measured terminal voltage and $\hat{V}_{Bi}(k)$ is the voltage estimated by the i$^{\text{th}}$ EKF.

However, RETV alone is insufficient for robust accuracy assessment in parallel algorithms. To enhance its reliability, we incorporate statistical properties of RETV into the weight calculation. Assuming RETV follows a normal distribution, Bayes' theorem is applied to derive a conditional probability density function (PDF) for each estimator at time k:

$$f(V_B(k)|p_i) = \frac{1}{\sqrt{2\pi S_i(k)}} \exp\left(-\frac{1}{2}\ \bar{r}_i^{\,2}(k) S_i(k)\right) \tag{10}$$

where:

$$\begin{cases} \bar{r}_i(k) = \frac{1}{L_m} \sum_{j=k-L_m+1}^{k} r_{ij} \\ S_i(k) = \frac{1}{L_m} \sum_{j=k-L_m+1}^{k} \left(r_{ij} - \bar{r}_{ik}\right)^2 \end{cases} \tag{11}$$

Here, p_i denotes the parameter set of the i^th EKF estimator, and $\bar{r}_i(k)$ and $S_i(k)$ represent the mean and variance of RETV over a sliding window of length L_m.The shape of the likelihood function is directly influenced by these RETV statistics: A lower mean error and variance result in a sharper, higher peak in the probability density function (PDF), indicating greater confidence in the estimator. Conversely, a higher mean or variance produces a flatter, lower peak, reflecting reduced reliability.

This probabilistic interpretation enables the fusion algorithm to dynamically favor estimators that demonstrate more consistent and accurate performance.

The value of L_m has a significant impact on the algorithm's performance. While increasing the length of L_m can improve accuracy, it also increases computational cost. Therefore, the optimal L_m should be chosen by balancing these two factors. Table VI presents the results, showing how different L_m values affect both the average computation time and SoC estimation accuracy. According to the data, when $L_m$exceeds 400, there is no further improvement in accuracy—only an increase in computation time. Considering this trade-off, a length of 300 was chosen for L_m in this study.

For sampling times $k < L_m$, the values of $\bar{r}_i(k)$ and $S_i(k)$ are initialized to one to ensure stability during startup. Finally, the weight for each estimator is computed using the normalized posterior probability:

$$W_i(k) = P(p_i|V_B(k))$$

$$= \left(1 - \frac{f(V_B(k)|p_i)S_i(k)}{\sum_{j=1}^{2} f(V_B(k)|p_j)S_j(k)}\right) \qquad (12)$$

This fusion strategy enhances the baseline SoC estimation algorithm (Section 3.1) by improving accuracy, robustness, and reliability with minimal additional computational load.

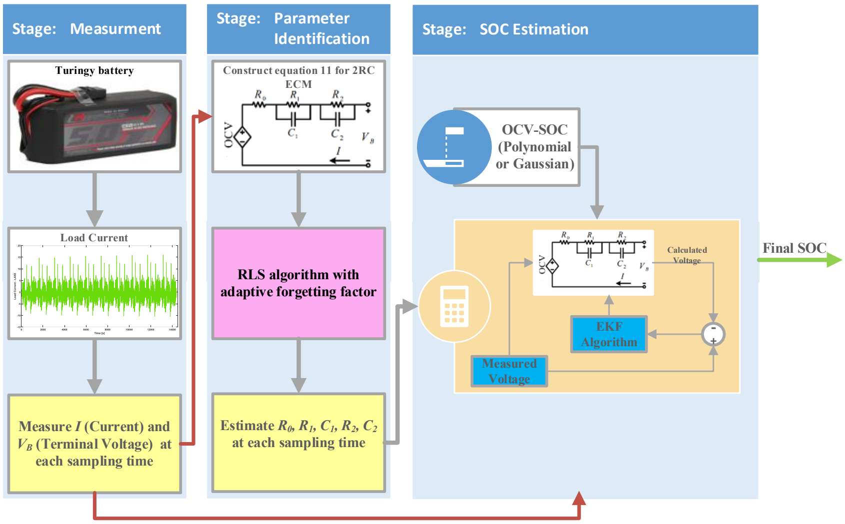

Fig. 2. SOC estimation scheme with EKF

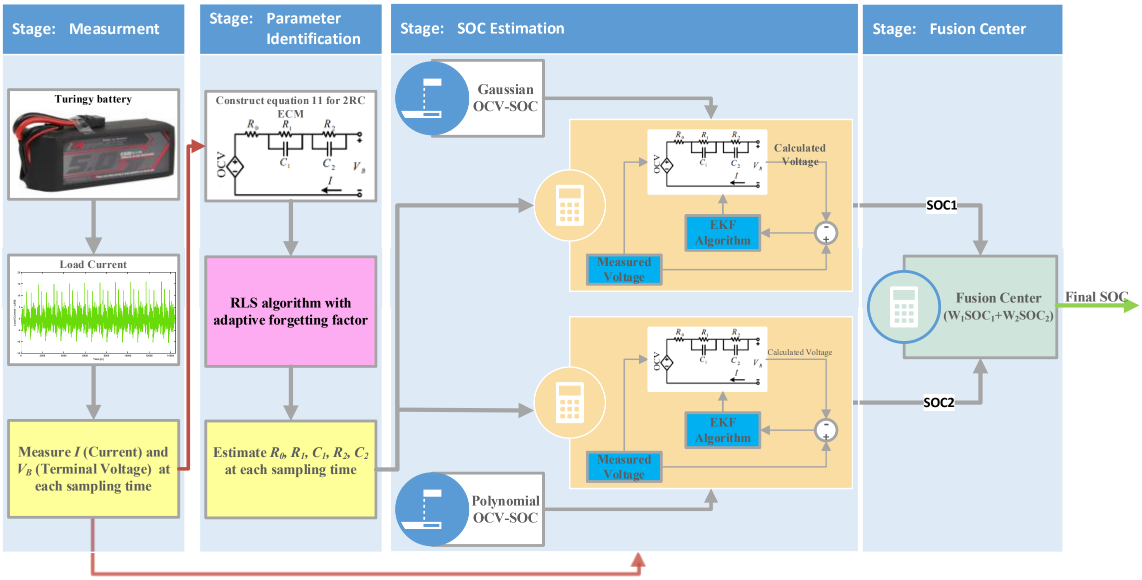

Fig. 3. SOC estimation scheme with proposed fusion algorithm

IV. Experimental Results

A. Battery data

In this section, the practical measured voltage and current of the new Turingy Graphene 5000mAh 65C battery during the LA-92 test are used to simulate and evaluate the proposed method and compare it with other methods. In addition, all the results have been obtained under the UDDS test. The main characteristics of the battery are shown [36].

TABLE II Battery specification of Turingy Graphene 5000mAh 65C

Chemistry	LiPO
Nominal Voltage	3.7 V
Charge	4.2V, 50mA End-Current (CC-CV) Fast
Discharge	2.8V End Voltage, 20A MAX Continuous Current
Nominal Capacity	5 Ah
Energy Density	134 (Wh/Kg)

The LA-92 and UDDS dynamic driving cycles at 25°C are chosen to evaluate the SOC estimation methods and to prove the effectiveness of the proposed method. These tests consider harsh dynamic conditions for the battery and include continuous and back-to-back charging and discharging. In addition, the C-Rate is also variable. For example, it increases up to 3C in LA-92 test. The battery current and voltage diagram during these tests is shown in Fig. 4.

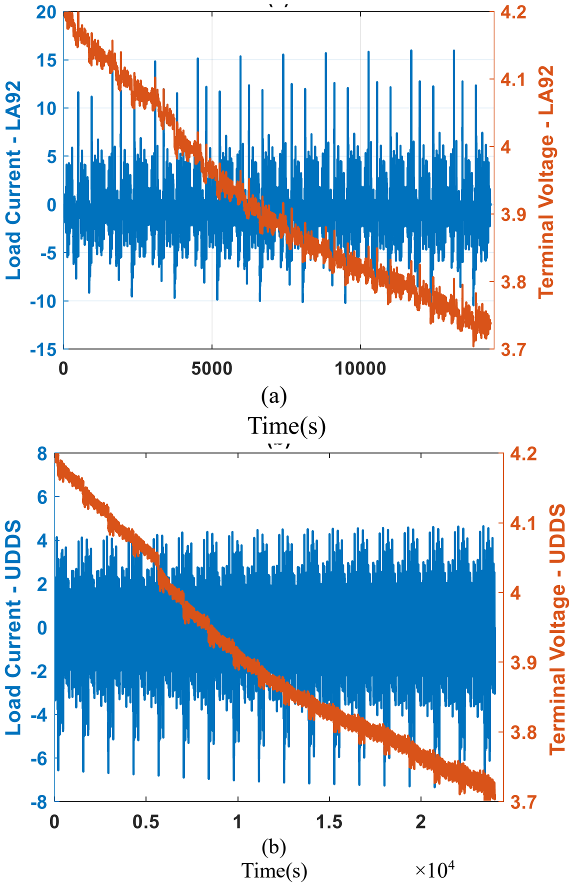

(a)

(b)

Fig. 4. Load Current and Terminal Voltage Profiles During LA92 and UDDS Driving Cycles. Figure (a) shows the LA92 cycle, where the load current exhibits sharp fluctuations, simulating aggressive acceleration and braking patterns. The terminal voltage gradually decreases. Figure (b) presents the UDDS cycle, characterized by frequent changes in load current. Both cycles impose harsh dynamic conditions on the battery, providing a rigorous test environment for evaluating its performance and durability.

Using MATLAB, six mathematical models (listed in Table 1) were fitted to 12 data points extracted from the experimentally obtained OCV-SOC curve of the Turingy Graphene 5000 mAh 65C battery. The resulting RMSE values from the fitting process are summarized in Table III.

TABLE III RMSE value of fitted curve

Model	**1**	**2**	**3**	**4**	**5**	**6**
RMSE	0.01281	0.0111	0.0327	0.0332	0.0036	0.0114

Models 3 and 4 exhibited the highest RMSE values, indicating poor accuracy for this specific battery type. Although Models 1 and 6 showed acceptable accuracy, their mathematical structures involve singularities and logarithmic terms that complicate derivative computation and may introduce instability in the estimation algorithm. To ensure compatibility with the SOC estimation framework (Eq. 5), the selected models must support both the mathematical expression and its derivative, i.e., $\frac{\mathrm{dOCV(soc(k))}}{\mathrm{dSOC(k)}}$. Based on a balance of fitting accuracy, analytical tractability, and numerical stability, Models 2 and 5 were chosen for implementation. Model 2 offers a smooth polynomial structure with straightforward differentiation, while Model 5 provides a flexible Gaussian formulation that captures nonlinear behavior effectively. These two models were selected for further integration into the SOC estimation framework.

To further evaluate the reliability and robustness of the selected polynomial and Gaussian models, a detailed sensitivity analysis was conducted. Each model was calibrated using experimental OCV data, and its parameters were individually perturbed by ±5% and ±10% to assess the impact on RMSE. As summarized in Table IV and Table V, which present the RMSE variation ranges and sensitivity levels for the polynomial and Gaussian models, respectively, the polynomial model exhibits a broad range of sensitivity. Specially coefficients K_2–K_5 showed high RMSE variation, indicating a strong influence on model accuracy, while parameters K_7 and K_8 had minimal impact. In contrast, the Gaussian model displayed distinct sensitivity patterns. Parameters govering the center and width of the dominant peak (notably β_1 and c_1) had the greatest effect on RMSE, while parameters associated with secondary peaks (α_3–c_3) contributed minimally, indicating limited influence on overall model performance. This analysis highlights the nuanced behavior of Gaussian model suggesting that careful tuning of its primary peak parameters is crucial for optimal performance. For polynomial model, attention to its middle-order coefficients is essential to maintain accuracy.

TABLE IV RMSE variation and sensitivity levels for polynomial model parameters under ±5% and ±10% perturbations.

p	±5% RMSE Range	±10% RMSE Range	Sensitivity Level
K_1	3.3796 – 3.402	6.7705 – 6.7929	Moderate
K_2	14.479 – 14.502	28.969 – 28.992	High
K_3	25.453 – 25.476	50.918 – 50.941	Very High
K_4	23.763 – 23.786	47.538 – 47.560	Very High
K_5	12.73 – 12.752	25.471 – 25.494	High
K_6	3.9367 – 3.9584	7.8843 – 7.906	Moderate
K_7	0.67946 – 0.69922	1.3687 – 1.3885	Low
K_8	0.11387 – 0.12761	0.23383 – 0.24762	Very Low

TABLE V RMSE variation and sensitivity levels for Gaussian model parameters under ±5% and ±10% perturbations

P	±5% RMSE Range	±10% RMSE Range	Sensitivity Level
K_1	0.13749 – 0.13772	0.27508 – 0.27531	High
α_1	0.18874 – 0.19105	0.37383 – 0.38222	Very High
β_1	0.11463 – 0.12261	0.22189 – 0.25279	High
K_2	0.075674 – 0.075951	0.15145 – 0.15173	Moderate
α_2	0.0042117 – 0.0044886	0.0079751 – 0.0082758	Low
β_2	0.05947 – 0.061608	0.11695 – 0.12481	Moderate
K_3	0.0022864 – 0.0023797	0.0034087 – 0.0035342	Very Low
α_3	0.0047283 – 0.0049324	0.0088647 – 0.0096019	Low
β_3	0.0022384 – 0.0022622	0.0031861 – 0.0032922	Very Low

Figure 5 shows experimental OCV-SOC data and its approximations with polynomial and Gaussian models.

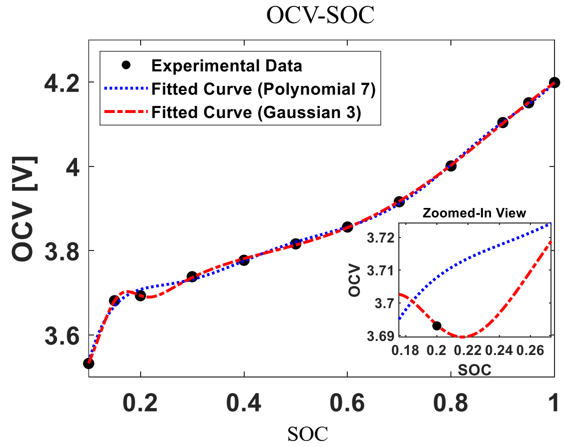

Fig, 5. Comparison of Polynomial and Gaussian fitting methods for OCV-SOC. Experimental data (black dots) are approximated using a 7th-order polynomial and a 3th-order Gaussian model. The inset zooms into the SOC range 0.18–0.26, highlighting subtle differences in curve behavior critical for battery performance modeling.

B. Performance evaluation indices

The study evaluates the proposed approach using error metrics such as Maximum Error (MAX), Mean Square Error (MSE), Root Mean Square Error (RMSE), and Mean Absolute Error (MAE). These metrics respectively measure reliability, robustness, and accuracy of the estimation method. Equation (11) contains the mathematical expressions for these criteria.

$$\begin{cases} MAE = \dfrac{1}{n}\displaystyle\sum_{k=1}^{n}\left|SOC_k - \widehat{SOC}_k\right| \\ MSE = \dfrac{1}{n}\displaystyle\sum_{k=1}^{n}\left(SOC_k - \widehat{SOC}_k\right)^2 \\ RMSE = \sqrt{\dfrac{1}{n}\displaystyle\sum_{k=1}^{n}\left(SOC_k - \widehat{SOC}_k\right)^2} \\ MAX = max\left|SOC_k - \widehat{SOC}_k\right| \end{cases} \tag{13}$$

C. Results and discussion

The SOC estimation results obtained using the EKF method during the LA-92 test are illustrated in Fig. 6. Specifically, Fig. 6(a) displays the SOC estimation outcomes for the 7th polynomial model and the 3rd Gaussian model, while Fig. 6(b) focuses on the corresponding estimation errors for these models. Notably, during certain intervals, such as from 8000 to 12000, the 7th polynomial model exhibits higher errors, whereas the 3rd Gaussian model demonstrates lower errors. Despite these differences, both models achieve acceptable accuracy, and the proposed approach combines their strengths to enhance overall performance.

The SOC estimation results and corresponding errors obtained through the proposed method during the LA-92 test are illustrated in Fig. 7. This approach combines two algorithms, resulting in improved overall estimation accuracy. As shown in Figure 7(b), the error range is narrower compared to the individual methods, highlighting enhanced performance throughout the test. Also, the resulting dynamic weights used in fusion are shown in Figure 8, which visually demonstrates how the statistical properties of RETV influence the probabilistic weighting of each estimator over time.

The evaluation criteria described in Section IV.B were computed for the proposed method and the two comparative methods during the LA-92 test, with results summarized in TABLE VI. To provide further insights, the UDDS test was conducted, and all evaluation criteria were recalculated, with the findings presented in TABLE VII.

TABLE VI Evaluation criteria for three SOC estimation scenarios throughout the LA92 test

Method	EKF (7th Polynomial model)	EKF (3rd Gaussian model)	Proposed method
MAX [%]	2.45	2.04	1.79
RMSE [%]	0.8813	0.6718	0.6040
MSE [%]	0.7766	0.4513	0.3648
MAE [%]	0.6547	0.5129	0.4823

TABLE VII Evaluation criteria for three SOC estimation scenarios throughout the UDDS

Method	**EKF (7th Polynomial model)**	**EKF (3rd Gaussian model)**	**Proposed method**
MAX [%]	2.52	3.05	2.49
RMSE [%]	0.9677	0.8079	0.7056
MSE [%]	0.9365	0.6526	0.4815
MAE [%]	0.7621	0.5810	0.4978

TABLE VIII Impact of L_m Values on SoC Estimation RMS and Average Computation Time

Lm	**SOC RMSE [%]**	**Average computation time [s]**
100	0.6043	1.8598
200	0.6042	1.8814
300	0.604	1.9072
400	0.6038	1.9309
500	0.6038	1.9529
600	0.6038	1.9704

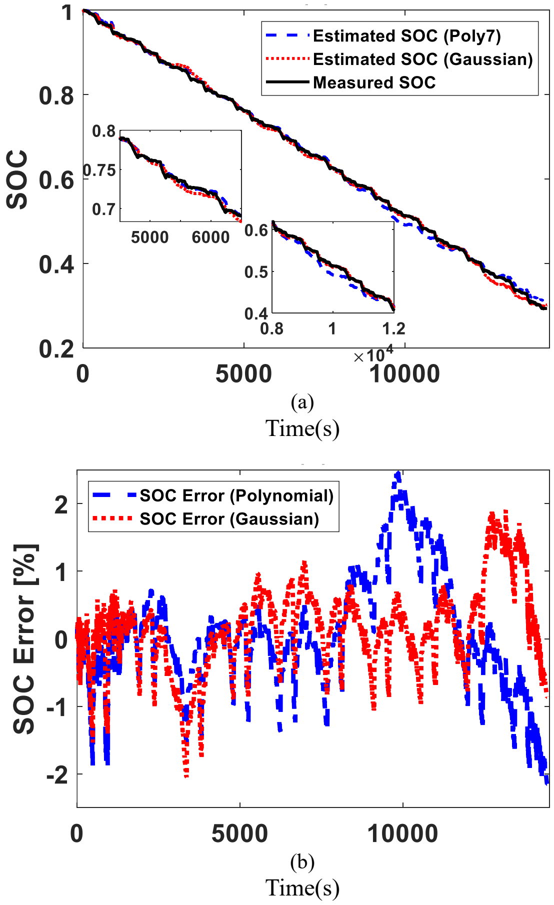

Fig. 6. Comparison of SOC Estimation and Error Using Polynomial and Gaussian Models During LA92. Figure (a) displays the SOC over the test cycle, comparing measured values with estimates from the Polynomial and Gaussian models. The two inset graphs zoom into specific time intervals (5000–6000 s and 8000–12000 s), illustrating regions where each method shows distinct performance characteristics—neither consistently outperforming the other. Figure (b) presents the corresponding SOC estimation error over time for both methods. The error fluctuates throughout the time span, indicating that each approach has its own strengths and limitations depending on the time segment.

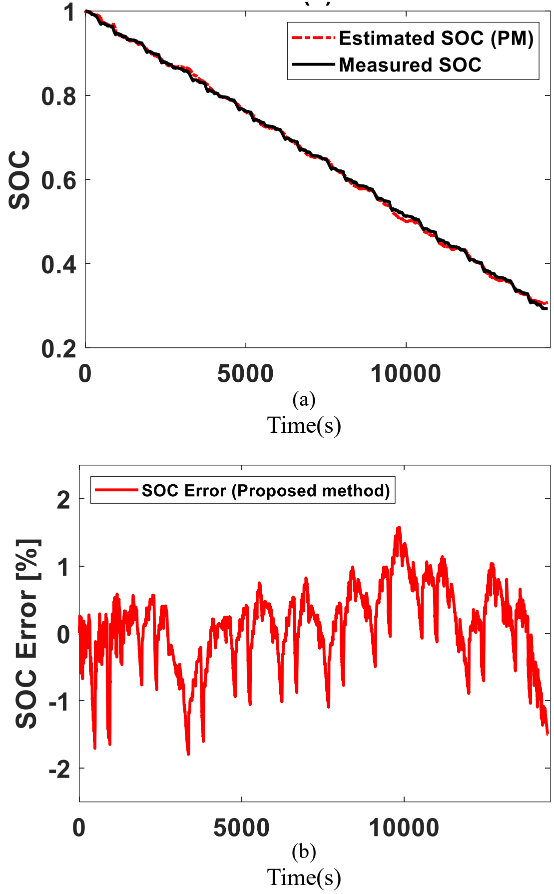

Fig .7. SOC Estimation and Error Using the Proposed Method During LA92 Cycle. shows the estimated SOC using the proposed method (PM) compared against measured SOC over time, demonstrating close alignment between the two curves. Figure (b) presents the corresponding SOC estimation error over time. The error fluctuates between approximately −1.79% and 1.79%, reflecting the dynamic accuracy of the proposed method throughout the test duration.

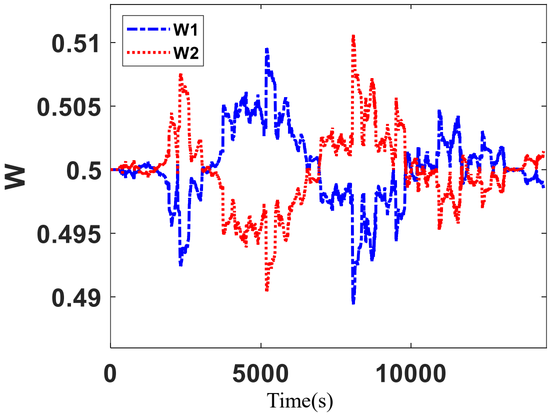

Fig. 8. Dynamic Weights Derived from the Multi-Model Fusion Approach. These dynamic weights reflect changes in system characteristics, as determined by the fusion strategy.

According to Table VI, the proposed method achieves a MAX of 1.79%, representing a 27% reduction compared to the EKF with the 7th-order polynomial model and a 13% reduction compared to the EKF with the 3rd-order Gaussian model. This improvement significantly enhances the reliability of SOC estimation. Furthermore, the proposed method yields an RMSE of 0.6043%, which is approximately 10% lower than the best results of the comparative methods, along with an MSE of 0.3652%, demonstrating superior robustness. The MAE of 0.4827% further confirms the high estimation accuracy throughout the LA92 test.

The UDDS test results, presented in Table VII, reinforce these findings. The proposed method consistently outperforms the other two approaches across all evaluation criteria, confirming its enhanced accuracy, reliability, and robustness under dynamic operating conditions. Notably, these results were obtained under rigorous test scenarios designed to simulate real-world battery behavior, including fluctuating loads and environmental variations. While simpler conditions would likely yield even better performance, the dynamic tests underscore the method's effectiveness in challenging environments. For broader context and comparison, Table VII also includes key benchmarks from existing literature, highlighting the competitive edge of the proposed approach.

TABLE IX . Main work of six papers related to the topic

Ref	Main estimation algorithm	Parameter identification	Battery type	Validation Profile	Error
[37]	AEKF-ESG	Online	LifePO4/2100 mAH	NEDC	RMSE = 0.79%
[38]	FTME-EKF	Online	Lithium-ion	BJDST	RMSE=0.86 MAE = 0.68 %
[19]	AUKF	Online	NCM 2.2Ah	BJDST	RMSE=0.97% MAE=1.13%
[39]	RB-AEKF	Online	Panasonic 18650 lithium-ion	FUDS	RMSE=1.08%
[40]	IFFRLS-UPF	Online	70 Ah lithium battery	BBDST	RMSE=0.72 MAE=0.63
[41]	Improved FFRLS-EXF	Online	27 Ah LG lithium power battery	DST	MAE=1.39% MAX=2.49

V. Conclusions

This paper presents a fusion-based SOC estimation method that integrates two EKFs, each coupled with a distinct OCV-SOC model, and dynamic weighting determined residual error statistics. By combining the strengths of multiple OCV-SOC models, the proposed approach achieves high accuracy, robustness, and computational efficiency under dynamic operating conditions. The fusion strategy, grounded in Bayesian probability and residual analysis, ensures that the most suitable model contributes more heavily to the final SOC estimate at any given time. This dynamic weighting mechanism enhances the adaptability of the framework, allowing it to maintain optimal performance across diverse battery conditions and operating profiles. Simulation results from LA92 and UDDS driving cycles demonstrate that the proposed method consistently outperforms conventional EKF approaches, reducing maximum estimation error by up to 26% and RMSE by over 10%. These improvements validate the effectiveness of the fusion strategy in enhancing SOC tracking precision, even under challenging load profiles.

The method's simplicity and adaptability make it highly suitable for real-time battery management systems in electric vehicles and energy storage applications. Future work may extend this framework to include state-of-health (SOH) estimation and investigate its performance under temperature variations and battery aging effects.

References

[1] A. Degla, M. Chikh, M. Mzir, and Y. Belabed, "State of charge estimation for Li-ion battery based intelligent algorithms," *Electrical Engineering*, vol. 105, no. 2, pp. 1179–1197, Apr. 2023, doi: 10.1007/S00202-022-01728-9/METRICS.

[2] Z. Wei, D. Zhao, H. He, W. Cao, and G. Dong, "A noise-tolerant model parameterization method for lithium-ion battery management system," Appl Energy, vol. 268, p. 114932, Jun. 2020, doi: 10.1016/J.APENERGY.2020.114932.

[3] L. Shen, J. Li, J. Liu, L. Zhu, and H. T. Shen, "Temperature Adaptive Transfer Network for Cross-Domain State-of-Charge Estimation of Li-Ion Batteries," IEEE Trans Power Electron, vol. 38, no. 3, pp. 3857–3869, Mar. 2023, doi: 10.1109/TPEL.2022.3220760.

[4] C. S. Huang, "A Lithium-Ion Batteries Fault Diagnosis Method for Accurate Coulomb Counting State-of-Charge Estimation," Journal of Electrical Engineering and Technology, vol. 19, no. 1, pp. 433–442, Jan. 2024, doi: 10.1007/S42835-023-01533-9/METRICS.

[5] S. Yang et al., "A parameter adaptive method for state of charge estimation of lithium-ion batteries with an improved extended Kalman filter," Scientific Reports 2021 11:1, vol. 11, no. 1, pp. 1–15, Mar. 2021, doi: 10.1038/s41598-021-84729-1.

[6] R. Havangi and F. Karimi, "Improvement of The Battery State of Charge Estimation Using Recursive Least Square Based Adaptive Extended Kalman Filter ," International Journal of Industrial Electronics Control and Optimization, vol. 7, no. 2, pp. 141–151, May 2024, doi: 10.22111/IECO.2024.47863.1537.

[7] K. Li, X. Gao, C. Liu, C. Chang, and X. Li, "A novel Co-estimation framework of state-of-charge, state-of-power and capacity for lithium-ion batteries using multi-parameters fusion method," Energy, vol. 269, p. 126820, Apr. 2023, doi: 10.1016/J.ENERGY.2023.126820.

[8] S. Rout and S. Das, "A robust modified adaptive extended Kalman filter for state- of-charge estimation of rechargeable battery under dynamic operating condition," Electrical Engineering, pp. 1–20, Jun. 2024, doi: 10.1007/S00202-024-02523-4/METRICS.

[9] E. Chemali, P. J. Kollmeyer, M. Preindl, R. Ahmed, and A. Emadi, "Long Short-Term Memory Networks for Accurate State-of-Charge Estimation of Li-ion Batteries," IEEE Transactions on Industrial Electronics, vol. 65, no. 8, pp. 6730–6739, Aug. 2018, doi: 10.1109/TIE.2017.2787586.

[10] C. Vidal et al., "Hybrid Energy Storage System State-Of-Charge Estimation Using Artificial Neural Network for Micro-Hybrid Applications," 2018 IEEE Transportation and Electrification Conference and Expo, ITEC 2018, pp. 868–873, Aug. 2018, doi: 10.1109/ITEC.2018.8450251.

[11] J. Meng, G. Luo, and F. Gao, "Lithium polymer battery state-of-charge estimation based on adaptive unscented kalman filter and support vector machine," IEEE Trans Power Electron, vol. 31, no. 3, pp. 2226–2238, Mar. 2016, doi: 10.1109/TPEL.2015.2439578.

[12] H. Pan, Z. Lü, W. Lin, J. Li, and L. Chen, "State of charge estimation of lithium-ion batteries using a grey extended Kalman filter and a novel open-circuit voltage model," Energy, vol. 138, pp. 764–775, Nov. 2017, doi: 10.1016/J.ENERGY.2017.07.099.

[13] Y. Tian, B. Xia, W. Sun, Z. Xu, and W. Zheng, "A modified model based state of charge estimation of power lithium-ion batteries using unscented Kalman filter," J Power Sources, vol. 270, pp. 619–626, Dec. 2014, doi: 10.1016/J.JPOWSOUR.2014.07.143.

[14] B. Fridholm, M. Nilsson, and T. Wik, "Robustness Comparison of Battery State of Charge Observers for Automotive Applications," IFAC Proceedings Volumes, vol. 47, no. 3, pp. 2138–2146, Jan. 2014, doi: 10.3182/20140824-6-ZA-1003.02296.

[15] P. Shrivastava, T. K. Soon, M. Y. I. Bin Idris, and S. Mekhilef, "Overview of model-based online state-of-charge estimation using Kalman filter family for lithium-ion batteries," Renewable and Sustainable Energy Reviews, vol. 113, p. 109233, Oct. 2019, doi: 10.1016/J.RSER.2019.06.040.

[16] J. Wu, D. Lei, Z. Liu, and Y. Zhang, "A fusion algorithm of multidimensional element space mapping architecture for SOC estimation of lithium-ion batteries under dynamic operating conditions," Energy, vol. 311, p. 133467, Dec. 2024, doi: 10.1016/J.ENERGY.2024.133467.

[17] X. Cheng, X. Liu, X. Li, and Q. Yu, "An intelligent fusion estimation method for state of charge estimation of lithium-ion batteries," Energy, vol. 286, p. 129462, Jan. 2024, doi: 10.1016/J.ENERGY.2023.129462.

[18] H. Zhou, J. Luo, and Z. Yu, "Co-estimation of SOC and SOH for Li-ion battery based on MIEKPF-EKPF fusion algorithm," Energy Reports, vol. 10, pp. 4420–4428, Nov. 2023, doi: 10.1016/J.EGYR.2023.11.017.

[19] J. Li, M. Ye, X. Ma, Q. Wang, and Y. Wang, "SOC estimation and fault diagnosis framework of battery based on multi-model fusion modeling," J Energy Storage, vol. 65, p. 107296, Aug. 2023, doi: 10.1016/J.EST.2023.107296.

[20] Y. Chen, W. Duan, X. Huang, and S. Wang, "Multi-output fusion SOC and SOE estimation algorithm based on deep network migration," Energy, vol. 308, p. 133032, Nov. 2024, doi: 10.1016/J.ENERGY.2024.133032.

[21] R. Zhang et al., "A Study on the Open Circuit Voltage and State of Charge Characterization of High Capacity Lithium-Ion Battery Under Different Temperature," Energies 2018, Vol. 11, Page 2408, vol. 11, no. 9, p. 2408, Sep. 2018, doi: 10.3390/EN11092408.

[22] I. Baccouche, S. Jemmali, B. Manai, N. Omar, and N. Essoukri Ben Amara, "Improved OCV Model of a Li-Ion NMC Battery for Online SOC Estimation Using the Extended Kalman Filter," Energies 2017, Vol. 10, Page 764, vol. 10, no. 6, p. 764, May 2017, doi: 10.3390/EN10060764.

[23] Q. Wang, J. Wang, P. Zhao, J. Kang, F. Yan, and C. Du, "Correlation between the model accuracy and model-based SOC estimation," Electrochim Acta, vol. 228, pp. 146–159, Feb. 2017, doi: 10.1016/J.ELECTACTA.2017.01.057.

[24] M. Cacciato, G. Nobile, G. Scarcella, and G. Scelba, "Real-Time Model-Based Estimation of SOC and SOH for Energy Storage Systems," IEEE Trans Power Electron, vol. 32, no. 1, pp. 794–803, Jan. 2017, doi: 10.1109/TPEL.2016.2535321.

[25] L. Ren, J. Dong, X. Wang, Z. Meng, L. Zhao, and M. J. Deen, "A Data-Driven Auto-CNN-LSTM Prediction Model for Lithium-Ion Battery Remaining Useful Life," IEEE Trans Industr Inform, vol. 17, no. 5, pp. 3478–3487, May 2021, doi: 10.1109/TII.2020.3008223.

[26] Q. Zhang, D. Wang, B. Yang, X. Cui, and X. Li, "Electrochemical model of lithium-ion battery for wide frequency range applications," Electrochim Acta, vol. 343, p. 136094, May 2020, doi: 10.1016/J.ELECTACTA.2020.136094.

[27] Y. Wang et al., "A comprehensive review of battery modeling and state estimation approaches for advanced battery management systems," Renewable and Sustainable Energy Reviews, vol. 131, p. 110015, Oct. 2020, doi: 10.1016/J.RSER.2020.110015.

[28] X. Lai, Y. Zheng, and T. Sun, "A comparative study of different equivalent circuit models for estimating state-of-charge of lithium-ion batteries," Electrochim Acta, vol. 259, pp. 566–577, Jan. 2018, doi: 10.1016/J.ELECTACTA.2017.10.153.

[29] M. R. Ramezani-al and M. Moodi, "A novel combined online method for SOC estimation of a Li-Ion battery with practical and industrial considerations," J Energy Storage, vol. 67, p. 107605, Sep. 2023, doi: 10.1016/J.EST.2023.107605.

[30] R. Xiong, Q. Yu, L. Y. Wang, and C. Lin, "A novel method to obtain the open circuit voltage for the state of charge of lithium ion batteries in electric vehicles by using H infinity filter," Appl Energy, vol. 207, pp. 346–353, Dec. 2017, doi: 10.1016/J.APENERGY.2017.05.136.

[31] R. Havangi and F. Karimi, "An Adaptive Robust Square Root Unscented Kalman Filter for State of Charge Estimation for Lithium-ion Batteries," International Journal of Industrial Electronics Control and Optimization, Jul. 2025, doi: 10.22111/IECO.2025.51512.1679.

[32] P. Shrivastava, T. K. Soon, M. Yamani Bin Idris, and S. Mekhilef, "Lithium-ion Battery Model Parameter Identification Using Modified Adaptive Forgetting Factor-Based Recursive Least Square Algorithm," Proceedings of the Energy Conversion Congress and Exposition - Asia, ECCE Asia 2021, pp. 2169–2174, May 2021, doi: 10.1109/ECCE-ASIA49820.2021.9479079.

[33] C. Lin, H. Mu, R. Xiong, and W. Shen, "A novel multi-model probability battery state of charge estimation approach for electric vehicles using H-infinity algorithm," Appl Energy, vol. 166, pp. 76–83, Mar. 2016, doi: 10.1016/J.APENERGY.2016.01.010.

[34] S. Sundaresan, B. C. Devabattini, P. Kumar, K. R. Pattipati, and B. Balasingam, "Tabular Open Circuit Voltage

Modelling of Li-Ion Batteries for Robust SOC Estimation," Energies 2022, Vol. 15, Page 9142, vol. 15, no. 23, p. 9142, Dec. 2022, doi: 10.3390/EN15239142.

[35] Y. Li, C. Wang, and J. Gong, "A multi-model probability SOC fusion estimation approach using an improved adaptive unscented Kalman filter technique," Energy, vol. 141, pp. 1402–1415, Dec. 2017, doi: 10.1016/J.ENERGY.2017.11.079.

[36] P. Kollmeyer and M. Skells, "Turnigy Graphene 5000mAh 65C Li-ion Battery Data," Mendeley Data, vol. 1, 2020, doi: 10.17632/4FX8CJPRXM.1.

[37] Y. Ye, Z. Li, J. Lin, and X. Wang, "State-of-charge estimation with adaptive extended Kalman filter and extended stochastic gradient algorithm for lithium-ion batteries," J Energy Storage, vol. 47, p. 103611, Mar. 2022, doi: 10.1016/J.EST.2021.103611.

[38] Z. Zhang et al., "State of charge estimation of lithium-ion batteries using a fractional-order multi-dimensional Taylor network with adaptive Kalman filter," Energy, vol. 316, p. 134577, Feb. 2025, doi: 10.1016/J.ENERGY.2025.134577.

[39] J. Li, L. Li, Z. Li, Z. Jiang, and J. Gu, "Co-estimation of parameters and state of charge for lithium-ion battery," Journal of Electroanalytical Chemistry, vol. 907, p. 116011, Feb. 2022, doi: 10.1016/J.JELECHEM.2022.116011.

[40] X. Hao, S. Wang, Y. Fan, Y. Xie, and C. Fernandez, "An improved forgetting factor recursive least square and unscented particle filtering algorithm for accurate lithium-ion battery state of charge estimation," J Energy Storage, vol. 59, p. 106478, Mar. 2023, doi: 10.1016/J.EST.2022.106478.

[41] C. Ge, Y. Zheng, and Y. Yu, "State of charge estimation of lithium-ion battery based on improved forgetting factor recursive least squares-extended Kalman filter joint algorithm," J Energy Storage, vol. 55, p. 105474, Nov. 2022, doi: 10.1016/J.EST.2022.105474.

Mohammad Moodi received his B.Sc. degree in Power Engineering from Shahid Rajaee Teacher Training University, Tehran, Iran, in 2019, and his M.Sc. degree in Control Engineering from Quchan University of Technology, Quchan, Iran, in 2022. His master's research focused on state-of-charge estimation algorithms for lithium-ion batteries. He is currently a teacher at a Technical and Vocational high school in Bojnurd, Iran. His research interests include battery management systems, control theory, and energy storage technologies.

Mohamad Reza Ramezani-al received his B.Sc. degree in 1998, his M.Sc. degree in 2002 and Ph.D. degree in 2014, all in Control Engineering from Ferdowsi University of Mashhad, Mashhad, Iran. His doctoral research focused on optimal control of switched linear systems. He is currently an Assistant Professor in the Department of Electrical Engineering, Faculty of Electrical and Computer Engineering, Quchan University of Technology, Quchan, Iran. His main research interests include switched systems, nonlinear control systems, control and tracking problems in autonomous underwater vehicles (AUVs), and application of control and estimation theories in power converters and battery management systems.

IECO

This page intentionally left blank.

IECO
International Journal Of
Industrial Electronics Control and Optimization
Print ISSN: 3517-2645
Online ISSN: 3568-2645
Homepage: https://ieco.usb.ac.ir/

A Semi-Quadratic Buck-Boost Converter with Two Operating Modes and a Sustained Input-Output Current for PV Applications

Mustafa Okati[1*] | Mohammad Osmani-Bojd[2]

Department of Electrical Engineering, Zabol Branch, Islamic Azad University, Zabol, Iran. [1]
Department of Electrical Engineering, Zahedan Branch, Islamic Azad University, Zahedan, Iran. [2]
Corresponding author's email: Mu.Okati@gmail.com

Article Info

Article type:
Research Article

Article history:
Received: 11-February-2025
Received in revised form:
04-June-2025
Accepted: 25-June-2025
Published online: 22-June-2026

Keywords:
Continuous input-output current,
dual mode operation,
parasitic conditions,
photo-voltaic application,
switching power device.

ABSTRACT

This study introduces a non-isolated semi-quadratic DC/DC buck-boost converter designed to enhance performance. Derived from a conventional CUK converter, the proposed topology operates in two distinct modes: one providing a semi-quadratic voltage gain of $D(2-D)/(1-D)^2$ and the other offering a gain of $D/(1-D)$. In addition, the proposed structure features constant input and output currents due to the presence of inductive filters at the input and output ports, which reduces the current stress on the capacitors at the output port and lowers the voltage ripple. Under steady-state conditions, the continuous conduction mode efficiency of the converter and small-signal modeling were analyzed by considering the effects of parasitic resistance. The results demonstrated lower total switching device power and a reduced component count than other buck-boost converters in dual-mode operation. The proposed converter was simulated using PLECS software. The experimental results were consistent with theoretical predictions due to their high efficiency and applications, particularly in photovoltaic systems and fuel cells.

I. Introduction

Fuel cells and photovoltaic (PV) systems are two examples of renewable energy (RE) sources that have recently received much attention as cost-effective solutions for electrical energy in domestic and industrial settings. The range of suitable energy transmission systems is constrained because these RE sources produce power with varying current and voltage magnitudes. For instance, their voltage needs to be raised when these sources are integrated into the grid to regulate energy flow. Similarly, it is crucial to lower the converter output voltage when using it as an energy source for particular appliances to prevent overvoltage damage [1]- [4]. Due to their intermittent nature and lower output voltage, PV panels must be equipped with an effective and reliable step-up DC-DC converter to ensure their output voltage meets the minimum requirements of power grid consumers. Studies presented various high-gain DC/DC converters to satisfy these requirements [5], [6]. Also, non-isolated traditional DC-DC converters were investigated [7], [8]. These sources also recognized the limitations imposed by traditional DC/DC converters and examined their efficiency in RE systems. Many buck-boost DC-DC converter designs have been presented based on conventional DC-DC converters, including boost, buck-boost, buck, SEPIC, ZETA, and CUK converters [9], [10]. Among the applications of a high-voltage gain converters is as a solar power optimizer (SPO) [11]-[13], a high-gain step-up/down converter to enhance the power delivery of a PV system to the grid. At the same time, it can be used as a buck-boost converter to charge DC batteries and sensitive DC loads. Among various types of converters used as SPO, the non-isolated converter topology has no isolation between the output and input sides. Thus, changes on the input side can directly affect the output. However, it has a lower component count than the isolated converter topology [14]. Other issues associated with this type of converter include poor voltage gain, high duty ratio, and more circuitry for optimal operations. In a study, a comprehensive analysis of various converter configurations was conducted through mathematical modeling to achieve a complete understanding of the dynamic behavior of the converters [15]. Related research provided a unique step-up/down DC converter by considering the KY design [16] to accomplish a steady output current across two power switches. It is crucial to note that this converter has a relatively low voltage gain ratio. The SEPIC converters were designed with various components to enhance voltage gain and reduce voltage stress on the primary switch [17]. However, a multi-output system that requires such a converter necessitates

Publisher: University of Sistan and Baluchestan

complex control. To increase the voltage gain, a unique quadratic buck-boost converter with two power switches, each requiring a separate gate driver, was suggested [18]. Moreover, the drawback of having discontinuous input and output currents makes the control system more complicated [18, 19]. To overcome these challenges, quadratic buck-boost converters with continuous input current and lower voltage gain have been introduced [20, 21]. A ZETA converter with double the voltage gain is shown in [22] to attain better voltage gains with the constant input current. A single switch converter with continuous input/output current, and an odd ground between the input and output is provided in [23] for the same purpose. Similar to the previous study, a new step-up buck-boost converter was recommended [24, 25] to increase gain while reducing stress across the primary switch. However, this converter increases the voltage strains across the diodes. To improve performance, a unique buck-boost converter with inductive filters at the input/output ports and lower switching stress was introduced [26]. Nevertheless, this converter has more semiconductor components than other comparable architectures. The discontinuity problem is addressed in [27] by a quadratic DC/DC buck-boost topology with a low component count and constant input/output current, but at the expense of the voltage gain ratio. In various studies, novel quadratic transformerless DC/DC converters with negative output have been introduced [28, 29]. The structure had constant input and output currents due to employment of inductive filters at the input and output ports. A new high-gain SEPIC-based converter is proposed for renewable energy applications. The circuit is developed by merging a standard SEPIC topology with a boosting unit to increase voltage gain [30]. Similar topologies were described in [31] and [32], where the output current is discontinuous, despite improved performance in both boosting and bucking modes. In a similar study [33], researchers described a DC-DC converter with a positive output and lower overall switching device power throughout two modes of operation. Two operating modes are a step-up mode and a step-up/down mode with a high gain ratio. To achieve this, several boosting approaches were investigated, such as including the use of voltage multipliers, switched inductors, magnetic coupling switched capacitors, and multistage techniques [34]. These techniques are used in several high-gain DC-DC converters.

The CUK and buck-boost converters are traditional negative output (NO) converters. However, due to their limitations, a new NO buck-boost converter was proposed using a combination of buck-boost and conventional boost converters [35]. However, the negative and discontinuous output voltage causes high stress across one of the switches. Another NO converter with a wide conversion ratio is suggested in [36]. Nonetheless, it suffered from sporadic input/output current. The NO polarity is key in industrial applications, including data transfer interfaces and wind and solar power generation. In the dual-mode converters category, a new transformer-less inverter was also presented and prototyped [37]. In this single-phase inverter, various voltage gain ratios can be obtained to solve the deficiencies of modern dual-mode inverters. The dual-mode time-sharing approach effectively reduces unwanted high-frequency switching losses by determining when to apply the DC or the inverter stage during each grid voltage period [10]. Based on this technique, the converter's step-up mode operates only when the level of PV voltage is lower than the instantaneous level of the grid voltage, and the step-down mode operates when the PV voltage level is higher than the instantaneous level of the grid voltage. As a result, the dual-mode converters are even more effective than the classical two-stage grid-tied transformerless converters.

Fig. 1 represents the application of solar PV systems in dual-mode buck-boost converters. A novel coupled-inductor buck-boost converter with a simple design and two cascading semi-stages is presented in a related work [38]. This converter's key features include a constant input current with minimal ripple, adjustable output voltage, ultra-extended output voltage, and a positive polarity of the common ground. The converter's quadratic gain enables it to outperform traditional buck-boost converters in terms of step-down and step-up characteristics whenever the duty cycle is greater or less than 50%, respectively [39]. The proposed converter's unique current consistency between input and output decreases the current stress on the input and filtration capacitors, making it an attractive choice for renewable energy applications. In the event of a power switch open-circuit malfunction, three different quadratic buck DC-DC converter schemes were presented, each with the ability to flip to a semi-quadratic buck-boost configuration. A topological structure was established to ensure a secure transition from one switch to another while preserving the functional contribution of all other components to achieve efficient power conversion [40]. A new fifth-order boost converter was proposed for dual operating modes, utilizing different control methods. This converter's dual modes also show lower switch voltage stress [41]. The design of two cascaded buck-boost nature converters is completed; the first converter can produce high step-up gains, while the second can provide high step-down gains. Applications such as LED systems, which are voltage-sensitive, can benefit from this feature [42]. A new transformerless DC-DC converter with continuous input current for photovoltaic applications is presented. By optimizing the turns ratio of the coupled inductor, the converter enhances voltage gain and minimizes its overall size. This design also helps lower voltage stress on switching components. Furthermore, using one power switch simplifies control circuitry and reduces costs [43]. A new transformerless high step-up DC/DC converter with low input current ripple for renewable energy systems is proposed. The topology is built upon a conventional quadratic boost converter integrated with a CUK circuit, preserving key advantages such as continuous input and output currents. To achieve enhanced voltage gain, the design incorporates switched capacitors and switched-inductor techniques [44]. This paper presents a comprehensive study and analysis of a novel non-isolated high step-up DC-DC converter based on a SEPIC topology for photovoltaic applications. Derived from the conventional SEPIC converter, the proposed structure incorporates a two-winding coupled inductor and an enhanced voltage multiplier cell to achieve an elevated voltage conversion ratio. This design approach enables the use of switches with lower on-state resistance, improving overall efficiency [45]. A novel high step-up DC-DC switched-mode converter featuring a shared ground connection between the input and output ports is introduced. Additionally, the converter prolongs the input source's service life by ensuring continuous current injection. The design also provides a fast dynamic response, achieved through its minimum-phase characteristics [46].

The CUK converter is the only common converter that achieves continuous output and input current with a smaller number of elements and flexible output, as mentioned before. Therefore, it is widely used for various applications. Studies showed that larger inductors with higher switching frequencies can minimize the input current ripple problem. However, bulky filters result in higher costs, larger sizes, and increased switching losses. To overcome these drawbacks, a novel DC/DC converter topology with low input current ripple and reduced filtering is developed in this study. This topology is based on a typical CUK converter. The proposed converter duty ratio provides a solution for controlling input current ripple in PV applications, achieving maximum overall efficiency without the need for a coupling inductor. The suggested converter features a wide range of conversion ratios, a buck-boost technique with two operating modes, and continuous input and output current in both buck and boost modes. Continuous input current (CIC) and continuous output current (COC) can be discussed in terms of their applications. For instance, CIC is an essential element in both PV and FC applications.

Regarding PV, CIC will increase energy extraction by reducing ripple power losses [44]; alternatively, in terms of FC, CIC will extend the lifetime of the FC stack by operating at nominal operating points. The COC feature, on the other hand, can reduce the size of the output capacitor while extending the battery's lifetime when used in charging applications. Due to its benefits, RE applications can significantly benefit from it.

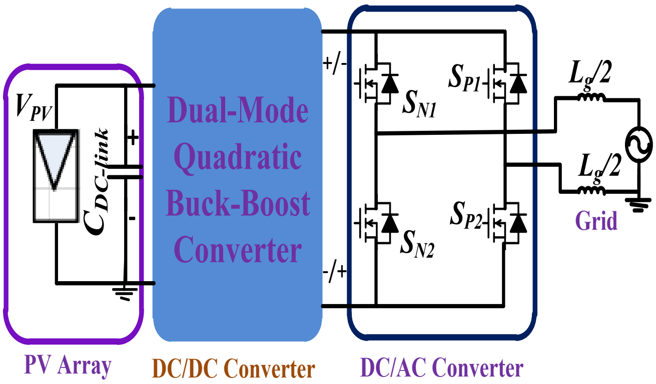

Fig. 1. Grid connected PV system through dual mode DC-DC converter.

The remainder of the paper is structured as follows. The suggested converter is introduced in Section 2 after theoretical analysis and steady-state validation. The evaluation of the small-signal modeling is presented in Section 3. The advantages of the suggested topology in comparison to other comparable conventional converters are covered in Section 4. The outcomes of the PLECS simulation are shown in Section 5. To support the theoretical arguments, Section 6 also offers the outcomes of the experimental prototype of the recommended converter. Lastly, Section 7 concludes.

II. Proposed Topology, Operation Principles, And Steady-State Evaluation

A. Proposed Topology

Constant input/output current port, cost-effectiveness, high efficiency, low noise and low input/output ripple currents are the most important characteristics of DC/DC semi quadratic buck-boost converter used in photovoltaic applications. Fig. 2 depicts the proposed semi-quadratic DC/DC buck-boost converter. The high-voltage gain proposed topology is made up of three inductors (L_1, L_2, L_3), three capacitors (C_1, C_2, C_o), two switches (S_1, S_2), two diodes (D_1, D_2), and a resistive load (R_o). The steady-state analysis of the suggested topology can be simplified by first considering the ideal components and then assuming all large enough capacitors to keep voltages virtually constant. As a result, their current and voltage were assumed to be constant across the whole duration. Fig. 3 depicts the proposed structure's distinctive waveforms.

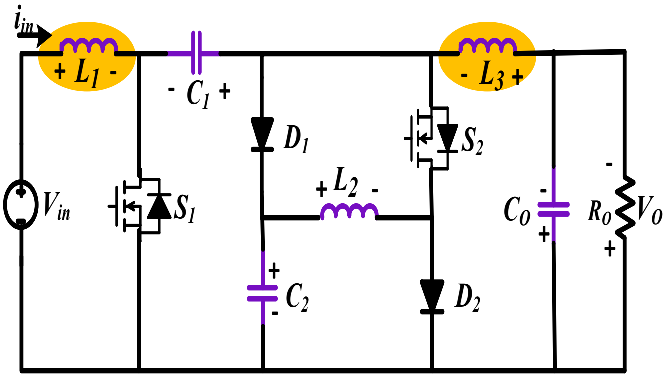

Fig. 2. The suggested converter's structure.

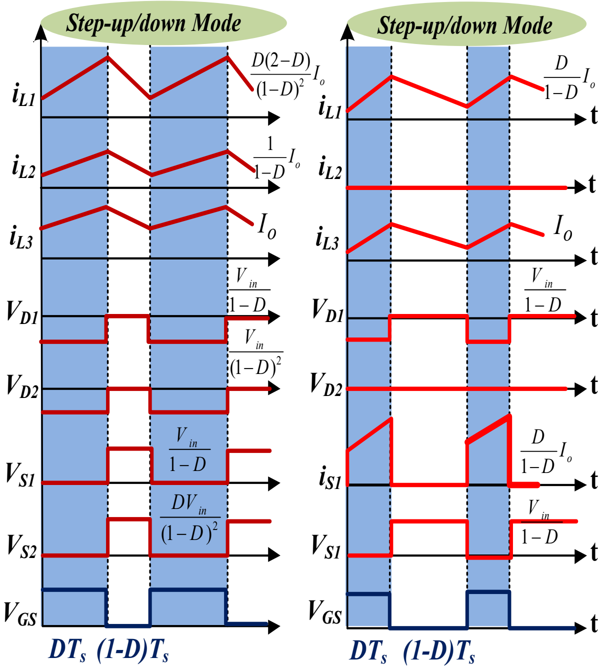

Fig. 3. The suggested structure's waveform characteristics for step-up/down mode.

B. Operation Principles of Proposed Topology

The steady-state conditions and continuous conduction mode (CCM) are taken into account while determining the features of the suggested converter. Thus, the consistent current and voltage are considered over a complete switching duration. As seen in Figs. 4 and 5, two major operating modes for the converter in the CCM are assumed.

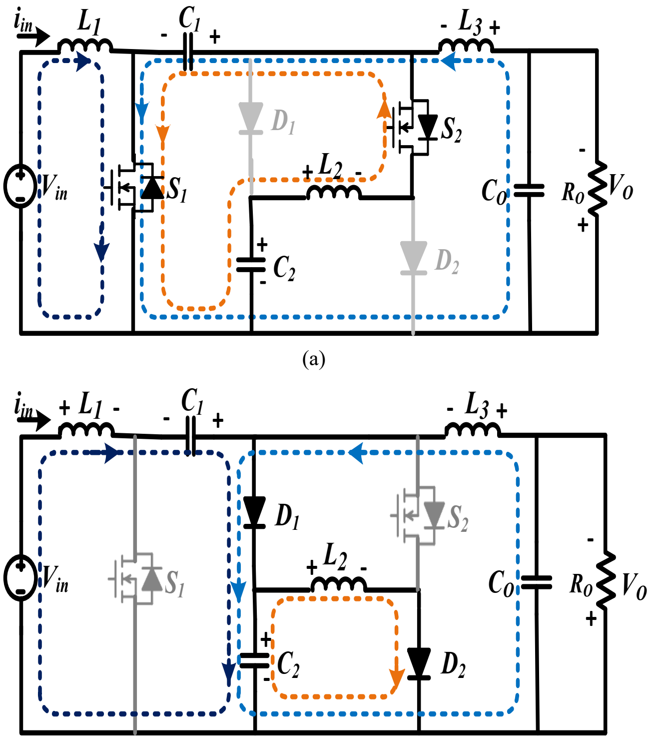

(a)

(b)

Fig. 4. The proposed converter's operational states for step-up mode (Mode I). (a) State 1; (b) State 2.

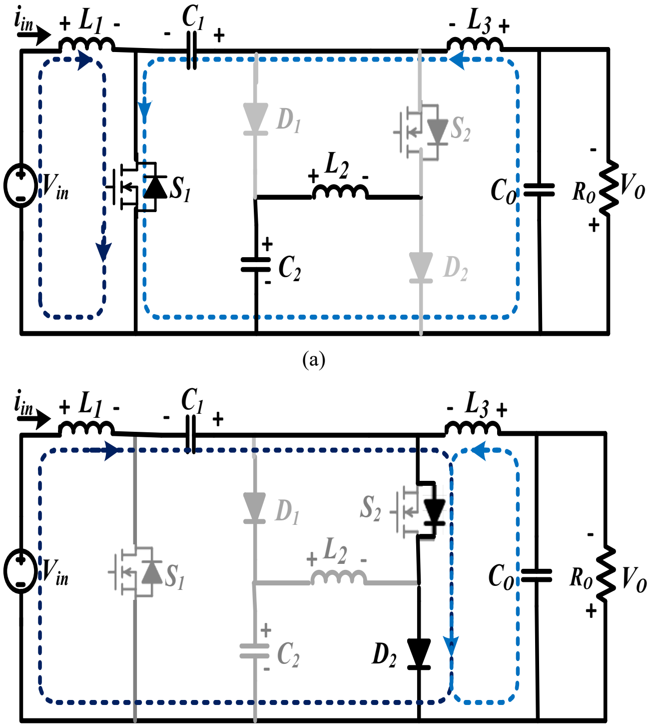

(a)

(b)

Fig. 5. The proposed converter's operational states for step-down mode (Mode II). (a) State 1; (b) State 2.

1) MODE I OPERATION

State 1 ($0 \leq t \leq DT$): The circuit is in this condition makes the power MOSFETs S_1 and S_2 are turned on and two diodes D_1 and D_2 are in reverse-biased mode as shown in Fig.4a. The inductors L_1, L_2, and L_3 are powered by the capacitor C_1 and the input source V_{in}. The capacitors C_1 and C_2 are discharged in this condition, and the current of the inductors (i_{L1}, i_{L2}, i_{L3}) rises. The output capacitor C_o supplies power to the output load R_o as seen in Fig.4a. The following relationships may be found using the KCL and KVL:

$$\begin{cases} V_{L1} = V_{in},\ \ V_{L2} = -V_{C1} + V_{C2},\ \ V_{L3} = -V_{C1} - V_o \\ i_{C1} = i_{L3} + i_{L2},\ \ i_{C2} = -i_{L2},\ \ i_{Co} = i_{L3} - \left({}^{V_o}/_{R_o}\right) \end{cases} \tag{1}$$

State 2 (DTs ≤ t ≤ Ts): Both power MOSFETs are switched off in this state. The diodes D1 and D2 are forward biased, and the inductors L1, L2, and L3 are de-energized as shown in Fig.4b. Here, the capacitor C1 and the capacitor C2 are charged. Moreover, inductor L3 feeds the output load Ro and also charges Co. Energy is discharged from capacitor C1 via the current paths of diodes D1 and D2. In this condition, the current and voltage equations are expressed as:

$$\begin{cases} V_{L1} = V_{in} + V_{C1} - V_{C2},\ \ V_{L2} = V_{C2},\ \ V_{L3} = -V_{C2} - V_o \\ i_{C1} = -i_{L1},\ \ i_{C2} = i_{L1} - i_{L2} + i_{L3},\ \ i_{Co} = i_{L3} - \left({}^{V_o}/_{R_o}\right) \end{cases} \tag{2}$$

2)*MODE II OPERATION*

State 1 ($0 \leq t \leq DT_s$): The power MOSFETs S_1 and S_2 are turned on and off during this period. Yet, diodes D_1 and D_2 are reverse-biased and forward-biased. The inductor L_1 is energized here by the input source, whereas L_2 is de-energized. The output capacitor C_o supplies power to the output load R_o. The equations relating to this period are calculated using the circuit depicted in Fig. 5a:

$$\begin{cases} V_{L1} = V_{in}, V_{L2} = 0, V_{L3} = -V_{C1} - V_o \\ i_{C1} = i_{L3},\ \ i_{C2} = -i_{L2} = 0,\ \ i_{Co} = i_{L3} - \left({}^{V_o}/_{R_o}\right) \end{cases} \tag{3}$$

State 2 ($DT_s \leq t \leq T_s$): In this condition, the power MOSFETs are switched off while diode D_1 is reverse-biased whereas diode D_2 is conducting. At this time frame, the capacitors C_1 and C_o are charged by releasing the stored energy in inductors L_1 and L_3, whereas L_2 is de-energized. Moreover, C_o is charged, and inductor L_3 supplies the output load R_o. As illustrated in Fig. 5b, the energy from all capacitors is discharged through the current route of the diode D_2, raising the current of each inductor. The voltage and current equations for this state, as represented by the KCL and KVL, are as follows:

$$\begin{cases} V_{L1} = V_{in} + V_{C1},\ \ V_{L2} = 0,\ \ V_{L3} = -V_o \\ i_{C1} = -i_{L1},\ \ i_{C2} = -i_{L2} = 0,\ \ i_{Co} = i_{L3} - \left({}^{V_o}/_{R_o}\right) \end{cases} \tag{4}$$

C. Steady-State Evaluation

This section derives the gain ratios and voltage and current relationships of the introduced converter shown in Figs. 4 and 5 (Mode I and II). Using the volt-second balance principle of inductors L_1, L_2, and L_3, the mean voltage value of all capacitors throughout the charge-discharge period can be calculated. Using

D as the duty cycle, the average voltages of capacitors C_1 and C_2 may thus be represented as:

$$\begin{cases} Mode\ I:\ V_{C1}=\dfrac{1}{(1-D)^2}V_{in},\ \ V_{C2}=\dfrac{D}{(1-D)^2}V_{in} \\ Mode\ II:\ V_{C1}=\dfrac{1}{1-D}V_{in},\ \ V_{C2}=0 \end{cases} \tag{5}$$

Therefore, the voltage gains are expressed as,

$$\begin{cases} Mode\ I:\ M_{CCM}=\left(\dfrac{V_o}{V_{in}}\right)=\dfrac{D(2-D)}{(1-D)^2} \\ Mode\ II:\ M_{CCM}=\left(\dfrac{V_o}{V_{in}}\right)=\dfrac{D}{(1-D)} \end{cases} \tag{6}$$

Assuming negligible circuit losses, it is possible to consider the input power along with output power as follows:

$$P_{in}=P_o\rightarrow V_{in}I_{in}=V_oI_o \tag{7}$$

The relationship between DC output current and DC input current can be expressed by, using the voltage gain calculated in (6) as follows:

$$\begin{cases} Mode\ I:\ \dfrac{I_o}{I_{in}}=\dfrac{(1-D)^2}{D(2-D)} \\ Mode\ II:\ \dfrac{I_o}{I_{in}}=\dfrac{(1-D)}{D} \end{cases} \tag{8}$$

Using the ampere-second balancing concept of capacitors C_1, C_2, and C_o, the average magnitude for every inductor current can be provided as:

$$\begin{cases} Mode\ I:\ I_{LI}=\frac{D(2-D)}{(1-D)^2}|I_o|,\ \ I_{L2}=\frac{|I_o|}{1-D},\ \ I_{L3}=|I_o| \\ Mode\ II:\ I_{LI}=\frac{D}{(1-D)}|I_o|,\ \ I_{L2}=0,\ \ I_{L3}=|I_o| \end{cases} \tag{9}$$

Then the current and voltage stress of the two diodes and two power MOSFETs can be calculated as follows:

$$\begin{cases} Mode\ I:\ V_{S1}=\dfrac{1}{1-D}V_{in},\ \ V_{S2}=\dfrac{D}{(1-D)^2}V_{in} \\ Mode\ II:\ V_{s1,2}=\dfrac{1}{1-D}V_{in} \end{cases} \tag{10}$$

$$\begin{cases} Mode\ I:\ I_{S1-avg}=\frac{D(2-D)}{(1-D)^2}|I_o|,\ I_{S2-avg}=\frac{D}{1-D}|I_o| \\ Mode\ II:\ I_{S1-avg}=\frac{D}{1-D}|I_o|,\ I_{S2-avg}=|I_o| \end{cases} \tag{11}$$

$$\begin{cases} Mode\ I:\ V_{D1}=\dfrac{1}{1-D}V_{in},\ V_{D2}=\dfrac{1}{(1-D)^2}V_{in} \\ Mode\ II:\ V_{D1}=\dfrac{1}{1-D}V_{in},\ V_{D2}=0 \end{cases} \tag{12}$$

$$\begin{cases} Mode\ I:\ I_{D1-avg}=\dfrac{1}{1-D}|I_o|,\ \ I_{D2-avg}=|I_o| \\ Mode\ II:\ I_{D1-avg}=0,\ \ I_{D2-avg}=|I_o| \end{cases} \tag{13}$$

D. Efficiency Inspection

The power loss in the proposed converter circuit is affected by several parameters, including the internal resistances of the converter's elements, the forward voltage drops of the diode, and the switching frequency. The circuit shown in Fig. 6 is utilized to compute the amount of loss in each circuit element. Currents flowing through switches and diodes are approximated using the following RMS values as follows:

$$I_{S1-RMS}\approx\frac{(2-D)\sqrt{D}}{(1-D)^2}|I_o|,I_{S2-RMS}=\frac{\sqrt{D}}{1-D}|I_o| \tag{14}$$

$$I_{D1-RMS}=\frac{I_o}{\sqrt{(1-D)^3}},I_{D2-RMS}=\frac{I_o}{\sqrt{(1-D)}} \tag{15}$$

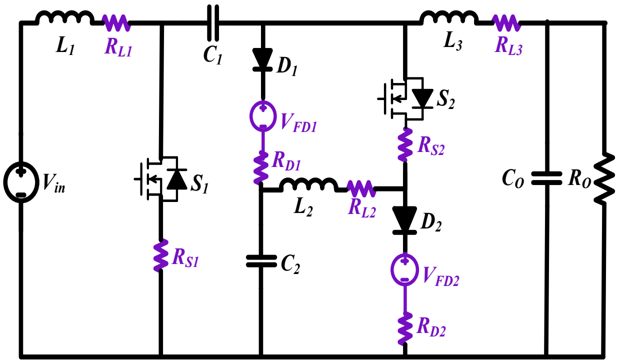

Fig. 6. The analogous circuit with parasitic components.

Moreover, the following equations are used to calculate the estimated RMS values of currents flowing between the inductors and capacitors:

$$I_{L1-RMS}\approx\frac{D(2-D)I_o}{(1-D)^2},I_{L2-RMS}\approx\frac{I_o}{1-D},I_{L3-RMS}\approx I_o \tag{16}$$

$$I_{C1-RMS}\approx\sqrt{\frac{D(2-D)}{(1-D)^3}}I_o,I_{C2-RMS}\approx\sqrt{\frac{D}{(1-D)^3}}I_o,\ I_{C3-RMS}\approx 0 \tag{17}$$

Power switch total power loss ($P_{S1,2\text{-}Total}$) is defined as the switching losses ($P_{S\text{-}L}$) and sum of conducting power dissipations ($P_{R\text{-}S}$). Using the R_S value as the power switch's conduction resistance, one may derive:

$$P_{S1,2-Total}=P_{s-L}+P_{R-S} \tag{18}$$

$$\begin{cases} P_{R-S1}=R_{S1}I_{S1-RMS}^2=R_{S1}\dfrac{(2-D)^4}{(1-D)^4}I_o^2 \\ P_{R-S2}=R_{S2}I_{S2-RMS}^2=R_{S2}\dfrac{D}{(1-D)^2}I_o^2 \\ P_{S1-L}=f_sC_{S1}V_{S1}^2=f_sC_{S1}\dfrac{1}{(1-D)^2}V_{in}^2 \\ P_{S2-L}=f_sC_{S2}V_{S2}^2=f_sC_{S2}\dfrac{D^2}{(1-D)^4}V_{in}^2 \end{cases} \tag{19}$$

Additionally, diode forward conduction resistance (R_{FD}) and forward bias voltage (V_{FD}) are used to calculate total diode losses (P_{FD} + P_{FR}), where P_{FD} signifies forward bias losses and P_{FR} denotes reverse bias losses, respectively.

$$P_{D-Total}=P_{FD}+P_{FR}=\textstyle\sum_{i=1}^{2}(R_{FD}I_{Di-RMS}^2)+\sum_{i=1}^{2}(V_{FDi}I_{Di}) \tag{20}$$

Using the equivalent series resistance (ESR) values (R_L and R_C) of inductors and capacitors, as well as their power losses, may be computed as:

$$P_{L-Total}=\textstyle\sum_{i=1}^{3}(P_{Li})=\sum_{i=1}^{3}(R_{Li}I_{Li-RMS}^2) \tag{21}$$

$$P_{C-Total}=P_{C1}+P_{C2}+P_{Co} \tag{22}$$

The proposed converter's overall power losses are the sum of the power losses of capacitors, inductors, diodes, and power MOSFETs, as shown below:

$$P_{loss-Total}=P_{s-Total}+P_{D-Total}+P_{L-Total}+P_{C-Total} \tag{23}$$

Eventually, the proposed converter's efficiency may be derived as:

$$\eta=\frac{P_o}{P_{loss-Total}+P_o}=\frac{1}{\frac{P_{loss-Total}}{RI_o^2}+1} \tag{24}$$

1) Circuit Simplification with Parasitic Parameters

Fig.6 depicts a simplified circuit with parasitic components, including parasitic parameters of inductors (L_1, L_2, and L_3), diodes (D_1 and D_2), and MOSFETs (S_1 and S_2). V_{FD1} and V_{FD2} are the threshold voltages of diodes. Then, as shown below, the inductor voltage equations with parasitic parameters (R_{S1}, R_{S2}, R_{D1}, R_{D2}, R_{L1}, R_{L2}, R_{L3}) can be determined.

For the two operation states (Mode I), the voltages across the inductors with parasitic parameters are determined as follows:

$$State\ 1: \begin{cases} V_{L1} = V_{in} - R_{L1}I_{L1} - R_{S1}I_{S1} = V_{in} - \\ R_{L1}\frac{D^2(2-D)^2}{(1-D)^4}\frac{V_{in}}{R_o} - R_{s1}\frac{D^2(2-D)^2}{(1-D)^4}\frac{V_{in}}{R_o} \\ V_{L2} = -R_{L2}I_{L2} - R_{S1}I_{S1} - R_{S2}I_{S2} - V_{C1} + V_{C2} \\ = -R_{L2}\frac{D(2-D)}{(1-D)^3}\frac{V_{in}}{R_o} - R_{s1}\frac{D^2(2-D)^2}{(1-D)^4}\frac{V_{in}}{R_o} \\ -R_{s2}\frac{D^2(2-D)^2}{(1-D)^3}\frac{V_{in}}{R_o} - V_{C1} + V_{C2} \\ V_{L3} = -R_{L3}I_{L3} - R_{S1}I_{S1} - V_{C1} - V_o = \\ -R_{L3}\frac{D(2-D)}{(1-D)^2}\frac{V_{in}}{R_o} - R_{s1}\frac{D^2(2-D)^2}{(1-D)^4}\frac{V_{in}}{R_o} - \\ V_{C1} - V_o \end{cases} \qquad (25)$$

$$State\ 2: \begin{cases} V_{L1} = V_{in} - R_{L1}I_{L1} - R_{D1}I_{D1} + V_{C1} - V_{C2} - \\ V_{FD1} = V_{in} - R_{L1}\frac{D^2(2-D)^2}{(1-D)^4}\frac{V_{in}}{R_o} - \\ R_{D1}\frac{D(2-D)}{(1-D)^3}\frac{V_{in}}{R_o} + V_{C1} - V_{C2} - V_{FD1} \\ V_{L2} = -R_{L2}I_{L2} - R_{D2}I_{D2} + V_{C2} - V_{FD2} \\ = -R_{L2}\frac{D(2-D)}{(1-D)^3}\frac{V_{in}}{R_o} - R_{D2}\frac{D(2-D)}{(1-D)^2}\frac{V_{in}}{R_o} + \\ V_{C2} - V_{FD2} \\ V_{L3} = -R_{L3}I_{L3} - R_{D1}I_{D1} - V_{C2} - V_{FD1} - \\ V_o = -R_{L3}\frac{D(2-D)}{(1-D)^2}\frac{V_{in}}{R_o} + R_{D1}\frac{D(2-D)}{(1-D)^3}\frac{V_{in}}{R_o} - \\ V_{C2} - V_{FD1} - V_o \end{cases} \qquad (26)$$

Using the voltage-second balancing concept of inductors one can yield the voltage gain with parasitic elements. As a consequence, the average capacitor voltages C_1 and C_2 and the voltage gain ratio with parasitic characteristics can be expressed as:

$$V_{C1} = \frac{\begin{array}{c} -(1-D)^4R_oV_{in} + D^2(2-D)^2R_{L1}V_{in} + \\ D(2-D)(1-D)^3R_{L2}V_{in} + \\ D^3(2-D)^2R_{S1}V_{in} + D^3(2-D)(1-D)^2R_{S2}V_{in} + \\ D(2-D)(1-D)^2R_{D1}V_{in} + D(2-D)(1-D)^4R_{D2}V_{in} + \\ (1-D)^5R_oV_{FD1} - (1-D)^6R_oV_{FD2} \end{array}}{(1-D)^6R_o} \qquad (27)$$

$$V_{C2} = \frac{\begin{array}{c} -D(1-D)^4R_oV_{in} + D^3(2-D)^2R_{L1}V_{in} + \\ D(2-D)(1-D)^3R_{L2}V_{in} + D^4(2-D)^2R_{S1}V_{in} + \\ D^3(2-D)(1-D)^2R_{S2}V_{in} + D^2(2-D)(1-D)^2R_{D1}V_{in} \\ +D(2-D)(1-D)^4R_{D2}V_{in} + D(1-D)^5R_oV_{FD1} + \\ (1-D)^6R_oV_{FD2} \end{array}}{(1-D)^6R_o} \qquad (28)$$

$$M = \frac{V_o}{V_{in}} = \frac{\begin{array}{c} D(2-D)(1-D)^4R_o - D^3(2-D)^3R_{L1} - D(2-D)(1-D)^3R_{L2} \\ -D(2-D)(1-D)^4R_{L3} + D^3(2-D)^2R_{S1} - D^3(2-D)(1-D)^2R_{S2} \\ -D(2-D)(1-D)^2R_{D1} - D(2-D)(1-D)^4R_{D2} - \\ (1-D)^5R_o\frac{V_{FD1}}{V_{in}} - (1-D)^6R_o\frac{V_{FD2}}{V_{in}} \end{array}}{(1-D)^6R_o} \qquad (29)$$

Likewise, by employing the volt-second balance principle of inductors, the mean output voltage can be determined while taking into consideration the presence of parasitic elements:

$$V_o = \frac{D(2-D)(1-D)^4V_{in} - (1-D)^6V_{FD_2} - (1-D)^5V_{FD_1}}{\begin{array}{c}(1-D)^6 + \alpha_1\frac{R_{L1}}{R_o} + \alpha_2\frac{R_{L2}}{R_o} + \alpha_3\frac{R_{L3}}{R_o} + \alpha_4\frac{R_{S1}}{R_o} + \alpha_5\frac{R_{S2}}{R_o} + \alpha_6\frac{R_{D1}}{R_o} \\ +\alpha_7\frac{R_{D2}}{R_o}\end{array}}$$

$$\begin{array}{c} \alpha_1 = D^2(2-D)^2(1-D)^2, \alpha_2 = (1-D)^5, \alpha_3 = (1-D)^6, \alpha_4 = D^2(2-D) \\ (1-D)^2, \alpha_5 = D^2(1-D)^4, \alpha_6 = (1-D)^4, \alpha_7 = (1-D)^6 \end{array} \qquad (30)$$

The plots presented in Fig.7 demonstrate that the voltage gain ratio $|M_{CCM}|$ is influenced by parasitic resistance R_L along with the forward drop in voltage of diode V_{FD}.

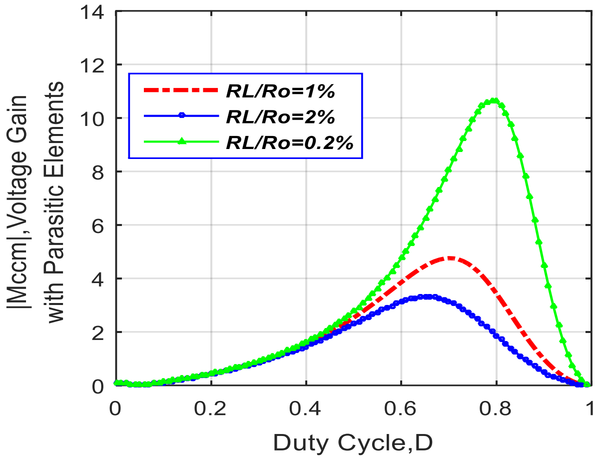

Fig. 7. |MCCM| with the parasitic resistance versus duty cycle (Mode I).

These points out those parasitic components have an effect on the voltage gain ratio. Hence, Vin=15V, $V_{FD1,2}$=0.8V and $R_{L1,2,3}$=Δ×Ro, where Δ=1%, 2%, 0.2%.

2) Proportion of Power Losses

Fig.8 illustrates the power loss distribution in Mode I, aiding in the understanding of the power losses of individual element sections. The step-down state exhibits lower efficiency compared to the step-up state. The converter operates in step-up mode whereby the input current is greater than the expected output current of the converter. In the step-down mode of operation, it is observed that the current flowing through the input port is lesser than the current flowing through the output port. As a result, as compared to the step-up mode, the step-down mode has a lower overall efficiency. In step-up/down mode, the power losses of inductors (*L*), capacitors (*C*), power MOSFETs (*S*), and diodes (*D*), and are given in (21), (22), (18), and (20).

E. Analysis and Design of Inductor

This section describes the detail design requirements of inductors used in the converter.

1) Inductor Ripples

The value of ripple of inductor currents i_{L1}, i_{L2}, and i_{L3} can be calculated using circuit diagram shown in Fig. 4(a) as expressed below [9].

$$\Delta i_L = \frac{DV_L}{Lf_s} \qquad (31)$$

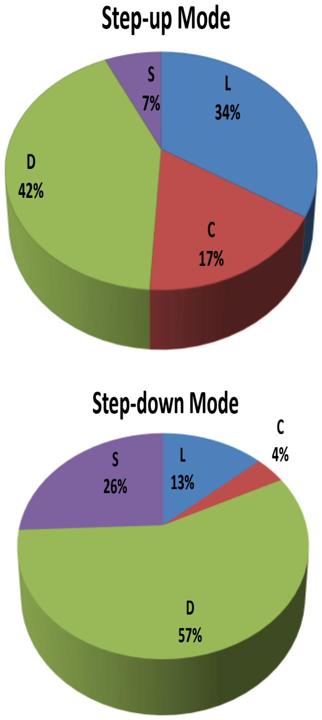

(a) (b)

Fig. 8. Power loss distribution for mode I. (a) Step-up mode, (b) Step-down mode.

Current ripples are taken into account when designing the inductors in the proposed converter. In relation to the peak-to-peak current displayed in Fig.4a, and assuming that current ripples inductors of (31), the needed inductances and ripples inductor currents as expressed below:

$$L=\frac{DV_L}{\alpha\%\Delta i_L f_s},\qquad \Delta i_L\le\alpha\% i_L\ \ \alpha\le 30\% \tag{32}$$

Substituting $I_{L1,2,3}$ from (9) to (32), the following relation can be obtained:

$$L_1\ge\frac{(1-D)^4}{\alpha\% D(2-D)^2}\times\frac{R_o}{f_s},L_{2,3}\ge\frac{D(1-D)}{\alpha\%(2-D)}\times\frac{R_o}{f_s} \tag{33}$$

2) Boundary Calculation

The inductor current minimum value zero marks the border between CCM and DCM (discontinuous conduction mode). It is critical to build the discrete inductors in such a way that the given converter can operate in continuous conduction mode. Taking this into consideration, the CCM condition is found using the circuit shown in Figs.4a and 5a for inductors L_3, L_2, and L_1as follows:

$$Mode\ I:\begin{cases}L_1\ge\dfrac{(1-D)^4}{D(2-D)^2}\times\dfrac{R_o}{f_s}\\ L_{2,3}\ge\dfrac{(1-D)^2}{(2-D)}\times\dfrac{R_o}{f_s}\end{cases}, \tag{34}$$

$$Mode\ II:\begin{cases}L_1\ge\dfrac{(1-D)^2}{D}\times\dfrac{R_o}{f_s}\\ L_3\ge(1-D)\times\dfrac{R_o}{f_s}\end{cases}$$

The boundary conditions (τ_{LB}) for L_3, L_2, and L_1 in Mode I and II are provided in the (35). The CCM is shown by the area above each curve in Fig.9, while the DCM is represented by the area below.

$$\begin{aligned}&Mode\ I:\begin{cases}\tau_{L1B}=\dfrac{(1-D)^4}{2D(2-D)^2}\\ \tau_{L2,3B}=\dfrac{(1-D)^2}{2(2-D)}\end{cases},\\ &Mode\ II:\begin{cases}\tau_{L1B}=\dfrac{(1-D)^2}{2D}\\ \tau_{L3B}=\dfrac{(1-D)}{2}\end{cases}\end{aligned} \tag{35}$$

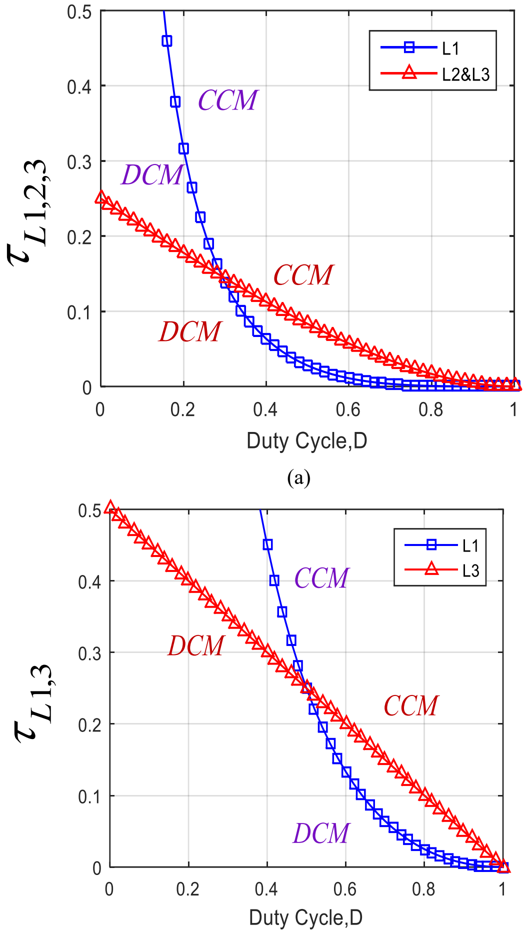

(a)

(b)

Fig. 9. Boundary conditions of Input and output current ripple versus duty cycle. (a) Mode I; (b) Mode II.

F. Capacitor Design and Analysis

The voltage ripples across capacitors C_1, C_2 and C_o may be represented as [9]:

$$\Delta V_{C1,2}=\frac{Di_{C1,2}}{C_{1,2}f_s},\Delta V_{Co}=\frac{Di_{Co}}{C_of_s} \tag{36}$$

Also, based on the following conditions, the capacitances of each capacitor can be obtained as:

$$\begin{cases} \Delta v_{C_{1,2}} \le \beta\% V_{C1,2} & \beta \le 2\% \\ \Delta v_{C_o} \le \delta\% V_o & \delta \le 0.5\% \end{cases} \tag{37}$$

$$\begin{cases} C_{1,2} = \dfrac{DI_{C1,2}}{\beta\% V_{C1,2} f_s} \\ C_o = \dfrac{DI_o}{\delta\% V_o f_s} \end{cases} \tag{38}$$

III. Small Signal Modeling

The equations required for small signal modelling for the dual states can be obtained from Figs. 4and 5, Following is a straightforward derivation of the state-average model using the averaging method and equations (39) and (40) for mode I and (41) and (42) for mode II [47], as below:

MODE I OPERATION

$$State1: \begin{cases} L_1 \dfrac{di_{L1}}{dt} = v_{in} \\ L_2 \dfrac{di_{L2}}{dt} = -v_{C1} + v_{C2} \\ L_3 \dfrac{di_{L3}}{dt} = -v_{C1} - v_{Co} \\ C_1 \dfrac{dv_{C1}}{dt} = i_{L3} + i_{L2} \\ C_2 \dfrac{dv_{C2}}{dt} = i_{L2} \\ C_o \dfrac{dv_{Co}}{dt} = i_{L3} - \dfrac{v_{Co}}{R_o} \end{cases},$$

$$State\ 2: \begin{cases} L_1 \frac{di_{L1}}{dt} = v_{in} + v_{C1} - v_{C2} \\ L_2 \frac{di_{L2}}{dt} = -v_{C2} \\ L_3 \frac{di_{L3}}{dt} = -v_{C2} - v_{Co} \\ C_1 \frac{dv_{C1}}{dt} = -i_{L1} \\ C_2 \frac{dv_{C2}}{dt} = i_{L1} - i_{L2} + i_{L3} \\ C_o \frac{dv_{Co}}{dt} = i_{L3} - \frac{v_{Co}}{R_o} \end{cases} \tag{39}$$

State1

$$\begin{cases} L_1 \dfrac{d\langle i_{L1}\rangle}{dt} = d(\langle v_{in}\rangle) + (1-d)(\langle v_{in}\rangle + \langle v_{C1}\rangle - \langle v_{C2}\rangle) \\ L_2 \dfrac{d\langle i_{L2}\rangle}{dt} = d(-\langle v_{C1}\rangle + \langle v_{C2}\rangle) - (1-d)\langle v_{C2}\rangle \\ L_3 \dfrac{d\langle i_{L3}\rangle}{dt} = -d(\langle v_{C1}\rangle + \langle v_{Co}\rangle) - (1-d)(\langle v_{C2}\rangle + \langle v_{Co}\rangle) \end{cases}$$

State2

$$\begin{cases} C_1 \dfrac{d\langle v_{C1}\rangle}{dt} = d(\langle i_{L3}\rangle + \langle i_{L2}\rangle) - (1-d)\langle i_{L1}\rangle \\ C_2 \dfrac{d\langle v_{C2}\rangle}{dt} = d(\langle i_{L2}\rangle) + (1-d)(\langle i_{L1}\rangle - \langle i_{L2}\rangle + \langle i_{L3}\rangle) \\ C_o \dfrac{d\langle v_{Co}\rangle}{dt} = d(\langle i_{L3}\rangle + \langle \frac{v_{Co}}{R_o}\rangle) - (1-d)(\langle i_{L3}\rangle + \langle \frac{v_{Co}}{R_o}\rangle) \end{cases} \tag{40}$$

MODE II OPERATION

$$State1: \begin{cases} L_1 \frac{di_{L1}}{dt} = v_{in} \\ L_2 \frac{di_{L2}}{dt} = 0 \\ L_3 \frac{di_{L3}}{dt} = -v_{C1} - v_{Co} \\ C_1 \frac{dv_{C1}}{dt} = i_{L3} \\ C_2 \frac{dv_{C2}}{dt} = -i_{L2} = 0 \\ C_o \frac{dv_{Co}}{dt} = i_{L3} - \frac{v_{Co}}{R_o} \end{cases}, \tag{41}$$

$$State\ 2: \begin{cases} L_1 \dfrac{di_{L1}}{dt} = v_{in} + v_{C1} \\ L_2 \dfrac{di_{L2}}{dt} = 0 \\ L_3 \dfrac{di_{L3}}{dt} = -v_{Co} \\ C_1 \dfrac{dv_{C1}}{dt} = -i_{L1} \\ C_2 \dfrac{dv_{C2}}{dt} = -i_{L2} = 0 \\ C_o \dfrac{dv_{Co}}{dt} = i_{L3} - \dfrac{v_{Co}}{R_o} \end{cases}$$

State1

$$\begin{cases} L_1 \frac{d\langle i_{L1}\rangle}{dt} = d(\langle v_{in}\rangle) + (1-d)(\langle v_{in}\rangle + \langle v_{C1}\rangle) \\ L_2 \frac{d\langle i_{L2}\rangle}{dt} = 0 \\ L_3 \frac{d\langle i_{L3}\rangle}{dt} = -d(\langle v_{C1}\rangle + \langle v_{Co}\rangle) - (1-d)(-\langle v_{Co}\rangle) \end{cases} \tag{42}$$

State2

$$\begin{cases} C_1 \frac{d\langle v_{C1}\rangle}{dt} = d(\langle i_{L3}\rangle) - (1-d)\langle i_{L1}\rangle \\ C_2 \frac{d\langle v_{C2}\rangle}{dt} = 0 \\ C_o \frac{d\langle v_{Co}\rangle}{dt} = d(\langle i_{L3}\rangle + \langle \frac{v_{Co}}{R_o}\rangle) - (1-d)(\langle i_{L3}\rangle + \langle \frac{v_{Co}}{R_o}\rangle) \end{cases}$$

where,$\langle v_{in}\rangle, \langle i_{L3}\rangle, \langle i_{L2}\rangle, \langle i_{L1}\rangle,$ $\langle v_{C2}\rangle, \langle v_{C1}\rangle$ and $\langle v_{C0}\rangle$are the average values of v_{in}, , i_{L3}, i_{L2}, i_{L1}, v_{C2}, v_{C1}, and v_{Co}, and respectively. Small AC values of the aforementioned elements are specified in order to produce the small-signal model as: $\widehat{v_{in}}, \widehat{\iota_{L3}}, \widehat{\iota_{L2}},\widehat{\iota_{L1}},\widehat{v_{c2}}, \widehat{v_{c1}},\widehat{v_{c0}}$, and $\hat{d}$. Besides, the associations among mean AC, and DC values can be expressed as:

$$\begin{cases} \langle v_{in}\rangle = V_{in} + \overset{\wedge}{v_{in}} \\ \langle v_{C1}\rangle = V_{C1} + \overset{\wedge}{v_{C1}} \\ \langle v_{C2}\rangle = V_{C2} + \overset{\wedge}{v_{C2}} \\ \langle v_{Co}\rangle = V_{Co} + \overset{\wedge}{v_{Co}} \\ \langle i_{L1}\rangle = I_{L1} + \overset{\wedge}{i_{L1}} \\ \langle i_{L2}\rangle = I_{L2} + \overset{\wedge}{i_{L2}} \\ \langle i_{L3}\rangle = I_{L3} + \overset{\wedge}{i_{L3}} \\ \langle d\rangle = D + \hat{d} \end{cases} \begin{cases} \left|\overset{\wedge}{v_{in}}\right| \ll |V_{in}|, \\ \left|\overset{\wedge}{v_{C1}}\right| \ll |V_{C1}| \\ \left|\overset{\wedge}{v_{C2}}\right| \ll |V_{C2}| \\ \left|\overset{\wedge}{v_{Co}}\right| \ll |V_{Co}| \\ \left|\overset{\wedge}{i_{L1}}\right| \ll |I_{L1}| \\ \left|\overset{\wedge}{i_{L2}}\right| \ll |I_{L2}| \\ \left|\overset{\wedge}{i_{L3}}\right| \ll |I_{L3}| \\ \left|\hat{d}\right| \ll |D| \end{cases} \tag{43}$$

By substituting (43) into (42) and (40), one may get AC and DC values while omitting the high-order small signal components as:

$$K\dot{x} = Ax + Bu, y = Cx + Eu \tag{44}$$

with

$$x = [\widehat{\iota_{L1}} \quad \widehat{\iota_{L2}} \quad \widehat{\iota_{L3}} \quad \widehat{v_{C1}} \quad \widehat{v_{C2}} \quad \widehat{v_{Co}}], u = [\hat{d} \quad \widehat{v_{in}}] \tag{45}$$

$$K = \begin{bmatrix} L_1 & 0 & 0 & 0 & 0 & 0 \\ 0 & L_2 & 0 & 0 & 0 & 0 \\ 0 & 0 & L_3 & 0 & 0 & 0 \\ 0 & 0 & 0 & C_1 & 0 & 0 \\ 0 & 0 & 0 & 0 & C_2 & 0 \\ 0 & 0 & 0 & 0 & 0 & C_o \end{bmatrix} \tag{46}$$

$A_{Mode\ I=}$

$$\begin{bmatrix} 0 & 0 & 0 & (1-D) & -(1-D) & 0 \\ 0 & 0 & 0 & -D & 1 & 0 \\ 0 & 0 & 0 & -D & -(1-D) & -1 \\ -(1-D) & D & D & 0 & 0 & 0 \\ (1-D) & -1 & -(1-D) & 0 & 0 & 0 \\ 0 & 0 & 1 & 0 & 0 & -\frac{1}{R_O} \end{bmatrix}$$

$$A_{Mode\,II} = \begin{bmatrix} 0 & 0 & 0 & 0 & (1-D) & 0 \\ 0 & 0 & 0 & 0 & 0 & 0 \\ 0 & 0 & 0 & -D & 0 & 0 \\ -(1-D) & 0 & D & 0 & 0 & 0 \\ 0 & 0 & 0 & 0 & 0 & 0 \\ 0 & 0 & 1 & 0 & 0 & -1/R_O \end{bmatrix} \tag{47}$$

$$B_{Mode\,I} = \begin{bmatrix} -V_{C1}+V_{C2} & 1 \\ -V_{C1} & 0 \\ -V_{C1}+V_{C2} & 0 \\ I_{L1}+I_{L2}+I_{L3} & 0 \\ -I_{L1}-I_{L3} & 0 \\ 0 & 0 \end{bmatrix}, B_{Mode\,II} = \begin{bmatrix} -V_{C1} & 1 \\ 0 & 0 \\ -V_{C1} & 0 \\ I_{L1}+I_{L3} & 0 \\ 0 & 0 \\ 0 & 0 \end{bmatrix} \tag{48}$$

And the V_o metrics can be obtained as below:

$$V_o = [0 \quad 0 \quad 0 \quad 0 \quad 0 \quad 1] \begin{bmatrix} \hat{i}_{L1} \\ \hat{i}_{L2} \\ \hat{i}_{L3} \\ \hat{v}_{C1} \\ \hat{v}_{C2} \\ \hat{v}_{Co} \end{bmatrix} + [0 \quad 0] \begin{bmatrix} \hat{d} \\ \hat{V}_{in} \end{bmatrix} \tag{49}$$

The extracted bode plots from the calculation procedure and simulations are displayed in Fig 10. It is used to generate the output transfer function to test the model. The parameters listed in Table III are used to draw the bode diagrams. As can be seen, the estimated model and simulation results are in good agreement. As a result, the suggested model may be used to exact controller design as well as dynamic behavior of the circuit. Fig.11 illustrates the control system parameters using SISOTOOL in MATLAB, which are determined according to the gain and phase margin. The PI controller's step-up/step-down functionality allows for an output voltage range of 15V to 60V. However, modifying the load in an open-loop control system results in alterations to the output voltage ripples.

IV. Comparison with Existing Converters

The characteristics of modes I and II of the suggested converter in step-up/down modes is shown in Table I. Fig.12 depicts the buck and boost zones of modes I and II. To compare the suggested converter to similar dual-mode converters, converters in [36] and [37] are explored independently in Table I. The number of semiconductor components and voltage gain ratio of mode I are lower and greater, respectively, than in [37]. The SDP of the suggested topology is lower than [37], as shown in Table I, and the elements are fewer. While having eight elements, the converter in [36] has discontinuous output and input currents, unlike the proposed converter. Moreover, in step-up/down mode, the suggested converter has a lower switching device power (SDP) than [37]. As a result, the proposed converter has more advantage. Table II summarizes the characteristics of the suggested DC/DC buck-boost topology and existing converters.

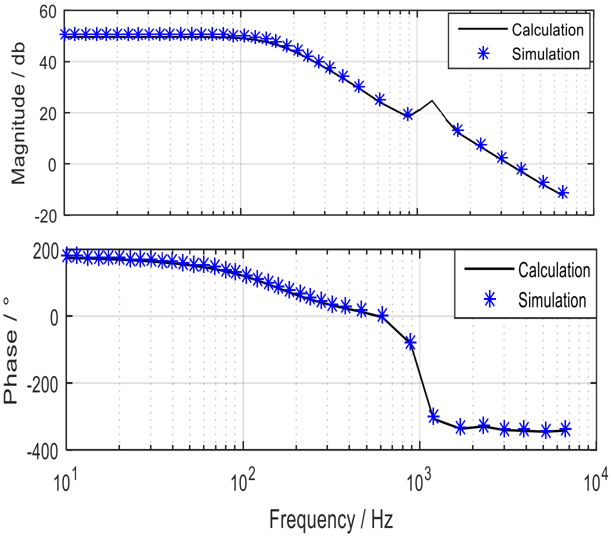

Fig. 10. Comparison of bode diagrams comparison the theoretical and simulation results.

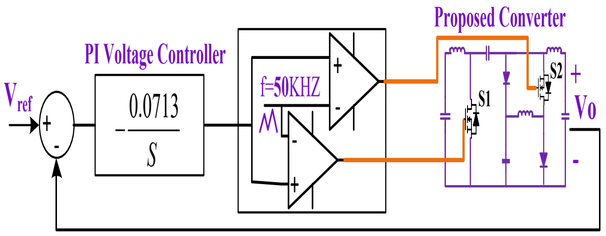

Fig. 11. PI controller system for the proposed

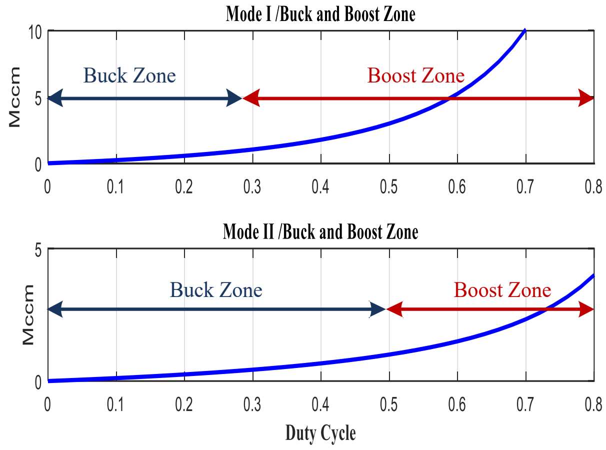

Fig. 12. Buck and Boost mode zone of modes I and II.

As shown in Table II, the number of semiconductor components, as well as the voltage stress of switches, voltage gain ratio, SDP_{avg} /P_o, output polarity, diode voltage stress, and continuous input/output current, were analyzed for the given converter and existing converters. Despite the suggested converter's continuous input current and correspondingly fewer semiconductor components, it may be a good solution for PV inverters. The suggested structure includes continuous input/output current. The subsequent section showcases the preeminence of the converter that has been recommended, with regard to voltage gain, effectiveness index, and SDP.

A. *Voltage Gain Ratio Differences*

Fig. 13 compares voltage gain ratios, and Table II contains statistics on the proposed and other competing converters. If D > 0.5, the investigated converter has a higher voltage gain than comparable converters. The horizontal axis, as displayed, represents the duty cycle (0 to 100%). Additionally, the vertical axis displays the output voltage in the 0-20V range. The higher the duty cycle, the higher the output voltage, but with more power loss.

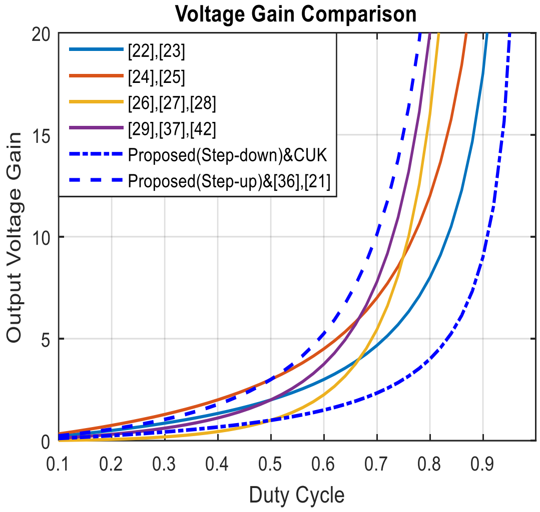

Fig. 13. Voltage gain ratios vs duty cycle comparison

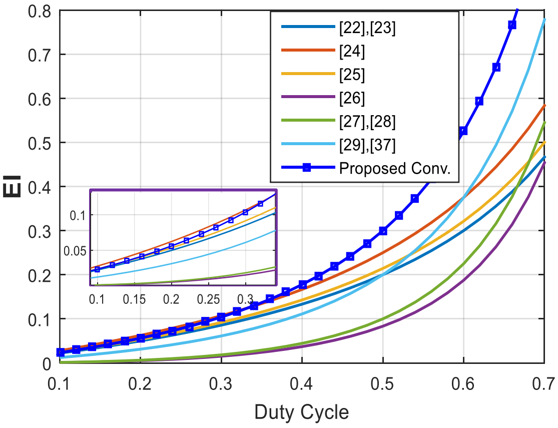

Fig. 14. Effectiveness index.

(1) *Effectiveness Index*

In this section, the performance of the provided converter is compared to that of other similar buck-boost converters in order to validate the aforementioned qualities. The complete comparative findings are shown in Table II based on the maximum voltage stress across diodes, common ground characteristics, voltage gain, input/output current ripple, voltage stress on switches, and total number of parts. In addition, an efficiency index (EI) is offered for measuring the ratio between the total number of elements used and the voltage gain value [32, 38]. The EI is calculated as:

$$EI = \frac{\frac{D(2-D)}{(1-D)^2}}{Total\ Number\ of\ Utilized\ Elements} \qquad (50)$$

This coefficient accurately represents the best usage of circuit parts and power density in the proposed converter. Fig. 14 depicts the EI vs duty cycle for the recommended converter as well as other comparable converters.

As shown in the figure, the suggested converter has a greater EI than the converters in [22-29] and [37] over the whole range of feasible duty ratio values. When the duty ratio is smaller than 0.4, the suggested converter and the converters in [24] and [25] have equivalent EI. However, at larger duty ratios, the EI of the suggested buck-boost converter is significantly better than that of current converters. This shows that the suggested converter has a higher power density.

B. Comparison Input Ripple Current

The comparison of input current ripple of the suggested converter with other competitor converters is shown in Fig.15. Fig.15 shows that the input current value of the suggested converter is lower than other buck-boost converters.

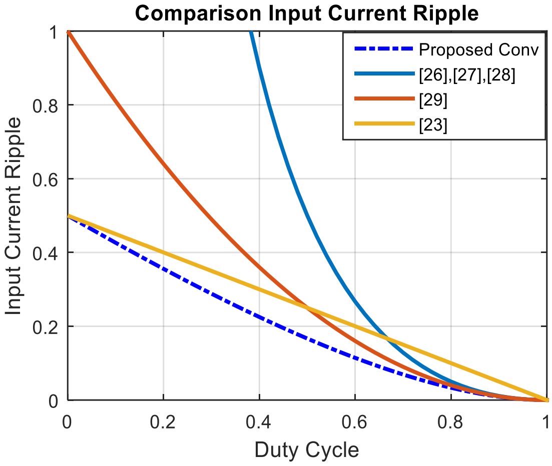

Fig. 15. Comparison the ripple input as a function of duty cycle with other converters.

(1) Total Switching Device Power (SDP)

SDP is a useful index for evaluating various switching device aspects such as cooling system requirements, possible expenses, and losses [48, 49]. It is worth noting that the voltage stress and current of the converter's diodes and switches are taken into account when calculating power loss and the overall cost of implementation. The total average switching device power (SDP_{avg}) is expressed as:

$$SDP_{avg} = \sum_{i=1}^{n} V_{S\_i} I_{Savg\_i} \qquad (51)$$

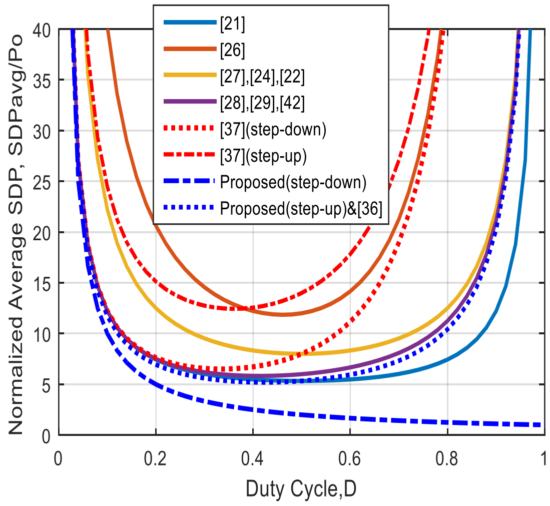

Fig. 16. Comparison of normalized SDPavg.

TABLE I Comparison of Modes (I, II)

Topology	**MODES**													
	Mode I							**Mode II**						
	D	**S**	**MCCM**	**C.I/O**	**C.G**	$\sum\frac{V_S}{V_{in}}$	**Norm. SDP**$_{avg}$ **/P**$_o$	**D**	**S**	**MCCM**	**C.I/O**	**C.G**	$\sum\frac{V_S}{V_{in}}$	**Norm. SDP**$_{avg}$ **/P**$_o$
IN [36]	2	2	$\frac{1-D+D^2}{D(1-D)}$	No/ No	Yes	$\frac{1+D}{D(1-\mathrm{D})}$	$\frac{1}{(D-\mathrm{D}^2)(1-D+\mathrm{D}^2)}$	2	2	$\frac{D(2-D)}{(1-D)^2}$	No/ No	Yes	$\frac{2-D}{(1-D)^2}$	$\frac{2}{D(1-D)(2-\mathrm{D})}$
IN [37]	4	2	$\frac{D}{(1-D)^2}$	Yes/ No	No	$\frac{2D^2-D+1}{(1-D)^2}$	$\frac{2D^3-D^2+1}{D(1-D)^2}$	3	1	$\left(\frac{D}{1-D}\right)^2$	No/ No	No	$\frac{1}{(1-D)^2}$	$\frac{2(D^3-D+1)}{D(1-D)^2}$
Proposed	2	2	$\frac{D(2-D)}{(1-D)^2}$	Yes/ Yes	Yes	$\frac{1}{(1-D)^2}$	$\frac{2}{D(1-D)(2-\mathrm{D})}$	1	1	$\frac{D}{1-D}$	Yes/ Yes	Yes	$\frac{1}{1-D}$	$\frac{1}{D(2-\mathrm{D})}$

C.I/O= Continuous Input/output, C.G= Common Ground, SDP= Switching Device Power.

TABLE II Comparison of the Buck-Boost Converter and Suggested Converter

Item	**Voltage Gain**	**Number of Elements***					**VS /Vin**	**VD /Vin**	**Norm. SDPavg /Po**	**O.P***	**C.I/O***	**If M =1**
Topology		S	D	C	L	T						
CUK Converter	$\frac{D}{1-D}$	1	1	2	2	6	$\frac{1}{1-D}$	$\frac{1}{1-D}$	------------	(–)	✓/✓	D=0.5
IN [21]	$\frac{D(2-D)}{(1-D)^2}$	1	3	2	2	8	$\frac{1}{(1-D)^2}$	$\frac{1}{1-D}\frac{D}{(1-D)^2}$ $\frac{1}{(1-D)^2}$	$\frac{4D^2-4D+2}{D(2-D)(1-D)}$	(–)	x/x	D=0.29
IN [22]	$\frac{2D}{1-D}$	1	3	3	3	10	$\frac{1}{1-D}$	$\frac{1}{1-D}\frac{1}{1-D}$	$\frac{2}{D(1-D)}$	(+)	x/✓	D=0.33
IN [23]	$\frac{2D}{1-D}$	1	2	4	3	10	$\frac{1}{1-D}$	$\frac{1}{1-D}\frac{1}{1-D}$	------------	(+)	✓/✓	D=0.33
IN [24]	$\frac{3D}{1-D}$	1	3	5	3	12	$\frac{1}{1-D}$	$\frac{1}{1-D}\frac{2D}{1-D}$ $\frac{1}{1-D}$	$\frac{2}{D(1-D)}$	(–)	x/x	D=0.25
IN [25]	$\frac{3D}{1-D}$	1	3	6	4	14	$\frac{1}{1-D}$	$\frac{1}{1-D}\frac{1}{1-D}\frac{1}{1-D}$	------------	(+)	✓/x	D=0.25
IN [26]	$\left(\frac{D}{1-D}\right)^2$	1	5	3	3	12	$\frac{1}{(1-D)^2}$	$\frac{1}{1-D}\frac{D}{(1-D)^2}$ $\frac{1}{(1-D)^2}\frac{1}{1-D}$ $\frac{D}{(1-D)^2}$	$\frac{6D^2-8D+4}{D(1-D)^2}$	(–)	✓/✓	D=0.5
IN [27]	$\left(\frac{D}{1-D}\right)^2$	2	2	3	3	10	$\frac{1}{(1-D)^2}\frac{D}{(1-D)}$	$\frac{1}{1-D}\frac{D}{(1-D)^2}$	$\frac{2}{D(1-D)}$	(+)	✓/✓	D=0.5
IN [28]	$\left(\frac{D}{1-D}\right)^2$	2	2	3	3	10	$\frac{1}{1-D}\frac{D}{(1-D)^2}$	$\frac{1}{1-D}\frac{D}{(1-D)^2}$	$\frac{1+D}{D(1-D)}$	(+)	✓/✓	D=0.5
IN [29]	$\frac{D}{(1-D)^2}$	2	2	3	3	10	$\frac{1}{1-D}\frac{1}{(1-D)^2}$	$\frac{1}{(1-D)^2}\frac{D}{(1-D)^2}$	$\frac{1+D}{D(1-D)}$	(–)	✓/✓	D=0.38
IN [36]	$\frac{D(2-D)}{(1-D)^2}$	2	2	2	2	8	$\frac{1}{1-D}\frac{1}{(1-D)^2}$	$\frac{1}{1-D}\frac{1}{(1-D)^2}$	$\frac{2}{D(1-D)(2-D)}$	(–)	x/x	D=0.29
IN [37]	$\frac{D}{(1-D)^2}$	2	4	2	2	10	$\frac{1}{(1-D)^2}$	$1\ \frac{D}{(1-D)^2}$ $\left(\frac{D}{1-D}\right)^2\frac{D}{1-D}$	$\frac{2D^3-D^2+1}{D(1-D)^2}$	(+)	x /x	D=0.38
IN [42]	$\frac{D}{(1-D)^2}$	2	2	2	2	8	$\frac{1}{1-D}\frac{1}{(1-D)^2}$	$\frac{1}{1-D}\frac{1}{(1-D)^2}$	$\frac{1+D}{D(1-D)}$	(–)	✓/x	D=0.38
Proposed	$\frac{D(2-D)}{(1-D)^2}$	2	2	3	3	10	$\frac{1}{1-D}\frac{D}{(1-D)^2}$	$\frac{1}{1-D}\frac{D}{(1-D)^2}$	$\frac{2}{D(1-D)(2-D)}$	(–)	✓/✓	D=0.29

* S=Switch, D= Diode, C= Capacitor, L= Inductor, O.P= Output Polarity, C.I/O= Continuous Input/output,
D=Duty cycle.

switching period. Fig. 16 depicts the overall average SDPs for various converters. As can be shown, the suggested converter achieves lower SDP in comparison to previous buck-boost converters by D > 0.5, which directly translates to lower semiconductor cost and power loss. The total average SDP in step-up/down mode is represented as

$$\begin{cases} Mode\ I: SDP_{avg(Step-up)} = \frac{2}{D(1-D)(2-D)}P_o \\ Mode\ II: SDP_{avg(Step-down)} = \frac{1}{D(2-D)}P_o \end{cases} \tag{52}$$

V. Experimental Verification

To confirm the theoretical claims for both modes of operation, the proposed DC/DC buck-boost converter was experimentally tested and inspected. Table III shows the components used in simulation and experimentation on the suggested converter. The values of these parameters were obtained through the mathematical solution of equations (36) -(38) and (31)- (33). The current ripples of inductors were set at a rate of 30%, whereas the voltage ripples through capacitors C_o, C_2 and C_1 were modified to 0.2, 5 and 5 percent, respectively. The capacitance values of C_o, C_2 and C_1 have been computed utilizing equations (36) -(38). The selection of the inductances of L_3, L_2, and L_1 based on the inductor current ripples as described in equations (31) -(33). In the step-up mode, the desired converter's input voltage level is varied between 15V DC and 60V DC with negative polarity. In the CCM mode, the waveforms of the L_3, L_2, and L_1 inductor currents are examined, together with the converter's input continuous current flow. In addition, with a 15V input voltage source and a duty cycle of 0.553, the mean current of inductors L_3, L_2, and L_1 are 1A, 2.24A, and 4.05A, respectively. The voltages of capacitors C_o, C_2 and C_1 are about -60.05V, -41.54V, and -75.09V, respectively, according to (5) and (6). The power MOSFETs S_2 and S_1, as well as the diodes D_2 and, D_1 were selected based on the components' current stress and voltage. After determining the rating of power MOSFETs and diodes, the mean voltage stress for these four elements is 41.51V, 18.54V, 18.56V, and 14.99V. The average current of inductors L_1, L_2, and L_3 is 0.6A, 0A, and 1A, in step-down mode, when the input voltage is 15V and the duty cycle is 0.375.

In addition, the voltage stress given to capacitors C_o, C_2 and C_1 is 8.099V, 0V, and -23.99V, respectively. Moreover, the voltage stresses delivered to power MOSFETs and diodes are 8.99V, 14.99V, 0V, and 8.99V, respectively, based on the analytic formulae.

TABLE III Experimental Setup Parameters

Parameters	**Mode I**	**Mode II**
	Step-up Mode	**Step-down Mode**
V_{in}	15V	15V
V_o	**60V**	**9V**
Duty Cycle	0.553	0.375
Output power	60W	9W
fs	50KHz	
L_1, L_2, L_3 ***R_{L1}, R_{L2}, R_{L3}***	138μH, 512μH, 512μH 0.064Ω, 0.137Ω, 0.143Ω	
C_1, C_2, Co ***R_{C1}, R_{C2}, R_{Co}***	33μF, 33μF, 160 μF 0.064Ω, 0.064Ω, 0.022Ω	
S_1,S_2	IRFP4668PBF (R_{DS}= 8mΩ) t_{on} = 41ns, t_{off} = 4ns,*Coss*=810PF	
D_1,D_2	MBR10100 (V_{FD} ~ 0.85V)	

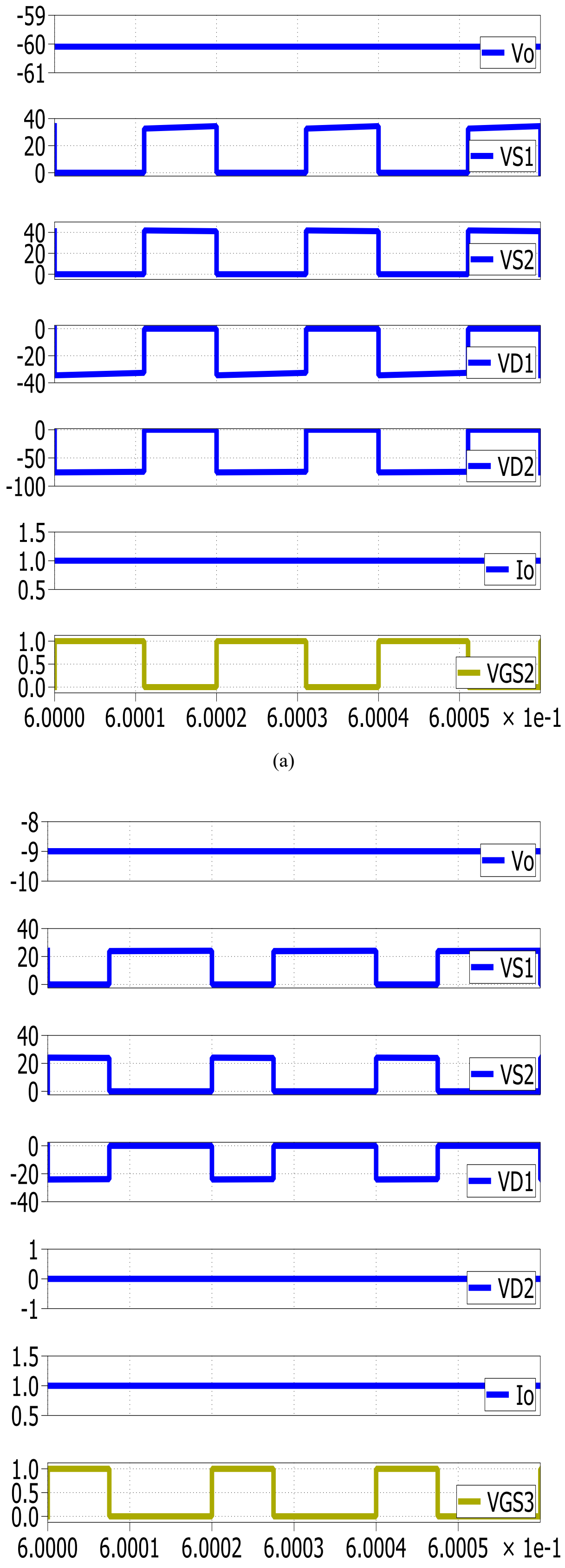

(a)

(b)

Fig. 17. Simulation waveforms in PLECS. (a) Boost mode; (b) Buck mode.

The simulation plots of the investigated converter in the two modes (step-up/down) simulation are shown in Fig.17 while operating in CCM mode through the PLECS software. It represents the current and output voltage, gate-source voltage, diodes voltage, and switch voltage of the MOSFETs. Fig. 17(a) shows the simulation waveforms in PLECS software in the boost mode and Fig. 17(b) shows the simulation waveform in the buck mode.

VI. Hardware Setup and Experimental Evaluation

Here, to verify the aforesaid properties of the suggested converter, an experimental prototype is used. The prototype was run and examined with 9W (buck mode) and 60W (boost mode) output powers. Figs. 18 and 19 show the experimental prototype and the driving circuit. The circuit elements corresponding to the experimental converter are presented in Table III. According to Table III, MOSFETs (IRFP4668PBF). MBR10100 diodes were selected for realizing the circuit.

The photocoupler TLP250 was utilized to drive the power MOSFETS S_1 and S_2. The experimental plots of the experimental prototype are shown in Figs. 20 and 21, which were recorded and measured via a GW INSTEK GDS-2102A oscilloscope and a Pintek PA- 667 1MHz current probes. The plots of the anticipated converter's currents and voltages exhibited in Figs. 20 and 21dual modes indicate a very slight variation between the experimental and PLECS simulation results. Fig. 20(a) depicts the recorded waveforms of the input and output voltage, Fig. 20(b) shows the measured currents of the inductors (L_1, L_2). Fig. 20(c) and Fig. 20(d) illustrate the voltage waveforms of the diodes and power switches in step-down mode, respectively. Fig. 21 shows the same values in step-up mode. Lastly, the test results showed that the proposed converter operation entirely follows the operation principles and characteristics mentioned in the theoretical claims. Fig 22 (a) and (b) show the theoretical and experimental efficiency curves of the proposed converter for varied output power in step-up and step-down modes, respectively.

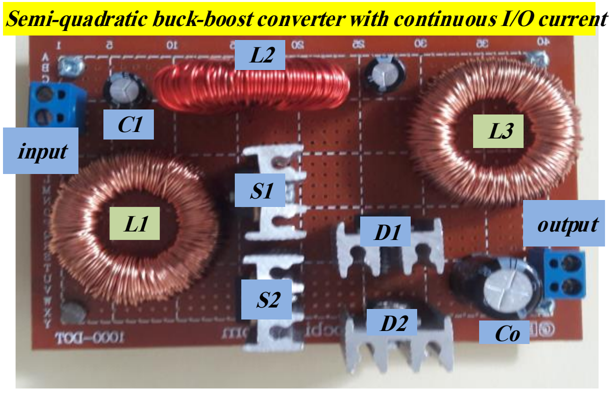

Fig. 18. Experimental hardware prototype.

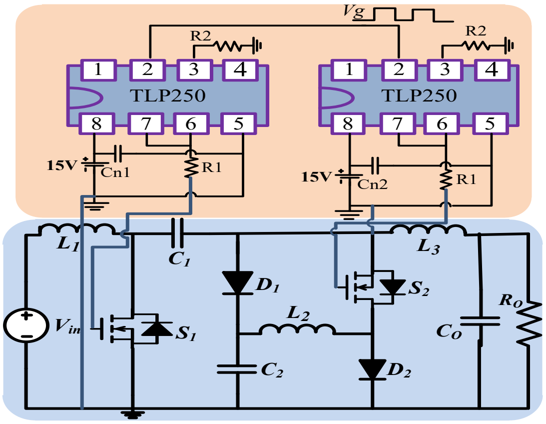

Fig. 19. MOSFET driver circuit

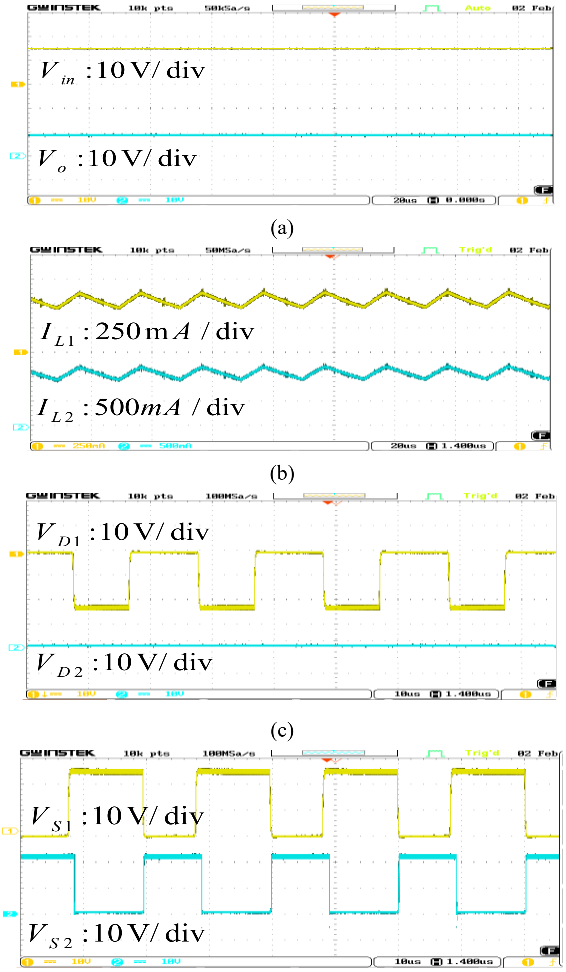

(a)

(b)

(c)

(d)

Fig. 20. Waveforms in the step-down mode; (a) V_{in}, V_o; (b) i_{L1}, i_{L2}; (c) V_{D1}, V_{D2}; (d) V_{S1}, V_{S2}.

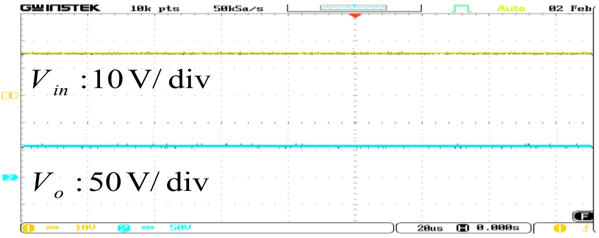

(a)

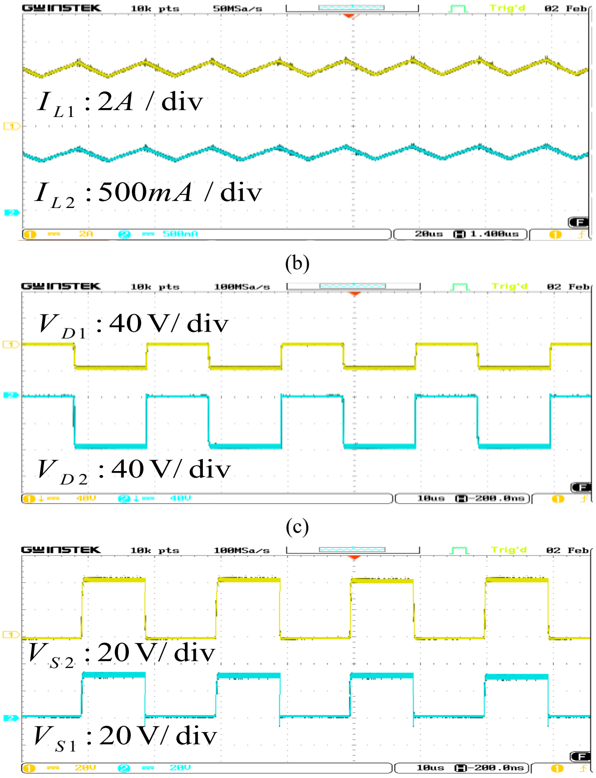

(b)

(c)

(d)

Fig. 21. Waveforms in the step-up mode; (a) V_{in}, V_o; (b) i_{L1}, i_{L2}; (c) V_{D1}, V_{D2}; (d) V_{S1}, V_{S2}

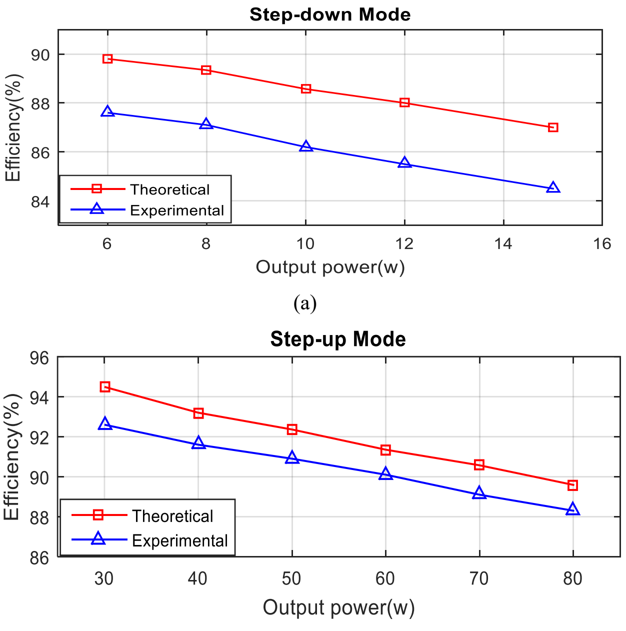

(a)

(b)

Fig. 22. Efficiency plot of experimental and theoretical result of the suggested converter. (a) Step-down mode (Mode II); (b) Step-up mode (Mode I).

VII. Conclusion

This paper presents a new semi-quadratic DC-DC converter featuring (a) continuous input and output current for reduced ripple and EMI suppression, (b) negative output polarity, (c) wide voltage range operation with minimal duty cycle variation, and (d) dual operating modes offering two distinct buck-boost voltage gain ratios. The working principle was analyzed in both operational modes, with steady-state analysis establishing the relationships between voltage and current. A comprehensive efficiency analysis incorporating component parasitic elements was presented, along with an estimation of power loss. The passive components were designed to meet the requirements for ripple voltage and current. The comparative evaluation demonstrates the converter's superior performance, achieving higher voltage gain, improved efficiency (92.6% in Mode I and 87.6% in Mode II), and lower switching device power (SDP) compared to existing quadratic converters. Experimental validation confirmed the converter's practical performance. With its continuous current characteristics and negative output capability, the proposed topology is particularly suitable for multifunction power supplies, photovoltaic systems, signal generators, audio amplifiers, and data transmission interfaces requiring negative voltage supplies.

REFERENCES

[1] R. Gopi and S. Sreejith, "Converter topologies in photovoltaic applications – A review," *Renew. Sustain. Energy Rev.,* vol. 94, pp. 1-14, 2018, doi: 10.1016/j.rser.2018.05.047.

[2] M. H. Taghvaee, M. A. M. Radzi, S. M. Moosavain, H. Hizam, and M. H. Marhaban, "A current and future study on non-isolated DC–DC converters for photovoltaic applications," *Renew. Sustain. Energy Rev.,* vol. 17, pp. 216-227, 2013, doi: 10.1016/j.asej.2021.06.027

[3] F. Blaabjerg, R. Teodorescu, Z. Chen, and M. Liserre, "Power converters and control of renewable energy systems," in *Proc. 6th Int. Conf. Power Electron*, pp. 1-20, Oct 18, 2004.

[4] F. Blaabjerg, C. Zhe, and S. B. Kjaer, "Power electronics as efficient interface in dispersed power generation systems," *IEEE Trans. Power Electron.,* vol. 19, pp. 1184-1194, 2004, doi: 10.1109/TPEL.2004.833453.

[5] K. Nathan, S. Ghosh, Y. Siwakoti and T. Long, "A new dc–dc converter for photovoltaic systems: coupled-inductors combined cuk-sepic converter, " *IEEE Trans. Energy Convers.,* vol. 34, no. 1, pp. 191-201, Mar 2019, doi: 10.1109/TEC.2018.2876454

[6] A. Torkan and M. Ehsani, "A novel nonisolated z-source dc–dc converter for photovoltaic applications, " *IEEE Trans. Ind. Appl.,* vol. 54, no. 5, pp. 4574-4583, Sept.-Oct. 2018, doi:10.1109/TIA.2018.2833821

[7] K. V. G. Raghavendra, et al. "A comprehensive review of DC–DC converter topologies and modulation strategies with recent advances in solar photovoltaic systems, " *J. Electron.*; vol. 9, no. 1, Dec 26, 2019, doi:10.3390/electronics9010031.

[8] L. J. Jeremy, C.A. Ooi, J. Teh, " Non-isolated conventional DC-DC converter comparison for a photovoltaic system: a review," *J. Renew. Sustain. Energy*; vol. 12, no. 1, 2020, doi:10.1063/1.5095811.

[9] R. W. Erickson and D. Maksimovic, in *Fundamentals of power electronics*, 2nd ed. Boston: Kluwer Academic Publishers, 2001.

[10] F. Mumtaz, N. Z. Yahaya, S. T. Meraj, B. Singh, R. Kannan, and O. Ibrahim, "Review on non-isolated DC-DC converters and their control techniques for renewable energy applications," Ain Shams Eng. J., 2021, doi: 10.1109/TIE.2016.2608321.

[11] M. Adly and K. Strunz, "Irradiance-adaptive pv module integrated converter for high efficiency and power quality in standalone and dc microgrid applications," IEEE Trans. Ind.

Electron., vol. 65, pp. 436-446, 2018, doi: 10.1109/TIE.2017.2723860.

[12] S. Chen, T. Liang and K. Hu, “Design, analysis, and implementation of solar power optimizer for dc distribution system,” in *IEEE Trans. Power Electron.*, vol. 28, no. 4, pp. 1764-1772, April 2013, **doi:** 10.1109/TPEL.2012.2213270.

[13] “SolarEdge Fixed String Voltage, Concept of Operation,” [Online]. Available: https://www.solaredge.com.

[14] J. D. Navamani, K. Vijayakumar, R. Jegatheesan, " Non-isolated high gain DC/DC converter by quadratic boost converter and voltage multiplier cell, " *Ain Shams Eng. J.*; pp.1397–406, 2018.

[15] J. D. Navamani, A. Lavanya, D. Almakhles, and M. J. Sathik, “A review on segregation of various high gain converter configurations for distributed energy sources,” *Alexandria Eng. J.,* vol. 61, no. 1, pp. 675-700, Jan 2022, doi: 10.1109/JESTPE.2022.2985844.

[16] K. I. Hwu and T. J. Peng, "A novel buck–boost converter combining ky and buck converters," *IEEE Trans. Power Electron.,* vol. 27, pp. 2236-2241, 2012, doi**:** 10.1109/TPEL.2011.2182208.

[17] H. Ardi and A. Ajami, "Study on a high voltage gain sepic-based dc–dc converter with continuous input current for sustainable energy applications," *IEEE Trans. Power Electron.,* vol. 33, pp. 10403-10409, 2018, doi: 10.1109/TPEL.2018.2811123.

[18] S. Miao, F. Wang, and X. Ma, "A new transformerless buck–boost converter with positive output voltage," *IEEE Trans. Ind. Electron.,* vol. 63, pp. 2965-2975, 2016, doi: 10.1109/TIE.2016.2518118

[19] M. R. Banaei, H. Ardi, and A. Farakhor, "Analysis and implementation of a new single-switch buck-boost dc/dc converter," *IET Power Electron.,* vol. 7, pp. 1906-1914, 2014, doi: 10.1049/iet-pel.2013.0762.

[20] J. C. Rosas-Caro, J. E. Valdez-Resendiz, J. C. Mayo-Maldonado, A. Alejo-Reyes, and A. Valderrabano-Gonzalez, "Quadratic buck–boost converter with positive output voltage and minimum ripple point design," *IET Power Electron.,* vol. 11, pp. 1306-1313, 2018, doi:10.1049/iet-pel.2017.0090.

[21] S. A. Gorji, A. Mostaan, H. T. My, and M. Ektesabi, "Non-isolated buck–boost dc–dc converter with quadratic voltage gain ratio," *IET Power Electron.,* vol. 12, pp. 1425-1433, 2019, doi:10.1049/iet-pel.2018.5703.

[22] M. R. Banaei, and H. A. F. Bonab, "A high efficiency non-isolated buck-boost converter based on zeta converter, " *IEEE Trans. Ind. Electron.*, pp. 1-1, 2019, doi: 10.1109/TIE.2019.2902785.

[23] S. H. Hosseini, R. Ghazi, and S. K. Movahhed, "A novel high gain single-switch dc-dc buck-boost converter with continuous input and output power," at the *24th IEEE Elect. Power Distribution Conf. (EPDC),* Khorramabad, Iran, pp. 10-15, 2019, doi: 10.1109/EPDC.2019.8903599.

[24] M. R. Banaei and H. A. F. Bonab, “A novel structure for single- switch nonisolated transformerless buck-boost dc-dc converter,” *IEEE Trans. Ind. Electron.,* vol. 64, no. 1, pp. 198-205, Jan. 2017, doi: 10.1109/TIE.2016.2608321.

[25] M. R. Banaei, and S. G. Sani, "Analysis and implementation of a new sepic-based single-switch buck-boost dc-dc converter with continuous input current" *IEEE Trans. on Power Electronics*, vol. 33, no. 12, pp. 10317–10325, 2018, doi: 10.1109/TPEL.2018.2799876.

[26] N. Zhang, G. Zhang, K. W. See, and B. Zhang, "A single-switch quadratic buck–boost converter with continuous input port current and continuous output port current," *IEEE Trans. Power Electron.*, vol. 33, pp. 4157-4166, 2018, doi: 10.1109/TPEL.2017.2717462.

[27] A. Sarikhani, B. Allahverdinejad, M. Hamzeh, and E. Afjei, "A continuous input and output current quadratic buck-boost converter with positive output voltage for photovoltaic applications," *J. Sol. Energy*, vol. 188, pp. 19-27, 2019, doi:10.1016/j.solener.2019.05.025.

[28] M. Veerachary, M.R. Khuntia, "Design and analysis of two-switch-based enhanced gain buck–boost converters". *IEEE Trans. Ind. Electron*., vol. 69, no. 4, pp. 3577–3587, 2022, doi:10.1109/TIE.2021.3071696.

[29] M. Okati, M. Eslami, M. J. Shahbazzadeh, H. Shareef, "A new transformerless quadratic buck–boost converter with high voltage gain ratio and continuous input/output current port,". *IET Power Electron.,* vol. 15, no. 13, pp. 1280-1294, 2022, doi: 10.1049/pel2.12304.

[30] P. K. Maroti, S. Padmanaban, J. B. Holm-Nielse, M. S. Bhaskar, M. Meraj, A. Iqbal, "A new structure of high voltage gain SEPIC converter for renewable energy application, ". *IEEE Access*, vol. 7, pp. 89857–89868, 2019, doi: 10.1109/ACCESS.2019.2925564.

[31] J. C. Mayo-Maldonado, J. E. Valdez-Resendiz, P. M. Garcia-Vite, J. C. Rosas-Caro, M. R. Rivera-Espinosa and A. Valderrabano-Gonzalez, "Quadratic buck–boost converter with zero output voltage ripple at a selectable operating point," *IEEE Trans. Ind. Appl.*, vol. 55, no. 3, pp. 2813-2822, May-June 2019, doi: 10.1109/ACCESS.2019.2925564.

[32] K. Yari, S. H. Shahalami and H. Mojallali, "A novel nonisolated buck–boost converter with continuous input current and semiquadratic voltage gain," in *IEEE J. Emerg. and Sel. Topics in Power Electron.*, vol. 9, no. 5, pp. 6124-6138, Oct. 2021, doi: 10.1109/JESTPE.2021.3069788.

[33] M. Okati, M. Eslami & M. J. Shahbazzadeh, "A non-isolated dc-dc converter with dual working modes and positive output voltage", *Electric Power Compon. and Syst.,* vol.49, pp. 1143-1157, 2022, doi: 10.1080/15325008.2022.2049662.

[34] A. Mahmood et al., "A non-inverting high gain dc-dc converter with continuous input current," in *IEEE Access*, vol. 9, pp. 54710-54721, 2021, doi: 10.1109/ACCESS.2021.3070554.

[35] A. Sarikhani, B. Allahverdinejad, M. Hamzeh, "A nonisolated buck–boost DC–DC converter with continuous input current for photovoltaic applications," in *IEEE J. Emerg. Sel. Top. Power Electron*, vol. 9, pp.804–811, 2021, doi: 10.1109/JESTPE.2020.2985844.

[36] J. Li and J. Liu, "A negative-output high quadratic conversion ratio dc-dc converter with dual working modes," *IEEE Trans. Power Electron*., vol. 34, no. 6, pp. 5563-5578, June 2019, doi: 10.1109/TPEL.2018.2870421.

[37] M. A. Abbaszadeh, M. Monfared, and H. Heydari-doostabad, "High buck in buck and high boost in boost dual-mode inverter (Hb^{2}DMI)," *IEEE Trans. Ind. Electron.*, vol. 68, pp. 4838-4847, 2021, doi: 10.1109/TIE.2020.2988240.

[38] S. Hasanpour, A. Baghramian and H. Mojallali, "analysis and modeling of a new coupled-inductor buck–boost dc–dc converter for renewable energy applications," in *IEEE Trans. Power Electron.*, vol. 35, no. 8, pp. 8088-8101, Aug. 2020, doi: 10.1109/TPEL.2019.2962325.

[39] H. Gholizadeh, S. A. Gorji and D. Sera, "A Quadratic Buck-Boost Converter with Continuous Input and Output Currents," in *IEEE Access*, vol. 11, pp. 22376-22393, 2023, doi: 10.1109/ ACCESS.2023.2981331.

[40] S. A. Gorji, "Reconfigurable Quadratic Converters for Electrolyzers Utilized in DC Microgrids," in *IEEE Access*, vol. 10, pp. 109677-109687, 2022, doi: 10.1109/ACCESS.2022.3214581

[41] S. Miao, N. Lyu, X. Jiang, W. Liu and Y. Jin, "A New Fifth-Order Boost Converter with Dual Operating Modes and Wider Conversion Ratios for Renewable Energy Applications," in *IEEE Transactions on Circuits and Systems II: Express Briefs*, vol. 69, no. 12, pp. 4914-4918, Dec. 2022, doi: 10.1109/TCSII.2022.3192641.

[42] SVK. Naresh, S. Peddapati. "Complementary switching enabled cascaded boost-buck-boost (BS-BB) and buck-boost-buck (BB-BU) converters". *Int J Circ Theor Appl*, vol. 49, no. 9, pp. 2736– 2753. 2021, doi: 10.1002/cta.3034.

[43] S. Toofan, B. Fathipour, and E. Babaei, "A Single Switch Transformer-Less DC-DC Converter with Continuous Input Current for Photovoltaic Applications,". *International Journal of Industrial Electronics Control and Optimization*, vol. 7, no. 4, pp. 281-290, 2024, doi:10.22111/ieco.2024.48295.1548.

[44] H. Gholizadeh, and S. Hasanpour, "A New Quadratic CUK-Based Step-Up DC/DC Converter Without Right Hand Plane Zero", *International Journal of Industrial Electronics Control and Optimization*, vol. 8, no. 1, pp. 25-35, 2025, doi.:10.22111/ieco.2024.48683.1565.

[45] M. Elmi, M.R. Banaei, and H. Afsharirad, "Study on a Non-Isolated High Step-Up SEPIC-Based DC-DC Converter with Continuous Input Current for Photovoltaic Applications", *International Journal of Industrial Electronics Control and* Optimization, vol. 8, no. 1, pp. 95-104, 2025, doi: 10.22111/ieco.2024.48587.1558.

[46] K. Yari, S. Hasanpour. "A Minimum Phase DC-DC Converter with Continuous Input Current and High Voltage Gain", *International Journal of Industrial Electronics Control and Optimization*, vol. 7, no. 4, pp. 301-312, 2024, doi:10.22111/ieco.2024.48842.1572.

[47] R. D. Middlebrook, "Small-signal modeling of pulse-width modulated switched-mode power converters," *Proc. of the IEEE*, vol. 76, pp. 343-354, 1988, doi: 10.1109/5.4421.

[48] Y. Zhang, J. Liu, X. Ma, J. Feng, "Comparison of conventional DC-DC converter and a family of diode-assisted DC-DC converter in renewable energy applications, *"Journal of Power Electron*. vol. 14, pp. 203–216, 2014, doi:10.6113/JPE.2014.14.2.203.

[49] M. Shen, A. Joseph, J. Wang, F. Z. Peng, and D. J. Adams, "Comparison of traditional inverters and z -source inverter for fuel cell vehicles," *IEEE Trans. Power Electron.*, vol. 22, pp. 1453-1463, 2007, doi: 10.1109/TPEL.2007.900505.

Mustafa Okati was born in Iran, in 1983. He received the B.S. degree in electronic engineering from Azad Islamic University, Zahedan Branch, Iran, in 2007, the M.S. degree from Azad Islamic University, Gonabad Branch, Iran, in 2009, and the Ph.D. degree in power electronics engineering from Azad Islamic University, Kerman Branch, Iran, in 2021. He is currently assistant professor at Azad Islamic University, Zabol Branch, Zabol, Iran. His main research interest is the application of power electronic technology, implementation of step-up/step-down switch-mode DC/DC converters with high-power density, PV inverters in power systems and renewable energy technologies.

Mohammad Osmani-Bojd was born in Zahedan, Iran, in 1975. He received his B.Sc. degree from the Faculty of Engineering at Shahid Bahonar University of Kerman, Iran, in 1997, and his M.Sc. degree in Electrical Engineering from the University of Tehran, Iran, in 2000. He earned his Ph.D. in Electrical Engineering from Ferdowsi University of Mashhad, Iran, in 2013. In 2002, he joined the Islamic Azad University, Zahedan Branch, as a Lecturer in the Department of Electrical Engineering. Since 2013, he has been serving as an Assistant Professor at the same institution.

IECO International Journal Of
Industrial Electronics Control and Optimization
Print ISSN: 3517-2645
Online ISSN: 3568-2645
Homepage: https://ieco.usb.ac.ir/

A Mathematical Framework for Designing Precise RBW Filters Using Standard Implementation Techniques in EMI Applications

Seyed Fariborz Zarei[1]* | Saeed Hasanzadeh[1]

Department of Electrical and Computer Engineering, Qom University of Technology, Qom, Iran.[1]
Corresponding author's email: zarei@qut.ac.ir

Article Info

Article type:
Research Article

Article history:
Received: 22-March-2025
Received in revised form:
24-July-2025
Accepted: 30-July-2025
Published online: 22-June-2026

Keywords:
CISPR-16 standard,
Conducted emissions,
Electromagnetic interference,
Filter design,
Resolution bandwidth filters.

ABSTRACT

This paper presents a comprehensive approach to the design of Resolution Bandwidth (RBW) filters specifically for Electromagnetic Interference (EMI) applications. We propose a mathematical modeling method that accurately captures the characteristics of standard RBW filters, which are essential for precise EMI noise measurements. The proposed approach utilizes paired complementary second-order filters with symmetrical cutoff frequencies to ensure compliance with CISPR-16 standards. The methodology underscores the importance of aligning theoretical models with real-world filter behavior, ensuring that the resulting models are both accurate and reliable. By establishing a robust framework for RBW filter design, the method enables optimized EMI system performance and the implementation of appropriate filtering solutions. Validation is carried out through simulations using a 150 kHz signal with a dynamically ramped amplitude increase, demonstrating high accuracy and strong performance under both transient and steady-state conditions. Despite the challenging test scenarios, the results confirm that the proposed filter model remains accurate and effective even under worst-case EMI conditions.

I. Introduction

The rapid proliferation of power electronic systems in areas such as renewable energy, electric vehicles, and wireless communications has significantly increased the need for effective Electromagnetic Interference (EMI) management to ensure reliable operation and compliance with standards such as CISPR-16. Resolution Bandwidth (RBW) filters play a crucial role in accurate EMI measurements; however, their design remains challenging in the context of modern, high-frequency systems. Recent studies on modular multilevel converters [1], gate driver optimization [2], and inverter-based networks [3] emphasize the persistent challenges associated with EMI. At the same time, advancements in high-efficiency converters [4], portable resonant chargers [5], and antenna designs incorporating artificial magnetic conductors [6] further highlight the need for precise filter modeling to effectively mitigate EMI in increasingly complex and compact systems.

Electromagnetic interference (EMI) presents significant challenges for power electronic converters, particularly as these systems become increasingly integrated into diverse applications such as renewable energy technologies and electric vehicles [7, 8]. The study of EMI is critical, as it directly affects the reliability, safety, and performance of power electronic devices. Effective management of conducted EMI is essential to ensure that these devices operate within acceptable limits and do not negatively impact surrounding equipment. A fundamental aspect of addressing EMI involves the accurate modeling of measurement components, which serves as the foundation for developing efficient mitigation strategies [9]. Precise modeling enables engineers to predict EMI behavior, optimize filter designs, and enhance overall system performance. As highlighted in various studies [10, 11], modern power electronic converters often operate at higher switching frequencies, which exacerbate both conducted and radiated EMI, necessitating more advanced modeling techniques for effective suppression [9]. Furthermore, the integration of innovative designs and materials, as discussed in [12], underscores the need for tailored EMI mitigation strategies to ensure safe and reliable operation across a broad range of applications. As the demand for high-performance power electronics continues to grow, understanding and mitigating EMI through robust and accurate modeling techniques becomes increasingly critical.

Research in the field of Electromagnetic Interference (EMI) has evolved significantly, with a growing focus on diverse modeling approaches and practical applications. For instance, [13] emphasizes the role of passive filters—particularly EMI filtering chokes—which are essential for

Publisher: University of Sistan and Baluchestan

noise mitigation and performance optimization in power electronic systems. This study highlights the need for systematic simulation and characterization methods to refine filter design. Similarly, [14] introduces a unified methodology for developing compact EMI filters tailored to high-frequency switched-mode power converters, stressing the importance of optimizing differential-mode (DM) filter stages for higher power densities while managing common-mode (CM) noise through detailed mathematical modeling. Reference [15] provides a comparative analysis of noise emissions across various converter topologies, clarifying how DM and CM noise characteristics influence filter design strategies. Time-domain simulation techniques, as explored in [16], reveal nonlinear circuit behaviors influenced by resolution bandwidth settings. Advanced models for dual three-phase active bridge rectifiers presented in [17] incorporate conducted EMI noise predictions to enhance filter design for high-power systems while ensuring compliance with international standards. Stabilization strategies for point-of-load converters with integrated EMI filters, discussed in [18], address voltage oscillations caused by LC filter interactions through active damping techniques to improve system stability. The mechanisms of radiated EMI, as analyzed in [12], account for switching behavior, PCB layout, and shielding—factors that are critical in mitigating interference in high-frequency power electronics. In the context of grid-tied solar inverters, [19] proposes filter designs that account for ground leakage currents and component tolerances, ensuring standard compliance while minimizing conducted emissions. Measurement-based equivalent circuit models derived from S-parameters, discussed in [20], have also proven effective in time-domain simulation of EMI filters. Further advancements include innovative algorithms for wide band-pass filter construction [21] and two-phase scanning models for EMI receiver simulations [22], both of which broaden analytical capabilities. Dithering techniques applied to voltage source inverters, as shown in [23], demonstrate how switching frequency modulation can effectively reduce conducted emissions while optimizing system cost and footprint. Methods for DM noise prediction in grid-tied inverters [24] offer high-accuracy analysis of low-frequency EMI up to 150 kHz, while frequency jittering optimization in [25] balances peak and average noise suppression. Finally, the use of artificial neural networks (ANNs) in [26] provides an efficient means of modeling and optimizing EMI filters, highlighting the growing role of intelligent algorithms in EMI management.

Collectively, these studies underscore the critical role that advanced modeling techniques play in addressing the multifaceted challenges posed by EMI in power electronic systems. In this context, the accurate modeling of measurement devices is of paramount importance. Because the output of these devices is evaluated against standardized limits, their faithful representation—aligned with standard-defined characteristics—directly influences the accuracy of EMI assessments and, by extension, the effectiveness of mitigation strategies. Precise models of measurement devices enable more reliable EMI analysis, supporting the development of EMI filters that are not only effective but also optimized in terms of cost, size, and performance. Existing RBW filter designs, such as those based on high-order Butterworth filters, often involve complex tuning procedures to comply with CISPR-16 standards and impose high computational costs. The proposed approach addresses these limitations by employing a simpler, standard-compliant structure based on paired second-order filters. To address these challenges, this paper proposes a novel approach for modeling Resolution Bandwidth (RBW) filters—key components in EMI measurements—using a mathematical framework grounded in standard implementations for EMI applications. This framework is designed to bridge the gap between theoretical models and practical EMI filter design, ensuring both accuracy and compliance with established standards.

The remainder of this paper is organized as follows: Section II provides an overview of the EMI measurement process, highlighting the critical components and procedures involved. Section III introduces the proposed mathematical framework for accurately modeling RBW filters, including detailed methodology and implementation. Section IV presents numerical results that demonstrate the effectiveness and precision of the proposed approach. Finally, Section V concludes the paper with a summary of findings and potential directions for future work.

II. An Overview of the EMI Measurement Circuit

Previous studies have extensively investigated conducted EMI modeling using both time-domain and frequency-domain (spectral) approaches. For accurate simulation of conducted EMI levels, it is essential to model the entire measurement setup in accordance with electromagnetic compatibility (EMC) standards. This section provides a concise overview of the modeling of two critical components within the measurement system: the Line Impedance Stabilization Network (LISN) and the EMI receiver. Notably, the RBW filter—central to this study—is an integral part of the EMI receiver.

A. LISN/AMN

Functioning either as a Line Impedance Stabilization Network (LISN) or, under more recent IEC standards, as an Artificial Mains Network (AMN), this component serves three essential functions: (a) providing high-frequency isolation between the power converter and the power source, (b) maintaining a consistent impedance for both line and ground currents, and (c) ensuring reproducible measurement conditions. A representative LISN circuit, compliant with CISPR 16 requirements for frequencies above 9 kHz, is illustrated in Fig. 1. The voltage representing conducted electrical noise, denoted as u_{noise}, is measured in the time domain. The 50 Ω resistor models the input impedance of the EMI receiver.

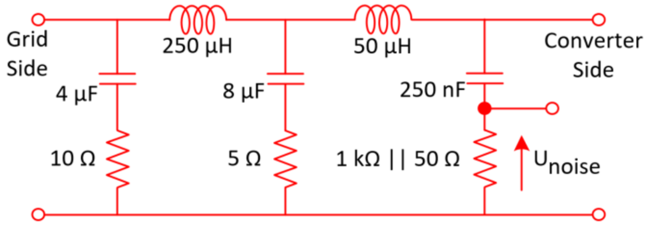

Fig. 1 Circuit diagram of LISN/AMN according to CISPR16 standards

B. *EMI Receiver*

The second essential component for EMI prediction is the EMI receiver model. As illustrated in Fig. 2, this model represents the general structure of a typical EMI receiver [27]. However, accurately modeling this component presents significant challenges, primarily because manufacturers often do not disclose detailed internal specifications. Consequently, simplified models are commonly employed in the literature as practical alternatives to detailed representations [27].

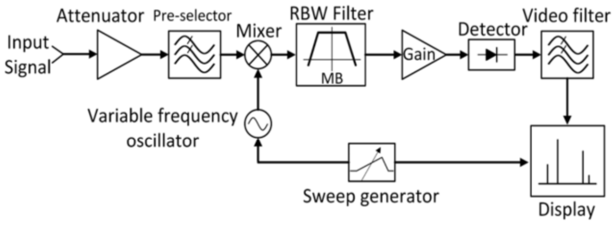

Fig. 2 overall representation diagram of the EMI receiver with different components [27]

C. *Resolution Bandwidth (RBW) Filter*

The band-pass filter—commonly known as the Resolution Bandwidth (RBW) filter—plays a critical role in determining the extent of EMI emissions captured during measurement. When applied to the voltage spectrum at the output of the LISN, the RBW filter directly influences the measured results. The filter's bandwidth, denoted as BW_{RBW}, is selected based on the frequency range being evaluated, in accordance with standardized guidelines. For the two primary CISPR-defined frequency bands—Band A (9–150 kHz) and Band B (150 kHz–30 MHz)—the corresponding RBW filter bandwidths are 200 Hz and 9 kHz, respectively. Figures 3(a) and 3(b) depict the upper and lower amplitude limits of the RBW filter response for Band A and Band B, respectively, as specified by the CISPR 16 standard.

III. Proposed Model of RBW-Filter and Design Procedure

In the previous section, the various components of the EMI measurement circuit were described. In this section, the proposed RBW filter is introduced, and the design procedure is presented in detail. Additionally, the filter's compliance with the CISPR-16 standard limits is thoroughly discussed.

A. *Funfamentals of the Proposed Approach*

With reference to Fig. 3 in Section III, the upper and lower bounds specified by the CISPR-16 standard highlight the limitations of conventional first- and second-order filters in meeting standard compliance. Specifically, two primary challenges arise in the implementation of RBW filters: achieving a sufficiently flat response around the mid-band frequency and ensuring compliance with the upper and lower attenuation limits across the remaining frequency range. To address these issues, more complex designs—such as the Butterworth filter—have been proposed in the literature [27]. However, such solutions complicate the mathematical modeling process and increase implementation complexity.

In contrast, this paper proposes a simple yet effective structure based on conventional second-order filters that achieves compliance with CISPR-16 requirements. The proposed method employs two pairs of filters, with each pair consisting of two complementary second-order filters. These filters share the same gain and quality factor but have distinct cutoff frequencies that are symmetrically placed around the center frequency. This configuration ensures that the resulting RBW filter exhibits the required flat mid-band response and adheres to standard roll-off constraints, while maintaining a mathematically tractable and computationally efficient structure.

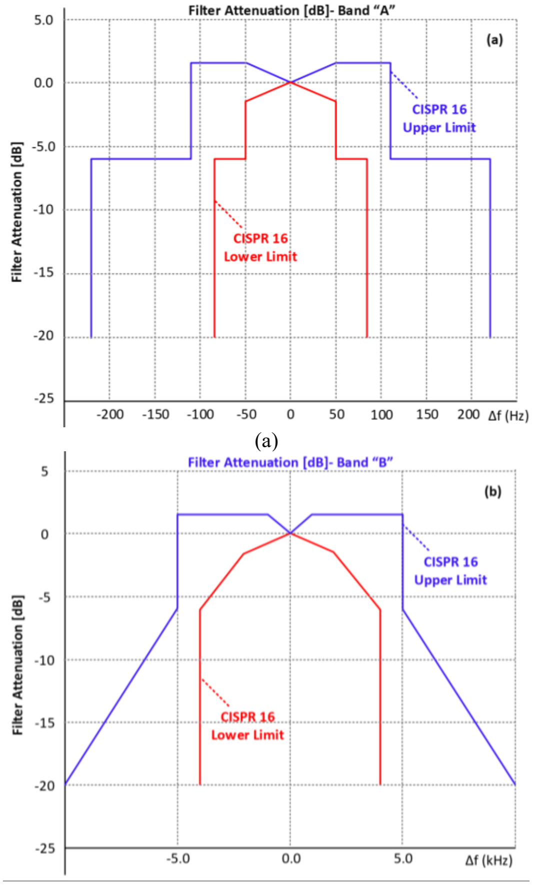

(a)

(b)

Fig. 3 overall representation diagram of the EMI receiver with different components

To clarify further, Fig. 4 illustrates the conceptual structure of the proposed RBW filter, designed in compliance with the CISPR-16 standard. As shown, the configuration consists of four band-pass filters connected in series. Each filter pair operates in a complementary manner to form the overall standard-compliant RBW filter response. The first two filters are centered at frequencies $f_0 \pm f_1$, and their mathematical formulation is provided in Equations (1) and (2). The resulting frequency response of this filter pair is depicted in Fig. 5(a). As shown, the amplification and attenuation characteristics of the individual filters effectively cancel each other out, yielding a combined response indicated by the dotted line in Fig. 5(a).

$$F_1 = G_1.\frac{2\xi\omega_{n1}s}{s^2 + 2\xi\omega_{n1}s + \omega_{n1}^2} \qquad \omega_{n1} = 2\pi.(f_0 + f_1) \qquad (1)$$

$$F_2 = G_2.\frac{2\xi\omega_{n2}s}{s^2 + 2\xi\omega_{n2}s + \omega_{n2}^2} \qquad \omega_{n2} = 2\pi.(f_0 - f_1) \qquad (2)$$

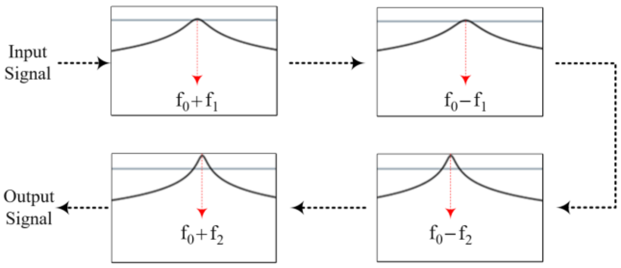

Fig. 4 Conceptual representation of the proposed RBW-filter structure compliant with the CISPR-16 standard

Similarly, the second pairs of the filters given in Fig. 4 are tuned on the frequency of $f_0 \pm f_2$ with $f_2 > f_1$. Fig. 5 (b) shows the resultant frequency characteristics of this pair of band-pass filters. The same equations of (1)-(2) can be defined for this pairs of filters, shown in (3)-(4). The simultaneous amplification and attenuation of the amplitudes of these filters compensate each other and produces the characteristics shown by dotted line in Fig. 5 (b).

$$F_3 = G_3.\frac{2\xi\omega_{n3}s}{s^2 + 2\xi\omega_{n3}s + \omega_{n3}^2} \qquad \omega_{n3} = 2\pi.(f_0 + f_2) \qquad (3)$$

$$F_4 = G_4.\frac{2\xi\omega_{n4}s}{s^2 + 2\xi\omega_{n4}s + \omega_{n4}^2} \qquad \omega_{n4} = 2\pi.(f_0 - f_2) \qquad (4)$$

Combining the two pair filters results in a filter with standard characteristics shown in Fig. 5 (c).

B. *Design of a Sample RBW Filter*

To exemplify the proposed structure for the RBW filter, a design example dedicated for power electronics application in power grid is presented in this section.

1- *The First Pair of Filters*:

The base frequency of 150 kHz is considered for this example. The frequency deviation of $f_1 = 2$ kHz is chosen for this study. The resultant filter gain and quality factor ($=\frac{1}{2\xi}$) are determined 1.08 and 13.5, respectively. The two filters in this pair, and the resulted output filter, dotted line, are given in Fig. 5 (a).

2- *The Second Pair of Filters:*

The base frequency of 150 kHz is considered for this case. The frequency deviation of $f_1 = 5$ kHz is chosen for this part. The resultant filter gain and quality factor ($=\frac{1}{2\xi}$) are determined 2.4 and 32.7, respectively. The two filters in this pair, and the resulted output filter, dotted line, are given in Fig. 5 (b).

The resulted filter is given in Fig. 5 (c), in which its fundamental parts $F_1 \times F_2$ and $F_3 \times F_4$ filters, shown respectively by red and blue waveform characteristic. These two filters together with each other results in a dotted line filter given in this figure. As shown in this figure, the dotted line filter has a flat characteristic in the base frequency, and the filter bandwidth is 9 kHz, which is within the standard region highlighted by cyan color in this figure.

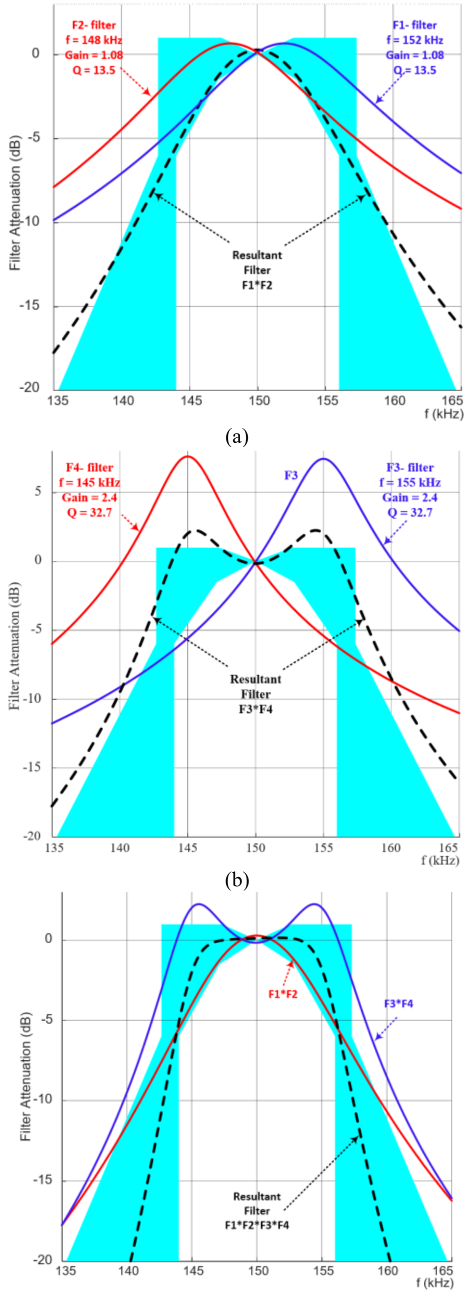

(a)

(b)

(c)

Fig. 5 overall representation diagram of the EMI receiver with different components

The gains ($G_1 = 1.08$, $G_3 = 2.4$) and quality factors ($Q_1 = 13.5$, $Q_3 = 32.7$) for the first and second filter pairs were optimized via iterative simulations to achieve a 9 kHz bandwidth and flat passband meeting CISPR-16 standards, as shown in Fig. 5 (c). The first pair ensures passband flatness around 150 kHz, while the second pair enhances roll-off and bandwidth control. Higher Q values improve selectivity but increase sensitivity to parameter variations, which was balanced to ensure robust performance.

3- *Implementation of the RBW Filters*:

To implement the RBW filters in practical applications, it is essential to utilize their discrete-time transfer functions. In this work, the backward Euler discretization method is adopted to maintain simplicity and avoid unnecessary computational complexity. This method approximates the derivative using two consecutive signal samples, enabling straightforward real-time implementation. By applying this approach, Equation (5) yields the discrete form necessary for realizing the proposed RBW filters in digital systems.

$$F_i(z) = G_i.\frac{\omega_{ni}.T_s}{Q_i}.\frac{1 - z^{-1}}{b_0 + b_1.z^{-1} + z^{-2}}$$

where,

$$b_0 = 1 + \frac{\omega_{ni}.T_s}{Q_i} + (\omega_{ni}.T_s)^2 \qquad (5)$$

$$b_1 = -2 - \frac{\omega_{ni}.T_s}{Q_i}$$

$$i = 1\sim 4$$

In this equation, the subscript "i" ranges from 1 to 4, corresponding to the filter numbering F1–F4 of (1)-(4). Also, ω_{ni} is the cutoff frequency (rad/s) for filters F1–F4, and T_s is the sample time.

The backward Euler method was selected to discretize Equation (5) due to its simplicity and unconditional stability, making it well-suited for real-time implementation. This method requires only 12 multiplications per sample, contributing to computational efficiency without compromising performance. For the 150 kHz RBW filter, it achieves 100% steady-state accuracy, as demonstrated in Fig. 6. At higher operating frequencies, such as 30 MHz, minor frequency warping may occur—resulting in a center frequency shift of less than 1%. This distortion can be mitigated by increasing the sampling rate to 2 MHz. While alternative discretization techniques, such as the bilinear transformation, offer more precise frequency mapping, they come at the cost of increased computational complexity.

The proposed RBW filter structure employs symmetrical cutoff frequencies to ensure a balanced frequency response aligned with the flat mid-band and steep roll-off characteristics required by CISPR-16 standards (see Fig. 3). This symmetry simplifies the design by ensuring that the amplification and attenuation effects of each filter pair—defined by Equations (1)–(4)—cancel each other appropriately outside the target passband. As a result, the filter exhibits a response that conforms to standard specifications, such as the 9 kHz bandwidth required for Band B. The filter configuration was analytically derived by setting the cutoff frequencies symmetrically around the center frequency (e.g., 150 kHz in the design example), enabling a flat band-pass response and controlled roll-off, as shown in Fig. 5(c).

It is important to note that asymmetric cutoff frequency configurations were evaluated during the design process. However, these designs produced undesirable band-pass ripples and insufficient stopband attenuation, failing to satisfy CISPR-16 criteria. In contrast, the symmetrical approach leverages the complementary behavior of filter pairs to achieve a flat passband (within ±0.5 dB) and strong stopband rejection, as illustrated in Fig. 5(c). Moreover, this configuration simplifies tuning and reduces computational overhead, reinforcing the practical advantages of the proposed methodology.

IV. Simulation Results

In this section, the performance of the proposed RBW filter is validated through time-domain simulations conducted in MATLAB/Simulink. A 150 kHz test signal is applied, with its amplitude increasing linearly via a ramp function at a slope of 0.25 V/s. The signal reaches its steady-state condition at approximately 4.0 seconds, as illustrated by the blue trace labeled "Original Signal" in Fig. 6. This input is processed using the proposed filter configuration shown in Fig. 5, and the corresponding filtered output is presented as the red trace in Fig. 6. To enable detailed waveform analysis, Figs. 6(a) through 6(e) display zoomed-in views of the signal at different time intervals. Visual inspection of these plots confirms a strong alignment between the original and filtered signals. Fig. 7 compares the amplitudes of the original and filtered signals, clearly demonstrating the close tracking achieved by the proposed RBW filter. Fig. 8 quantifies the percentage error between the amplitudes of the original and filtered signals. The error remains consistently below 0.02 per unit (p.u.) throughout both the transient and steady-state periods. Notably, the highest error values occur in the low-amplitude region; however, the error decreases to below 3% once the input signal amplitude exceeds 0.6 p.u.

These results confirm that the proposed RBW filter maintains high accuracy even during dynamic amplitude transitions. Specifically, the filter's accuracy improves significantly after t=2.5 seconds, when the input amplitude surpasses 60%, and reaches 100% accuracy under steady-state conditions beyond 4.0 seconds, as depicted in Fig. 8. It is important to highlight that, in practical EMI measurement scenarios, steady-state behavior is of primary importance, as dynamic conditions are not typically considered standard criteria for assessment. Nevertheless, dynamic amplitude changes serve as stringent test conditions, challenging the stability and accuracy of amplitude extraction methods. The strong performance of the proposed RBW filter under such conditions underscores its robustness and reliability.

It is also worth noting that the proposed 8th-order RBW filter, which requires only 12 multiplications per sample due

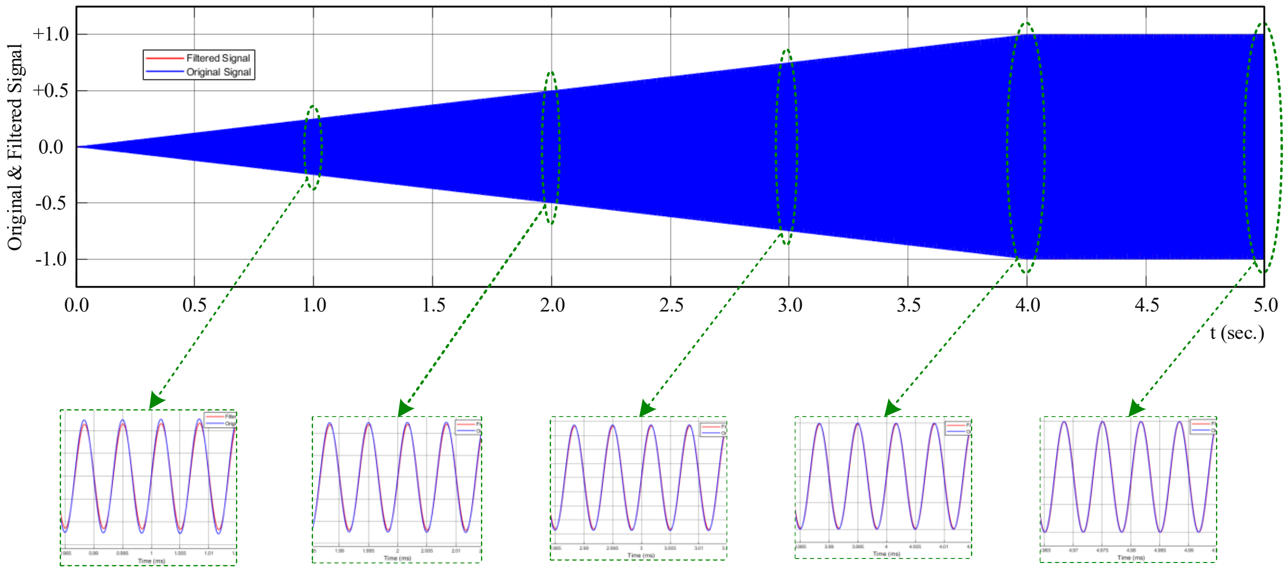

(a) (b) (c) (d) (e)

Fig. 6 the 150 kHz signal with ramp increase in the amplitude with the ramp rate of 0.25 volts/sec., signal waveforms shown in (a) to (e) corresponding to time slots of 1.0, 2.0, 3.0, 4.0, and 5.0 seconds, respectively.

to its paired second-order structure, achieves 100% steady-state accuracy and less than 3% error during transient conditions for a 150 kHz signal, as shown in Fig. 6. In contrast, a fourth-order Butterworth filter—while requiring fewer operations (8 multiplications per sample) and offering comparable passband flatness—features a less steep roll-off and increased complexity when scaled to higher orders to meet CISPR-16 requirements. The simpler tuning and high accuracy of the proposed approach thus offer a favorable trade-off between computational efficiency and regulatory compliance.

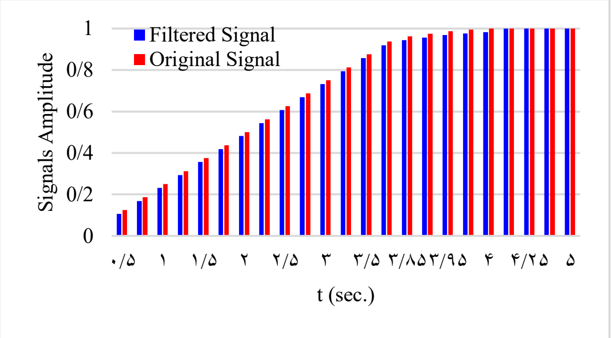

Fig. 7 the amplitudes of original and the filtered signals shown in Fig. 6, showing close proximity of these signals using the proposed RBW-filter

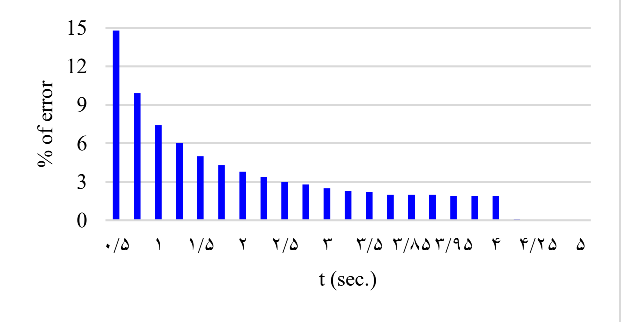

Fig. 8 the percent of error between amplitudes of original and the filtered signals shown in Fig. 6, showing the improved performance during higher amplitudes and under the steady-state region.

V. Conclusions

This paper presents a comprehensive approach to the design of Resolution Bandwidth (RBW) filters for Electromagnetic Interference (EMI) applications, addressing key challenges in modern measurement systems. The proposed structure employs paired complementary second-order filters with symmetrical cutoff frequencies (e.g., $f_0 \pm f_1$ and $f_0 \pm f_2$), achieving full compliance with CISPR-16 requirements while maintaining computational simplicity. Filter performance is validated through simulations using a 150 kHz signal with a dynamically ramped amplitude, demonstrating 100% accuracy under steady-state conditions. Additionally, the filter exhibits a robust dynamic response, achieving over 97% accuracy when the signal amplitude exceeds 60%. This methodology not only offers a practical and reproducible framework for developing standard-compliant RBW filters but also balances mathematical rigor with real-world applicability, making it a valuable tool for engineers engaged in EMI mitigation strategies.

VI. Acknowledgment

Acknowledge the use of Perplexity AI (https://www.perplexity.ai) to enhance the clarity and language of the manuscript. The tool was used solely for checking sentence grammar and writing during the drafting phase. All suggestions and generated content were critically reviewed and edited by the authors to ensure compliance with academic standards.

REFERENCES

[1] M. Rahmani, S. M. Barakati, S. Yousofi Darmian, V. Barahouei, and M. Bagheri Hashkavayi, “Optimized algorithm for open-circuit fault detection in switches and

capacitor voltage balancing control in modular multilevel converters," International Journal of Industrial Electronics Control and Optimization, vol. 7, no. 1, pp. 15-27, 2024.

[2] S. Ahmadi, K. Khalaj Monfared, M. Khalilzadeh, and H. Imaneini, "A Technical Review on the Proper Design of Gate Drivers in Industrial Power Electronics Applications," International Journal of Industrial Electronics Control and Optimization, vol. 7, no. 2, pp. 109-117, 2024.

[3] M. Behbahanipour, S. F. Zarei, and M. Shateri, "Impedance-Based Approach for Locating Short-Circuit Faults in Inverter-Based Active Distribution Networks," International Journal of Industrial Electronics Control and Optimization, vol. 7, no. 3, pp. 225-233, 2024.

[4] H. A. H. Al-Ameedee, M. Delshad, N. A. Shalash, and B. Fani, "A new soft switching dual-input high step-up converter for renewable energy systems," International Journal of Industrial Electronics Control and Optimization, vol. 8, no. 2, pp. 211-219, 2025.

[5] J. Shahsevani and R. Beiranvand, "A Compact, High Efficiency, and Portable Wireless EV Resonant Charger," International Journal of Industrial Electronics Control and Optimization, vol. 8, no. 2, pp. 137-148, 2025.

[6] H. Malekpoor and M. Hamidkhani, "Radiation Improvement of Low-Profile Microstrip Antenna by Utilizing AMC Surface for MIMO and Wireless Systems," International Journal of Industrial Electronics Control and Optimization, vol. 8, no. 2, pp. 129-136, 2025.

[7] S. F. Zarei, M. A. Ghasemi, S. Peyghami, P. Davari, H. Mokhtari, and F. Blaabjerg, "Characterization of proportional-integral-resonant compensator for DC link voltage control," in 2018 IEEE 19th Workshop on Control and Modeling for Power Electronics (COMPEL), 2018: IEEE, pp. 1-8.

[8] M. A. Ghasemi, M. Parniani, S. F. Zarei, and H. M. Foroushani, "Fast maximum power point tracking for PV arrays under partial shaded conditions," in *2016 18th European Conference on Power Electronics and Applications (EPE'16 ECCE Europe)*, 2016: IEEE, pp. 1-12.

[9] S. F. Zarei and S. Khankalantary, "A simplified frequency model for industrial common-mode chocks used in high-power converters," *Journal of Electromagnetic Engineering and Science,* vol. 21, no. 1, pp. 15-22, 2021.

[10] L. Yuan, J. Zhang, Z. Liang, M. Hu, G. Chen, and W. Lu, "EMI challenges in modern power electronic-based converters: recent advances and mitigation techniques," *Frontiers in Electronics,* vol. 4, p. 1274258, 2023.

[11] Z. Zhang, Y. Hu, X. Chen, G. W. Jewell, and H. Li, "A review on conductive common-mode EMI suppression methods in inverter fed motor drives," *IEEE Access,* vol. 9, pp. 18345-18360, 2021.

[12] Z. Ma, Y. Lai, Y. Yang, Q. Huang, and S. Wang, "Review of radiated EMI modeling and mitigation techniques in power electronics systems," in *2023 IEEE Applied Power Electronics Conference and Exposition (APEC)*, 2023: IEEE, pp. 1776-1783.

[13] H. Jie, Z. Zhao, H. Li, C. Wang, Y. Chang, and K. Y. See, "Characterization and Circuit Modeling of Electromagnetic Interference Filtering Chokes in Power Electronics: A Review," *IEEE Transactions on Power Electronics,* 2024.

[14] S. Dey, A. Mallik, and S. Mishra, "A mathematical design approach to volumetric optimization of EMI filter and modeling of CM noise sources in a three-phase PFC," *IEEE Transactions on Power Electronics,* vol. 37, no. 1, pp. 462-472, 2021.

[15] D. Zhang, M. Leibl, J. Muhlethaler, J. Huber, and J. W. Kolar, "Analytical Modeling and Comparison of EMI Pre-Filter Noise Emissions of Three-Phase Voltage and Current DC-Link Converters," *IEEE Transactions on Power Electronics,* 2024.

[16] S. Negri, G. Spadacini, F. Grassi, and S. A. Pignari, "Prediction of EMI filter attenuation in power-electronic converters via circuit simulation," *IEEE Transactions on Electromagnetic Compatibility,* vol. 64, no. 4, pp. 1086-1096, 2022.

[17] M. J. Heller, F. Krismer, and J. W. Kolar, "EMI filter design for the integrated dual three-phase active bridge (D3AB) PFC rectifier," *IEEE Transactions on Power Electronics,* vol. 37, no. 12, pp. 14527-14546, 2022.

[18] R. Kumar and C. N. Bhende, "Model predictive control-based voltage oscillations stabilizer for point-of-load converter with EMI filter in DC microgrids," *IEEE Journal of Emerging and Selected Topics in Industrial Electronics,* 2024.

[19] H. Hizarci, U. Pekperlak, and U. Arifoglu, "Conducted emission suppression using an EMI filter for grid-tied three-phase/level T-type solar inverter," *IEEE Access,* vol. 9, pp. 67417-67431, 2021.

[20] S. Negri, G. Spadacini, F. Grassi, and S. Pignari, "Measurement-based equivalent circuit model for time-domain simulation of EMI filters," in *2022 International Symposium on Electromagnetic Compatibility–EMC Europe*, 2022: IEEE, pp. 793-798.

[21] D. Nesic and T. Milosevic, "Application of a New Algorithm for the Wide Bandpass Filters," in *2021 15th International Conference on Advanced Technologies, Systems and Services in Telecommunications (TELSIKS)*, 2021: IEEE, pp. 92-95.

[22] J. Yan, X. Pei, Y. Yu, K. Zhang, and T. Li, "EMI Receiver Modeling Based on Two-phase Scanning Mode," in *2021 IEEE 1st International Power Electronics and Application Symposium (PEAS)*, 2021: IEEE, pp. 1-5.

[23] S. Nayak, V. Pandey, and K. Hatua, "A Dithering Technique for Mitigation of Conducted Emission Noise of SiC MOSFET Based VSI Driving an Induction Motor," *IEEE Transactions on Power Electronics,* 2023.

[24] N. N. Esfetanaj, J. Meyer, H. Wang, F. Blaabjerg, and P. Davari, "Differential mode noise prediction and analysis in single and three phase grid-tied inverters for the frequency range of 9-150 kHz," in *2021 23rd European Conference on Power Electronics and Applications (EPE'21 ECCE Europe)*, 2021: IEEE, pp. 1-10.

[25] Z. Chen, J. Zhang, and S. Shao, "Optimization of Frequency Jittering Parameters for Conducted EMI Suppression in Switching Mode Power Supplies," in *2023 IEEE 3rd International Conference on Industrial Electronics for Sustainable Energy Systems (IESES)*, 2023: IEEE, pp. 1-6.

[26] H. Chen and S. Ye, "Modeling and optimization of EMI filter by using artificial neural network," *IEEE Transactions on Electromagnetic Compatibility,* vol. 61, no. 6, pp. 1979-1987, 2019.

[27] P. Davari, F. Blaabjerg, E. Hoene, and F. Zare, "Improving 9-150 kHz EMI performance of single-phase PFC rectifier," in *CIPS 2018; 10th International Conference on Integrated Power Electronics Systems*, 2018: VDE, pp. 1-6.

Seyed Fariborz Zarei received his B.Sc. in Electrical Engineering from Amirkabir University of Technology (2012) and his M.Sc. and Ph.D. from Sharif University of Technology (2014, 2019). He was a Visiting Ph.D. Scholar at Aalborg University in 2018. Since 2021, he has been with Qom University of Technology, promoted to Associate Professor in 2025. Dr. Zarei has published over 45 papers on power electronics and power grids, focusing on modeling, control, protection, and stability. He founded the Power Electronic and Grid Laboratory in 2022, studying DC/AC converters and their interaction with AC grids through advanced experimental platforms.

Saeed Hasanzadeh earned his B.Sc. from Shahroud University of Technology (2003) and his M.Sc. and Ph.D. from the University of Tehran (2006, 2012), specializing in High Voltage Engineering and Wireless Power Transfer. He joined Qom University of Technology in 2013, became an Associate Professor in 2022, and served as Dean from 2018 to 2023. He is a member of the editorial board of PELSI, IEEE PEDSTC Technical Program Committee, and Scientific Chair of ICREDG2025. He has received top research awards (2019, 2023) and was named Qom Province’s top innovator (2023). His research interests include power electronics, electrical machines, WPT, and high voltage engineering.